

NUMERICAL MODELING OF THERMO-ACOUSTIC INSTABILITY IN A
SELF-EXCITED RESONANCE COMBUSTOR USING FLAMELET MODELING
APPROACH AND TRANSPORTED PROBABILITY DENSITY FUNCTION
METHOD

A Dissertation

Submitted to the Faculty

of

Purdue University

by

Tejas Pant

In Partial Fulfillment of the

Requirements for the Degree

of

Doctor of Philosophy

August 2019

Purdue University

West Lafayette, Indiana

THE PURDUE UNIVERSITY GRADUATE SCHOOL
STATEMENT OF DISSERTATION APPROVAL

Dr. Haifeng Wang, Chair

School of Aeronautics and Astronautics

Dr. Carson Slabaugh

School of Aeronautics and Astronautics

Dr. Tom Shih

School of Aeronautics and Astronautics

Dr. William Anderson

School of Aeronautics and Astronautics

Approved by:

Dr. Wayne Chen

Head of the School Graduate Program

Dedicated to my grandfather and grandmother for making my dream of coming to
Purdue University a reality

ACKNOWLEDGMENTS

Firstly, I would like to thank my adviser, Professor Haifeng Wang for giving me the opportunity to work with him for the last seven years. I still remember the first day I went to his office to talk to him about joining his research group and how welcoming he has been to everything since then. He has been a constant source of inspiration for me and his guidance and support has helped me during the worst times in my PhD study. I am grateful to him for being so patient with me and giving me the freedom to experiment with new ideas and provide useful constructive criticism whenever I did something wrong.

Secondly, I would like to thank Professor William Anderson for giving me the opportunity to collaborate with him on a number of projects. It was an honour to learn about combustion instability from one of the world's best.

I would also like to thank Professor Tom Shih and Professor Carson Slabaugh who graciously agreed to be on my committee.

Next, I would like to thank my parents and my grandparents without whom I would have never been able to realize my dream of coming to Purdue University. I will forever be indebted to you. I would like to thank my sister, brother-in-law and my little baby niece for making US feel like home to me and helping me out financially whenever the need be. My parents-in-law, sister-in-law and brother-in-law have always cared for me as if I am their own son and have always encouraged me no matter what the circumstances are and I cannot thank them enough.

I would like to thank the wonderful friends I made during my time here, Aalok, Maithilee, Eshaan, Nitin, Aditya, Harshad, Gowtham, Rajas, Chinmay, Aditi, Kaushtubh, Ninad, Pulkit P., Pulkit A., Mrudula, Chao, Pei, Yu-Chi, Lalit, Ravi, Shanmukesh, Paht, Nyansafo, Rufat, Jie, Utsav, Shashank, Tianfang, Nilesh, Akshay, Adwiteey.

Last but not the least, I would like to thank the special friend, back home in India during Masters study who later came here to the US, and now is my better half, Shabnam. She has had to sacrifice a lot for making this dream of mine come true and I owe the future years to her. I always tell her, if my parents brought me to the US, you are the one who helped me survive here.

TABLE OF CONTENTS

	Page
LIST OF TABLES	x
LIST OF FIGURES	xii
ABSTRACT	xxi
1 INTRODUCTION	1
1.1 Overview of Thermo-Acoustic Instability	1
1.2 Challenges in Numerical Modeling	1
1.2.1 Thermo-Acoustic Interaction	4
1.2.2 Compressibility	4
1.2.3 Wide Range of Length and Time Scales	5
1.2.4 Detailed Chemical Kinetics	5
1.2.5 Turbulence-Chemistry Interactions	5
1.2.6 Differential Molecular Diffusion	6
1.3 Current Status of Modeling	6
1.3.1 Lower Order Modeling	7
1.3.2 Higher Order Modeling	8
1.4 Objectives and Outline	10
1.5 Major Contributions	12
2 PURDUE SELF-EXCITED MODEL ROCKET COMBUSTOR	14
2.1 Overview of Rocket Combustor	14
2.2 Experimental Results	15
2.3 Numerical Modeling	18
3 PHYSICAL MODELS	22
3.1 Compressible and Turbulent Flow modeling	22
3.2 Flamelet Models	24
3.2.1 Steady Laminar Flamelet Model	24
3.2.2 Flamelet/Progress Variable Model	27
3.2.3 Flamelet/Progress Variable Model with only Burning Branch	28
3.2.4 Flamelet/Progress Variable Model with Zero Mixture Fraction Variance	29
3.3 Transported Probability Density Function Method for Turbulent Com- bustion Modeling	29
3.4 Eulerian Monte Carlo Fields Method	32
3.5 Mixing Model	34

	Page
3.5.1	IEM Mixing Model 34
3.5.2	Interaction by Partially Exchanging with Mean Mixing Model . 35
3.6	Stochastic Partial Differential Equation for Enthalpy 36
3.7	Stochastic Terms and Model Consistency in the EMCF method 39
3.7.1	EMCF-O Method 41
3.7.2	EMCF-M Method 41
3.7.3	EMCF-C2 Method 41
3.8	Coupling between Flow and Turbulence Solver and EMCF Solver . . . 42
3.8.1	Method 1 to Calculate filtered Density 43
3.8.2	Method 2 to Calculate filtered Density 44
4	NUMERICAL APPROACHES 46
4.1	Governing Equations in Conservative Coupled Form 46
4.2	Flamelet Model Implementation 47
4.3	Flamelet Solver 50
4.3.1	Presumed-PDF Table Integration Approaches 50
4.3.2	Comparison of Different Presumed-PDF Integration Approaches 54
4.4	Presumed β -PDF Integration for Mixture Fraction 55
4.4.1	β -PDF Integration in Flamelet Models 55
4.4.2	Traditional Schemes for the β -PDF Integration 56
4.4.3	Piece-Wise Semi-Analytical (PWSA) Integration 56
4.5	Transported PDF Model Implementation 57
4.5.1	Implementation of Mixing Models 61
4.5.2	Discretization of Stochastic Term 62
4.6	Finite-Volume Approach for Solving Governing Equations 63
5	EFFECT OF DIFFERENT PRESUMED-PDF TABLE INTEGRATION APPROACHES ON FLAMELET MODELING OF A TURBULENT JET FLAME AND A SELF-EXCITED RESONANCE ROCKET COMBUSTOR 67
5.1	Sandia Piloted Flame D 67
5.1.1	Sandia Flame D and Model Approaches 68
5.1.2	Examination of Numerical β -PDF Integration for Mixture Fraction 68
5.1.3	Examination of Integrated Flamelet Tables 70
5.1.4	Predictions of Flow and Turbulence Fields 71
5.1.5	Predictions of Mixture Fraction and Progress Variable 72
5.1.6	A Priori Testing of Flamelet Table Accuracy 74
5.1.7	<i>A Posteriori</i> Testing of Flamelet Table Accuracy 78
5.2	Self-Excited Resonance Model Rocket Combustor 82
5.2.1	Examination of Integrated Flamelet Tables 83
5.2.2	Predictions of Pressure Fluctuation and Power Spectral Density (PSD) 84
5.2.3	Predictions of Time-Averaged Fields 87

	Page
6 EFFECT OF COMBUSTION DYNAMICS, TURBULENCE AND CHEMICAL KINETICS, AND THEIR INTERACTIONS ON THERMO-ACOUSTIC INSTABILITY MODELING	90
6.1 Experimental Validation	90
6.1.1 Simulation Setup	91
6.1.2 Predictions of Pressure Signals	92
6.1.3 Prediction of Flow Field and Scalars	96
6.2 Parametric Studies of Modeling of Thermo-Acoustic instability	99
6.2.1 Effect of Transient Flame Dynamics	99
6.2.2 Effect of Artificial Amplification of Global Damkohler Number	101
6.2.3 Effect of Neglecting Mixture Fraction Fluctuations	102
6.3 Examination of Transient Flame Dynamics	104
6.3.1 Effect of Local Dynamic Flame Events on Thermo-Acoustic Instability	104
6.3.2 Effect of Thermo-Acoustic Instability on Transient Flame Dynamics	108
7 TRANSPORTED PDF MODELING OF COMPRESSIBLE TURBULENT REACTIVE FLOWS BY USING THE EULERIAN MONTE CARLO FIELDS METHOD	113
7.1 One-Dimensional Turbulent Mixing Layer	113
7.2 Subsonic Non-Reactive Propane Round Jet	117
7.3 Subsonic Turbulent Jet Flame	120
7.4 Supersonic Hydrogen Jet Flame	126
7.5 Self-Excited Resonance Model Rocket Combustor	131
7.5.1 Prediction of Fluctuating Pressure Signal	135
7.5.2 Prediction of Flow Field and Scalars	138
7.5.3 Parametric Studies of the EMCF Method	141
8 CONCLUSIONS	148
8.1 Scope for Future Work	152
REFERENCES	153
A Derivation and Analysis of Piece-Wise Semi-Analytical (PWSA) Integration Scheme	164
B Formulation of Jacobians $\bar{\Gamma}_p$ and $\bar{\Gamma}_p^{-1}$	166
C Formulation of Inviscid Jacobian $\bar{\Gamma}_f$, Viscous Jacobian $\bar{\Gamma}_g$, and Source Term Jacobian $\bar{\Gamma}_h$	172
C.1 Formulation of Jacobians $\bar{\Gamma}_f$, $\bar{\Gamma}_g$, $\bar{\Gamma}_h$ and $\bar{\Gamma}_p^{-1}$	172
C.1.1 Inviscid Flux Jacobian	172
C.1.2 Viscous Flux Jacobian	174
C.1.3 Source Term Jacobian	176

VITA 180

LIST OF TABLES

Table	Page
2.1 Details of model rocket combustor experiment [76] for the stable and unstable operating condition.	17
3.1 Correction parameters Γ_{cY_i} , Γ_{ch} and W_c^n for the EMCF-O, EMCF-M and EMCF-C2 methods.	40
5.1 Comparison of the time-averaged pressure $\langle P_c \rangle$ in the combustor, the level of combustion instability ($\langle P_{pp} \rangle / \langle P_c \rangle$), the frequency (f_1) and the amplitude (A_1) of the first mode from the experiment [76] with simulations using the different table integration approaches.	84
6.1 Experimental inlet conditions for the fuel stream and oxidizer stream for the numerical simulations of the model rocket combustor.	91
6.2 Comparison of the time-averaged pressure $\langle P_c \rangle$ at $x/D_{ox} = 18$ near the combustor wall, level of thermo-acoustic instability $\langle P_{pp} \rangle / \langle P_c \rangle$, frequency f_1 and amplitude A_1 of the first mode from the experiment [76] with the simulations using the SLF model and FPV model for the stable operating condition and the unstable operating condition in the model rocket combustor [76].	93
7.1 Parameters for one-dimensional turbulent mixing layer.	114
7.2 Inlet conditions for the numerical simulations of the subsonic turbulent round jet based on experiment [143].	117
7.3 Inlet conditions for the numerical simulations of the subsonic turbulent jet flame based on experiment [145].	121
7.4 Inlet conditions for the numerical simulations of the supersonic turbulent jet flame based on experiment [147].	127
7.5 Inlet conditions for the fuel stream and oxidizer stream for the numerical simulations of the model rocket combustor based on experiment [76]. . .	135

Table	Page
7.6 Comparison of the level of thermo-acoustic instability ($\langle P_{pp} \rangle / \langle P_c \rangle$) and the frequencies (f_1, f_2) and the amplitudes (A_1, A_2) of the first two modes from the experiment [76] with the simulations for $L_{ox} = 13.97\text{cm}$. The pressure data is measured at measured at $x/D_{ox} = 18$ near the combustor wall. The model results are obtained for the EMCF-O method with analytical implementation of the IEM mixing model and Density 2 formulation with gradient limiters.	136
7.7 Comparison of the level of thermo-acoustic instability ($\langle P_{pp} \rangle / \langle P_c \rangle$) and the frequencies (f_1, f_2) and the amplitudes (A_1, A_2) of the first two modes from the experiment [76] with the simulations using the PDF model for the stable operating condition and the unstable operating condition. The pressure data is measured at measured at $x/D_{ox} = 18$ near the combustor wall. The model results are obtained for the EMCF method parameters $N_{sf} = 8$ and $C_\phi = 2.0$	138
7.8 Comparison of the level of thermo-acoustic instability ($\langle P_{pp} \rangle / \langle P_c \rangle$) and the frequencies (f_1, f_2) and amplitudes (A_1, A_2) of the first two modes from the experiment [76] with simulations using the PDF model for the unstable operating condition. The pressure data is measured at measured at $x/D_{ox} = 18$ near the combustor wall. The model results are obtained for $N_{sf} = 4, 8$ and 16 and $C_\phi = 2.0$	143
7.9 Comparison of the level of thermo-acoustic instability ($\langle P_{pp} \rangle / \langle P_c \rangle$) and the frequencies (f_1, f_2) and amplitudes (A_1, A_2) of the first two modes from the experiment [76] with simulations using the PDF model for the unstable operating condition. The pressure data is measured at measured at $x/D_{ox} = 18$ near the combustor wall. The model results are obtained for the EMCF method parameters $N_{sf} = 8$ and $C_\phi = 2.0, 4.0$ and 8.0 . . .	145

LIST OF FIGURES

Figure	Page
1.1 Damaged components of a gas turbine engine due to thermo-acoustic instability [1].	2
1.2 Feedback mechanism driving thermo-acoustic instability [3].	3
2.1 Schematic of self-excited model rocket combustor [59, 75, 76].	14
2.2 Fluctuation pressure signal p' at $x/D_{ox} = 18$ in model rocket combustor [76] for stable operating condition.	17
2.3 Fluctuation pressure signal p' at $x/D_{ox} = 18$ in model rocket combustor experiment [76] for unstable operating condition.	18
3.1 Variation of maximum flame temperature T_{max} with mixture fraction dissipation rate at stoichiometric condition χ_{st} obtained from laminar flamelet solutions. The boundary conditions of the model rocket combustor are used.	25
5.1 Comparison of the different β -PDF numerical integration schemes with $\tilde{\xi} = 0.352$ and the normalized mixture fraction variance $\xi_v = \tilde{\xi}''^2/(\tilde{\xi}(1 - \tilde{\xi})) = 0.2$ (first row) and $\tilde{\xi} = 0.352$ and $\xi_v = 0.6$ (second row). Left column: the shapes of the β -PDF used for the integration; middle column: the convergence of the numerical integration error against n_ξ^{-1} ; Right column: the convergence of the error of the PDF normalization condition against n_ξ^{-1} .	69
5.2 Contour plots of the mean temperature \tilde{T} , the mean mass fractions of species H_2O , CO , and OH , and the mean reaction rate $\tilde{\omega}_C$ for the progress variable C , in the mean mixture fractions $\tilde{\xi}$ and mean progress variable space \tilde{C} from the integrated flamelet tables are shown for the LFSP method (the first row), the FMNPV method (the second row), and the FMNMF method (the third row) in Sandia flame D. The normalized variance of the mixture fraction is fixed at $\xi_v = \tilde{\xi}''^2/(\tilde{\xi}(1 - \tilde{\xi})) = 0.1$	70
5.3 Radial profiles of the mean axial velocity \tilde{U} (top) and turbulent kinetic energy \tilde{k} (bottom) at the axial locations $x/D = 7.5, 15,$ and 30 along with the centerline profile in Sandia flame D. The model results are obtained using the FPV model with the three different table integration approaches.	71

Figure	Page
5.4 Radial profiles of the mean mixture fraction $\tilde{\xi}$ (top), RMS mixture fraction ξ_{RMS} (middle) and mean progress variable \tilde{C} (bottom) at the axial locations $x/D = 7.5, 15,$ and 30 along with the centerline profile in Sandia flame D. The model results are obtained using the FPV model with the three different table integration approaches.	73
5.5 Radial profiles of the dependent variables mean temperature \tilde{T} , mean mass fractions of species $\text{CO}_2, \text{H}_2\text{O}, \text{CO},$ and OH at the axial locations $x/D = 7.5, 15,$ and 30 along with the centerline profile in Sandia flame D. The values of $(\tilde{\xi}, \xi_{RMS}, \tilde{C})$ used for looking up the table are taken directly from the experiment [7].	74
5.6 The profiles of dependent variables mean temperature \tilde{T} , mean mass fractions of species $\text{CO}_2, \text{H}_2\text{O}, \text{CO},$ and OH against the mean mixture fraction $\tilde{\xi}$ at the axial locations $x/D = 7.5, 15,$ and 30 along with the centerline in Sandia flame D. The values of $(\tilde{\xi}, \xi_{RMS}, \tilde{C})$ used for looking up the table are taken directly from the experiment [7].	75
5.7 The profiles of dependent variables mean temperature \tilde{T} , mean mass fractions of species $\text{CO}_2, \text{H}_2\text{O}, \text{CO},$ and OH against the RMS mixture fraction ξ_{RMS} at the axial locations $x/D = 7.5, 15,$ and 30 along with the centerline in Sandia flame D. The values of $(\tilde{\xi}, \xi_{RMS}, \tilde{C})$ used for looking up the table are taken directly from the experiment [7].	76
5.8 The profiles of dependent variables mean temperature \tilde{T} , mean mass fractions of species $\text{CO}_2, \text{H}_2\text{O}, \text{CO},$ and OH against the mean progress variable \tilde{C} at the axial locations $x/D = 7.5, 15,$ and 30 along with the centerline in Sandia flame D. The values of $(\tilde{\xi}, \xi_{RMS}, \tilde{C})$ used for looking up the table are taken directly from the experiment [7].	77
5.9 Radial profiles of the mean temperature \tilde{T} , mean mass fraction of species $\text{CO}_2, \text{H}_2\text{O}, \text{CO},$ and OH at the axial locations $x/D = 7.5, 15,$ and 30 along with the centerline profiles. The model results are obtained using the FPV model with the three different table integration approaches.	79
5.10 The profiles of the mean temperature \tilde{T} , mean mass fractions of species $\text{CO}_2, \text{H}_2\text{O}, \text{CO},$ and OH against the mean mixture fraction $\tilde{\xi}$ at the axial locations $x/D = 7.5, 15,$ and 30 along with the centerline in Sandia flame D. The model results are obtained using the FPV model with the three different table integration approaches.	80

Figure	Page
5.11 The profiles of the mean temperature \tilde{T} , mean mass fractions of species CO_2 , H_2O , CO , and OH against the mixture fraction RMS ξ_{RMS} at the axial locations $x/D = 7.5, 15,$ and 30 along with the centerline in Sandia flame D. The model results are obtained using the FPV model with the three different table integration approaches.	81
5.12 The profiles of the mean temperature \tilde{T} , mean mass fractions of species CO_2 , H_2O , CO , and OH against the mean progress variable \tilde{C} at the axial locations $x/D = 7.5, 15,$ and 30 along with the centerline in Sandia flame D. The model results are obtained using the FPV model with the three different table integration approaches.	82
5.13 Contour plots of the mean temperature \tilde{T} , the mean mass fractions of species H_2O , CO , and OH , and the mean reaction rate $\tilde{\omega}_C$ for the progress variable C , in the mean mixture fractions $\tilde{\xi}$ and mean progress variable space \tilde{C} are shown from the integrated flamelet tables for the LFSP method (the first row), the FMNPV method (the second row) and the FM-NMF method (the third row) in the model rocket combustor. The normalized variance of the mixture fraction is fixed at $\xi_v = \tilde{\xi}''^2 / (\tilde{\xi}(1 - \tilde{\xi})) = 0.1$ and the pressure is at 15 atm.	83
5.14 Fluctuating pressure signal p' at $x/D_{ox} = 18$ in the model rocket combustor. The model results are obtained by using the FPV model with the three different table integration approaches.	85
5.15 PSD of raw pressure data at $x/D_{ox} = 18$ in the model rocket combustor. The model results are obtained by using the FPV model with the three different table integration approaches.	86
5.16 Radial profiles of the time-averaged axial velocity $\langle \tilde{U} \rangle$, time-averaged turbulent kinetic energy $\langle \tilde{k} \rangle$, time-averaged mixture fraction $\langle \tilde{\xi} \rangle$, RMS mixture fraction $\langle \xi_{RMS} \rangle$, time-averaged progress variable $\langle \tilde{C} \rangle$, time-averaged temperature $\langle \tilde{T} \rangle$ and mass fractions of species CO_2 , H_2O , CO , and OH at the axial location $x/D_{ox} = 10$ in the model rocket combustor. The model results are obtained using the FPV model with the three different table integration approaches.	87
6.1 Fluctuating pressure signal p' at $x/D_{ox} = 18$ near the combustor wall for stable operating condition (left) and unstable operating condition (right). The model results are obtained by using the SLF model and the FPV model.	94
6.2 PSD of raw pressure data at $x/D_{ox} = 18$ near the combustor wall for stable operating condition (left) and unstable operating condition (right). The model results are obtained by using the SLF model and the FPV model.	95

Figure	Page
6.3 Contour plots of the axial velocity \tilde{U} (with streamlines) (top), temperature \tilde{T} (middle) and the mass fraction of OH species (bottom) for the SLF model (top contour plot for each variable) and the FPV model (bottom contour plot for each variable) for the unstable operating condition. The upper half of each contour plot is the time-averaged result and the lower half is the instantaneous result.	96
6.4 Contour plot of temperature \tilde{T} near the dump plane for the SLF model (top contour plot) and the FPV model (bottom contour plot) for the unstable operating condition. The upper half of the contour plot is the time-averaged result and the lower half is the instantaneous result.	97
6.5 Fluctuating pressure signal p' at $x/D_{ox} = 18$ near the combustor wall for unstable operating condition. The model results are obtained by using the SLF model and FPV model (top left), FPV-B model (top right), FPV model with amplified Damkohler number Da (bottom left) and FPV-ZV model (bottom right).	100
6.6 Contour plots of the instantaneous temperature \tilde{T} for the SLF model, FPV model and FPV-B model. The bottom plot shows the 26 computational bins into which the combustor computational domain is divided.	104
6.7 Zoomed-in view of contour plots of the instantaneous temperature \tilde{T} for Bin-6, Bin-7, Bin-8 and Bin-9 for the SLF model, FPV model and FPV-B model.	105
6.8 Scatter plot of the instantaneous temperature \tilde{T} against mixture fraction ξ for Bin-6, Bin-7, Bin-8, Bin-9, Bin-16 and Bin-21 for unstable operating condition. The model results are obtained using the SLF model, FPV model and FPV-B model. The red solid lines indicate the burning flamelet solutions for a near-equilibrium condition $\tilde{\xi}''^2 = 0$, $\chi_{st} = 0.1 \text{ s}^{-1}$, $\bar{p} = 1.5 \text{ MPa}$ and close to extinction limit condition $\tilde{\xi}''^2 = 0$, $\chi_{st} = 2668.18 \text{ s}^{-1}$, $\bar{p} = 1.5 \text{ MPa}$. The red dash-dotted lines indicate pure mixing between fuel and oxidizer for the condition $\tilde{\xi}''^2 = 0$, $\chi_{st} = 2668.18 \text{ s}^{-1}$, $\bar{p} = 1.5 \text{ MPa}$	106
6.9 Contour plots of instantaneous pressure \bar{p} at different times for the unstable operating condition. The model results are obtained by using the FPV model.	108

Figure	Page
6.10 Scatter plot of the instantaneous temperature \tilde{T} against mixture fraction $\tilde{\xi}$ in Bin-6 when pressure wave inside the combustion chamber is far away from the bin (left) and when it passes through the bin (right). The red solid lines indicate the burning flamelet solutions for a near-equilibrium condition $\widetilde{\xi''^2} = 0$, $\chi_{st} = 0.1 \text{ s}^{-1}$, $\bar{p} = 1.5 \text{ MPa}$ and close to extinction limit condition $\widetilde{\xi''^2} = 0$, $\chi_{st} = 2668.18 \text{ s}^{-1}$, $\bar{p} = 1.5 \text{ MPa}$. The red dash-dotted lines indicate pure mixing between fuel and oxidizer for the condition $\widetilde{\xi''^2} = 0$, $\chi_{st} = 2668.18 \text{ s}^{-1}$, $\bar{p} = 1.5 \text{ MPa}$. The model results are obtained using the FPV model for the unstable operating condition.	109
6.11 Scatter plot of the instantaneous temperature \tilde{T} against mixture fraction $\tilde{\xi}$ in Bin-7 when pressure wave inside the combustion chamber is far away from the bin (left) and when it passes through the bin (right). The red solid lines indicate the burning flamelet solutions for a near-equilibrium condition $\widetilde{\xi''^2} = 0$, $\chi_{st} = 0.1 \text{ s}^{-1}$, $\bar{p} = 1.5 \text{ MPa}$ and close to extinction limit condition $\widetilde{\xi''^2} = 0$, $\chi_{st} = 2668.18 \text{ s}^{-1}$, $\bar{p} = 1.5 \text{ MPa}$. The red dash-dotted lines indicate pure mixing between fuel and oxidizer for the condition $\widetilde{\xi''^2} = 0$, $\chi_{st} = 2668.18 \text{ s}^{-1}$, $\bar{p} = 1.5 \text{ MPa}$. The model results are obtained using the FPV model for the unstable operating condition.	110
6.12 Scatter plot of the instantaneous temperature \tilde{T} against mixture fraction $\tilde{\xi}$ in Bin-16 when pressure wave inside the combustion chamber is far away from the bin (left) and when it passes through the bin (right). The red solid lines indicate the burning flamelet solutions for a near-equilibrium condition $\widetilde{\xi''^2} = 0$, $\chi_{st} = 0.1 \text{ s}^{-1}$, $\bar{p} = 1.5 \text{ MPa}$ and close to extinction limit condition $\widetilde{\xi''^2} = 0$, $\chi_{st} = 2668.18 \text{ s}^{-1}$, $\bar{p} = 1.5 \text{ MPa}$. The red dash-dotted lines indicate pure mixing between fuel and oxidizer for the condition $\widetilde{\xi''^2} = 0$, $\chi_{st} = 2668.18 \text{ s}^{-1}$, $\bar{p} = 1.5 \text{ MPa}$. The model results are obtained using the FPV model for the unstable operating condition.	111
7.1 The predicted profiles of the scalar mean $\langle\phi\rangle$, scalar RMS ϕ_{RMS} , scalar skewness ϕ_γ and scalar kurtosis ϕ_κ for the single-scalar turbulent mixing layer by using the FV approach and IEM and IPEM mixing models. . . .	115
7.2 The predicted profiles of the scalar mean $\langle\phi\rangle$ and scalar RMS ϕ_{RMS} for the single-scalar turbulent mixing layer by using the FV approach and EMCF-O, EMCF-M and EMCF-C2 methods.	115

Figure	Page
7.3 Radial profile of mean velocity \tilde{U} , mean mixture fraction $\tilde{\xi}$ and mixture fraction RMS ξ_{RMS} at the axial locations $x/D = 15, 30$ and 50 along with the centerline profile for the propane round jet test case for the EMCF-O method and EMCF-C2 method with analytical IEM model, EMCF-O method with analytical IPEM model and EMCF-O method with Euler IEM model.	118
7.4 Radial profile of mixture fraction skewness ξ_γ and mixture fraction kurtosis ξ_κ at the axial locations $x/D = 15, 30$ and 50 along with the centerline profile for the propane round jet test case for the EMCF-O method and EMCF-C2 with analytical IEM model, EMCF-O method with analytical IPEM model and EMCF-O method with Euler IEM model.	119
7.5 Radial profile of mean velocity \tilde{U} , mean mixture fraction $\tilde{\xi}$ and mixture fraction RMS ξ_{RMS} at the axial locations $x/D = 15, 30$ and 50 along with the centerline profile for the propane round jet test case for the Density 1 with gradient limiter, Density 2 with gradient limiter and Density 2 without gradient limiter.	120
7.6 Radial profile of mean axial velocity \tilde{U} at the axial locations $x/D = 8, 9, 11$ and 14 for Cabra flame for the EMCF-O, EMCF-M and EMCF-C2 methods.	121
7.7 Radial profile of mean temperature \tilde{T} , temperature RMS T' , mean mass fraction of H_2 species \tilde{Y}_{H_2} , RMS mass fraction of H_2 species Y'_{H_2} , mean mass fraction of H_2O species and RMS mass fraction of H_2O species Y'_{H_2O} at the axial locations $x/D = 8, 9, 11$ and 14 for Cabra flame for EMCF-O, EMCF-M and EMCF-C2 methods.	122
7.8 Radial profile of mean axial velocity \tilde{U} at the axial locations $x/D = 8, 9, 11$ and 14 for Cabra flame for EMCF-O method with the analytical IEM mixing model, analytical IPEM mixing model and Euler IEM mixing model.	123
7.9 Radial profile of mean temperature \tilde{T} , temperature RMS T' , mean mass fraction of H_2 species \tilde{Y}_{H_2} , RMS mass fraction of H_2 species Y'_{H_2} , mean mass fraction of H_2O species and RMS mass fraction of H_2O species Y'_{H_2O} at the axial locations $x/D = 8, 11, 14$ and 26 for Cabra flame for EMCF-O method with the analytical IEM mixing model, analytical IPEM mixing model and Euler IEM mixing model.	124
7.10 Radial profile of mean axial velocity \tilde{U} at the axial locations $x/D = 8, 9, 11$ and 14 for Cabra flame for Density 1 with gradient limiter, Density 2 with gradient limiter and Density 2 without gradient limiter.	125

Figure	Page
7.11 Radial profile of mean temperature \tilde{T} , RMS temperature T' , mean mass fraction of H ₂ species \tilde{Y}_{H_2} , RMS mass fraction of H ₂ species Y'_{H_2} , mean mass fraction of H ₂ O species and RMS mass fraction of H ₂ O species Y'_{H_2O} at the axial locations $x/D = 8, 11, 14$ and 26 for Cabra flame for Density 1 with gradient limiter, Density 2 with gradient limiter and Density 2 without gradient limiter.	126
7.12 Radial profile of the normalized pitot pressure P_{pit}/P_{ref} at the axial locations $x/D = 6.56, 13.8, 20$ and 26.2 for the supersonic turbulent jet test case for the EMCF-O, EMCF-M and EMCF-C2 methods.	128
7.13 Radial profile of mean mass fraction of H ₂ O species \tilde{Y}_{H_2O} , H ₂ species \tilde{Y}_{H_2} , O ₂ species \tilde{Y}_{O_2} and N ₂ species \tilde{Y}_{N_2} at the axial locations $x/D = 8.26, 15.5, 21.7$ and 27.9 for the supersonic turbulent jet test case for the EMCF-O, EMCF-M and EMCF-C2 methods.	129
7.14 Radial profile of the RMS temperature T' , RMS mass fraction of H ₂ O species Y'_{H_2O} , H ₂ species Y'_{H_2} , O ₂ species Y'_{O_2} and N ₂ species Y'_{N_2} at the axial locations $x/D = 8.26, 15.5, 21.7$ and 27.9 for the supersonic turbulent jet test case for the EMCF-O, EMCF-M and EMCF-C2 methods.	130
7.15 Radial profile of the normalized pitot pressure P_{pit}/P_{ref} at the axial locations $x/D = 6.56, 13.8, 20$ and 26.2 for the supersonic turbulent jet test case for EMCF-O method with the analytical IEM mixing model and the Euler IEM mixing model.	130
7.16 Radial profile of mean mass fraction of H ₂ O species \tilde{Y}_{H_2O} , H ₂ species \tilde{Y}_{H_2} , O ₂ species \tilde{Y}_{O_2} and N ₂ species \tilde{Y}_{N_2} at the axial locations $x/D = 8.26, 15.5, 21.7$ and 27.9 for the supersonic turbulent jet test case for EMCF-O method with the analytical IEM mixing model and the Euler IEM mixing model.	131
7.17 Radial profile of the RMS temperature T' , RMS mass fraction of H ₂ O species Y'_{H_2O} , H ₂ species Y'_{H_2} , O ₂ species Y'_{O_2} and N ₂ species Y'_{N_2} at the axial locations $x/D = 8.26, 15.5, 21.7$ and 27.9 for the supersonic turbulent jet test case for for EMCF-O method with the analytical IEM mixing model and the Euler IEM mixing model.	132
7.18 Radial profile of the normalized pitot pressure P_{pit}/P_{ref} at the axial locations $x/D = 6.56, 13.8, 20$ and 26.2 for the supersonic turbulent jet test case for Density 1 with gradient limiters, Density 2 with gradient limiters and Density 2 without gradient limiters.	132

Figure	Page
7.19 Radial profile of mean mass fraction of H ₂ O species \tilde{Y}_{H_2O} , H ₂ species \tilde{Y}_{H_2} , O ₂ species \tilde{Y}_{O_2} and N ₂ species \tilde{Y}_{N_2} at the axial locations $x/D = 8.26, 15.5, 21.7$ and 27.9 for the supersonic turbulent jet test case for Density 1 with gradient limiters, Density 2 with gradient limiters and Density 2 without gradient limiters.	133
7.20 Radial profile of the RMS temperature T' , RMS mass fraction of H ₂ O species Y'_{H_2O} , H ₂ species Y'_{H_2} , O ₂ species Y'_{O_2} and N ₂ species Y'_{N_2} at the axial locations $x/D = 8.26, 15.5, 21.7$ and 27.9 for the supersonic turbulent jet test case for Density 1 with gradient limiters, Density 2 with gradient limiters and Density 2 without gradient limiters.	134
7.21 Fluctuating pressure signal p' (left) and PSD of raw pressure data (right) measured at $x/D_{ox} = 18$ near the combustor wall in the model rocket combustor for the stable operating condition (top row) and unstable operating condition (bottom row). The model results are obtained for the EMCF method parameters $N_{sf} = 8$ and $C_\phi = 2.0$	137
7.22 Contour plots of the mean axial velocity \tilde{U} , temperature \tilde{T} , mass fraction of CO ₂ species and heat release rate \dot{Q} (left column) and sub-grid RMS of mass fraction of CH ₄ species, temperature T' , CO ₂ species and heat release rate \dot{Q}' (right column) for the stable operating condition. The upper half of each contour plot is the time-averaged result and the lower half is the instantaneous results. The model results are obtained for the EMCF method parameters $N_{sf} = 8$ and $C_\phi = 2.0$	139
7.23 Contour plots of the mean axial velocity \tilde{U} , temperature \tilde{T} , mass fraction of CO ₂ species and heat release rate \dot{Q} (left column) and sub-grid RMS of mass fraction of CH ₄ species, temperature T' , CO ₂ species and heat release rate \dot{Q}' (right column) for the unstable operating condition. The upper half of each contour plot is the time-averaged result and the lower half is the instantaneous results. The model results are obtained for the EMCF method parameters $N_{sf} = 8$ and $C_\phi = 2.0$	140
7.24 Fluctuating pressure signal p' (left) and PSD of raw pressure data (right) measured at $x/D_{ox} = 18$ near the combustor wall in the model rocket combustor for the unstable operating condition. The model results are obtained for $N_{sf} = 4, 8$ and 16 for $C_\phi = 2.0$	142
7.25 Initial raw pressure signal measured at $x/D_{ox} = 18$ in the model rocket combustor. The model results are obtained for $N_{sf} = 4, 8$ and 16 for $C_\phi = 2.0$	143

Figure	Page
7.26 Fluctuating pressure signal p' (left) and PSD of raw pressure data (right) measured at $x/D_{ox} = 18$ near the combustor wall in the model rocket combustor for the unstable operating condition. The model results are obtained for $N_{sf} = 8$ and for $C_\phi = 2.0, 4.0$ and 8.0	144
7.27 Radial profiles of the time-averaged axial velocity $\langle \tilde{U} \rangle$, time-averaged turbulent kinetic energy $\langle k \rangle$, time-averaged temperature $\langle \tilde{T} \rangle$, time-averaged SGS temperature $\langle \tilde{T}_{SGS} \rangle$, time-averaged CO_2 mass fraction and time-averaged SGS CO_2 mass fraction $\langle \tilde{Y}_{\text{CO}_2, \text{SGS}} \rangle$ at the axial locations $x/D_{ox} = 2, 8$ and 18 in the model rocket combustor. The model results are obtained for $C_\phi = 2.0, 4.0$ and 8.0	146

ABSTRACT

Pant Tejas Ph.D., Purdue University, August 2019. Numerical Modeling of Thermo-Acoustic Instability in a Self-Excited Resonance Combustor using Flamelet Modeling Approach and Transported Probability Density Function Method. Major Professor: Haifeng Wang.

Combustion instability due to thermo-acoustic interactions in high-speed propulsion devices such as gas turbines and rocket engines result from pressure waves with very large amplitudes propagating back and forth in the combustion chamber. Exposure to the pressure fluctuations over a long period of time can lead to a catastrophic failure of engines. The underlying physics governing the generation of the thermo-acoustic instability is a complex interaction among heat release, turbulence, and acoustic waves. Currently, it is very difficult to accurately predict the expected level of oscillations in a combustor. Hence development of strategies and engineering solutions to mitigate thermo-acoustic instability is an active area of research in both academia and industry. In this work, we carry out numerical modeling of thermo-acoustic instability in a self-excited, laboratory scale, model rocket combustor developed at Purdue University. Two different turbulent combustion models to account for turbulence-chemistry interactions are considered in this study, the flamelet model and the transported probability density function (PDF) method.

In the flamelet modeling approach, detailed chemical kinetics can be easily incorporated at a relatively low cost in comparison to other turbulent combustion models and it also accounts for turbulence-chemistry interactions. The flamelet model study is divided into two parts. In first part, we examine the effect of different numerical approaches for implementing the flamelet model. In advanced modeling and simulations of turbulent combustion, the accuracy of model predictions is affected by physical model errors as well as errors that arise from the numerical implementation

of models in simulation codes. Here we are mainly concerned with the effect of numerical implementation on model predictions of turbulent combustion. Particularly, we employ the flamelet/progress variable (FPV) model and examine the effect of various numerical approaches for the flamelet table integration, with presumed shapes of PDF, on the FPV modeling results. Three different presumed-PDF table integration approaches are examined in detail by employing different numerical integration strategies. The effect of the different presumed-PDF table integration approaches is examined on predictions of two real flames, a laboratory-scale turbulent free jet flame, Sandia Flame D and the self-excited resonance model rocket combustor. Significant difference is observed in the predictions both of the flames. The results in this study further support the claims made in previous studies that it is imperative to preserve the laminar flamelet structure during integration while using the flamelet model to achieve better predictions in simulations. In the second part of the flamelet modeling study, computational investigations of the coupling between the transient flame dynamics such as the ignition delay and local extinction and the thermo-acoustic instability developed in a self-excited resonance combustor to gain deep insights into the mechanisms of thermo-acoustic instability. A modeling framework that employs different flamelet models (the steady flamelet model and the flamelet/progress variable approach) is developed to enable the examination of the effect of the transient flame dynamics caused by the strong coupling of the turbulent mixing and finite-rate chemical kinetics on the occurrence of thermo-acoustic instability. The models are validated by using the available experimental data for the pressure signal. Parametric studies are performed to examine the effect of the occurrence of the transient flame dynamics, the effect of artificial amplification of the Damkohler number, and the effect of neglecting mixture fraction fluctuations on the predictions of the thermo-acoustic instability. The parametric studies reveal that the occurrence of transient flame dynamics has a strong influence on the onset of the thermo-acoustic instability. Further analysis is then conducted to localize the effect of a particular flame dynamic event, the ignition delay, on the thermo-acoustic instability. The reverse effect of

the occurrence of the thermo-acoustic instability on the transient flame dynamics in the combustor is also investigated by examining the temporal evolution of the local flame events in conjunction with the pressure wave propagation. The above observed two-way coupling between the transient flame dynamics (the ignition delay) and the thermo-acoustic instability provides a plausible mechanism of the self-excited and sustained thermo-acoustic instability observed in the combustor.

The second turbulent combustion model considered in this study is the transported PDF method. The transported PDF method is one of the most attractive models because it treats the highly-nonlinear chemical reaction source term without a closure requirement and it is a generalized model for a wide range of turbulent combustion problems. Traditionally, the transported PDF method has been used to model low-Mach number, incompressible flows where the pressure is assumed to be thermodynamically constant. Since there is significant pressure fluctuations in the model rocket combustor, the flow is highly compressible and it is necessary to account for this compressibility in the transported PDF method. In the past there has been very little work to model compressible reactive flows using the transported PDF and no effort has been made to model thermo-acoustic instability using the transported PDF method. There is a pressing need to further examine and develop the transported PDF method for compressible reactive flows to broaden our understanding of physical phenomenon like thermo-acoustic instability, interaction between combustion and strong shock and expansion waves, coupling between acoustic and heat release which are observed in high-speed turbulent combustion problems. To address this, a modeling framework for compressible turbulent reactive flows by the using the transported PDF method is developed. This framework is validated in a series of test cases ranging from pure mixing to a supersonic turbulent jet flame. The framework is then used to study the thermo-acoustic interactions in the self-excited model rocket combustor.

1. INTRODUCTION

1.1 Overview of Thermo-Acoustic Instability

Thermo-acoustic instability is an undesirable physical phenomenon observed in almost all combustion devices ranging from land-based gas turbines used for power generation purposes to high-speed propulsion devices like rocket engines, ramjets, gas turbines, etc. It is characterized by very large amplitude pressure (acoustic) waves propagating back and forth in the combustion chamber of a combustor. The pressure fluctuations give rise to high levels of thermal and mechanical stresses in critical components of the combustor such as fuel injectors, oxidizer post and combustor liner. Incessant exposure to such periodic stresses can cause damage to these components as shown in Figure 1.1, which can ultimately result in a cataclysmic failure of the engine. The underlying physics governing the generation of thermo-acoustic instability is a complex coupling between chemical kinetics, heat release, turbulence and acoustic waves. Currently, it is difficult to accurately predict this highly complicated interaction. As such, mitigation of thermo-acoustic instability is one of the biggest challenges the aerospace industry is facing for more than half a century [2]. In the following section we briefly describe the multi-physics involved in thermo-acoustic instability and some of the challenges in numerically modeling these physics.

1.2 Challenges in Numerical Modeling

Thermo-acoustic instability is driven by a feedback mechanism as shown in Figure 1.2. In this feedback mechanism, perturbations in the flow due to for e.g. turbulence, can lead to fluctuations in the heat release. Since heat-release in a constant volume combustor leads to an increase in the pressure, fluctuations in the heat-release can

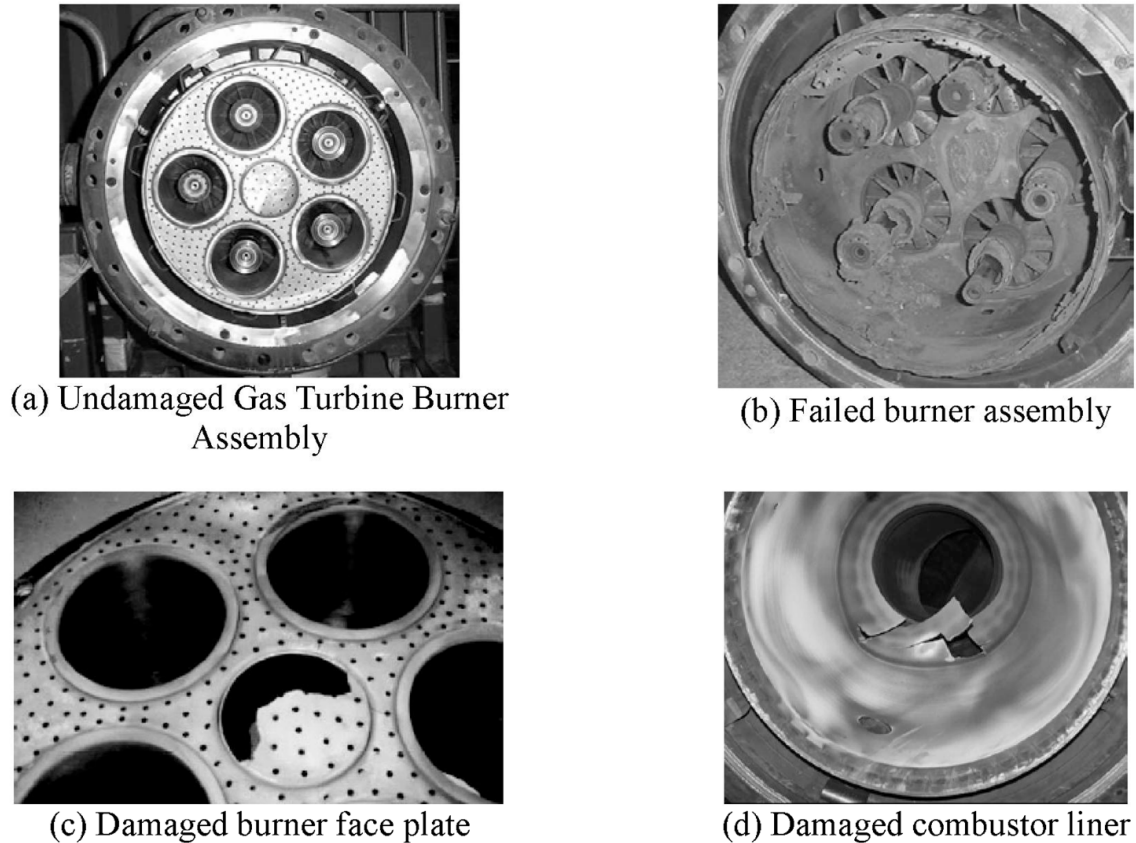


Figure 1.1.: Damaged components of a gas turbine engine due to thermo-acoustic instability [1].

lead to oscillations in the pressure or the acoustic waves generated in the combustor. As these pressure waves propagate through the combustor, they generate local vortex structures, mixing or shear layers. In this way the flow is perturbed and thus the feedback mechanism is set up.

The interaction between the heat release and acoustic field mainly determines whether amplitude of the pressure oscillation inside the combustor will increase, decrease or remain constant. This can be explained well using the Rayleigh criterion [4]. According to this criterion, if the heat-release fluctuations and pressure oscillations are in-phase (phase difference between the two quantities is between 0° and 90°), energy is added into the acoustic field from the heat-release and the amplitude of

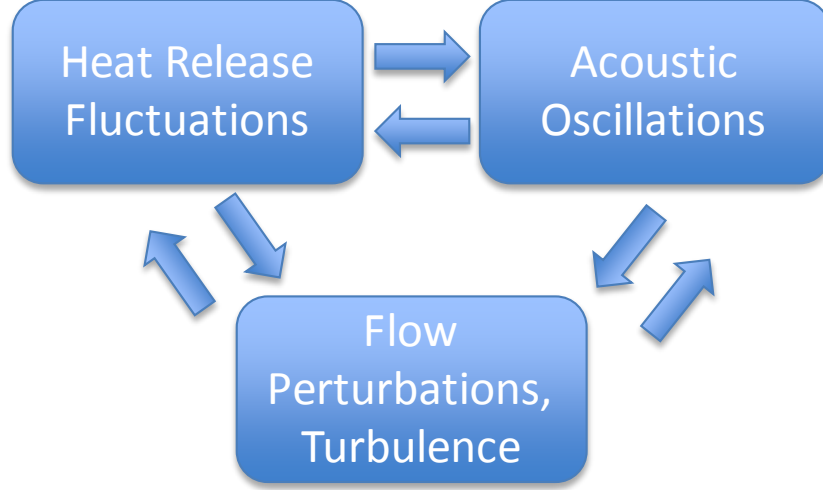


Figure 1.2.: Feedback mechanism driving thermo-acoustic instability [3].

the pressure oscillations increases. Conversely, if the heat-release and acoustic field oscillations are out-of-phase (phase difference is between 90° and 180°), energy is removed from the acoustic field resulting in a decrease of the amplitude of the pressure oscillations. Mathematically, the Raleigh criterion can be represented as [5, 6],

$$R = \frac{1}{t_e - t_s} \int_{t_s}^{t_e} \int_V p'(x, t) q'(x, t) dt dV, \quad (1.1)$$

where R is the Raleigh index, t_s is the start time for integration, t_e is the end time, V is a control volume, p' is the fluctuation in pressure, q' is the fluctuation in heat-release and x, t are the spatial and temporal co-ordinates respectively. For $R > 0$, the pressure oscillations are amplified and for $R < 0$ they are damped.

The feedback mechanism driving thermo-acoustic instability is governed by a number of unit physics like chemical kinetics, flow dynamics, turbulence, molecular diffusion and acoustics, and the interactions between them. As a result of these complicated interactions, it is very difficult to isolate the different physics and study them individually in laboratory-scale canonical jet flames like the Sandia flame series C-F [7, 8], Cambridge stratified flame series [9, 10] and Sydney piloted flames with

transient effects like extinction and re-ignition [11–13]. Here we highlight some of the major challenges in the numerical modeling of thermo-acoustic instability:

1.2.1 Thermo-Acoustic Interaction

Thermo-acoustic instability is driven and sustained by a strong interaction between the instantaneous heat release and acoustic waves. Numerical modeling of this interaction is not straight forward because currently it is not possible to accurately calculate the instantaneous heat release using the existing combustion models. Secondly, we still do not have a very fundamental understanding of the interaction between the heat release and acoustics to be able to develop numerical models. A thorough understanding of the thermo-acoustic interaction is foremost importance for accurate modeling of thermo-acoustic instability.

1.2.2 Compressibility

The amplitude of the pressure oscillations due to thermo-acoustic instability in a combustor can be anywhere in the range of 5% to 20% of the mean pressure. In the presence of such high magnitude of pressure oscillations it is not feasible to neglect the compressibility effects on the flow physics and combustion. Compressibility effects can lead to discontinuities like shocks especially in ram jets. Numerical modeling of shocks is very challenging because of the effect of numerical diffusion which tends to smear the predicted discontinuity. Most of the turbulent combustion models neglect the effect of pressure since incorporation of compressibility in the closure models is not trivial. Neglecting the effect of pressure may lead to inaccurate prediction of scalars like temperature, species mass fraction and heat release.

1.2.3 Wide Range of Length and Time Scales

The interaction among the different physics in the feedback mechanism in Figure 1.2 occurs on a wide spectrum of length and velocity scales. The length scales can vary from the order of 10^{-6} m corresponding to the Kolmogorov length to the diameter of the combustor in meters. In case of the velocity scales, the scales range from 10^{-1} m/s corresponding to the laminar flame speed to the acoustic speed of the order of 10^2 m/s. Resolving all of these scales would require Direct numerical simulations (DNS) studies which are prohibitively expensive for complicated geometries like gas-turbine or rocket combustors.

1.2.4 Detailed Chemical Kinetics

Accurate modeling of reacting flows requires detailed chemical kinetics. This can be incorporated using detailed chemical reaction mechanisms. For hydrocarbons, detailed mechanisms can involve up to 1000-2000 species and 4000-5000 species. Using such detailed mechanisms is computationally very expensive and is not a feasible option currently. To mitigate this issue, reduced reaction mechanisms with around 50-100 species and 300-500 reaction mechanisms or even global single-step reaction mechanisms are used. Using reduced mechanisms may affect the prediction of quantities such as laminar flame speed, flame thickness, ignition delay and local flame structure which might ultimately affect the predictions of thermo-acoustic instability.

1.2.5 Turbulence-Chemistry Interactions

Turbulent combustion involves a two way interaction between turbulence and chemistry. Interactions between a flame and turbulent flow field leads to local acceleration of the flow because of heat release and changes in diffusion coefficients due to the heat release. This acceleration of the flow generates turbulence which in turn interacts with the flame front by stretching or wrinkling it. These changes in the flame

structure may affect the chemical kinetics. The two way interaction between turbulence and chemical kinetics is highly nonlinear and it is caused by the nonlinearity in the reaction source term of species. When using the Reynolds average Navier-Stokes (RANS) or Large eddy simulation (LES) turbulence models, turbulent combustion models are required to model the reaction source term for accurate predictions.

1.2.6 Differential Molecular Diffusion

Differential molecular diffusion (DMD) effects may be significant in localized regions of a combustor with low Reynolds number such as the recirculating zone in a dump-plane combustor. Neglecting DMD can have an effect on the predictions of combustion. Incorporating DMD in turbulent combustion models is not trivial and requires a thorough understanding of the effect of DMD.

Having discussed some of the challenges in the numerical modeling of thermo-acoustic instability we now look at the current modeling approaches in following section.

1.3 Current Status of Modeling

Numerical modeling of thermo-acoustic instability can broadly be classified into two categories based on the level of fidelity. The first category involves decoupling the acoustic field from the unsteady heat release in the simulations and is often referred to as lower order or reduced order modeling. The unsteady heat release is calculated using either a flame transfer function (FTF) [14] or a flame describing function (FDF) [15] while the acoustic field is captured using a low-order combustor model [16] or a linear Helmholtz solver [17]. The modeling techniques in this category relatively have low fidelity but are an attractive option as a practical industry tool because of their low computational cost. The second category or the higher order modeling approaches entail coupling the acoustic field, instantaneous heat release, and fluid dynamics via the complete set of 3D Navier-Stokes equations [18] using

computational fluid dynamics (CFD) simulations. These type of simulations have higher fidelity and are able to capture more physics in comparison to the models in the first category. In the following sections we briefly review the work done in both the lower order and higher order modeling techniques.

1.3.1 Lower Order Modeling

One of the first low order models developed was Crocco's [19] $n - \tau$ model. In this model, the unsteady heat release rate is related to the pressure fluctuations using two model parameters, the interactive index n and the time lag τ . These two parameters are unknowns and need to be determined *a priori* through experiments. The heat release rate can be obtained as a function of the frequency using an FTF [20–22]. Similar time lag models were developed by Summerfield [23], Marble and Cox [24], Crocco and Cheng [25]. Although these models are popular because of their simple formulation and low computational cost, their major drawback is that they can be used only for linear analysis. Linear analysis methods are applicable only in predicting the initial growth rate of pressure fluctuations. In practical combustors, once the initial growth of pressure fluctuations has taken place, a limit cycle behavior is observed and the amplitude of pressure fluctuations remains constant. This limiting behavior is because of non-linear processes mentioned in Figure 1.2. Linear analysis methods are not able to predict the limit cycle behavior and predict a monotonic increase in the amplitude of the pressure fluctuations.

To resolve this issue, nonlinear low order models have been developed. Zinn and Lores [26] used a modified version of the Galerkin Method to predict the initial transient and the final limit cycle behavior for low Mach number flows. Poinot and Candel [27] used the thin flame sheet (TFS) model [28] to predict nonlinear large amplitude pressure oscillations in a ducted flame and the response of the flame to incident perturbations. Dowling [29, 30] extended the nonlinear analysis by incorporating nonlinear flame dynamics. The model was able to capture flame

distortion, necking and reattachment to the flame holder to a large extent for large pressure fluctuations. A more detailed discussion of the lower order modeling can be found in [31, 32]. The other, relatively higher fidelity approach is discussed in the following section.

1.3.2 Higher Order Modeling

In higher order modeling, the full 3D Navier-Stokes equations are solved using numerical flow solvers. In the higher order models, there are two important sub-models, turbulence model and turbulent combustion models. Turbulence models like RANS [33–38], LES [39–41] and hybrid RANS-LES model like detached eddy simulation (DES) [42] have been used to investigate thermo-acoustic instability. In RANS models, all the turbulence length scales are modeled while for LES models, turbulence length scales greater than the spatial filter length scale are resolved and only the length scales smaller than the filter length scale are modeled. DES model combines the RANS and LES models by using RANS model in near-wall regions and LES model away from the wall. Turbulent combustion models take into account the effect of turbulence on chemical kinetics which is neglected if a simple laminar chemistry model is used. For modeling thermo-acoustic instability, the most commonly used turbulent combustion models are the dynamic thickened flame (DTF) model [43, 44] and the linear eddy mixing model (LEM) [45] with single step or reduced chemical reaction mechanisms.

Smith and Leonard [46] carried out 2D axisymmetric simulations of an industrial type premixed gas turbine engine [47] using the Renormalization Group (RNG) [35] RANS turbulence model. A single step global reaction mechanism for methane was used to model the chemistry. The predicted pressure oscillations compared well with the limit cycle oscillations measure in the experiments. However in the simulations it appears that the limit-cycle behavior has not been achieved. Brookes et al. [48] performed 2D axisymmetric RANS simulations to predict the onset of self-

excited thermo-acoustic instability in a bluff-body stabilized premixed flame [49] in a long duct. In comparison to the experiments, the frequency of oscillations was over-predicted for all equivalence ratios. Traditionally, RANS models have primarily been used to capture the mean flow. The inherent unsteadiness in thermo-acoustic instability limits the performance of the RANS modeling approach to some extent and hence LES is a more attractive option where part of the turbulence is resolved.

Menon and Jou [50] used the LES modeling approach with reasonable success to predict Thermo-acoustic instability in an axisymmetric ramjet configuration [51]. A thin-flame model which uses the local flame speed was used to carry out the chemistry calculations. In the LES framework, the thickened flame [43] and the DTF model [44] with reduced chemical kinetics have been used quite effectively to predict pressure oscillations in both premixed dump and swirl stabilized combustors [52–54]. Schmitt et al. [55] carried out LES simulations to predict the NO emissions and Thermo-acoustic instability in a high-pressure swirled combustor [56] using the DTF model with a 3-step reduced chemical mechanism. To analyze the unsteady combustion dynamics and thermo-acoustic instability in annular combustion chambers, Wolf et al. [57] used the DTF model with a single step global reaction mechanism.

Besides the DTF model, the LEM model has also been used for Thermo-acoustic instability modeling studies. Srinivasan et al. [58] studied the limit cycle behavior in a self-excited single-element rocket combustor [59] using the LEM turbulent combustion model with a 2-step reaction mechanism. The amplitude of the peak-to-peak pressure oscillations was under-predicted for both the stable and unstable operating condition. This study was further extended [60] to account for reflection of acoustic waves at the boundaries by employing time-domain impedance boundary condition.

Some studies on modeling thermo-acoustic instability have completely neglected the effect of turbulence on chemistry calculations by employing a simple laminar chemistry model. Huang et al. [61] used the level-set flamelet approach [62] to model thermo-acoustic instability in a lean-premixed swirl-stabilized combustor [63]. In the level-set approach, a flamelet library is generated *a priori* and is used to retrieve

thermodynamic scalars like the temperature, species mass fractions and heat release. The flamelet library used in this study was generated without considering the influence of turbulence. Harvazinski et al. [64] analyzed the interaction between flow field, acoustics and heat release in a self-excited rocket combustor [59]. In this study, the turbulence-chemistry interaction was neglected and a single step reaction mechanism was used. For the same combustor, the use of detailed chemical kinetics with a laminar chemistry model yielded better agreement with experiments in terms of amplitude of peak-to-peak pressure oscillations [65]. Matsuyama et al. [66] performed LES simulations of a H_2/O_2 combustor [67] using a 13-step reaction mechanism while neglecting turbulence-chemistry interactions. For different pressure probes in the experiments, the simulation results are either under-predicted or over-predicted.

Numerical modeling approaches for thermo-acoustic instability are not limited to the above discussion in Section 1.3. A comprehensive discussion on the different modeling approaches of thermo-acoustic instability and their challenges can be found in [2, 14, 68–70].

1.4 Objectives and Outline

From the brief overview of the different numerical modeling approaches for thermo-acoustic instability in Section 1.3 it can be seen that almost all of the studies have been based on highly reduced chemical kinetics primarily because detailed chemistry simulations are computationally expensive. These studies have also highlighted the importance of turbulent combustion models. In the Favre averaged or filtered Navier-Stokes equations, the chemical reaction source term in the species transport equation is not closed and a suitable turbulent combustion model is needed to provide a closure for this term. The laminar chemistry model evaluates the reaction source term using the Favre averaged or filtered quantities, which can be highly inaccurate given the high nonlinearity of the chemical reaction terms. Examples of turbulent combustion models include the transported probability density function (PDF) method [71],

the flamelet models [72, 73], the DTF model [44], the LEM model [45] etc. This work focuses on using the two popular flamelet models, the steady flamelet model (SFL) [72] and the flamelet/progress variable model (FPV) [73] along with the transported PDF method [71] with the Eulerian Monte Carlo Fields (EMCF) method [74] to model thermo-acoustic instability in a single-element self excited model rocket combustor [59] developed at Purdue University. To the best of our knowledge these two combustion models have not been used to model instabilities in the model rocket combustor. This study aims to fill the gap in assessing the capability of two advanced turbulent combustion models, flamelet model and PDF method in modeling thermo-acoustic instability. Specifically, the objectives of this work are:

- Examine the effect of different presumed-PDF table integration approaches in flamelet modeling
- Investigate the coupling between transient flame dynamics, turbulence and chemical kinetics and thermo-acoustic instability in the rocket combustor
- Establish a modeling framework for compressible turbulent reactive flows by the using the transported PDF method with the EMCF method
- Verify and validate the developed modeling framework in a series of test cases ranging from pure mixing to a model rocket combustor and recommend suitable physical models and numerical implementation approaches for accurate modeling

In Chapter 2 the experimental setup of the single-element self-excited model rocket combustor is discussed. The details of the experiment and the different operating conditions of the combustor are discussed in detail. Then, a brief review of the numerical modeling work of the model rocket combustor is provided to identify potential issues in modeling.

Chapter 3 establishes the framework for the study by discussing the governing equations, turbulence model, the flamelet combustion models and the transported PDF method in detail.

In Chapter 4 the numerical discretization schemes for solving the governing equations in the flow solver is detailed. In the flamelet modeling framework, different approaches exist for integrating the laminar flamelet table to make it suitable for turbulent simulations. These integration approaches are discussed in detail in this chapter. For the EMCF method, the implementation of the mixing model and discretization of the stochastic term is detailed.

In Chapter 5 the effect of the different table integration approaches on the predictions of a free turbulent jet flame and the self excited rocket combustor is examined and a particular integration approach is suggested.

Using this integration approach, thermo-acoustic instability in the model rocket combustor is modeled in Chapter 6 by using the flamelet models discussed in Chapter 3. A two-coupling between transient flame dynamics and thermo-acoustic instability is identified which provides a plausible mechanism for the self-excited and sustained instability observed in the model rocket combustor.

In Chapter 7, the EMCF method is validated with a series of test cases ranging from pure mixing to subsonic and supersonic turbulent jet flames. The EMCF method is then used to model thermo-acoustic instability in the model rocket combustor.

The conclusions are drawn in Chapter 8.

1.5 Major Contributions

The major contributions of this work are:

1. Development of a framework to model thermo-acoustic instability in a self-excited model resonance combustor using detailed chemical kinetics with the flamelet modeling approach to account for turbulence-chemistry interaction
2. Comprehensive analysis of a two-way coupling between transient flame dynamics and thermo-acoustic instability in the combustor using flamelet models

3. Model advancement studies of the transported PDF method to extend its application to compressible turbulent reactive flows
4. Development of a transported PDF method solver using the EMCF method in an in-house flow solver and modeling of thermo-acoustic instability in the model resonance combustor

2. PURDUE SELF-EXCITED MODEL ROCKET COMBUSTOR

As mentioned in Chapter 1, in this study we conduct numerical simulations of a single-element self-excited model rocket combustor. Primarily, longitudinal instabilities are observed in the rocket combustor. In this chapter we briefly discuss the development of the model rocket combustor and details of the experiment and the available data. Finally, a brief overview of the numerical approaches that have been used to model combustion instabilities inside the combustor is provided in the final section of the chapter.

2.1 Overview of Rocket Combustor

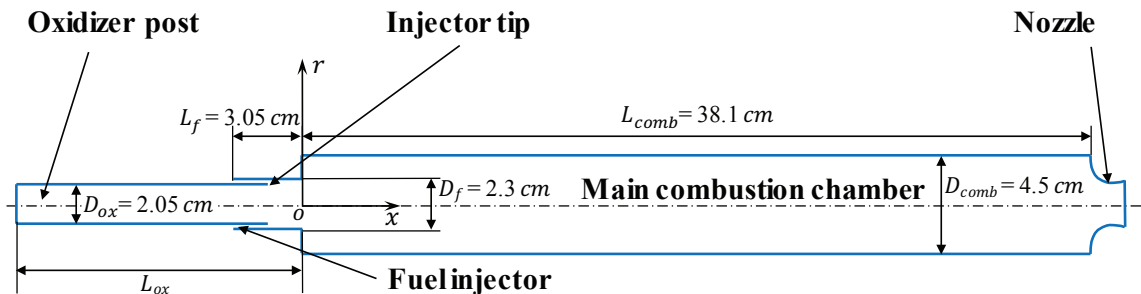


Figure 2.1.: Schematic of self-excited model rocket combustor [59, 75, 76].

At Purdue University, three generations of a single-element, self-excited, laboratory scale rocket combustor have been studied. The first generation was developed by Miller [77] to study the different levels of longitudinal instabilities. JP-8 was used as the fuel injected through a coaxial swirl injector. The oxidizer was decomposed hydrogen peroxide injected radially upstream of the fuel. Different combustion chamber

lengths were tested to get different levels of instability. Sisco [78] designed the second generation to investigate the effect of vortex shedding by changing the combustion chamber to oxidizer tube ratio. It was observed that the smaller area ratio was more unstable. Based on the conclusions drawn by Miller et al. [77] and Sisco et. al [78] that geometric changes lead to different stability behavior, Yu et. al [59, 75] developed the third generation of the single-element combustor called the continuously variable resonance combustor (CVRC), shown in Figure 2.1. In CVRC, the length of the oxidizer post L_{ox} can be changed continuously to get different levels of pressure oscillations. Based on the amplitude of the peak-to-peak oscillations three operating conditions are identified [64]:

- Moderately stable operating condition: $8.89 \text{ cm} \leq L_{ox} \leq 10 \text{ cm}$
- Unstable operating condition: $10 \text{ cm} \leq L_{ox} \leq 18 \text{ cm}$
- Bifurcated operating condition: $18 \text{ cm} \leq L_{ox} \leq 19.05 \text{ cm}$

In the experiment carried out by Yu et al. [59, 75], for the moderately stable operating condition the instantaneous peak-to-peak amplitude is about 160 kPa and around 400 kPa and 120 kPa for the unstable and bifurcated operating condition respectively. It has been observed in the experiments that the bifurcated regime shows both stable and unstable behavior. Recently, Hardi et al. [76] analyzed the combustion instabilities in self-excited rocket combustor for two fixed lengths of the oxidizer post, 8.89 cm and 13.97 cm corresponding to the stable and unstable operating condition respectively. The data from this experiment is used for validating the numerical modeling results in this study. In the following section we look at the details of this experiment and the pressure oscillations observed for the two oxidizer post lengths.

2.2 Experimental Results

Hardi et al. [76] conducted experiments for a stable operating condition ($L_{ox} = 8.89 \text{ cm}$) and an unstable operating condition ($L_{ox} = 13.97 \text{ cm}$) to obtain raw

pressure data inside the combustor and temporally resolved OH^* chemiluminescence images for validation of numerical simulations. In the experiment, gaseous methane is used as the fuel and hydrogen peroxide as the oxidizer. The fuel enters through the fuel inlet shown in Figure 2.1 just upstream of the dump plane which is located at $x/D_{ox} = 0$. Hydrogen peroxide is first forced through a catalyst bed producing hot oxygen and steam before it enters the combustor. This causes the hydrogen peroxide to decompose to oxygen and water. The decomposed hydrogen peroxide then passes through a choked orifice plate into the oxidizer post. The choked orifice plate provides a reflecting boundary condition for numerical simulations. At the other end of the combustor, the nozzle is also choked for the same reason. The fuel and the oxidizer mix in the region between the fuel lip and the dump plane before entering into the combustion chamber. The details of the experiment for the two operating conditions can be found in Table 2.1 where $\langle P_c \rangle$ is the time-averaged pressure inside the combustor measured at $x/D_{ox} = 18$ (close to the nozzle entrance) near the combustor wall, ϕ is the equivalence ratio of the inlet mixture of methane and hydrogen peroxide, T_{ox} is the oxidizer temperature, T_f is the fuel temperature, \dot{m}_{total} is the total mass flow rate of the fuel and oxidizer. The level of combustion instability is characterized by the ratio $\langle P_{pp} \rangle / \langle P_c \rangle$ where $\langle P_{pp} \rangle$ is the time-averaged peak-to-peak amplitude of the pressure fluctuation and $\langle P_c \rangle$ is the time-averaged pressure in the combustor. Here, ' $\langle \rangle$ ' denotes time-averaging of a variable. For the stable operating condition, the ratio $\langle P_{pp} \rangle / \langle P_c \rangle$, based on the pressure measured at $x/D_{ox} = 18$ is around 10% and for the unstable operating condition it is about 45%.

Figure 2.2 and Figure 2.3 show the fluctuating pressure signal p' measured inside the rocket combustor at the location $x/D_{ox} = 18$ for the stable and unstable operating condition respectively. It can be seen that the amplitude of the peak-to-peak oscillations for the stable operating condition is significantly higher as compared to the unstable operating condition. In this study, we use only the fluctuation pressure signal to validate our numerical simulations.

Table 2.1.: Details of model rocket combustor experiment [76] for the stable and unstable operating condition.

	Stable condition	Unstable condition
$\langle P_c \rangle$ (MPa)	1.43	1.44
ϕ	0.71	0.70
T_{ox} (K)	573	554
T_f (K)	298	291
\dot{m}_{total} (kg/s)	0.347	0.345
$\langle P_{pp} \rangle / \langle P_c \rangle$	10%	45%

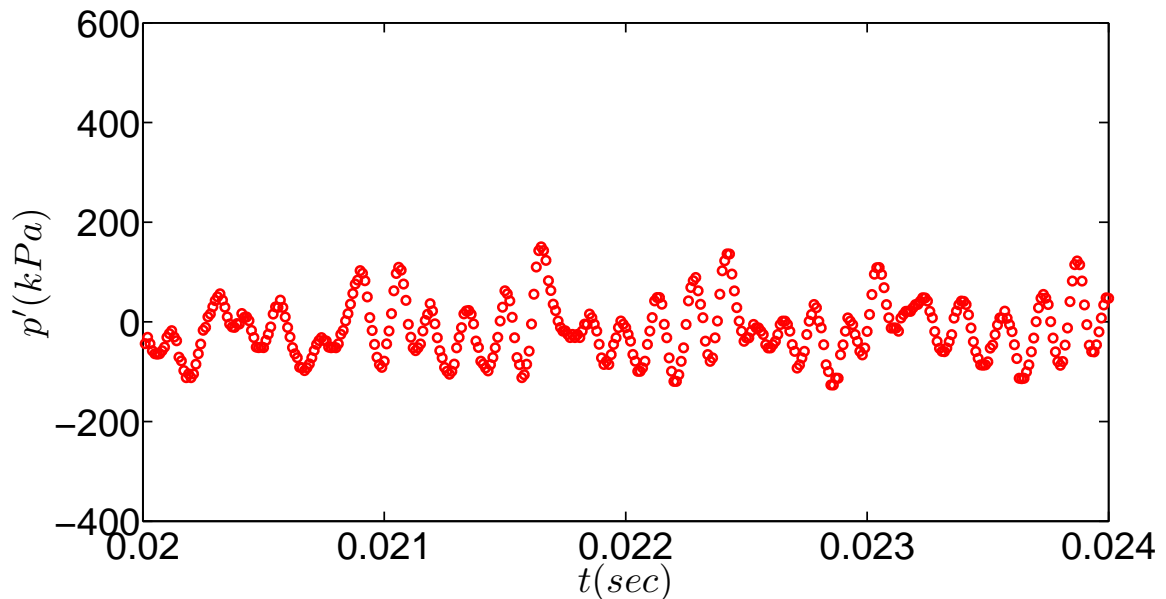


Figure 2.2.: Fluctuation pressure signal p' at $x/D_{ox} = 18$ in model rocket combustor [76] for stable operating condition.

Having discussed the details of the experiment, in the following section we now look at the different CFD based modeling approaches that have been used to predict combustion instabilities in the combustor.

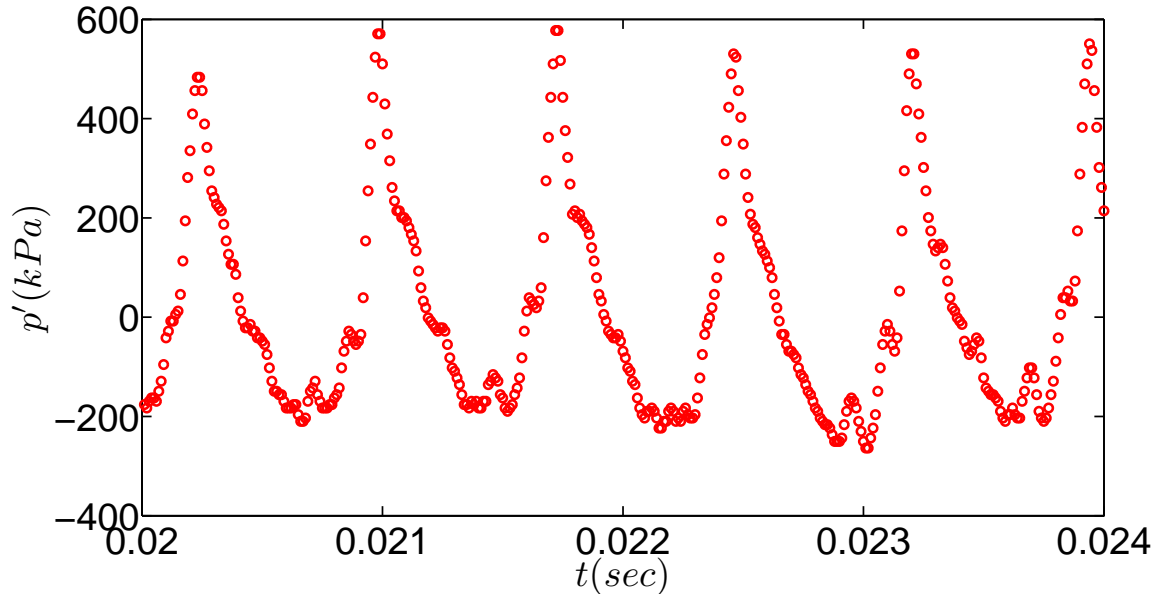


Figure 2.3.: Fluctuation pressure signal p' at $x/D_{ox} = 18$ in model rocket combustor experiment [76] for unstable operating condition.

2.3 Numerical Modeling

Computational modeling can provide quantitative information that is not accessible in most experiments. Computational studies of the model rocket combustor have been restricted only to a few combustion models and there is no model which can accurately predict combustion instability for a given operating condition.

The model rocket combustor has been previously modeled using the DES turbulence model with a laminar chemistry model. Both reduced and detailed kinetics have been used in the modeling. A comparison between two and three dimensional DES simulations [79] using a single-step methane mechanism [80] for an unstable operating condition ($L_{ox} = 13.97$ cm) showed that three dimensional simulations yield better agreement with the experiments. Harvazinski et.al [64] extended this study to three dimensional simulations of stable and bifurcated operating condition which shows both stable and unstable behavior. The simulations showed good agreement

with the experimental results for the stable condition. For the bifurcated condition, the simulations were not able to capture the transition from the stable to the unstable condition yielding inaccurate predictions of the modal frequencies. Sardeshmukh et al. [65] implemented a detailed chemical reaction mechanism, GRI-1.2 [81] in two dimensional simulations of the rocket combustor. With a detailed kinetic model, the two dimensional simulations produced much better agreement with the experiments as compared to a single-step reaction mechanism.

In addition to the laminar chemistry model, more advanced models have been used to account for turbulence-chemistry interaction which is ignored in the laminar chemistry model. Garby et al. [82] used LES along with the DTF combustion model to study the fundamental frequency of the combustor with two and three dimensional simulations. Both simulations over-predicted the frequency when a two-step reaction mechanism [83] was used. Harvazinski [79] also carried out a study of the turbulence-chemistry interaction with the DTF model using a four-step reaction mechanisms [84] for a fuel lean condition. The DTF model showed measurable differences only in regions close to the backstep where the mesh was fine. Srinivasan et al. [58,60] used the same reaction mechanism as that used by Garby et al. [82] in combination with the LEM combustion model to account for the turbulence-chemistry interaction, for three different operating conditions, $L_{ox} = 8.89$ cm, 12 cm and 13.97 cm. There was good agreement of the peak-to-peak pressure fluctuations of the computations with the experiments but the frequency of the different modes was over-predicted for all the oxidizer post lengths. Harvazinski et al. [85] compared the performance of the laminar chemistry model and LEM model. LEM did not show significant improvement over the laminar chemistry model.

All the previous studies of the model rocket combustor have used highly reduced chemical mechanisms, except for the study by Sardeshmukh et al. [65], primarily because of the high computational cost involved by incorporating detailed chemical mechanisms. These studies have highlighted the importance of turbulent combustion models. Sardeshmukh et al. [65] pointed out the importance of detailed chemistry in

predicting the correct ignition delay and heat release which has a significant impact on the amplitude of instability. To the best of our knowledge, no effort has been made to study the combined effect of using a turbulent combustion model with detailed chemical kinetics for the model rocket combustor. Turbulent combustion models account for turbulence-chemistry interaction and provide closure for the highly nonlinear unclosed reaction source term in the species transport equation of the Favre averaged or Filtered Navier-Stokes equations. The laminar chemistry model completely neglects the effect of turbulence-chemistry interactions and uses Favre averaged or Filtered quantities to evaluate the reaction source term. This approach can be highly inaccurate given the high nonlinearity of the chemical reaction term. In this study we evaluate the capability of the flamelet model [72,73] to predict combustion instabilities in the rocket combustor.

In the flamelet model, the complex chemistry calculations are decoupled from the flow equations by using a conserved scalar called the mixture fraction. The thermo-chemical properties like temperature and species mass fraction are stored in a flamelet table which can be generated independent of the flow equations and can be looked up for thermo-chemical properties during simulations. In an actual flow simulation, only the flow equations and the conserved scalar transport equations are solved instead of the transport equations for all the species. Because of the pre-tabulation, the computational cost of using the flamelet models is relatively low as compared to other turbulent combustion models and hence any detailed chemistry can be easily incorporated in the flamelet models without a significant increase of the computational cost. Two popular flamelet models are considered here, the steady flamelet (SFL) model [72] and the flamelet/progress variable (FPV) model [73]. The steady flamelet assumes that the Damkohler number (Da) is very high ($Da \gg 1$) so that combustion is in the flamelet regime and the flame is always burning with no extinction and re-ignition. The FPV model is an extension of the SFL model and it can account for extinction and re-ignition. The flamelet model has been principally developed for modeling low Mach number, incompressible flows. For modeling the

self-excited rocket combustor it is necessary to account for compressibility effects and suitable modifications are needed which are discussed in the next chapter.

In summary, in this chapter, firstly a brief description of the self-excited model rocket combustor experiment is provided which is used to validate numerical modeling work in this study. Two widely different operating conditions, stable and unstable condition are identified for carrying out modeling work. Next, a brief overview of the current state of numerical modeling of the combustor is provided. It is recognized that majority of the modeling work has used highly reduced chemical kinetics while neglecting turbulence-chemistry interaction. The flamelet turbulent combustion model is proposed for modeling combustion instabilities of the rocket combustor. In the following part of this report, in Chapter 3, the governing equations and the different sub-models like turbulence and turbulent combustion models are discussed.

3. PHYSICAL MODELS

In this study the flamelet modeling and the transported PDF modeling approach is used for predicting combustion instabilities in a self-excited model rocket combustor. In this chapter we provided details of the modeling framework. The physics of combustion instabilities is governed by the full, 3D compressible Navier-Stokes equations. Two important sub-models, turbulence model and turbulent combustion model provide closure to the set of governing equations. The detailed description of the modeling framework is provided below.

3.1 Compressible and Turbulent Flow modeling

The flamelet modeling and transported PDF modeling framework is implemented in an in-house compressible flow solver called GEMS [86–88]. The GEMS solver is second-order accurate in space and time. The turbulence is modeled in GEMS by using a hybrid RANS/LES approach called Detached Eddy Simulation (DES) [42]. In the DES model, a RANS model like the $k-\omega$ model [36,37] is used in the near-wall region and the LES approach is used in regions away from the wall. The compressible flow equations are,

$$\frac{\partial \bar{\rho}}{\partial t} + \frac{\partial \bar{\rho} \tilde{u}_k}{\partial x_k} = 0, \quad (3.1)$$

$$\frac{\partial \bar{\rho} \tilde{u}_j}{\partial t} + \frac{\partial \bar{\rho} \tilde{u}_j \tilde{u}_k}{\partial x_k} = -\frac{\partial \bar{p}}{\partial x_j} + \frac{\partial \tilde{\tau}_{e,jk}}{\partial x_k}, \quad (3.2)$$

and the turbulence modeling governing equations are,

$$\frac{\partial \bar{\rho} k}{\partial t} + \frac{\partial \bar{\rho} \tilde{u}_k k}{\partial x_k} = \frac{\partial}{\partial x_k} \left(\Gamma_{ke} \frac{\partial k}{\partial x_k} \right) + \tilde{\tau}_{t,jk} \frac{\partial \tilde{u}_j}{\partial x_k} - \beta^* \bar{\rho} k \omega, \quad (3.3)$$

$$\frac{\partial \bar{\rho} \omega}{\partial t} + \frac{\partial \bar{\rho} \tilde{u}_k \omega}{\partial x_k} = \frac{\partial}{\partial x_k} \left(\Gamma_\omega \frac{\partial \omega}{\partial x_k} \right) + \frac{\gamma \omega}{k} \tilde{\tau}_{t,jk} \frac{\partial \tilde{u}_j}{\partial x_k} - \beta \bar{\rho} \omega^2 + \bar{\rho} \frac{\sigma_d}{\omega} \frac{\partial k}{\partial x_k} \frac{\partial \omega}{\partial x_k}, \quad (3.4)$$

where “ $-$ ” denotes Reynolds averaging or filtering depending on whether RANS or LES is used, “ \sim ” denotes Favre averaging or density-weighted filtering, $\bar{\rho}$ is the density, \tilde{u} , \tilde{v} , \tilde{w} is the velocity in the x, y, z , directions respectively, k is the turbulent kinetic energy and ω is the turbulence frequency. The conservation of energy and conservation of species mass fraction equations needed for closure of compressible turbulent combustion will be discussed in Section 3.2 and Section 3.3. All of the above equations represent both, the RANS and LES modeling approach simultaneously. The choice of the modeling approach is decided locally based on the grid size and turbulent length scale in the DES model framework [42]. For simplicity, in the following description, we use LES terminology to describe all the equations. In the momentum conservation equation in Equation (3.2), $\tilde{\tau}_{e,jk} = \tilde{\tau}_{jk} + \tilde{\tau}_{t,jk}$ is the sum of the viscous shear stress, $\tilde{\tau}_{jk} = \mu [2S_{jk} - 2(\partial\tilde{u}_m/\partial x_m)\delta_{jk}/3]$, and the Reynolds stress, $\tilde{\tau}_{t,jk} = \mu_t [2S_{jk} - 2(\partial\tilde{u}_m/\partial x_m)\delta_{jk}/3] - 2\bar{\rho}k\delta_{jk}/3$, in the j^{th} direction in a plane with normal in the k^{th} direction, $S_{jk} = 1/2(\partial\tilde{u}_j/\partial x_k + \partial\tilde{u}_k/\partial x_j)$ is the strain rate tensor, δ_{jk} is the Kronecker delta, μ is the molecular viscosity, and μ_t is the turbulent eddy viscosity. The diffusion coefficients for k and ω in Equation (3.3) and Equation (3.4) are $\Gamma_{ke} = \mu + \sigma_k\bar{\rho}k/\omega$ and $\Gamma_\omega = \mu + \sigma_\omega\bar{\rho}k/\omega$, respectively, where $\sigma_k = 0.6$ and $\sigma_\omega = 0.5$ are the model constants of the $k - \omega$ turbulence model [37]. The turbulent eddy viscosity is modeled as $\mu_t = \bar{\rho}k/\hat{\omega}$ where $\hat{\omega}$ is an effective turbulence frequency and is evaluated as [37],

$$\hat{\omega} = \max\left(\omega, \frac{7}{8}\sqrt{\frac{2S_{jk}S_{jk}}{\beta^*}}\right), \quad (3.5)$$

with $\beta^* = 0.09$. In Equation (3.4), $\gamma = 13/25$ is a model constant in the $k - \omega$ model, and the formulations of β and σ_d can be found in [37]. The set of Equations (3.1)-(3.4) constitute the governing equations for the flow and turbulence fields. In a reactive flow system, along with Equations (3.1)-(3.4), conservation of energy and conservation of species mass fractions equations need to be solved.

For the flamelet modeling approach, the conservation of energy is,

$$\frac{\partial \bar{\rho} \tilde{h}^0}{\partial t} + \frac{\partial \bar{\rho} \tilde{u}_k \tilde{h}^0}{\partial x_k} = \frac{\partial \bar{p}}{\partial t} + \frac{\partial}{\partial x_k} \left(\tilde{u}_k \tau_{e,jk} + K \frac{\partial \tilde{T}}{\partial x_j} + \frac{\mu_t}{Pr_t} \frac{\partial \tilde{h}}{\partial x_j} \right), \quad (3.6)$$

where K is the thermal conductivity and $Pr_t = 0.7$ is the turbulent Prandtl number. The mass fraction \tilde{Y}_i will be obtained from the flamelet models discussed in Section 3.2. It is worthwhile to note that the enthalpy or temperature is obtained by directly solving the enthalpy equation in Equation (3.6) rather than obtained from the flamelet models in this work.

For the PDF modeling approach, the conservation of energy and species mass fraction equations are described in detail in the following Section 3.3 where we describe the transported PDF method.

3.2 Flamelet Models

The flamelet models [72] are based on a concept according to which a turbulent diffusion flame can be approximated by an ensemble of laminar stretched thin flames called laminar flamelets. The complex chemistry calculations can be decoupled from the flow equations by using a conserved scalar, mixture fraction. The thermo-chemical properties like the temperature and species mass fraction are stored in a flamelet table which can be generated independent of the flow equations and can be looked up for thermo-chemical properties during simulations. This pre-tabulation helps reduce the computational cost significantly and hence any detailed chemistry can be incorporated in the flamelet models without a substantial increase of the computational cost. There are different flamelet models, and in this study we consider two popular flamelet models, the SLF model [72] and the FPV model [73].

3.2.1 Steady Laminar Flamelet Model

In the SLF model, the transport equations for the mixture fraction $\tilde{\xi}$ and variance of the mixture fraction $\tilde{\xi}''^2$ are solved which are included in Equation (4.1). The

species mass fraction \tilde{Y}_i is obtained from a flamelet table by using the value of the mixture fraction $\tilde{\xi}$, the mixture fraction variance $\tilde{\xi}''^2$ and the dissipation rate for the mixture fraction at stoichiometric condition $\tilde{\chi}_{st}$.

The laminar flamelet solutions are obtained by solving the following steady flamelet equations [72] and are stored in a laminar flamelet table,

$$0 = \frac{\rho\chi}{2} \frac{\partial^2 T}{\partial \xi^2} - \sum_{i=1}^{N_s} \frac{\dot{\omega}_i h_i}{c_p} + \frac{\rho\chi}{2} \frac{1}{c_p} \frac{\partial c_p}{\partial \xi} \frac{\partial T}{\partial \xi} + \frac{\rho\chi}{2} \sum_{i=1}^{N_s} \frac{\partial Y_i}{\partial \xi} \frac{\partial T}{\partial \xi} \frac{c_{p,i}}{c_p}, \quad (3.7)$$

$$0 = \frac{\rho\chi}{2} \frac{\partial^2 Y_i}{\partial \xi^2} + \dot{\omega}_i, \quad (3.8)$$

where $\chi = 2D(\partial\xi/\partial x_j \cdot \partial\xi/\partial x_j)$ is the dissipation rate for mixture fraction, T is the temperature, N_s is the number of species, c_p is the specific heat of the mixture, and $c_{p,i}$, $\dot{\omega}_i$, and h_i are the specific heat, reaction rate and enthalpy of the i^{th} species, respectively. For χ , a common model based on a potential flow theory for an opposed

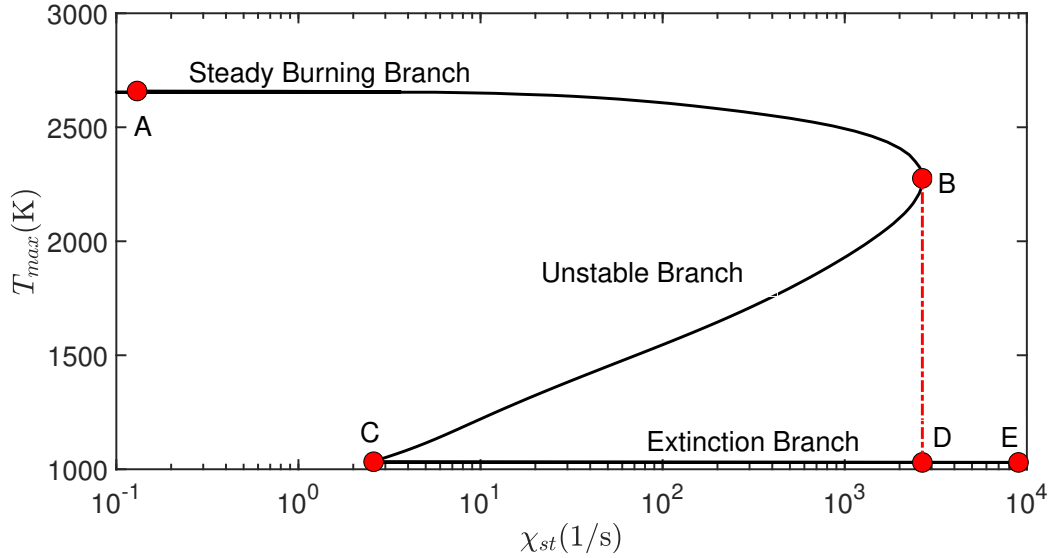


Figure 3.1.: Variation of maximum flame temperature T_{max} with mixture fraction dissipation rate at stoichiometric condition χ_{st} obtained from laminar flamelet solutions. The boundary conditions of the model rocket combustor are used.

jet flow is used [72],

$$\chi(\xi) = \chi_{st} \frac{\exp[-2(\operatorname{erfc}^{-1}(2\xi))^2]}{\exp[-2(\operatorname{erfc}^{-1}(2\xi_{st}))^2]}. \quad (3.9)$$

Figure 3.1 shows the variation of the maximum flame temperature T_{max} of each flamelet against χ_{st} which is often referred as the S-curve. It is obtained by solving the above steady flamelet equations, Equation (3.7) and Equation (3.8), by using the FlameMaster code [89] with the GRI 1.2 reaction mechanism [81] (the boundary conditions for the simulations are specified in Section 6.1.1). The GRI 1.2 mechanism is a detailed chemical kinetic model for methane oxidization and is expected to be suitable for the current study to capture the finite-rate chemistry effects. There are three important branches on the S-curve in Figure 3.1. The branch from point A to point B is a steady burning branch. Along the steady burning branch, the maximum flame temperature decreases monotonically with the dissipation rate and a burning solution of the flame is always obtained on this branch. Point B is the steady-state flame extinction limit. The second branch is an unstable burning branch from point B to point C and an extinction branch extends from point C to point D. In the SLF model, only the laminar flamelet solutions along the burning branch A-B are considered, while in the FPV model, the whole S-curve is considered.

The conventional SLF model [72] is suitable only for incompressible flows in which the thermodynamic pressure is assumed to be constant. In the current model rocket combustor, there exist significant pressure fluctuations and the conventional SLF model needs an extension to account for the pressure variation. In this study, a background pressure p is added into the flamelet parameterization so that the species mass fraction Y_i in the laminar flamelet table can be written as $Y_i(\xi, \chi_{st}, p)$. Within each flamelet, the background pressure p is assumed to be uniform, implying that the thickness of flamelet is assumed to be smaller than the pressure variation length scale. This assumption is expected to be reasonable when the flame is thin.

A presumed-probability density function (PDF) approach [90] is used to integrate the laminar solutions so that an integrated flamelet table of the form $\tilde{\phi}(\tilde{\xi}, \tilde{\xi}''^2, \tilde{\chi}, \tilde{p})$ can be obtained that can be used for turbulent flame calculations. The presumed-PDF integration can be written as,

$$\tilde{\phi} = \int \int \int \phi(\eta_1, \eta_2, \eta_3) \tilde{P}(\eta_1, \eta_2, \eta_3) d\eta_1 d\eta_2 d\eta_3, \quad (3.10)$$

where η_1, η_2, η_3 are the sample space variables for ξ , χ_{st} and p and \tilde{P} is the density-weighted joint PDF of these three variables. In the integration, a β -PDF is assumed for ξ and a δ -PDF is assumed for χ_{st} and p . The variables ξ , χ_{st} and p are assumed to be statistically independent so that their joint PDF \tilde{P} is the product of the marginal PDF of each variable. The integrated flamelet lookup table is generated prior to the flow simulations in which all the equations in Equation (4.1) except for the last equation for the progress variable C are solved in the SLF model. The species mass fraction \tilde{Y}_i is then obtained from the integrated flamelet lookup table using local values of $(\tilde{\xi}, \tilde{\xi}''^2, \tilde{\chi}, \tilde{p})$. The temperature is obtained from solving the enthalpy equation in Equation (4.1) to account for the effect of temporal pressure variation on the energy conservation which is not considered in the flamelet equations, Equation (3.7) and Equation (3.8), and the temperature in the flamelet table is not used.

There are many assumptions involved in the SLF model including: steady state, very high Damkohler number ($Da \gg 1$) so that the combustion regime is in the flamelet regime, always burning without extinction or re-ignition, much larger length scale of pressure variation in comparison to the flamelet length scale.

3.2.2 Flamelet/Progress Variable Model

The FPV model [73] was developed to include transient flame dynamics like re-ignition and extinction [91–93] which cannot be accounted for by the SLF model. The capability of the FPV model for local extinction and re-ignition has been discussed in [91–93]. In the FPV model, the laminar flamelet solutions are obtained from the entire S-curve as opposed to only the burning branch in the SLF model. A progress variable C is introduced to replace χ_{st} to parametrize the flamelet in the FPV model,

$$C = Y_{CO} + Y_{CO_2} + Y_{H_2} + Y_{H_2O}, \quad (3.11)$$

where Y_{CO} , Y_{CO_2} , Y_{H_2} , Y_{H_2O} are the mass fractions of CO, CO₂, H₂ and H₂O respectively. Similar to the modified SLF model discussed in Section 3.2.1, the conventional FPV model is also extended to account for the compressibility effect by using

different background pressure p as an additional parameter to identify a flamelet. Saghafian et al. [94] introduced an approximation approach to include the pressure dependence in a compressible FPV model in order to reduce the memory requirement. In this work, we directly consider the pressure effect on the flamelet and hence the pressure-energy-species coupling is accurately described within each flamelet. A presumed-PDF approach is used to integrate the laminar flamelet solutions to obtain an integrated flamelet table of the form $\tilde{\phi}(\tilde{\xi}, \tilde{\xi}''^2, \tilde{C}, \tilde{p})$ by using an flamelet preserving integration approach [?, 90]. In the flow simulations, along with $\tilde{\xi}$ and $\tilde{\xi}''^2$, an additional equation for the progress variable \tilde{C} is solved as is included in Equation (4.1). The species mass fraction \tilde{Y}_i is obtained from the flamelet table as $\tilde{Y}_i(\tilde{\xi}, \tilde{\xi}''^2, \tilde{C}, \tilde{p})$. With the obtained species mass fractions from the flamelet tables, the Equation (1) is closed.

3.2.3 Flamelet/Progress Variable Model with only Burning Branch

To investigate the combustion dynamics in the rocket combustor and the effect of turbulence-chemistry interactions we consider two variants of the FPV model obtained by slightly modifying the FPV model. In the first variant of the FPV model, only the laminar flamelet solutions along the burning branch of the S-curve are considered similar to the SLF model. The burning reaction rate for the progress variable is used for integrating the progress variable, i.e., there is no delay of ignition or the ignition delay is significantly shortened. The predicted burning by this FPV variant is instantaneous just like the SFL model. We reference this FPV variant as the FPV model with only burning branch (FPV-B). With the FPV-B model, a direct comparison can be made with the FPV model to examine the effect of the unstable branch representing transient flame dynamics on the predictions of the thermo-acoustic instability in the model rocket combustor.

3.2.4 Flamelet/Progress Variable Model with Zero Mixture Fraction Variance

The second variant of the FPV model neglects the effect of turbulence on the chemical kinetics by assuming zero mixture fraction variance $\widetilde{\xi''^2}$ while looking up the integrated flamelet table. This replicates the laminar chemistry model with the mean (or filtered) chemical reaction rate a function of the mean (or filtered) thermochemical properties. We denote this variant of the FPV model as the FPV model with zero mixture fraction variance (FPV-ZV). A direct comparison between the FPV model and the FPV-ZV model is done in Section 6.2.3 to examine the effect of turbulence-chemistry interactions in the model rocket combustor.

The two FPV model variants (FPV-B and FPV-ZV) discussed above are considered in this study only for the purpose of aiding our analysis and are not new turbulent combustion models. In the following Section 3.3 we discuss the transported PDF modeling approach.

3.3 Transported Probability Density Function Method for Turbulent Combustion Modeling

In the transported composition PDF method [71], the transport equation for the Eulerian joint-PDF of a set of variables for a single point and time is solved. In this study we consider the joint-PDF $\tilde{f}(\Psi; \mathbf{x}, t)$ of the composition vector $\Phi = [\phi_1, \phi_2, \dots, \phi_{N_s+1}] = [Y_1, Y_2, \dots, Y_{N_s}, h_s]$ comprising of mass fraction of a total of N_s species, with Y_i representing the mass fraction of the i^{th} species, and the sensible enthalpy h_s . The vector $\Psi = (\psi_1, \psi_2, \dots, \psi_{N_s+1})$ represents the sample space variable corresponding to Φ , \mathbf{x} is the position vector, and t represents time. Assuming

equal molecular diffusivity and unity Lewis number for all species, the exact transport equation for $\tilde{f}(\Psi : \mathbf{x}, t)$ is derived [71] as,

$$\begin{aligned} \frac{\partial \bar{\rho} \tilde{f}}{\partial t} + \frac{\partial}{\partial x_k} (\overline{u_k | \psi \bar{\rho} \tilde{f}}) &= - \frac{\partial}{\partial \psi_i} \left(\overline{\frac{\partial}{\partial x_k} \left(\Gamma \frac{\partial \phi_i}{\partial x_k} \right) | \psi \tilde{f}} \right) - \frac{\partial}{\partial \psi_i} \left(\dot{\omega}_i \bar{\rho} \tilde{f} \right) \\ - \delta_{N_s+1} \frac{\partial}{\partial \psi_{N_s+1}} \left(\dot{Q}_{hr} \bar{\rho} \tilde{f} \right) &- \delta_{N_s+1} \frac{\partial}{\partial \psi_{N_s+1}} \left(\overline{\left(\frac{Dp}{Dt} + \tau_{jk} \frac{\partial u_k}{\partial x_k} \right) | \psi \tilde{f}} \right), \end{aligned} \quad (3.12)$$

where “ $\overline{|\psi}$ ” indicates conditional mean, Γ is the molecular diffusivity, $\dot{\omega}_i$ is the chemical reaction source term for the i^{th} species, δ_{N_s+1} is used to indicate that the term appears only for the sensible enthalpy equation, \dot{Q}_{hr} is the heat release due to chemical kinetics and is given by $\dot{Q}_{hr} = - \sum_{i=1}^{N_s} \Delta h_{f,i}^0 \dot{\omega}_i$ where $\Delta h_{f,i}^0$ is the enthalpy of formation for the i^{th} species and DP/Dt is the material derivative for pressure and is defined as $Dp/Dt = \partial p/\partial t + u_k \partial p/\partial x_k$. The first term on the right hand side of Equation (3.12) represents the evolution of PDF in the composition space due to mean of the molecular diffusion term. The second and third terms on the right hand side represent the chemical reaction source term and chemical heat release term, respectively. The chemical reaction source and the heat release term is closed, representing a great advantage of the transported PDF method. The last term accounts for the coupling between pressure, viscous dissipation and sensible enthalpy. The second term on the left hand side of Equation (3.12) along with the first and the last term on the right hand side need to be modeled and we now discuss the modeling of these three terms.

The convection term (second term on left hand side of Equation (3.12)) can be decomposed into its filtered and sub-grid scale component as,

$$\frac{\partial}{\partial x_k} \left(\overline{u_k | \psi \bar{\rho} \tilde{f}} \right) = \frac{\partial \tilde{u}_k \bar{\rho} \tilde{f}}{\partial x_k} + \frac{\partial}{\partial x_k} \left(\overline{u_k'' | \psi \bar{\rho} \tilde{f}} \right), \quad (3.13)$$

where u_k'' is the sub-grid scale component of the velocity in the k^{th} direction. For regions where RANS modeling is used, the filtered and sub-grid components represent the mean and varying quantities respectively. The sub-grid scale component is modeled with a gradient-diffusion type closure [71],

$$\frac{\partial}{\partial x_k} \left(\overline{u_k'' | \psi \bar{\rho} \tilde{f}} \right) \approx - \frac{\partial}{\partial x_k} \left(\Gamma_t \frac{\partial \tilde{f}}{\partial x_k} \right), \quad (3.14)$$

where $\Gamma_t = \mu_t/Pr_t$ is the turbulent diffusivity assuming turbulent Prandtl number Pr_t is equal to the turbulent Schmidt number Sc_t ($Pr_t = Sc_t = 0.7$). The conditional diffusion terms for species mass fraction and enthalpy (first term on the right hand side of Equation (3.12)) are commonly modeled by using the mixing models like the interaction by exchange with the mean (IEM) model [95], modified Curl model [96,97] and the euclidean minimum spanning tree (EMST) model [98]. For the IEM model, the conditional diffusion term is written as,

$$-\frac{\partial}{\partial \psi_i} \left(\overline{\left(\frac{\partial}{\partial x_k} \left(\Gamma \frac{\partial \phi_i}{\partial x_k} \right) \right) | \psi \tilde{f}} \right) \approx \frac{\partial}{\partial x_k} \left(\Gamma \frac{\partial \tilde{f}}{\partial x_k} \right) - \frac{\partial}{\partial \psi_i} \left[\frac{1}{\tau} (\psi_i - \tilde{\phi}_i) \bar{\rho} \tilde{f} \right], \quad (3.15)$$

where τ is the scalar mixing time scale and needs to be modeled. The most popular model for τ is $\tau = \tau_f/C_\phi$ [71], where $\tau_f = k/\epsilon$ represents the turbulence time scale, ϵ is the turbulence dissipation rate and C_ϕ is the mixing constant (typical value 2.0). The last term on the right hand side of Equation (3.12) considers the effect of pressure and viscous dissipation on sensible enthalpy. The common practice in the past studies to treat the pressure term is to neglect the pressure fluctuation except the work by Delarue et al. [99,100] in which they solved the joint velocity-frequency-energy-pressure PDF by using a modeled equation for pressure. In this work, we follow the common practice of neglecting pressure in the PDF formulation. As a result, the temporal pressure term is modeled as,

$$\overline{\left(\frac{DP}{Dt} \right) | \psi \tilde{f}} = \left(\frac{\partial \bar{p}}{\partial t} + \tilde{u}_k \frac{\partial \bar{p}}{\partial x_k} \right) \tilde{f}. \quad (3.16)$$

Similarly, for the viscous dissipation, the sub-grid scale effect is neglected [101,102],

$$\overline{\left(\tau_{jk} \frac{\partial u_k}{\partial x_k} \right) | \psi \tilde{f}} = \left(\tilde{\tau}_{jk} \frac{\partial \tilde{u}_k}{\partial x_k} \right) \tilde{f}, \quad (3.17)$$

The effect of neglecting the sub-grid scale terms on the predictions is beyond the scope of this study and will not be addressed here.

Using the models defined in Equations (3.14, 3.15, 3.16, 3.17), the PDF transport equation in Equation (3.12) is now closed as follows,

$$\begin{aligned} \frac{\partial \tilde{f}}{\partial t} + \frac{\partial \tilde{u}_k \bar{\rho} \tilde{f}}{\partial x_k} = & \frac{\partial}{\partial x_k} \left((\Gamma + \Gamma_t) \frac{\partial \tilde{f}}{\partial x_k} \right) - \frac{\partial}{\partial \psi_i} \left[\frac{1}{\tau} (\psi_i - \tilde{\phi}_i) \bar{\rho} \tilde{f} \right] - \frac{\partial}{\partial \psi_i} (\dot{\omega}_i \bar{\rho} \tilde{f}) \\ & - \delta_{N_s+1} \frac{\partial}{\partial \psi_{N_s+1}} (\dot{Q}_{hr} \bar{\rho} \tilde{f}) - \delta_{N_s+1} \frac{\partial}{\partial \psi_{N_s+1}} \left(\left(\frac{\partial \bar{p}}{\partial t} + \tilde{u}_k \frac{\partial \bar{p}}{\partial x_k} + \tilde{\tau}_{jk} \frac{\partial \tilde{u}_k}{\partial x_k} \right) \tilde{f} \right), \end{aligned} \quad (3.18)$$

and can be solved numerically. However it is not straightforward to solve the modeled PDF transport equation. The PDF $\tilde{f}(\Psi; \mathbf{x}, t)$ has $N_s + 1$ dimensions corresponding to N_s number of species and sensible enthalpy. For detailed reaction mechanisms, the number of dimensions of $\tilde{f}(\Psi; \mathbf{x}, t)$ can be very large, e.g., up to 100 for a detailed reaction mechanism for methane oxidization. As a result of this high-dimensionality, it is not possible to use conventional finite-difference or finite-volume numerical methods to solve the modeled PDF transport equation. There are primarily two different classes of numerical approaches to solve Equation (3.12). The first class is the Lagrangian Monte Carlo particle approach [71] and the second class is an Eulerian approach [74, 101, 103]. In this study we use an Eulerian approach based on the Eulerian Monte Carlo fields (EMCF) method [74, 103] to solve the PDF transport equation. We describe the EMCF method in the following Section 3.4.

3.4 Eulerian Monte Carlo Fields Method

The EMCF method [74, 103, 104] introduces the concept of Eulerian stochastic fields $\phi_\alpha^n(\mathbf{x}, t)$ to approximately represent the PDF $\tilde{f}(\Psi; \mathbf{x}, t)$ where $\alpha = 1, 2, \dots, N_s + 1$ is the index for the scalar and $n = 1, 2, \dots, N_f$ represents the n^{th} stochastic field. Each of the $N_s + 1$ scalars in the PDF $\tilde{f}(\Psi; \mathbf{x}, t)$ is represented by an ensemble of N_f discrete stochastic fields to yield a stochastic system which represents a PDF $\tilde{f}^*(\Psi : \mathbf{x}, t)$ given by,

$$\tilde{f}^*(\Psi; \mathbf{x}, t) = \frac{1}{N_f} \sum_{n=1}^{N_f} \prod_{\alpha=1}^{N_s+1} \delta(\psi_\alpha - \phi_\alpha^n(\mathbf{x}, t)). \quad (3.19)$$

It can be readily verified that when $N_f \rightarrow \infty$, $\tilde{f}(\Psi; \mathbf{x}, t) = \tilde{f}^*(\Psi : \mathbf{x}, t)$. Here we use the Ito formulation [74], to describe the evolution of ϕ_α^n , governed by the stochastic partial differential equation (SPDE),

$$\bar{\rho}d\phi_\alpha^n = -\bar{\rho}\tilde{u}_k \frac{\partial\phi_\alpha^n}{\partial x_k} dt + \frac{\partial}{\partial x_k} ((\Gamma + \Gamma_t) \frac{\partial\phi_\alpha^n}{\partial x_k}) dt + \bar{\rho}\omega_\alpha^n dt + M_{\phi_\alpha^n} dt + \bar{\rho} \sqrt{2 \frac{(\Gamma + \Gamma_t)}{\bar{\rho}}} \frac{\partial\phi_\alpha^n}{\partial x_k} dW_k^n. \quad (3.20)$$

The first and second term on the right hand side represent transport of ϕ_α^n due to the mean flow and molecular and turbulent diffusion respectively, the third term ω_α^n is the reaction source term for ϕ_α^n , the fourth term $M_{\phi_\alpha^n}$ represents the micro-mixing process and is modeled using a mixing model and the last term denotes the Wiener process which represents the production of scalar fluctuations do to turbulence. The Wiener term dW_k^n varies with time but is independent in space thereby ensuring that all the stochastic fields are smooth and continuous. The Wiener term is approximated as $dW_k^n = \eta_k^n \sqrt{dt}$, where η_k^n is a k (number of physical dimensions) dimensional vector of Gaussian random numbers with zero mean and unity variance for the n^{th} stochastic field. In order to reduce the statistical fluctuations, we use $\{-1, +1\}$ to approximate the Gaussian random numbers. To ensure zero mean of dW_k^n , we consider only even number of stochastic fields and assign $\eta_k^n = 1$ to a randomly chosen half of the total number of stochastic fields, and $\eta_k^n = -1$ for the other half of the fields, repeating this for each of the physical dimensions. From ϕ_α^n , the m^{th} central moments ($m = 1, 2, \dots, \infty$) of the scalars can be easily obtained using,

$$\widetilde{\phi}_\alpha^m = \frac{1}{N_f} \sum_{n=1}^{N_f} (\phi_\alpha^n)^m. \quad (3.21)$$

Specifically the filtered mean $\tilde{\phi}_\alpha$ and sub-grid variance $\widetilde{\phi''^2}$ components of the scalars are,

$$\tilde{\phi}_\alpha = \frac{1}{N_f} \sum_{n=1}^{N_f} \phi_\alpha^n, \quad (3.22)$$

$$\widetilde{\phi''^2} = \frac{1}{N_f} \sum_{n=1}^{N_f} (\phi_\alpha^n - \tilde{\phi}_\alpha)^2. \quad (3.23)$$

In the following sections we further discuss the details of the EMCF method. In Section 3.5 we describe the two mixing models considered in this study to model the $M_{\phi_\alpha^n}$ term in Equation (3.20). The SPDEs for the thermo-chemical scalars are detailed in Section 3.6. The consistency issue and the corrections to make the EMCF method consistent with the PDF transport equation is discussed in Section 3.7. Section 3.8 explains the coupling between the EMCF method and the flow and turbulence equations described in Section 3.1.

3.5 Mixing Model

As discussed in Section 3.3, the conditional diffusion term for the thermo-chemical scalars of the joint-PDF is modeled using a mixing model. In the Lagrangian particle approach, significant amount of work has been to develop a number of mixing models like the IEM model [105], modified Curl model [95] and EMST model [98]. However for the EMCF method, currently only the IEM model [105] is commonly used. The main reason is that the IEM model ensures spatial smoothness of the stochastic fields which cannot guaranteed by the other mixing models. In this work, we add a new choice to the mixing models that are suitable for the EMCF method, called interaction by partially exchanging with the mean (IPEM) model. The IPEM model is described in Section 3.5.2, following a brief summary of the IEM model in Section 3.5.1.

3.5.1 IEM Mixing Model

For the the IEM mixing model [95] the mixing term $M_{\phi_\alpha^n}$ for the n^{th} stochastic field of a scalar ϕ_α in Equation (3.20) can be written as,

$$M_{\phi_\alpha^n} = -\frac{1}{2}\bar{\rho}C_\phi\Omega\left(\phi_\alpha^n - \tilde{\phi}_\alpha\right), \quad (3.24)$$

where $\Omega = 1/\tau_f = \epsilon/k$ is the mixing frequency. The mixing frequency Ω in the DES turbulence model depends on whether the model is using the LES approach or RANS approach. For the regions using the LES approach we use [106–108],

$$\Omega = C_\phi \frac{\mu + \mu_t}{\bar{\rho} \Delta^2}, \quad (3.25)$$

where Δ is the cube root of the volume of the grid cell. In the RANS region, Ω is calculated as [37],

$$\Omega = \beta^* \omega. \quad (3.26)$$

The IEM model introduces smooth variations to ϕ_α^n in space and time, which is necessary for the spatial and temporal evolution of the continuous stochastic fields. Many other mixing models developed for the Lagrangian Monte Carlo method do not satisfy this property and hence cannot be used here. This makes the choice of mixing models in the EMCF method very limited. The IEM model is fundamentally flawed because it preserves the shape of a PDF subject to homogeneous mixing. This is inconsistent with DNS studies which show that mixing relaxes the PDF towards Gaussian distribution under the effect of homogeneous mixing. Thus, we seek an improved IEM model to allow more realistic evolution of PDF subject to homogeneous mixing.

3.5.2 Interaction by Partially Exchanging with Mean Mixing Model

To improve the IEM mixing model, we introduce an intermittency property to the stochastic fields. At any time, a stochastic field is in mixing state or nonmixing state. In the mixing state, the field changes due to mixing, while in a nonmixing state, the field remains unchanged. This intermittency property has been used in other models such as the EMST mixing model [98] for the Lagrangian Monte Carlo particle method. This intermittency property is to some extent justified by experimental evidence [109] which shows that around 90% of the total scalar mixing takes place in about 45% of the total volume and hence the mixing is not uniform.

In the IPEM mixing model, we randomly select N_{IPEM} fields for mixing out of the total number of stochastic fields N_f . For these N_{IPEM} fields in the mixing state, the change in composition due to mixing is given by,

$$M_{\phi_\alpha^n} = -\frac{1}{2N_{IPEM}} \bar{\rho} C_\phi \Omega \left(\phi_\alpha^n - \tilde{\phi}_{\alpha, IPEM} \right), \quad n = 1, 2, \dots, N_{IPEM}, \quad (3.27)$$

$$\tilde{\phi}_{\alpha, IPEM} = \frac{1}{N_{IPEM}} \sum_{n=1}^{N_{IPEM}} \phi_\alpha^n, \quad (3.28)$$

and for the remaining $N_f - N_{IPEM}$ fields in the nonmixing state,

$$M_{\phi_\alpha^n} = 0, \quad n = N_{IPEM} + 1, \dots, N_f. \quad (3.29)$$

The IPEM mixing model is able to preserve the scalar mean $\tilde{\phi}_\alpha$ and causes the variance of the scalar ϕ''^2 to decay. While the IEM is not able predict the correct shape of the PDF, the IPEM mixing model does relax the PDF towards a Gaussian distribution for a homogenous mixing case.

3.6 Stochastic Partial Differential Equation for Enthalpy

In all of the previous studies [106, 107, 110–112] using the EMCF method, the thermo-chemical scalars ϕ_α^n considered are the species mass fraction and sensible enthalpy or static enthalpy. In highly compressible flows, it is generally preferred to consider stagnation enthalpy for the energy equation to ensure total energy conservation. In this work, we introduce a pseudo stagnation enthalpy for the stochastic fields to enable the use of the stagnation enthalpy in the EMCF methods in the context of the joint-scalar PDF method. The SPDE for the mass fraction i^{th} species Y_i^n and sensible enthalpy h_s^n of the n^{th} stochastic field is [106],

$$d(\bar{\rho} Y_i^n) = -\frac{\partial(\bar{\rho} \tilde{u}_k Y_i^n)}{\partial x_k} dt + \frac{\partial}{\partial x_k} \left((\Gamma + \Gamma_t) \frac{\partial Y_i^n}{\partial x_k} \right) dt + \bar{\rho} \dot{\omega}_i^n dt + M_{Y_i^n} dt + \bar{\rho} \sqrt{2 \frac{(\Gamma + \Gamma_t)}{\bar{\rho}} \frac{\partial Y_i^n}{\partial x_k}} dW_k^n, \quad (3.30)$$

and

$$\begin{aligned}
d(\bar{\rho}h_s^n) = & -\frac{\partial(\bar{\rho}\tilde{u}_k h_s^n)}{\partial x_k} dt + \frac{\partial}{\partial x_k} \left((\Gamma + \Gamma_t) \frac{\partial h_s^n}{\partial x_k} \right) dt + \left(\frac{D\bar{p}}{Dt} + \tilde{\tau}_{jk} \frac{\partial \tilde{u}_j}{\partial x_k} \right) dt \\
& - \sum_{i=1}^{N_s} \bar{\rho} \Delta h_{f,i}^0 \dot{\omega}_i^n dt + M_{h_s^n} dt + \bar{\rho} \sqrt{2 \frac{(\Gamma + \Gamma_t)}{\bar{\rho}}} \frac{\partial h_s^n}{\partial x_k} dW_k^n,
\end{aligned} \tag{3.31}$$

where $M_{Y_i^n}$ is the mixing term for n^{th} stochastic field of the mass fraction of the i^{th} species, $D\bar{p}/Dt = \partial\bar{p}/\partial t + \tilde{u}_k \partial\bar{p}/\partial x_k$ and $M_{h_s^n}$ is the mixing term for the n^{th} stochastic field of sensible enthalpy h_s . The mixing terms $M_{Y_i^n}$ and $M_{h_s^n}$ can be easily obtained from Equation (3.24) or Equation (3.27), depending on the choice of the mixing model, by replacing ϕ_α^n with Y_i^n and h_s^n . The static enthalpy h^n for the n^{th} stochastic field is given by [113],

$$h^n = h_s^n + \sum_{i=1}^{N_s} \Delta h_{f,i}^0 Y_i^n. \tag{3.32}$$

Using Equation (3.30), Equation(3.31) and Equation (3.32), the SPDE for h^n can be obtained as,

$$\begin{aligned}
d(\bar{\rho}h^n) = & -\frac{\partial(\bar{\rho}\tilde{u}_k h^n)}{\partial x_k} dt + \frac{\partial}{\partial x_k} \left((\Gamma + \Gamma_t) \frac{\partial h^n}{\partial x_k} \right) dt + \left(\frac{D\bar{p}}{Dt} + \tilde{\tau}_{jk} \frac{\partial \tilde{u}_j}{\partial x_k} \right) dt + M_{h^n} dt \\
& + \bar{\rho} \sqrt{2 \frac{(\Gamma + \Gamma_t)}{\bar{\rho}}} \frac{\partial h^n}{\partial x_k} dW_k^n,
\end{aligned} \tag{3.33}$$

where M_{h^n} is the mixing term for static enthalpy h .

The stagnation enthalpy of the n^{th} stochastic field h^{0n} can be generally defined as $h^{0n} = h^n + 1/2 u_k^n u_k^n$ where u_k^n is the velocity component in the k^{th} direction for the n^{th} field. The statistical distribution of the velocity component u_k in the composition PDF method is, however, not known unless the velocity component is included in the definition of the PDF, i.e., the velocity-composition joint PDF method. To utilize the stagnation enthalpy in the EMCF methods for the composition PDF, we introduce a pseudo stagnation enthalpy for the stochastic fields, based on the mean velocity \tilde{u}_k and the turbulent kinetic energy k [113],

$$h^{0n} = h^n + \frac{1}{2} \tilde{u}_k \tilde{u}_k + k. \tag{3.34}$$

The mean of the pseudo stagnation enthalpy is the same as the mean stagnation enthalpy. Thus the use of the pseudo stagnation enthalpy can ensure the conservation of the mean stagnation enthalpy. The fluctuations in h^{0n} is purely due to the fluctuations in h^n , and the fluctuations in kinetic energy is not included. To derive the SPDE for h^{0n} , we first need to obtain the transport equation for the filtered kinetic energy $1/2\tilde{u}_k\tilde{u}_k$ from the transport equation of the instantaneous kinetic energy equation $1/2u_ku_k$ which is [113],

$$\frac{\partial}{\partial t} \left(\rho \left(\frac{1}{2} u_k u_k \right) \right) + \frac{\partial}{\partial x_j} \left(\rho u_j \left(\frac{1}{2} u_k u_k \right) \right) = u_j \frac{\partial \sigma_{kj}}{\partial x_k}, \quad (3.35)$$

where $\sigma_{jk} = \tau_{jk} - p\delta_{jk}$. Taking Favre-average of Equation (3.35) we get,

$$\begin{aligned} \frac{\partial}{\partial t} \left(\bar{\rho} \left(\frac{1}{2} \tilde{u}_k \tilde{u}_k + k \right) \right) + \frac{\partial}{\partial x_j} \left(\bar{\rho} \tilde{u}_j \left(\frac{1}{2} \tilde{u}_k \tilde{u}_k + k \right) \right) &= \widetilde{u_j \frac{\partial \sigma_{kj}}{\partial x_k}} - \frac{\partial}{\partial x_k} \left(\widetilde{\bar{\rho} \tilde{u}_j u''_k u''_j} \right) \\ &\quad - \frac{1}{2} \frac{\partial}{\partial x_k} \left(\widetilde{\bar{\rho} u''_k u''_j u''_j} \right). \end{aligned} \quad (3.36)$$

The terms on the right hand side of Equation (3.36) are unclosed and they are commonly modeled as [113],

$$\begin{aligned} \widetilde{u_j \frac{\partial \sigma_{kj}}{\partial x_k}} &= \tilde{u}_j \frac{\partial \tilde{\sigma}_{kj}}{\partial x_k} = \tilde{u}_j \frac{\partial \tilde{\tau}_{kj}}{\partial x_k} - \tilde{u}_j \frac{\partial \bar{p}}{\partial x_k} \delta_{jk}, \\ -\widetilde{\bar{\rho} \tilde{u}_j u''_k u''_j} &= \tilde{u}_j \tilde{\tau}_{t,kj}, \\ \widetilde{\bar{\rho} u''_k u''_j u''_j} &= 0. \end{aligned} \quad (3.37)$$

Using these modeled terms, Equation (3.36) can be rewritten as,

$$\begin{aligned} \frac{\partial}{\partial t} \left(\bar{\rho} \left(\frac{1}{2} \tilde{u}_k \tilde{u}_k + k \right) \right) + \frac{\partial}{\partial x_k} \left(\bar{\rho} \tilde{u}_k \left(\frac{1}{2} \tilde{u}_j \tilde{u}_j + k \right) \right) &= \tilde{u}_j \frac{\partial \tilde{\tau}_{kj}}{\partial x_k} \\ &\quad - \tilde{u}_j \frac{\partial \bar{p}}{\partial x_k} \delta_{jk} + \frac{\partial}{\partial x_k} (\tilde{u}_j \tilde{\tau}_{t,kj}). \end{aligned} \quad (3.38)$$

We can further write Equation (3.38) in a form similar to the SPDE,

$$\begin{aligned} d \left(\bar{\rho} \left(\frac{1}{2} \tilde{u}_k \tilde{u}_k + k \right) \right) &= - \frac{\partial}{\partial x_k} \left(\bar{\rho} \tilde{u}_k \left(\frac{1}{2} \tilde{u}_j \tilde{u}_j + k \right) \right) dt + \tilde{u}_j \frac{\partial \tilde{\tau}_{kj}}{\partial x_k} dt - \tilde{u}_j \frac{\partial \bar{p}}{\partial x_k} \delta_{jk} dt \\ &\quad + \frac{\partial}{\partial x_k} (\tilde{u}_j \tilde{\tau}_{t,kj}) dt. \end{aligned} \quad (3.39)$$

Finally we arrive at the SPDE for h^{0n} by adding Equation (3.33) and Equation (3.39),

$$d(\bar{\rho}h^{0n}) = -\frac{\partial(\bar{\rho}\tilde{u}_k h^{0n})}{\partial x_k}dt + \frac{\partial}{\partial x_k} \left((\Gamma + \Gamma_t) \frac{\partial h^n}{\partial x_k} \right) dt + \left(\frac{\partial \bar{p}}{\partial t} + \frac{\partial \tilde{u}_j \tilde{\tau}_{e,jk}}{\partial x_k} \right) dt + M_{h^n} dt + \bar{\rho} \sqrt{2 \frac{(\Gamma + \Gamma_t)}{\bar{\rho}} \frac{\partial h^n}{\partial x_k}} dW_k^n. \quad (3.40)$$

In Equation (3.40) we can see that both the mixing term M_{h^n} is the same as the mixing term for h^n is Equation (3.33) and the Wiener term is a function of h^n and not h^{0n} . This is because the velocity field is the same for all of the stochastic fields and it does not contribute to the stochastic process.

In summary, we introduced a pseudo stagnation enthalpy h^{0n} for each stochastic field and derived the SPDE for h^{0n} in Equation (3.40). The use of the pseudo stagnation enthalpy ensure conservation of mean stagnation enthalpy, which is desired for highly compressible flows. Along with the SPDE for h^{0n} , the SPDE system consists of the mass and momentum conservation equations (3.1)-(3.2), turbulence modeling equations (3.3) - (3.4) and the species equations (3.30).

3.7 Stochastic Terms and Model Consistency in the EMCF method

The stochastic terms in the SPDEs presented in previous sections are written based on the the original EMCF method by Valino [74], which we call the EMCF-O method. Valino et al. [103] pointed an issue of the model inconsistency in the stochastic terms in the EMCF methods and attempted to develop a modified method which we call EMCF-M method. Wang et al. [114] systematically analyzed the existing EMCF methods and further pointed out the model inconsistency even in the EMCF-M method. They developed consistency corrections to the EMCF methods called EMCF-C1 and EMCF-C2. In this work, we continue to examine these these different EMCF methods and apply them to more realistic turbulence and turbulent combustion cases to further examine the effect of model inconsistency.

For the EMCF-O, EMCF-M and EMCF-C2 methods, the SPDEs for the pseudo stagnation enthalpy h^{0n} and the species mass fraction Y_i^n can be written in a general form as,

$$d(\bar{\rho}h^{0n}) = -\frac{\partial(\bar{\rho}\tilde{u}_k h^{0n})}{\partial x_k} dt + \frac{\partial}{\partial x_k} \left((\Gamma + \Gamma_t) \frac{\partial h^n}{\partial x_k} \right) dt + \left(\frac{\partial \bar{\rho}}{\partial t} + \frac{\partial \tilde{u}_j \tilde{\tau}_{e,jk}}{\partial x_k} \right) dt + M_{h^n} dt + \bar{\rho} \sqrt{2 \frac{(\Gamma_{ch} + \Gamma_t)}{\bar{\rho}} \frac{\partial h^n}{\partial x_k}} dW_k^n, \quad (3.41)$$

$$d(\bar{\rho}Y_i^n) = -\frac{\partial(\bar{\rho}\tilde{u}_k Y_i^n)}{\partial x_k} dt + \frac{\partial}{\partial x_k} \left((\Gamma + \Gamma_t) \frac{\partial Y_i^n}{\partial x_k} \right) dt + \bar{\rho} \dot{\omega}_i^n dt + M_{Y_i^n} dt + \bar{\rho} \sqrt{2 \frac{(\Gamma_{cY_i} + \Gamma_t)}{\bar{\rho}} \frac{\partial Y_i^n}{\partial x_k}} dW_k^n - W_c^n, \quad (3.42)$$

where Γ_{ch} and Γ_{cY_i} are correction parameters for h^{0n} and Y_i^n respectively and W_c^n is a correction parameter for Y_i^n so that summation of Equation (3.42) over all the N_s species gives the continuity equation in Equation (3.1). Table 3.1 specifies Γ_{ch} , Γ_{cY_i} , and W_c^n for the three methods. In the following three sections we briefly describe

Table 3.1.: Correction parameters Γ_{cY_i} , Γ_{ch} and W_c^n for the EMCF-O, EMCF-M and EMCF-C2 methods.

	Γ_{cY_i}	Γ_{ch}	W_c^n
EMCF-O	Γ	Γ	0
EMCF-M	0	0	0
EMCF-C2	$\Gamma \left(1 - \frac{\nabla \tilde{Y}_i \cdot \nabla \tilde{Y}_i}{\nabla \tilde{Y}_i \cdot \nabla \tilde{Y}_i} \right)$	$\Gamma \left(1 - \frac{\nabla \tilde{h} \cdot \nabla \tilde{h}}{\nabla \tilde{h} \cdot \nabla \tilde{h}} \right)$	$\frac{1}{2} \frac{\bar{\rho}}{N_s} \sum_{i=1}^{N_s} \left(\bar{\rho} \sqrt{2 \frac{(\Gamma_{cY_i} + \Gamma_t)}{\bar{\rho}} \frac{\partial Y_i^n}{\partial x_k}} dW_k^n \right)$

these methods.

3.7.1 EMCF-O Method

The EMCF method discussed in Section 3.4 is the original method developed by Valino [74]. We denote this version of the EMCF method as the EMCF-O method. In the EMCF-O method, the SPDE for the n^{th} stochastic field of the stagnation enthalpy h^{0n} and the species mass fraction Y_i^n is given by Equation (3.40) and Equation (3.30). The EMCF-O method is not mathematically consistent with the PDF transport equation for low Re turbulence because of the presence of a spurious production term in the transport equation of the variance of scalars [103].

3.7.2 EMCF-M Method

The inconsistency in the EMCF-O method was recently identified and corrected by Valino et al. [103] to eliminate the spurious production of variance of scalars. We term this version of the EMCF method the EMCF-M method. In the EMCF-M method, molecular diffusion coefficient Γ is removed from the Wiener term of the SPDEs for Y_i^n and h^{0n} in Equation (3.30) and Equation (3.40) respectively. Valino et al. [103] argued that by eliminating Γ , all the stochastic fields become equal and deterministic in nature in the laminar limit ($\Gamma_t \rightarrow 0$) resulting in zero scalar variance.

3.7.3 EMCF-C2 Method

Wang et al. [115] identified that the EMCF-M method is also not mathematically consistent with the PDF transport equation since it introduces a spurious dissipation term in the transport equation of scalar variance. They used a more a general approach [71] compared to Valino et al. [103] to establish mathematical inconsistency of the EMCF-O method for all moments greater than 1. They concluded that it is very difficult to develop a EMCF method that is consistent for all the moments of the scalars. To make the EMCF method consistent for the second scalar moment i.e.

the scalar variance, they introduced two new parameters $\omega_{c\phi_\alpha}$ and $\Gamma_{c\alpha}$ in the SPDE for ϕ_α^n in Equation (3.20) so that it can be written as,

$$\begin{aligned} \bar{\rho}d\phi_\alpha^n = & -\bar{\rho}\tilde{u}_k \frac{\partial\phi_\alpha^n}{\partial x_k} dt + \frac{\partial}{\partial x_k} ((\Gamma + \Gamma_t) \frac{\partial\phi_\alpha^n}{\partial x_k}) dt + \bar{\rho}\omega_\alpha^n dt + M_{c\phi_\alpha^n} dt \\ & + \bar{\rho} \sqrt{2 \frac{(\Gamma_{c\alpha} + \Gamma_t)}{\bar{\rho}}} \frac{\partial\phi_\alpha^n}{\partial x_k} dW_k^n, \end{aligned} \quad (3.43)$$

where $M_{c\phi_\alpha^n}$ is the corrected mixing model and for the IEM mixing model it is,

$$M_{c\phi_\alpha^n} = -\frac{1}{2}\bar{\rho}(C_\phi\Omega + \omega_{c\phi_\alpha}) \left(\phi_\alpha^n - \tilde{\phi}_\alpha \right). \quad (3.44)$$

Similar formulation of $M_{c\phi_\alpha^n}$ for the IPFM mixing model can be obtained by adding the correction term $\omega_{c\phi_\alpha}$ to the scalar mixing frequency $C_\phi\Omega$. By incorporating $\omega_{c\phi_\alpha}$ and $\Gamma_{c\alpha}$ in the SPDE of ϕ_α^n , the spurious variance production observed in the EMCF-O method is eliminated. Wang et al. [115] recognized that $\omega_{c\phi_\alpha}$ and $\Gamma_{c\alpha}$ can have infinite number of specifications. One set of values from among the infinite sets is [115],

$$\begin{cases} \omega_{c\alpha} = 0 \\ \Gamma_{c\alpha} = \Gamma \left(1 - \frac{\nabla\tilde{\phi}_\alpha \cdot \nabla\tilde{\phi}_\alpha}{\nabla\phi_\alpha \cdot \nabla\phi_\alpha} \right) \end{cases}. \quad (3.45)$$

The corrected EMCF method with these values for $\omega_{c\phi_\alpha}$ and $\Gamma_{c\alpha}$ is denoted EMCF-C2 method [115]. Wang at al. [115] compared the predictions of the EMCF-C2 method with the EMCF method for another set of values of $\omega_{c\phi_\alpha}$ and $\Gamma_{c\alpha}$ named the EMCF-C1 method in an opposed-jet turbulent mixing layer test case and a thermal wake behind a line source in grid turbulence experimental case. They did not observe significant difference between the predictions of the two methods and hence in this study we consider only the EMCF-C2 method.

In the following Section 3.8 we describe the calculation of the filtered density $\bar{\rho}$.

3.8 Coupling between Flow and Turbulence Solver and EMCF Solver

For a turbulent combustion problem using the EMCF method, we solve the flow and turbulence field using Equations (3.1) - (3.4) along with the thermo-chemical

scalars h^{0n} and Y_i^n in Equation (3.41) and Equation (3.42) respectively. These set of equations are strongly coupled through the filtered density $\bar{\rho}$ and hence it is critical to accurately calculate $\bar{\rho}$ while trying to minimize the statistical error in its calculation. We use the ideal gas law to determine $\bar{\rho}$ and there are two different approaches to calculate $\bar{\rho}$. In the following sections we briefly discuss these two approaches.

3.8.1 Method 1 to Calculate filtered Density

In Method 1, we first calculate the filtered density for the i^{th} species of the n^{th} stochastic field Θ_i^n , using the filtered pressure \bar{p} , $\Theta_i^n = \bar{p}W_i / (RT^n)$, where W_i is the filtered molecular weight of the i^{th} species respectively. The density of the mixture for the n^{th} stochastic field ρ^n is then given by,

$$\rho^n = \left(\sum_{i=1}^{N_s} \frac{Y_i^n}{\Theta_i^n} \right)^{-1}, \quad (3.46)$$

$$\bar{\rho} = \left(\frac{1}{N_f} \sum_{n=1}^{N_f} \frac{1}{\rho^n} \right)^{-1} = \left(\frac{R}{\bar{p}N_f} \sum_{n=1}^{N_f} T^n \left(\sum_{i=1}^{N_s} \frac{Y_i^n}{W_i} \right) \right)^{-1} = \frac{\bar{p}}{R \left(\frac{1}{N_f} \sum_{n=1}^{N_f} \frac{T^n}{W_{mix}^n} \right)}, \quad (3.47)$$

where W_{mix}^n is the molecular weight of the mixture for the n^{th} stochastic field is defined as $1/W_{mix}^n = \sum_{i=1}^{N_s} (Y_i^n/W_i)$. The partial derivatives of $\bar{\rho}$ with respect to \bar{p} , T^n and Y_i^n are required in the numerical implementation of the EMCF method discussed later in Section 4.5. For Method 1, these derivatives are,

$$\frac{\partial \bar{\rho}}{\partial \bar{p}} = \frac{1}{N_f} \sum_{n=1}^{N_f} \left[\sum_{i=1}^{N_s} \left(\frac{\rho^n}{\Theta_i^n} \right)^2 Y_i^n \Theta_{i,\bar{p}}^n \right], \quad (3.48)$$

$$\frac{\partial \bar{\rho}}{\partial T^n} = \frac{1}{N_f} \sum_{i=1}^{N_s} \left(\frac{\rho^n}{\Theta_i^n} \right)^2 Y_i^n \Theta_{i,T^n}^n, \quad (3.49)$$

$$\frac{\partial \bar{\rho}}{\partial Y_i^n} = -\frac{1}{N_f} \left[\rho^{n2} \left(\frac{1}{\Theta_i^n} - \frac{1}{\Theta_{N_s}^n} \right) \right], \quad (3.50)$$

where,

$$\Theta_{i,\bar{p}}^n = \frac{\partial \Theta_i^n}{\partial \bar{p}} = \frac{\Theta_i^n}{\bar{p}}, \quad (3.51)$$

$$\Theta_{i,T^n}^n = \frac{\partial \Theta_i^n}{\partial T^n} = -\frac{\Theta_i^n}{T^n}, \quad (3.52)$$

and $\Theta_{N_s}^n$ is the density based on the filtered pressure for the last species.

3.8.2 Method 2 to Calculate filtered Density

In Method 2, we use the the partial filtered pressure for the i^{th} species \bar{p}_i , in the ideal gas law to calculate the density of the i^{th} species for the n^{th} stochastic field ρ_i^n [113],

$$\rho_i^n = \frac{\bar{p}_i W_i}{RT^n}. \quad (3.53)$$

$\bar{\rho}_i$ can be calculated from Equation (3.53) as,

$$\frac{1}{\bar{\rho}_i} = \frac{1}{N_f} \sum_{n=1}^{N_f} \frac{1}{\rho_i^n} = \frac{R\tilde{T}}{\bar{p}_i W_i}, \quad (3.54)$$

and the filtered density $\bar{\rho}$ is given by,

$$\bar{\rho} = \frac{\bar{\rho}_i}{\tilde{Y}_i} = \frac{\bar{p} \tilde{X}_i W_i}{R\tilde{T} \tilde{Y}_i} = \frac{\bar{p} W_{mix}}{R\tilde{T}}, \quad (3.55)$$

where \tilde{X}_i is the filtered mole fraction of the i^{th} species and $W_{mix} = \tilde{X}_i W_i$ is the molecular weight of the mixture based on the filtered mole fraction. The partial derivatives $\partial \bar{\rho} / \partial \bar{p}$, $\partial \bar{\rho} / \partial T^n$ and $\partial \bar{\rho} / \partial Y_i^n$ for Method 2 can be written as,

$$\frac{\partial \bar{\rho}}{\partial \bar{p}} = \frac{W_{mix}}{R\tilde{T}} = \frac{\bar{\rho}}{\bar{p}}, \quad (3.56)$$

$$\frac{\partial \bar{\rho}}{\partial T^n} = -\frac{1}{N_f} \frac{\bar{\rho}}{\tilde{T}}, \quad (3.57)$$

$$\frac{\partial \bar{\rho}}{\partial Y_i^n} = \frac{\bar{p}}{R\tilde{T}} \frac{\partial W_{mix}}{\partial Y_i^n} = \frac{\bar{p}}{R\tilde{T}} \frac{\partial}{\partial Y_i^n} \left(\sum_{i=1}^{N_s} \frac{\tilde{Y}_i}{W_i} \right)^{-1} = -\frac{\bar{\rho} W_{mix}}{N_f} \left(\frac{1}{W_i} - \frac{1}{W_{N_s}} \right), \quad (3.58)$$

where W_{N_s} is the molecular weight of the N_s^{th} species or the last species. The filtered density calculated using Method 1 (Equation (3.47)) is not the same as the filtered density calculated using Method 2 (Equation (3.55)). In the limit of laminar flow where the variance is zero for all the scalars, W_{mix}^n is the same for all the fields and is equal to W_{mix} and the filtered density predicted by both the methods is identical. It

is possible to have two additional methods to calculate $\bar{\rho}$ based on Method 1, firstly by replacing Y_i^n with \tilde{Y}_i in Equation (3.46) and secondly by using $\bar{\Theta}_i$ instead of Θ_i^n in Equation (3.46). The $\bar{\rho}$ obtained by using these two methods is identical to $\bar{\rho}$ calculated using Method 2. We demonstrate the effect of Method 1 and Method 2 for calculation of filtered density on the predictions of a series of test cases in Chapter 7.

To summarize, in this chapter we described different physical models used in the current framework for modeling combustion instabilities. In the following chapter we describe their numerical implementation.

4. NUMERICAL APPROACHES

The numerical implementation of the modeling framework detailed in Chapter 3 is presented here. Details about the spatial and temporal discretization schemes, numerical algorithm of the in-house flow solver is provided. For the flamelet model, specifically the FPV model, three different presumed-PDF table integration approaches are discussed. Lastly, the implementation of the flamelet models in the flow solver is described.

4.1 Governing Equations in Conservative Coupled Form

In the GEMS solver, the governing equations are implemented in a conservative vector form and can be written as,

$$\frac{\partial Q}{\partial t} + \nabla \cdot (\vec{F} - \vec{G}) = H, \quad (4.1)$$

where Q is the vector of conserved variables, \vec{F} is the inviscid flux vector with F_x, F_y, F_z being the components of \vec{F} in the x, y, z direction respectively, \vec{G} is the viscous flux vector with G_x, G_y, G_z the x, y, z components and H is the source term vector. A finite-volume numerical approach with a dual-time algorithm [116] is used to solve the set of equations in Equation (4.1). In the dual-time algorithm, a pseudo derivative $\partial Q/\partial \tau$ is added to Equation (4.1),

$$\frac{\partial Q}{\partial \tau} + \frac{\partial Q}{\partial t} + \nabla \cdot (\vec{F} - \vec{G}) = H. \quad (4.2)$$

For each physical time step, time marching is carried out for the pseudo time derivative until a steady state is reached and the original set of equations in Equation (4.1) is recovered. The pseudo time marching helps improve the rate of convergence especially for low Mach number problems [116]. For calculating the pseudo derivative $\partial Q/\partial \tau$,

a set of primitive variables Q_p is used and in terms of Q_p , the pseudo derivative can be written as $\partial Q/\partial\tau = (\partial Q/\partial Q_p)(\partial Q_p/\partial\tau) = \Gamma_p(\partial Q_p/\partial\tau)$ where the jacobian $\Gamma_p = \partial Q/\partial Q_p$ [79].

In the following sections we discuss the formulations of Q , \vec{F} , \vec{G} , H , Q_p and Γ_p for the flamelet models in Section 4.2 and for the transported PDF model in Section 4.5.

4.2 Flamelet Model Implementation

For the flamelet models discussed in Section 3.2, the Q vector is written,

$$Q = \left[\bar{\rho}, \bar{\rho}\tilde{u}, \bar{\rho}\tilde{v}, \bar{\rho}\tilde{w}, \bar{\rho}\tilde{h}^0 - \bar{p}, \bar{\rho}k, \bar{\rho}\omega, \bar{\rho}\tilde{\xi}, \bar{\rho}\tilde{\xi}''^2, \bar{\rho}\tilde{C} \right]^T. \quad (4.3)$$

The inviscid (F_x , F_y , and F_z) and viscous (G_x , G_y , and G_z) flux components in Equation (4.1) are,

$$F_x = \left[\bar{\rho}\tilde{u}, \bar{\rho}\tilde{u}^2 + \bar{p}, \bar{\rho}\tilde{u}\tilde{v}, \bar{\rho}\tilde{u}\tilde{w}, \bar{\rho}\tilde{u}\tilde{h}^0, \bar{\rho}\tilde{u}k, \bar{\rho}\tilde{u}\omega, \bar{\rho}\tilde{u}\tilde{\xi}, \bar{\rho}\tilde{u}\tilde{\xi}''^2, \bar{\rho}\tilde{u}\tilde{C} \right]^T, \quad (4.4)$$

$$F_y = \left[\bar{\rho}\tilde{v}, \bar{\rho}\tilde{v}\tilde{u}, \bar{\rho}\tilde{v}^2 + \bar{p}, \bar{\rho}\tilde{v}\tilde{w}, \bar{\rho}\tilde{v}\tilde{h}^0, \bar{\rho}\tilde{v}k, \bar{\rho}\tilde{v}\omega, \bar{\rho}\tilde{v}\tilde{\xi}, \bar{\rho}\tilde{v}\tilde{\xi}''^2, \bar{\rho}\tilde{v}\tilde{C} \right]^T, \quad (4.5)$$

$$F_z = \left[\bar{\rho}\tilde{w}, \bar{\rho}\tilde{w}\tilde{u}, \bar{\rho}\tilde{w}\tilde{v}, \bar{\rho}\tilde{w}^2 + \bar{p}, \bar{\rho}\tilde{w}\tilde{h}^0, \bar{\rho}\tilde{w}k, \bar{\rho}\tilde{w}\omega, \bar{\rho}\tilde{w}\tilde{\xi}, \bar{\rho}\tilde{w}\tilde{\xi}''^2, \bar{\rho}\tilde{w}\tilde{C} \right]^T, \quad (4.6)$$

$$G_x = \left[0, \tau_{e,xx}, \tau_{e,xy}, \tau_{e,xz}, Q_x, \Gamma_k \frac{\partial k}{\partial x}, \Gamma_\omega \frac{\partial \omega}{\partial x}, \Gamma_e \frac{\partial \tilde{\xi}}{\partial x}, \Gamma_e \frac{\partial \tilde{\xi}''^2}{\partial x}, \Gamma_e \frac{\partial \tilde{C}}{\partial x} \right]^T, \quad (4.7)$$

$$G_y = \left[0, \tau_{e,yx}, \tau_{e,yy}, \tau_{e,yz}, Q_y, \Gamma_k \frac{\partial k}{\partial y}, \Gamma_\omega \frac{\partial \omega}{\partial y}, \Gamma_e \frac{\partial \tilde{\xi}}{\partial y}, \Gamma_e \frac{\partial \tilde{\xi}''^2}{\partial y}, \Gamma_e \frac{\partial \tilde{C}}{\partial y} \right]^T, \quad (4.8)$$

$$G_z = \left[0, \tau_{e,zx}, \tau_{e,zy}, \tau_{e,zz}, Q_z, \Gamma_k \frac{\partial k}{\partial z}, \Gamma_\omega \frac{\partial \omega}{\partial z}, \Gamma_e \frac{\partial \tilde{\xi}}{\partial z}, \Gamma_e \frac{\partial \tilde{\xi}''^2}{\partial z}, \Gamma_e \frac{\partial \tilde{C}}{\partial z} \right]^T, \quad (4.9)$$

where in the viscous flux components G_x , G_y , G_z in Equations (4.7 - 4.9), $Q_j = \tilde{u}_k \tau_{e,jk} + K \partial \tilde{T} / \partial x_j + \mu_t (\partial \tilde{h} / \partial x_j) / Pr_t D_t$ and $\Gamma_e = \Gamma + \Gamma_t$. The source term vector H is,

$$H = \left[0, 0, 0, 0, 0, \dot{\omega}_k, \dot{\omega}_\omega, 0, \dot{\omega}_{\tilde{\xi}''^2}, \dot{\rho}\tilde{\omega}_c \right]^T, \quad (4.10)$$

where,

$$\dot{\omega}_k = \tau_{t,jk} \frac{\partial \tilde{u}_j}{\partial x_k} - \beta^* \bar{\rho} k \omega,$$

$$\begin{aligned}\dot{\omega}_\omega &= \frac{\gamma\omega}{k}\tau_{t,jk}\frac{\partial\tilde{u}_j}{\partial x_k} - \beta\bar{\rho}\omega^2 + \bar{\rho}\frac{\sigma_d}{\omega}\frac{\partial k}{\partial x_j}\frac{\partial\omega}{\partial x_j}, \\ \dot{\omega}_{\xi''^2} &= 2\frac{\mu_t}{Sc_t}\frac{\partial\tilde{\xi}}{\partial x_j}\frac{\partial\tilde{\xi}}{\partial x_j} - \tilde{\chi}, \\ \tilde{\chi} &= 2\bar{\rho}C_\phi\beta^*\omega\xi''^2,\end{aligned}$$

$\tilde{\omega}_c$ is the reaction source term for the progress variable C and $C_\phi = 2.0$ is a constant. The ideal gas law for the i^{th} species is $\bar{\rho}_i = \bar{p}W_i / (RT)$, and the density of the mixture $\bar{\rho}$ is given by,

$$\bar{\rho} = \left(\sum_{i=1}^{N_s} \frac{\tilde{Y}_i}{\bar{\rho}_i} \right)^{-1}, \quad (4.11)$$

where $\bar{\rho}_i$, W_i , \tilde{Y}_i are the density, molecular weight and mass fraction of the i^{th} species respectively. The set of primitive variables Q_p for the flamelet models is defined as,

$$Q_p = \left[\bar{p}, \tilde{u}, \tilde{v}, \tilde{w}, \tilde{T}, k, \omega, \tilde{\xi}, \xi''^2, \tilde{C} \right]^T, \quad (4.12)$$

and the jacobian $\Gamma_p = \partial Q / \partial Q_p$ [117, 118] is given by,

$$\Gamma_p = \begin{bmatrix} \rho_{\bar{p}} & 0 & 0 & 0 & \rho_{\tilde{T}} & 0 & 0 & \rho_{\tilde{\xi}} & \rho_{\xi''^2} & \rho_{\tilde{C}} \\ \rho_{\bar{p}\tilde{u}} & \bar{\rho} & 0 & 0 & \rho_{\tilde{T}\tilde{u}} & 0 & 0 & \rho_{\tilde{\xi}\tilde{u}} & \rho_{\xi''^2\tilde{u}} & \rho_{\tilde{C}\tilde{u}} \\ \rho_{\bar{p}\tilde{v}} & 0 & \bar{\rho} & 0 & \rho_{\tilde{T}\tilde{v}} & 0 & 0 & \rho_{\tilde{\xi}\tilde{v}} & \rho_{\xi''^2\tilde{v}} & \rho_{\tilde{C}\tilde{v}} \\ \rho_{\bar{p}\tilde{w}} & 0 & 0 & \bar{\rho} & \rho_{\tilde{T}\tilde{w}} & 0 & 0 & \rho_{\tilde{\xi}\tilde{w}} & \rho_{\xi''^2\tilde{w}} & \rho_{\tilde{C}\tilde{w}} \\ H_{\bar{p}} & \bar{\rho}\tilde{u} & \bar{\rho}\tilde{v} & \bar{\rho}\tilde{w} & H_{\tilde{T}} & 0 & 0 & H_{\tilde{\xi}} & H_{\xi''^2} & H_{\tilde{C}} \\ \rho_{\bar{p}k} & 0 & 0 & 0 & \rho_{\tilde{T}k} & \bar{\rho} & 0 & \rho_{\tilde{\xi}k} & \rho_{\xi''^2k} & \rho_{\tilde{C}k} \\ \rho_{\bar{p}\omega} & 0 & 0 & 0 & \rho_{\tilde{T}\omega} & 0 & \bar{\rho} & \rho_{\tilde{\xi}\omega} & \rho_{\xi''^2\omega} & \rho_{\tilde{C}\omega} \\ \rho_{\bar{p}\tilde{\xi}} & 0 & 0 & 0 & \rho_{\tilde{T}\tilde{\xi}} & 0 & 0 & \rho_{\tilde{\xi}\tilde{\xi}} + \bar{\rho} & \rho_{\xi''^2\tilde{\xi}} & \rho_{\tilde{C}\tilde{\xi}} \\ \rho_{\bar{p}\xi''^2} & 0 & 0 & 0 & \rho_{\tilde{T}\xi''^2} & 0 & 0 & \rho_{\tilde{\xi}\xi''^2} & \rho_{\xi''^2\xi''^2} + \bar{\rho} & \rho_{\tilde{C}\xi''^2} \\ \rho_{\bar{p}\tilde{C}} & 0 & 0 & 0 & \rho_{\tilde{T}\tilde{C}} & 0 & 0 & \rho_{\tilde{\xi}\tilde{C}} & \rho_{\xi''^2\tilde{C}} & \rho_{\tilde{C}\tilde{C}} + \bar{\rho} \end{bmatrix} \quad (4.13)$$

The terms in Γ_p are,

$$\begin{aligned}\rho_{\bar{p}} &= \frac{\partial\bar{\rho}}{\partial\bar{p}} = \sum_{i=1}^{N_s} \left[\left(\frac{\bar{\rho}}{\bar{\rho}_i} \right)^2 \tilde{Y}_i \frac{W_i}{RT} \right], \\ \rho_{\tilde{T}} &= \frac{\partial\bar{\rho}}{\partial\tilde{T}} = - \sum_{i=1}^{N_s} \left[\left(\frac{\bar{\rho}}{\bar{\rho}_i} \right)^2 \tilde{Y}_i \frac{\bar{\rho}_i}{\tilde{T}} \right],\end{aligned}$$

$$\begin{aligned}
H_{\bar{p}} &= \rho_{\bar{p}} \tilde{h}^0 + \bar{\rho} h_{\bar{p}}^0 - 1, \\
H_{\tilde{T}} &= \rho_{\tilde{T}} \tilde{h}^0 + \bar{\rho} h_{\tilde{T}}^0, \\
H_{\tilde{\xi}} &= \rho_{\tilde{\xi}} \tilde{h}^0 + \bar{\rho} h_{\tilde{\xi}}^0, \\
H_{\widetilde{\xi''^2}} &= \rho_{\widetilde{\xi''^2}} \tilde{h}^0 + \bar{\rho} h_{\widetilde{\xi''^2}}^0, \\
H_{\tilde{C}} &= \rho_{\tilde{C}} \tilde{h}^0 + \bar{\rho} h_{\tilde{C}}^0, \\
h_p^0 &= \frac{\partial \tilde{h}^0}{\partial \bar{p}} = \frac{\partial \tilde{h}}{\partial \bar{p}} = 0, \\
h_{\tilde{T}}^0 &= \frac{\partial \tilde{h}^0}{\partial \tilde{T}} = \frac{\partial \tilde{h}}{\partial \tilde{T}} = c_p.
\end{aligned}$$

Since generally $\bar{\rho} = f(\tilde{Y}_i, \tilde{T}, \bar{p})$, the derivatives of $\bar{\rho}$ with respect to $\tilde{\xi}$, $\widetilde{\xi''^2}$ and \tilde{C} are,

$$\begin{aligned}
\rho_{\tilde{\xi}} &= \frac{\partial \bar{\rho}}{\partial \tilde{\xi}} = \sum_{i=1}^{N_s} \left(\frac{\partial \bar{\rho}}{\partial \tilde{Y}_i} \frac{\partial \tilde{Y}_i}{\partial \tilde{\xi}} \right) + \frac{\partial \bar{\rho}}{\partial \tilde{T}} \frac{\partial \tilde{T}}{\partial \tilde{\xi}} + \frac{\partial \bar{\rho}}{\partial \bar{p}} \frac{\partial \bar{p}}{\partial \tilde{\xi}}, \\
\rho_{\widetilde{\xi''^2}} &= \frac{\partial \bar{\rho}}{\partial \widetilde{\xi''^2}} = \sum_{i=1}^{N_s} \left(\frac{\partial \bar{\rho}}{\partial \tilde{Y}_i} \frac{\partial \tilde{Y}_i}{\partial \widetilde{\xi''^2}} \right) + \frac{\partial \bar{\rho}}{\partial \tilde{T}} \frac{\partial \tilde{T}}{\partial \widetilde{\xi''^2}} + \frac{\partial \bar{\rho}}{\partial \bar{p}} \frac{\partial \bar{p}}{\partial \widetilde{\xi''^2}}, \\
\rho_{\tilde{C}} &= \frac{\partial \bar{\rho}}{\partial \tilde{C}} = \sum_{i=1}^{N_s} \left(\frac{\partial \bar{\rho}}{\partial \tilde{Y}_i} \frac{\partial \tilde{Y}_i}{\partial \tilde{C}} \right) + \frac{\partial \bar{\rho}}{\partial \tilde{T}} \frac{\partial \tilde{T}}{\partial \tilde{C}} + \frac{\partial \bar{\rho}}{\partial \bar{p}} \frac{\partial \bar{p}}{\partial \tilde{C}}.
\end{aligned}$$

The term $\partial \bar{\rho} / \partial \tilde{Y}_i$ in the above equations for gradients of $\bar{\rho}$ is obtained by taking derivative of $\bar{\rho}$ in Equation (4.11) with respect to \tilde{Y}_i , $\partial \bar{\rho} / \partial \tilde{Y}_i = -\bar{\rho}^2 / \bar{\rho}_i$. The terms $\partial \tilde{Y}_i / \partial \tilde{\xi}$, $\partial \tilde{Y}_i / \partial \widetilde{\xi''^2}$, $\partial \tilde{Y}_i / \partial \tilde{C}$ are obtained from the flamelet tables and the terms $\partial \tilde{T} / \partial \tilde{\xi}$, $\partial \tilde{T} / \partial \widetilde{\xi''^2}$ and $\partial \tilde{T} / \partial \tilde{C}$ are calculated from the solutions of Equation (4.1). Based on the assumption in Section 3.2 that the length scale of change in pressure is greater than the thickness of the flamelet, $\partial \bar{p} / \partial \tilde{\xi} = \partial \bar{p} / \partial \widetilde{\xi''^2} = \partial \bar{p} / \partial \tilde{C} = 0$. The derivatives of the static enthalpy $\tilde{h} = f(\tilde{Y}_i, \tilde{T})$ with respect to $\tilde{\xi}$, $\widetilde{\xi''^2}$ and \tilde{C} are,

$$\begin{aligned}
h_{\tilde{\xi}}^0 &= \frac{\partial \tilde{h}^0}{\partial \tilde{\xi}} = \frac{\partial \tilde{h}}{\partial \tilde{\xi}} = \sum_{i=1}^{N_s} \left(\frac{\partial \tilde{h}}{\partial \tilde{Y}_i} \frac{\partial \tilde{Y}_i}{\partial \tilde{\xi}} \right) + \frac{\partial \tilde{h}}{\partial \tilde{T}} \frac{\partial \tilde{T}}{\partial \tilde{\xi}}, \\
h_{\widetilde{\xi''^2}}^0 &= \frac{\partial \tilde{h}^0}{\partial \widetilde{\xi''^2}} = \frac{\partial \tilde{h}}{\partial \widetilde{\xi''^2}} = \sum_{i=1}^{N_s} \left(\frac{\partial \tilde{h}}{\partial \tilde{Y}_i} \frac{\partial \tilde{Y}_i}{\partial \widetilde{\xi''^2}} \right) + \frac{\partial \tilde{h}}{\partial \tilde{T}} \frac{\partial \tilde{T}}{\partial \widetilde{\xi''^2}},
\end{aligned}$$

$$h_{\tilde{C}}^0 = \frac{\partial \tilde{h}^0}{\partial \tilde{C}} = \frac{\partial \tilde{h}}{\partial \tilde{C}} = \sum_{i=1}^{N_s} \left(\frac{\partial \tilde{h}}{\partial \tilde{Y}_i} \frac{\partial \tilde{Y}_i}{\partial \tilde{C}} \right) + \frac{\partial \tilde{h}}{\partial \tilde{T}} \frac{\partial \tilde{T}}{\partial \tilde{C}},$$

where, $\tilde{h} = \sum_{i=1}^{N_s} \tilde{h}_i \tilde{Y}_i$.

As discussed in Section 3.2, in the flamelet models the thermo-chemical properties like the temperature and species mass fraction are stored in a flamelet table which can be generated independent of the flow equations and can be looked up for thermo-chemical properties during simulations. In the following section we discuss the generation of the flamelet lookup table.

4.3 Flamelet Solver

Generally, there are two steps to implement a flamelet model. In the first step, a set of laminar flamelet solutions is generated by conducting simulations of simple laminar flames that are typically one-dimensional such as opposed jet laminar flames. In the second step, these laminar flamelet solutions are integrated with a presumed shape joint PDF to generate flamelet lookup tables that can be used in turbulent flame simulations. In this work we focus on the second step, which is studying the effect of different presumed-PDF integration approaches.

4.3.1 Presumed-PDF Table Integration Approaches

Han and Wang [90] pointed out that the presumed-PDF table integration approach is not unique for generating a flamelet table. For the same flamelet model, different flamelet tables can be constructed by using different approaches. This is highly undesired and can lead to serious consequences. Firstly, non-unique solutions from the same model, say the FPV model, is produced, which can cause serious ambiguity issues. Secondly, the details of flamelet table integration are often not reported in the past publications along with the description of the flamelet models which makes the published results difficult to reproduce. In the FPV model, substantial difference among the different flamelet tables generated by different approaches has been thor-

oughly demonstrated in a partially stirred reactor (PaSR) [90]. It was observed that an approach that preserves laminar flamelet structure during the flamelet integration is in general superior to other approaches that do not.

While the difference of the different integration approaches for the FPV table has been demonstrated in an idealized test case, PaSR [90], the validity of the conclusions drawn in Han and Wang [90] has not been verified in real flame simulations. Olbricht et al. [119] compared two approaches for integrating flamelet tables in the flamelet generated manifolds (FGM) model for a non-premixed bluff-body stabilized flame [120, 121], and observed insignificant difference in the results for the different approaches. This leads to inconsistent conclusions regarding the difference of flamelet table integration approaches. To clear out the inconsistency, in this study, we further compare the difference of the three different table integration approaches discussed by Han and Wang [90] in two real flame test cases. The first flame case is the turbulent piloted methane/air diffusion flame, Sandia Flame D [7, 8], which has been investigated extensively both computationally [106, 122–126] and experimentally [7, 8]. The second test case is the model rocket combustor. The results of these two test cases are discussed in the following Chapter 5

We use the FPV model as the baseline model for our discussions, although the same discussion can be extended straightforwardly to other flamelet models like the SFL model. As discussed in Section 3.2.2, in the FPV model, a flamelet table is constructed by integrating laminar flamelet solutions with a presumed-PDF. The integrated flamelet table has the form $\tilde{\phi}(\tilde{\xi}, \tilde{\xi}''^2, \tilde{C})$, where ϕ is a thermo-chemical property like temperature, $\tilde{\xi}$ is the mean mixture fraction, $\tilde{\xi}''^2$ is the variance of mixture fraction and \tilde{C} is the mean progress variable. By employing different presumed-PDF table integration approaches, different flamelet tables can be generated from the identical set of laminar flamelet solutions. The three different presumed-PDF table integration approaches [90] that are used in this study are briefly discussed below.

Integration with Laminar Flamelet Structure Preservation

The first approach is to integrate each laminar flamelet in the mixture fraction space first by using a presumed β -PDF and then mapping the integrated results into the final table in the form $\tilde{\phi}(\tilde{\xi}, \tilde{\xi}''^2, \tilde{C})$. We call this method the integration with laminar flamelet structure preservation (LFSP) method. We denote the laminar flamelet solutions obtained from the whole S-curve as $\phi(\xi, I)$, where I is an index used to identify each flamelet. A presumed β -PDF is assumed for the mixture fraction and the integration is then done in the mixture fraction space to obtain an intermediate flamelet table $\tilde{\phi}(\tilde{\xi}, \tilde{\xi}''^2, I)$. The intermediate flamelet table is then converted to the final flamelet table $\tilde{\phi}(\tilde{\xi}, \tilde{\xi}''^2, \tilde{C})$, by using an approximate mapping $\tilde{C} = \tilde{C}(\tilde{\xi}, \tilde{\xi}''^2, I)$ [90] and a presumed δ -PDF for the progress variable. An important feature of the LFSP method is that the individual one-dimensional laminar flamelet structures are, in some sense, preserved during the integration (*i.e.*, the β -PDF integration uses data from the same flamelet), which is a feature that is not present in many other methods. The LFSP method is presumably the most used method in existing studies [73,91–93].

Integration with Flamelet Mapping and Normalized Progress Variable

The mapping step in the LFSP method can also be done before β -PDF [90]. We can map the above laminar flamelet solutions $\phi(\xi, I)$ to $\phi(\xi, C)$ by using an approximate mapping $C = C(\xi, I)$ [90]. The mapped results $\phi(\xi, C)$ represents a low-dimensional manifold in the scalar space. Hence this method is a natural choice for the FGM model, especially if the laminar flamelet solutions are not from one-dimensional flame simulations. It is noted that this mapping is not reversible and during this mapping the one dimensional laminar flamelet structure is simply lost, *i.e.*, it does not have the property of laminar flamelet structure preservation. In other words, given the flamelet solutions expressed in the form $\phi(\xi, C)$, each individual laminar flamelet cannot be identified anymore. This represents a significant loss of

information which is the fundamental difference between this method and the LFSP method in Section 2.2.1. After the mapping, a normalized progress variable c ,

$$c = \frac{C}{C_{max}(\xi)}, \quad (4.14)$$

is introduced to transform the the integration domain into a rectangular one for ease of integration, where C_{max} is the maximum value of C at a given value of ξ . A presumed β -PDF for ξ and a δ -PDF for c (with statistical independence between them) are then assumed to integrate the laminar flamelet solutions $\phi = \phi(\xi, c)$ to obtain the integrated flamelet table $\tilde{\phi}(\tilde{\xi}, \tilde{\xi}''^2, \tilde{C})$. We call this method the integration with flamelet mapping and normalized progress variable (FMNPV) method. The FMNPV method has been used in a few previous studies (*e.g.*, [90, 119, 124]).

Integration with Flamelet Mapping and Normalized Mixture Fraction

The conformal mapping to a rectangular integration domain in Equation (5) can also be done differently. Instead of C being normalized, the mixture fraction can be normalized as φ ,

$$\varphi = \frac{\xi - \xi_{min}(C)}{\xi_{max}(C) - \xi_{min}(C)}, \quad (4.15)$$

where ξ_{min} and ξ_{max} are the minimum and maximum values of ξ at a given value of C , respectively. The presumed-PDF integration is then done by using a β -PDF for the normalized mixture fraction φ and δ -PDF for C (statistically independent) to obtain the integrated table $\tilde{\phi}(\tilde{\xi}, \tilde{\xi}''^2, \tilde{C})$. We call this method the integration with flamelet mapping and normalized mixture fraction (FMNMF) method. Similar to the FMNPV method, the FMNMF method does not preserve the one-dimensional laminar flamelet structures during integration. This method has been discussed by Han and Wang [90] in a simple partially stirred reactor. To our best knowledge, this method has not been used in existing studies of real flames (or at least has not been reported). The implementation and the complexity level of FMNPV are similar to those of FMNMF. It is valuable to examine the approach to see if it provides any advantage.

4.3.2 Comparison of Different Presumed-PDF Integration Approaches

There are possibly more table integration approaches that are different from the three approaches summarized above. We do not consider more approaches in this work since these three approaches are representative examples of two fundamentally different categories of table integration approaches. One category preserves the one-dimensional laminar flamelet structures during integration while the other one does not. The LFSP method falls in the first category of table integration approaches, and the FMNPV and FMNMF methods belong to the second category. Mathematically, the underlying difference among the different table integration approaches in Section 4.3.1 is the difference of the implied joint PDFs of ξ and C . The three approaches assume the same shapes of the presumed-PDFs for the different random variables, resulting in the difference of the implied joint PDFs of ξ and C . The details of the difference of the joint PDFs of the different approaches have been discussed elsewhere [90]. The plausible evidence is also provided in [90] to support that the presumed joint PDF implied in the LFSP method is better than others in the partially stirred reactor. The previous results and conclusions on the effect of different table integration approaches are yet to be confirmed in real turbulent flames, which is one of the focuses of this study.

The accuracy of the current FPV modeling results depends mainly on the prediction accuracy of the flamelet independent variables ($\tilde{\xi}$, $\widetilde{\xi''^2}$, \tilde{C}) and the accuracy of the flamelet table to represent the thermo-chemical properties given the values of the independent variables [90]. The integrated flamelet tables affect both, and it is desirable to have a thorough understanding of the effect of table integration on the accuracy of predictions of both categories of quantities. This effect will be investigated for two real flame cases: Sandia flame D [7, 8] and the model rocket combustor [76] in Chapter 5.

4.4 Presumed β -PDF Integration for Mixture Fraction

In most flamelet models, a presumed β -PDF integration is commonly needed in the mixture fraction space. We conduct careful studies of the effect of β -PDF integration in this work as well, in addition to the different table integration approaches.

4.4.1 β -PDF Integration in Flamelet Models

The β -PDF integration task in flamelet models can be expressed as,

$$\widetilde{\phi}^n(\widetilde{\xi}, \widetilde{\xi}''^2) = \int_0^1 \phi^n(\eta) \widetilde{f}_\xi(\eta; a, b) d\eta, \quad (4.16)$$

where $\widetilde{f}_\xi(\eta; a, b)$ is the density-weighted β -PDF of ξ , η is the sample space variable of ξ , and $\widetilde{\phi}^n$ is the n -th moment to calculate. The β -PDF $\widetilde{f}_\xi(\eta; a, b)$ is written as,

$$\widetilde{f}_\xi(\eta; a, b) = \frac{1}{B(a, b)} \eta^{a-1} (1 - \eta)^{b-1}, \quad (4.17)$$

in which $B(a, b)$ is the β -function and the parameters a and b are related to the mean and variance, $a = \widetilde{\xi} \left[\widetilde{\xi}(1 - \widetilde{\xi}) / \widetilde{\xi}''^2 - 1 \right]$, $b = a / \widetilde{\xi} - a$. The dependence of the laminar flamelet solutions ϕ on other quantities such as scalar dissipation rate is omitted in Equation (4.16) to focus on the presumed β -PDF integration. Given a pair of the mean and variance $(\widetilde{\xi}, \widetilde{\xi}''^2)$, a and b can be computed and the shape of the β -PDF is uniquely determined. The integration in Equation (4.16) can then be readily performed. The laminar flamelet solutions $\phi(\xi)$ are typically stored on discrete points $\xi_i, i = 1, 2, \dots, n_\xi$, where n_ξ is the number of grid points in the mixture fraction space. A numerical integration scheme is needed to integrate Equation (4.16). Such integration is not trivial and singularities can be generated in the integrated results because the β -PDF is highly non-linear and can be singular at $\xi = 0$ or $\xi = 1$ for certain conditions, *e.g.*, $\widetilde{f}_\xi(0; a = 1, b = 3) = \infty$. In this work, we will examine a few traditional numerical integration schemes in Section 4.4.2 and a semi-analytical integration scheme in Section 4.4.3.

4.4.2 Traditional Schemes for the β -PDF Integration

There are many general numerical integration schemes available and in this work we consider two typical integration schemes based on the trapezoidal rule [127] and the Simpson rule [127]. The trapezoidal rule is second-order accurate and the Simpson rule is fourth-order accurate. The advantage of using these integration schemes is that they are well-developed and there are many existing tools available to readily perform the numerical integration in Equation (4.16). The disadvantage of these general schemes is also very clear: they have difficulties to perform the β -PDF integration when the PDF has singularities. A more reliable β -PDF integration scheme is needed to treat singularity properly.

4.4.3 Piece-Wise Semi-Analytical (PWSA) Integration

An integration scheme called PWSA is discussed in Appendix A that can avoid the aforementioned singularity issue. The scheme assumes a piece-wise linear function of $\phi(\xi)$ between grid points in the mixture fraction space and is largely based on the work by lien2009development where an integration scheme only for the first-order moment is provided. Here the scheme is generalized to the integration of an arbitrary order moment. The formal second-order order accuracy of the scheme is also analyzed in Appendix A, although the PWSA scheme is generally not limited to second-order accuracy and high-order accuracy can be achieved by using higher-order polynomials for $\phi(\xi)$. In this work, we limit ourselves to second-order accurate PWSA scheme. Lien et al. [128] suggested to construct piecewise segments (between 3 to 7) for $\phi(\xi)$ in the mixture fraction space for the integration. We simply construct a piecewise linear function for $\phi(\xi)$ between the grid points of the flamelet solution, since integrating the flamelet table is a one-time cost which consumes a small fraction of the time for an actual flow simulation. The scheme will be examined in more detail in Section 5.1.2.

In summary, in Sections 4.3 - 4.4, we discussed the different flamelet table integration approaches and the PWSA scheme to carry out the flamelet table integration using the different approaches. In the following Section 4.5, we discuss the numerical implementation of the PDF model.

4.5 Transported PDF Model Implementation

For the EMCF method, the formulation of Q is,

$$Q = \begin{bmatrix} \bar{\rho} \\ \bar{\rho}\tilde{u} \\ \bar{\rho}\tilde{v} \\ \bar{\rho}\tilde{w} \\ \bar{\rho}h^{01} - \bar{p} \\ \dots \\ \bar{\rho}h^{0N_f} - \bar{p} \\ \bar{\rho}k \\ \bar{\rho}\omega \\ \bar{\rho}Y_1^1 \\ \dots \\ \bar{\rho}Y_1^{N_f} \\ \dots \\ \bar{\rho}Y_{N_s}^{N_f} \\ \dots \\ \bar{\rho}Y_{N_s}^{N_f} \end{bmatrix}. \quad (4.18)$$

The components of the inviscid flux vector \vec{F} (F_x , F_y , and F_z) and viscous flux vector \vec{G} (G_x , G_y , and G_z) are,

$$\begin{aligned}
 F_x = & \begin{bmatrix} \bar{\rho}\tilde{u} \\ \bar{\rho}\tilde{u}^2 + \bar{p} \\ \bar{\rho}\tilde{u}\tilde{v} \\ \bar{\rho}\tilde{u}\tilde{w} \\ \bar{\rho}\tilde{u}h^{01} \\ \dots \\ \bar{\rho}\tilde{u}h^{0N_f} \\ \bar{\rho}\tilde{u}k \\ \bar{\rho}\tilde{u}\omega \\ \bar{\rho}\tilde{u}Y_1^1 \\ \dots \\ \bar{\rho}\tilde{u}Y_1^{N_f} \\ \dots \\ \bar{\rho}\tilde{u}Y_{N_s}^1 \\ \dots \\ \bar{\rho}\tilde{u}Y_{N_s}^{N_f} \end{bmatrix}, F_y = \begin{bmatrix} \bar{\rho}\tilde{v} \\ \bar{\rho}\tilde{v}\tilde{u} \\ \bar{\rho}\tilde{v}^2 + \bar{p} \\ \bar{\rho}\tilde{v}\tilde{w} \\ \bar{\rho}\tilde{v}h^{01} \\ \dots \\ \bar{\rho}\tilde{v}h^{0N_f} \\ \bar{\rho}\tilde{v}k \\ \bar{\rho}\tilde{v}\omega \\ \bar{\rho}\tilde{v}Y_1^1 \\ \dots \\ \bar{\rho}\tilde{v}Y_1^{N_f} \\ \dots \\ \bar{\rho}\tilde{v}Y_{N_s}^1 \\ \dots \\ \bar{\rho}\tilde{v}Y_{N_s}^{N_f} \end{bmatrix}, F_z = \begin{bmatrix} \bar{\rho}\tilde{w} \\ \bar{\rho}\tilde{w}\tilde{u} \\ \bar{\rho}\tilde{w}\tilde{v} \\ \bar{\rho}\tilde{w}^2 + \bar{p} \\ \bar{\rho}\tilde{w}h^{01} \\ \dots \\ \bar{\rho}\tilde{w}h^{0N_f} \\ \bar{\rho}\tilde{w}k \\ \bar{\rho}\tilde{w}\omega \\ \bar{\rho}\tilde{w}Y_1^1 \\ \dots \\ \bar{\rho}\tilde{w}Y_1^{N_f} \\ \dots \\ \bar{\rho}\tilde{w}Y_{N_s}^1 \\ \dots \\ \bar{\rho}\tilde{w}Y_{N_s}^{N_f} \end{bmatrix}, \quad (4.19)
 \end{aligned}$$

$$G_x = \begin{bmatrix} 0, \\ \tilde{\tau}_{e,xx}, \\ \tilde{\tau}_{e,xy}, \\ \tilde{\tau}_{e,xz}, \\ Q_x^1, \\ \dots \\ Q_x^{N_f}, \\ \Gamma_k \frac{\partial k}{\partial x}, \\ \Gamma_\omega \frac{\partial \omega}{\partial x}, \\ \Gamma_e \frac{\partial Y_1^1}{\partial x}, \\ \dots \\ \Gamma_e \frac{\partial Y_1^{N_f}}{\partial x}, \\ \dots \\ \Gamma_e \frac{\partial Y_{N_s}^1}{\partial x}, \\ \dots \\ \Gamma_e \frac{\partial Y_{N_s}^{N_f}}{\partial x} \end{bmatrix}, G_y = \begin{bmatrix} 0, \\ \tilde{\tau}_{e,yx}, \\ \tilde{\tau}_{e,yy}, \\ \tilde{\tau}_{e,yz}, \\ Q_y^1, \\ \dots \\ Q_y^{N_f}, \\ \Gamma_k \frac{\partial k}{\partial y}, \\ \Gamma_\omega \frac{\partial \omega}{\partial y}, \\ \Gamma_e \frac{\partial Y_1^1}{\partial y}, \\ \dots \\ \Gamma_e \frac{\partial Y_1^{N_f}}{\partial y}, \\ \dots \\ \Gamma_e \frac{\partial Y_{N_s}^1}{\partial y}, \\ \dots \\ \Gamma_e \frac{\partial Y_{N_s}^{N_f}}{\partial y} \end{bmatrix}, G_z = \begin{bmatrix} 0, \\ \tilde{\tau}_{e,zx}, \\ \tilde{\tau}_{e,zy}, \\ \tilde{\tau}_{e,zz}, \\ Q_z^1, \\ \dots \\ Q_z^{N_f}, \\ \Gamma_k \frac{\partial k}{\partial z}, \\ \Gamma_\omega \frac{\partial \omega}{\partial z}, \\ \Gamma_e \frac{\partial Y_1^1}{\partial z}, \\ \dots \\ \Gamma_e \frac{\partial Y_1^{N_f}}{\partial z}, \\ \dots \\ \Gamma_e \frac{\partial Y_{N_s}^1}{\partial z}, \\ \dots \\ \Gamma_e \frac{\partial Y_{N_s}^{N_f}}{\partial z} \end{bmatrix}, \quad (4.20)$$

and the vector of the primitive variables Q_p is,

$$Q_p = \left[\bar{p}, \tilde{u}, \tilde{v}, \tilde{w}, T^1, \dots, T^n, k, \omega, Y_1^1, \dots, Y_1^{N_f}, \dots, Y_{N_s}^1, \dots, Y_{N_s}^{N_f} \right]^T. \quad (4.21)$$

The source term vector H is,

$$H = \begin{bmatrix} 0 \\ 0 \\ 0 \\ 0 \\ \dot{\omega}_{h^0 1} \\ \dots \\ \dot{\omega}_{h^0 N_f} \\ \dot{\omega}_k \\ \dot{\omega}_\omega \\ \dot{\omega}_{Y_1^1} \\ \dots \\ \dot{\omega}_{Y_1^{N_f}} \\ \dots \\ \dot{\omega}_{Y_{N_s}^1} \\ \dots \\ \dot{\omega}_{Y_{N_s}^{N_f}} \end{bmatrix}, \quad (4.22)$$

where,

$$\begin{aligned} \dot{\omega}_{h^0 1} &= M_{h^1} + \bar{\rho} \sqrt{2 \frac{(\Gamma_{ch} + \Gamma_t)}{\bar{\rho}}} \phi_{h^1} \frac{\partial h^1}{\partial x_k} \frac{\eta_k}{\sqrt{dt}}, \\ \dot{\omega}_{h^0 N_f} &= M_{h^{N_f}} + \bar{\rho} \sqrt{2 \frac{(\Gamma_{ch} + \Gamma_t)}{\bar{\rho}}} \phi_{h^{N_f}} \frac{\partial h^{N_f}}{\partial x_k} \frac{\eta_k}{\sqrt{dt}}, \\ \dot{\omega}_k &= \tilde{\tau}_{t,jk} \frac{\partial \tilde{u}_j}{\partial x_k} - \beta^* \bar{\rho} k \omega, \\ \dot{\omega}_\omega &= \frac{\gamma \omega}{k} \tilde{\tau}_{t,jk} \frac{\partial \tilde{u}_j}{\partial x_k} - \beta \bar{\rho} \omega^2 + \bar{\rho} \frac{\sigma_d}{\omega} \frac{\partial k}{\partial x_j} \frac{\partial \omega}{\partial x_j}, \\ \dot{\omega}_{Y_1^1} &= \bar{\rho} \dot{\omega}_1(Y_i^1) + M_{Y_1^1} + \bar{\rho} \sqrt{2 \frac{(\Gamma_{cY_1} + \Gamma_t)}{\bar{\rho}}} \phi_{Y_1^1} \frac{\partial Y_1^1}{\partial x_k} \frac{\eta_k}{\sqrt{dt}}, \\ \dot{\omega}_{Y_1^{N_f}} &= \bar{\rho} \dot{\omega}_1(Y_i^{N_f}) + M_{Y_1^{N_f}} + \bar{\rho} \sqrt{2 \frac{(\Gamma_{cY_1} + \Gamma_t)}{\bar{\rho}}} \phi_{Y_1^{N_f}} \frac{\partial Y_1^{N_f}}{\partial x_k} \frac{\eta_k}{\sqrt{dt}}, \end{aligned}$$

$$\dot{\omega}_{Y_{N_s}^1} = \bar{\rho}\dot{\omega}_{N_s}(Y_i^1) + M_{Y_{N_s}^1} + \bar{\rho}\sqrt{2\frac{(\Gamma_{cY_{N_s}} + \Gamma_t)}{\bar{\rho}}}\phi_{Y_{N_s}^1}\frac{\partial Y_{N_s}^1}{\partial x_k}\frac{\eta_k}{\sqrt{dt}},$$

$$\dot{\omega}_{Y_{N_s}^{N_f}} = \bar{\rho}\dot{\omega}_{N_s}(Y_i^{N_f}) + M_{Y_{N_s}^{N_f}} + \bar{\rho}\sqrt{2\frac{(\Gamma_{cY_{N_s}} + \Gamma_t)}{\bar{\rho}}}\phi_{Y_{N_s}^{N_f}}\frac{\partial Y_{N_s}^{N_f}}{\partial x_k}\frac{\eta_k}{\sqrt{dt}},$$

and ϕ_{h^n} and $\phi_{Y_i^n}$ are the limiters for the gradients of h^n and Y_i^n respectively. The numerical implementation of the mixing models is described in Section 4.5.1 and the formulation of the gradient limiters is discussed in detail in Section 4.5.2. The jacobian Γ_p is given in Appendix B.

4.5.1 Implementation of Mixing Models

For the sake of the discussion, here we discuss the implementation of only the IEM model. The implementation for the IPEM model is similar. Using the IEM mixing model, the mixing process can be represented by Equation (3.44). In the near-wall regions, Ω becomes very large and in order to numerically integrate Equation (3.24) we have to use a very small time step size Δt which would significantly increase the computational cost of the EMCF method. To resolve this issue we use an analytical implementation of the IEM model. The analytical expression for the IEM model can be obtained by integrating both sides of Equation (3.24) from k^{th} to the $(k+1)^{th}$ pseudo iteration at the m^{th} physical time step,

$$\bar{\rho}(\phi_\alpha^{n,k+1} - \tilde{\phi}_\alpha^m) = \bar{\rho}(\phi_\alpha^{n,k} - \tilde{\phi}_\alpha^m)e^{(-\frac{1}{2}C_\phi\Omega\Delta t)}. \quad (4.23)$$

Rearranging Equation (4.23) and dividing both sides of the equation by Δt we get,

$$\frac{\bar{\rho}(\phi_\alpha^{n,k+1} - \phi_\alpha^{n,k})}{\Delta t} = -\frac{\bar{\rho}(\phi_\alpha^{n,k} - \tilde{\phi}_\alpha^m)}{\Delta t}(1 - e^{(-\frac{1}{2}C_\phi\Omega\Delta t)}). \quad (4.24)$$

Implementing the IEM model using Equation (4.24) ensures that the model is numerically stable even in the near-wall regions.

4.5.2 Discretization of Stochastic Term

In the source terms for the n^{th} stochastic field of the stagnation enthalpy $\dot{\omega}_{h^n}$ and the species mass fraction of the i^{th} species, $\dot{\omega}_{Y_i^n}$ we use the gradient limiters ϕ_{h^n} and $\phi_{Y_i^n}$ respectively. These limiters help to smear out the spurious numerical oscillations in the gradient terms $\partial h^n / \partial x_k$ and $\partial Y_i^n / \partial x_k$ which may lead to unphysical values of the thermo-chemical scalars like temperature and species mass fraction. To formulate ϕ_{h^n} and $\phi_{Y_i^n}$ we use a Barth face limiter [129]. The gradient limiters ensure that values of the scalars h^n and Y_i^n at the cell center lie between the minimum and maximum values of the respective scalars in the neighboring cells. To calculate ϕ_{h^n} at the center of a cell, we first compare the value of h^n at the center of the cell under consideration with the cell center values in the neighboring cells to determine the minimum h_{min}^n and maximum h_{max}^n value of the static enthalpy,

$$\begin{aligned} h_{min}^n &= \min(h^n, h_{k,neighbors}^n), \\ h_{max}^n &= \max(h^n, h_{k,neighbors}^n), \end{aligned} \quad (4.25)$$

where $h_{k,neighbors}^n$ is the value of the static enthalpy at cell center of the k^{th} neighboring cell. In next step, we loop over all the faces of the cell under consideration and calculate ϕ_{h^n} using,

$$\phi_{h^n} = \begin{cases} \min\left(1, \frac{h_{max}^n - h^n}{h_{k,face}^n - h^n}\right), & h_{k,face}^n - h^n < 0, \\ \min\left(1, \frac{h_{min}^n - h^n}{h_{k,face}^n - h^n}\right), & h_{k,face}^n - h^n > 0, \\ 1, & h_{k,face}^n - h^n = 0. \end{cases} \quad (4.26)$$

where $h_{k,face}^n$ is the face center value of the static enthalpy for the k^{th} face of the cell. Similarly the gradient limiter for species mass fraction $\phi_{Y_i^n}$ is calculated using,

$$\begin{aligned} Y_{i,min}^n &= \min(Y_i^n, Y_{i,k,neighbors}^n), \\ Y_{i,max}^n &= \max(Y_i^n, Y_{i,k,neighbors}^n), \end{aligned} \quad (4.27)$$

$$\phi_{Y_i^n} = \begin{cases} \min\left(1, \frac{Y_{i,max}^n - Y_i^n}{Y_{i,k,face}^n - Y_i^n}\right), Y_{i,k,face}^n - Y_i^n < 0, \\ \min\left(1, \frac{Y_{i,min}^n - Y_i^n}{Y_{i,k,face}^n - Y_i^n}\right), Y_{i,k,face}^n - Y_i^n > 0, \\ 1, Y_{i,k,face}^n - Y_i^n = 0. \end{cases} \quad (4.28)$$

The gradient limiters for the thermo-chemical scalars on the EMCF method improves the robustness of the method and prevents divergence in the presence of strong gradients.

4.6 Finite-Volume Approach for Solving Governing Equations

We can rewrite Equation (4.2) in terms of the jacobian Γ_p ,

$$\Gamma_p \frac{\partial Q_p}{\partial \tau} + \frac{\partial Q}{\partial t} + \nabla \cdot (\vec{F} - \vec{G}) = H. \quad (4.29)$$

The finite-volume approach with the dual-time algorithm [116] is used to solve Equation (4.29). In the finite-volume approach, Equation (4.29) is integrated over each cell in the computational domain,

$$\int_{\Omega} \left(\Gamma_p \frac{\partial Q_p}{\partial \tau} + \frac{\partial Q}{\partial t} \right) dV + \int_{\Omega} \nabla \cdot (\vec{F} - \vec{G}) dV = \int_{\Omega} H dV, \quad (4.30)$$

where Ω is the volume of a computational cell and dV is the differential volume. Using volume-averaged quantities $\bar{Q} = (1/\Omega) \int_{\Omega} Q dV$, $\bar{Q}_p = (1/\Omega) \int_{\Omega} Q_p dV$, $\bar{\Gamma}_p = (1/\Omega) \int_{\Omega} \Gamma_p dV$, $\bar{H} = (1/\Omega) \int_{\Omega} H dV$, Equation (4.30) can be rewritten as,

$$\Omega \left(\bar{\Gamma}_p \frac{\partial \bar{Q}_p}{\partial \tau} + \frac{\partial \bar{Q}}{\partial t} \right) + \int_{\Omega} \nabla \cdot (\vec{F} - \vec{G}) dV = \Omega \bar{H}. \quad (4.31)$$

For the integral of the flux terms $\int_{\Omega} \nabla \cdot (\vec{F} - \vec{G}) dV$ in Equation (4.31) we use the Gauss divergence theorem [130],

$$\int_{\Omega} \nabla \cdot (\vec{F} - \vec{G}) dV = \int_{\delta\Omega} (\vec{F} - \vec{G}) \cdot \vec{n} dS, \quad (4.32)$$

where $\delta\Omega$ is the control surface area enclosing the control volume Ω . The control surface $\delta\Omega$ can be divided into K distinct surfaces of area S_k and normal vector \vec{n}_k so that the flux can be calculated numerically as,

$$\int_{\delta\Omega} (\vec{F} - \vec{G}) \cdot \vec{n} dS = \sum_{k=1}^K (\vec{F} - \vec{G}) \cdot \vec{n}_k S_k = \nabla_D \cdot (\vec{F} - \vec{G}), \quad (4.33)$$

where the flux vectors \vec{F} and \vec{G} can be regarded as the average inviscid and viscous flux respectively, over the control surface $\delta\Omega$ and $\nabla_{D\cdot}$ is an operator defined to represent the inner product of $\vec{F} - \vec{G}$ and \vec{n}_k . The inviscid flux \vec{F} is determined using an approximate Reimann solver [131] and the viscous flux \vec{G} is determined using the Green-Gauss reconstruction method [132]. Details about the implementation of the approximate Reimann solver and the Green-Gauss reconstruction method can be found in [133].

The dual-time algorithm discussed in Equation (4.31) has two time derivatives, the pseudo time derivative $\partial\bar{Q}_p/\partial\tau$ and the physical time derivative $\partial\bar{Q}/\partial t$. For the pseudo time derivative, a first order implicit Euler scheme is used,

$$\frac{\partial\bar{Q}_p}{\partial\tau} = \frac{\bar{Q}_p^{k+1} - \bar{Q}_p^k}{\Delta\tau}, \quad (4.34)$$

where k is the k^{th} iteration of the pseudo iterations and $\Delta\tau$ is the pseudo time step size. For the physical time derivative $\partial\bar{Q}/\partial t$, a second order implicit scheme is used,

$$\frac{\partial\bar{Q}}{\partial t} = \frac{3\bar{Q}^{n+1} - 4\bar{Q}^n + \bar{Q}^{n-1}}{2\Delta t}. \quad (4.35)$$

In the above equation, n represents the n^{th} time level for the physical time iteration and Δt is the physical time step size. In the dual-time algorithm, the pseudo time derivative improves the stability and convergence while the physical time derivative determines the numerical accuracy of the algorithm. Hence, a second order scheme is used for the physical time derivative while a first order scheme is sufficient for the pseudo time derivative. Substituting Equation (4.34) and Equation (4.35) into Equation (4.31) we get,

$$\bar{\Gamma}_p \frac{\bar{Q}_p^{k+1} - \bar{Q}_p^k}{\Delta\tau} + \frac{3\bar{Q}^{n+1} - 4\bar{Q}^n + \bar{Q}^{n-1}}{2\Delta t} + \nabla_{D\cdot} \cdot \left(\vec{F} - \vec{G} \right)^{k+1} = \bar{H}^{k+1}. \quad (4.36)$$

In the dual-time algorithm, as we advance in the physical time from from time step n to time step $n + 1$, the pseudo-time is also advanced to convergence so that time level

$k + 1$ is equivalent to time step $n + 1$. Using this, Equation (4.36) can be rewritten as,

$$\bar{\Gamma}_p \frac{\bar{Q}_p^{k+1} - \bar{Q}_p^k}{\Delta\tau} + \frac{3}{2} \left(\frac{\bar{Q}^{k+1} - \bar{Q}^k}{\Delta t} \right) = - \left(\frac{3\bar{Q}^k - 4\bar{Q}^n + \bar{Q}^{n-1}}{2\Delta t} \right) - \nabla_D \cdot \left(\vec{F} - \vec{G} \right)^{k+1} + \bar{H}^{k+1}. \quad (4.37)$$

To solve Equation (4.37), the terms $\nabla_D \cdot \left(\vec{F} - \vec{G} \right)^{k+1}$ and \bar{H}^{k+1} have to be written in terms of the k^{th} time level which is done using a first order approximation with the Taylor series,

$$\begin{aligned} \nabla_D \cdot \vec{F}^{k+1} &\approx \nabla_D \cdot \vec{F}^k + \nabla \cdot \bar{\Gamma}_f \Delta \bar{Q}_p, \\ \nabla_D \cdot \vec{G}^{k+1} &\approx \nabla_D \cdot \vec{G}^k + \nabla \cdot \bar{\Gamma}_g \Delta \bar{Q}_p, \\ H^{k+1} &\approx H^k + \bar{\Gamma}_h \Delta \bar{Q}_p, \end{aligned} \quad (4.38)$$

where $\Delta \bar{Q}_p = \bar{Q}_p^{k+1} - \bar{Q}_p^k$, $\bar{\Gamma}_f = \partial \vec{F} / \partial Q_p$, $\bar{\Gamma}_g = \partial \vec{G} / \partial Q_p$ and $\bar{\Gamma}_h = \partial H / \partial Q_p$. For the transported PDF method the formulation of the jacobians $\bar{\Gamma}_f$, $\bar{\Gamma}_g$ and $\bar{\Gamma}_h$ can be found in Appendix C. For the flamelet model, the derivation of the jacobians is straightforward and can be obtained from the laminar chemistry formulation in [79]. Substituting Equation (4.38) into Equation (4.37) we get,

$$\begin{aligned} \left(\frac{\bar{\Gamma}_p}{\Delta\tau} + \frac{3\bar{\Gamma}_p^{-1}}{2\Delta t} + \nabla \cdot (\bar{\Gamma}_f - \bar{\Gamma}_g) - \bar{\Gamma}_h \right) \Delta \bar{Q}_p = - \left(\frac{3\bar{Q}^k - 4\bar{Q}^n + \bar{Q}^{n-1}}{2\Delta t} \right) - \nabla_D \cdot \left(\vec{F} - \vec{G} \right)^k + \bar{H}^k. \end{aligned} \quad (4.39)$$

The analytical expression for $\bar{\Gamma}_p^{-1}$ is in Appendix B. $\Delta \bar{Q}_p$ can be obtained by inverting Equation (4.39) which is done using a line Gauss-Seidel procedure and details of the approach can be found in [133, 134]. More details of the numerical algorithms can be found in [116]

In summary in this section we described the numerical implementation of the physical models discussed for the flamelet modeling approach and the transported PDF model in the GEMS solver. For the flamelet model we first study the effect of the different flamelet table integration approaches on predictions of Sandia Flame D and the model rocket combustor in Chapter 5. Then in Chapter 6 we examine the effect of combustion dynamics, turbulence-chemistry interactions on combustion

instabilities in the model rocket combustor. For the transported PDF model we validate the numerical implementation using a series of test cases in Chapter 7 and then model combustion instabilities in model rocket combustor at the end of the chapter.

5. EFFECT OF DIFFERENT PRESUMED-PDF TABLE INTEGRATION APPROACHES ON FLAMELET MODELING OF A TURBULENT JET FLAME AND A SELF-EXCITED RESONANCE ROCKET COMBUSTOR

As mentioned in Chapter 4, the presumed-PDF integration in the flamelet model is non-unique and different flamelet tables can be obtained from the same set of laminar flamelet solutions. In this chapter we study the effect of three different table integration approaches on the predictions of two real flames. The first flame is a laboratory scale, piloted turbulent jet flame, Sandia Flame D [7]. The second flame is the more complicated self-excited model rocket combustor [76].

5.1 Sandia Piloted Flame D

In this section, we first describe the Sandia flame D test case in Section 5.1.1. Then, we compare the β -PDF integration for mixture fraction in Section 5.1.2 with the traditional schemes from Section 4.4.2 and the PWSA scheme from Section 4.4.3. Next, we examine the flamelet tables generated by using the different table integration approaches in Section 5.1.3. After looking into the different flamelet tables, we compare the predictions of the flow and turbulence fields in Section 5.1.4 and flamelet independent variables (mixture fraction and progress variable) in Section 5.1.5. Finally, we carry out an *a priori* and *a posteriori* testing of the different table integration approaches in Sandia flame D in Section 5.1.6 and Section 5.1.7, respectively.

5.1.1 Sandia Flame D and Model Approaches

Sandia flame D [7, 8] is a piloted methane/air diffusion flame with a fuel jet consisting of a pre-mixture of 25% methane and 75% air by volume. The flame is placed in a coflow of air and is stabilized with a high temperature pilot. The Reynolds number is $Re = 22,400$ based on the fuel jet bulk velocity of $U_b = 49.6$ m/s and the fuel nozzle diameter $D = 7.2$ mm. Additional details of the flame can be found in [7, 8].

Numerical simulations in this study are carried out by using an in-house compressible flow solver called GEMS [86–88]. The solver is second order accurate in space and time. Two-dimensional axisymmetric RANS simulations are carried out with a $k - \omega$ turbulence model [36]. The laminar flamelet solutions are generated using the FlameMaster code [89] with the GRI 1.2 reaction mechanism [81]. The computational grid is finalized based on grid convergence studies and the final grid has around 7500 cells.

5.1.2 Examination of Numerical β -PDF Integration for Mixture Fraction

Several numerical schemes are discussed in Section 2.3 for integrating the flamelet solutions in the mixture fraction space with a presumed β -PDF. Here, we make a quantitative comparison of the different numerical integration schemes. For the comparison, we consider temperature T as a representative thermo-chemical property. The temperature data from a laminar flamelet solution of Sandia flame D are stored originally on a grid with 1000 points in mixture fraction and are interpolated into a uniform grid with n_ξ points for a grid convergence study. Three schemes discussed in Section 4.4.2 and Section 4.4.3 are considered: the Trapezoidal scheme (second-order accurate), the Simpson scheme (fourth-order accurate), and the PWSA scheme (second-order accurate).

For the accuracy convergence test of the three numerical β -PDF integration schemes, two shapes of β -PDF are chosen, one without singularity ($a = 1.40$, $b = 2.59$) and the other with singularity at $\eta = 0$ and 1 ($a = 0.23$, $b = 0.43$). The shapes of the

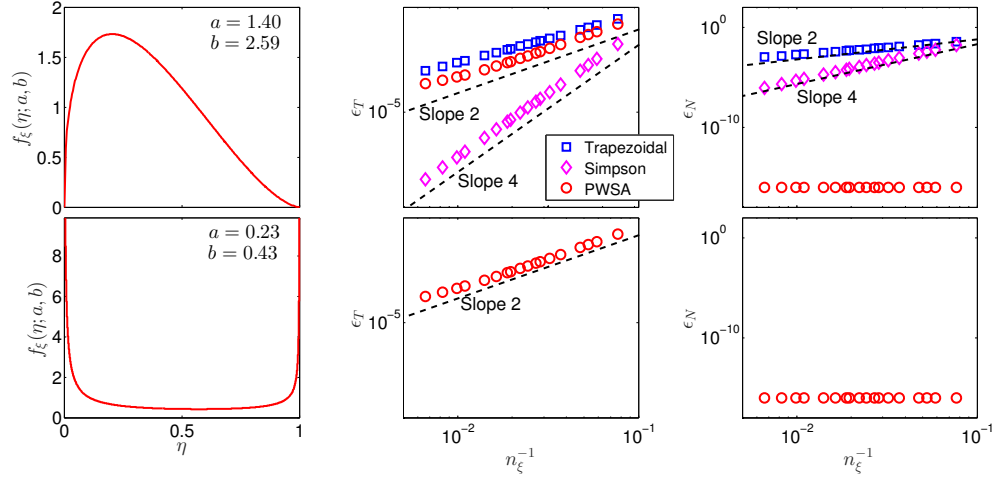


Figure 5.1.: Comparison of the different β -PDF numerical integration schemes with $\tilde{\xi} = 0.352$ and the normalized mixture fraction variance $\xi_v = \tilde{\xi}^2/(\tilde{\xi}(1 - \tilde{\xi})) = 0.2$ (first row) and $\tilde{\xi} = 0.352$ and $\xi_v = 0.6$ (second row). Left column: the shapes of the β -PDF used for the integration; middle column: the convergence of the numerical integration error against n_ξ^{-1} ; Right column: the convergence of the error of the PDF normalization condition against n_ξ^{-1} .

presumed β -PDF and the convergence results with respect to the variation of n_ξ are shown in Figure 5.1. For each integration scheme, the integrated temperature \tilde{T} is fit into a curve $\tilde{T} = \tilde{T}_0 + c_T/n_\xi^p$, by using different values of n_ξ . Here, \tilde{T}_0 and c_T are curve fitting constants and p is the expected order of accuracy for the scheme. The numerical integration error ϵ_T is then estimated as $\epsilon_T = \left| \tilde{T} - \tilde{T}_0 \right| / \tilde{T}_0$. The convergence of the error in the PDF normalization condition $\epsilon_N = \left| \int_0^1 \tilde{f}_\xi(\eta; a, b) d\eta - 1 \right|$ is also shown. From the first row of Figure 5.1, we confirm that the Trapezoidal scheme and the PWSA scheme are second-order accurate and the Simpson scheme is fourth-order accurate, for problems without singularity. The PWSA performs slightly better than the Trapezoidal scheme for this particular test case. Since the analytical expression of the PDF is used in the PWSA method, the error ϵ_N in the normalization condition is only the round-off error $O(10^{-15})$. From the second row of Figure 5.1, we can see

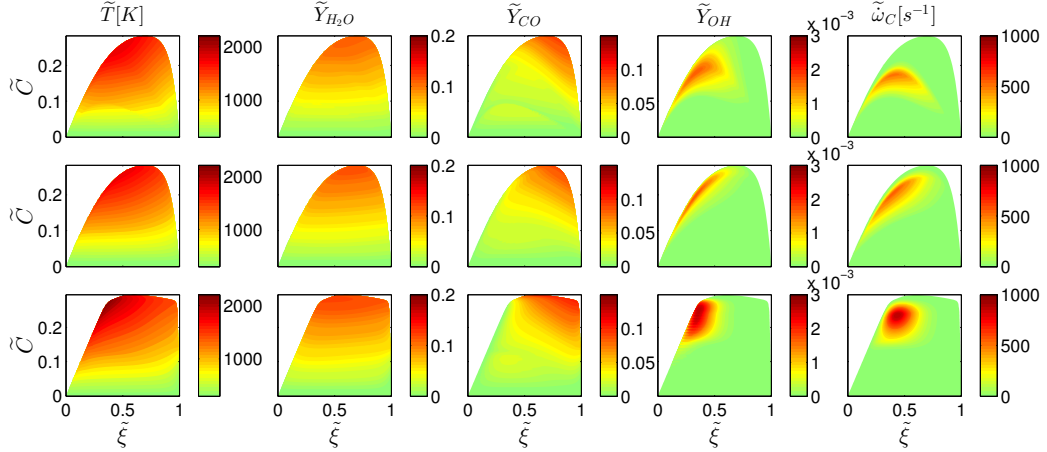


Figure 5.2.: Contour plots of the mean temperature \tilde{T} , the mean mass fractions of species H_2O , CO , and OH , and the mean reaction rate $\tilde{\omega}_C$ for the progress variable C , in the mean mixture fractions $\tilde{\xi}$ and mean progress variable space \tilde{C} from the integrated flamelet tables are shown for the LFSP method (the first row), the FMNPV method (the second row), and the FMNMF method (the third row) in Sandia flame D. The normalized variance of the mixture fraction is fixed at $\xi_v = \tilde{\xi}^2 / (\tilde{\xi}(1 - \tilde{\xi})) = 0.1$.

that, for the β -PDF with singularity, the PWSA scheme still has the second-order accuracy while both the Trapezoidal scheme and the Simpson scheme fail to handle this case. These tests indicate that the PWSA scheme yields satisfactory accuracy and can handle all β -PDF including singular ones without difficulty. We will use PWSA with $n_\xi=100$ for all the later discussions. The value of $n_\xi=100$ yields an error of about 0.01% for the temperature integration, which is sufficiently small for the current discussions.

5.1.3 Examination of Integrated Flamelet Tables

Here, we examine the difference among the integrated flamelet tables generated by using the different table integration approaches discussed in Section 4.3.1. The same set of laminar flamelet solutions obtained from solving Equation (3.7) and Equation

(3.8) under the conditions of Sandia flame D are used in the different table integration approaches. A two dimensional slice is taken from each of the integrated flamelet tables for a fixed value of the normalized variance, $\xi_v = \widetilde{\xi'^2}/(\widetilde{\xi}(1-\widetilde{\xi})) = 0.1$. For this slice, comparison is made in Figure 5.2 in the mean mixture fraction $\widetilde{\xi}$ and the mean progress variable \widetilde{C} space for the mean temperature \widetilde{T} , the mean mass fractions of species H₂O, CO, and OH, and the mean reaction rate $\widetilde{\omega}_C$ for the progress variable C . From the figure, we can see that the flamelet tables generated from the same set of flamelet solutions using the different approaches are different in two aspects. Firstly, the domain size covered by the table in the $(\widetilde{\xi}, \widetilde{C})$ space changes with the table integration approach. In the LFSP method and the FMNPV method, the domains approximately cover the same area. In the FMNMF method, the domain is much larger than those in the LFSP method and the FMNPV method. Secondly, the table values at the same point are different. For example, the mean reaction rate $\widetilde{\omega}_C$ peaks at different locations and the shapes of the contour lines are quite different with the three different table integration approaches.

5.1.4 Predictions of Flow and Turbulence Fields

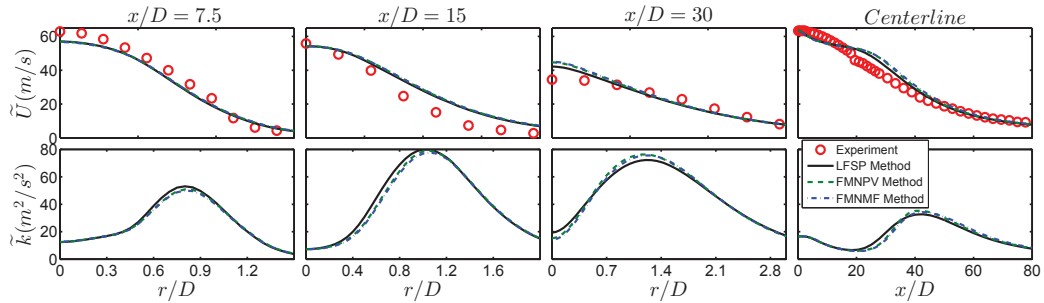


Figure 5.3.: Radial profiles of the mean axial velocity \widetilde{U} (top) and turbulent kinetic energy \widetilde{k} (bottom) at the axial locations $x/D = 7.5, 15,$ and 30 along with the centerline profile in Sandia flame D. The model results are obtained using the FPV model with the three different table integration approaches.

Figure 5.3 shows the radial profiles of the mean axial velocity \tilde{U} and turbulent kinetic energy \tilde{k} in Sandia flame D predicted by using the three flamelet table integration approaches at the three axial locations $x/D = 7.5, 15,$ and 30 along with the centerline profile. The axial and radial profiles of \tilde{U} predicted by all the three table integration approaches almost overlap and show good agreements with the experiment [8]. The profiles for \tilde{k} are also not affected significantly by the different table integration approaches with the maximum relative difference about 7% among the results with the different table integration approaches. The relative difference such as the above reported 7% relevance difference and all the other percentage differences reported below is generally defined as

$$\frac{|F_1 - F_2|}{\max(|F_1|_{peak}, |F_2|_{peak})}, \quad (5.1)$$

where F_1 and F_2 are the two compared results and the subscript “peak” denotes the peak result along the radial or axial direction.

5.1.5 Predictions of Mixture Fraction and Progress Variable

Next, we examine the predictions of the flamelet independent variables, mixture fraction and progress variable, which are used for looking up the flamelet tables. Inaccuracy in the prediction of the independent variables can directly lead to poor performance of the flamelet model and hence it is important to examine the effect of the different table integration approaches on these variables.

Figure 5.4 shows the axial and radial profiles of the predicted mean mixture fraction $\tilde{\xi}$, the root mean square (RMS) of mixture fraction ξ_{RMS} , and the mean progress variable \tilde{C} . From the first and the second rows in Figure 5.4, we can see that there is not a significant difference in the predictions of $\tilde{\xi}$ and ξ_{RMS} by using the three table integration approaches. This is similar to the observation made for the flow and turbulence fields in the Section 5.1.4 and it indicates that the mixture fraction is only weakly coupled to the flamelet table (mainly through density and transport properties).

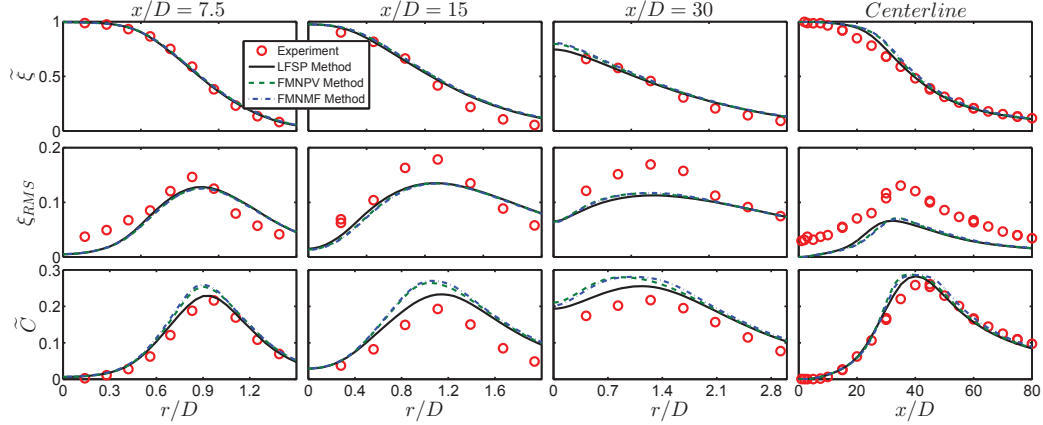


Figure 5.4.: Radial profiles of the mean mixture fraction $\tilde{\xi}$ (top), RMS mixture fraction ξ_{RMS} (middle) and mean progress variable \tilde{C} (bottom) at the axial locations $x/D = 7.5, 15,$ and 30 along with the centerline profile in Sandia flame D. The model results are obtained using the FPV model with the three different table integration approaches.

The predictions of the mean progress variable \tilde{C} , defined in Equation (3.11), by the three different table integration approaches can be seen in the last row in Figure 5.4. Evidently, the predictions of \tilde{C} depend on the table integration approaches stronger than the mixture fraction. This is mainly because the source term in the transport equation for \tilde{C} is obtained from the flamelet table which is shown to be different in Figure 5.2 and therefore the different table integration approaches can influence the predictions of \tilde{C} more significantly. The LFSM method yields the best agreement with the experiment [7] for the predictions of \tilde{C} with the maximum relative error up to 18% at the peak locations. The predictions for the FMNPV method and the FMNMF method are close to each other with the maximum relative errors approximately 27% and 29% respectively, near the peak locations, in comparison with the experiment [7].

Having examined the predictions of the flamelet independent variables, next, we will examine the effect of the different table integration approaches on the dependent variables. As discussed in Section 4.3.2, the predictions of the dependent variables are affected by two types of errors, namely the error in the predictions of the independent

variables and the error due to the tabulation of the thermochemical properties. To isolate the effect of the error due to the tabulation with the different table integration approaches, in the following Section 5.1.6, we first perform an *a priori* analysis of the flamelet table accuracy by using the values of the independent variables directly from the experiment of Sandia flame D barlow1998effects to predict the dependent variables. Then, in Section 5.1.7, we carry out an *a posteriori* analysis by comparing the predictions of the dependent variables from the actual numerical simulations of Sandia flame D with the different table integration approaches.

5.1.6 A Prioiri Testing of Flamelet Table Accuracy

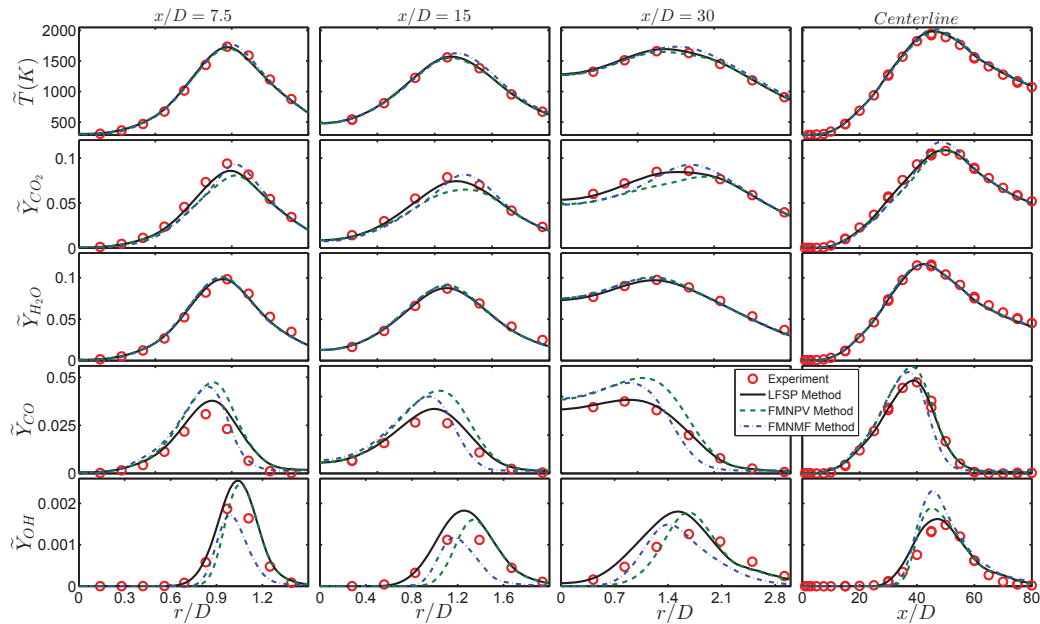


Figure 5.5.: Radial profiles of the dependent variables mean temperature \tilde{T} , mean mass fractions of species CO_2 , H_2O , CO , and OH at the axial locations $x/D = 7.5, 15,$ and 30 along with the centerline profile in Sandia flame D. The values of $(\tilde{\xi}, \xi_{RMS}, \tilde{C})$ used for looking up the table are taken directly from the experiment [7].

We conduct *a priori* testing to examine the effect of the different table integration approaches on the predictions of the thermo-chemical scalars in Sandia flame D. The

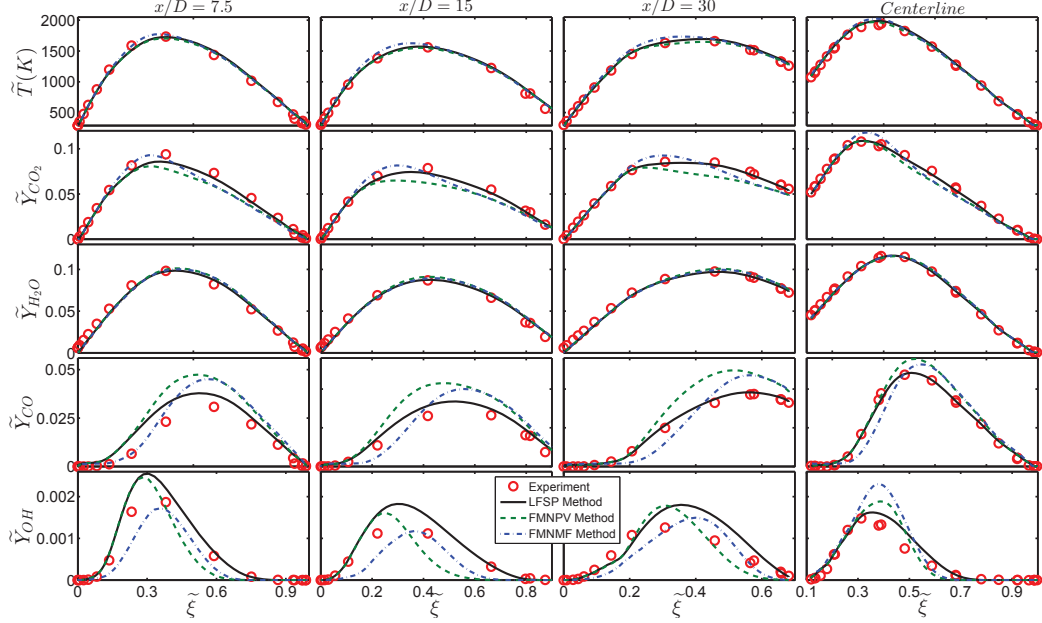


Figure 5.6.: The profiles of dependent variables mean temperature \tilde{T} , mean mass fractions of species CO_2 , H_2O , CO , and OH against the mean mixture fraction $\tilde{\xi}$ at the axial locations $x/D = 7.5$, 15 , and 30 along with the centerline in Sandia flame D. The values of $(\tilde{\xi}, \xi_{RMS}, \tilde{C})$ used for looking up the table are taken directly from the experiment [7].

difference among the three table integration approaches has been briefly discussed in Section 5.1.3. Here, we further investigate the difference by comparing the predictions of the dependent variables for the different flamelet tables by using the same values of the independent variables taken directly from the experiment [7]. Similar *a priori* testing for the flamelet models has also been reported in the literature, e.g. [135–137].

Figure 5.5 compares the predictions of the mean temperature \tilde{T} and the mean mass fractions of species CO_2 , H_2O , CO , and OH for the three table integration approaches. To obtain these quantities from the integrated flamelet tables, we use the values $(\tilde{\xi}, \xi_{RMS}, \tilde{C})$ directly from the experiment [7]. By doing this, we eliminate the error in the predictions of the independent variables and highlight the difference among the different flamelet tables generated by using the different table integration

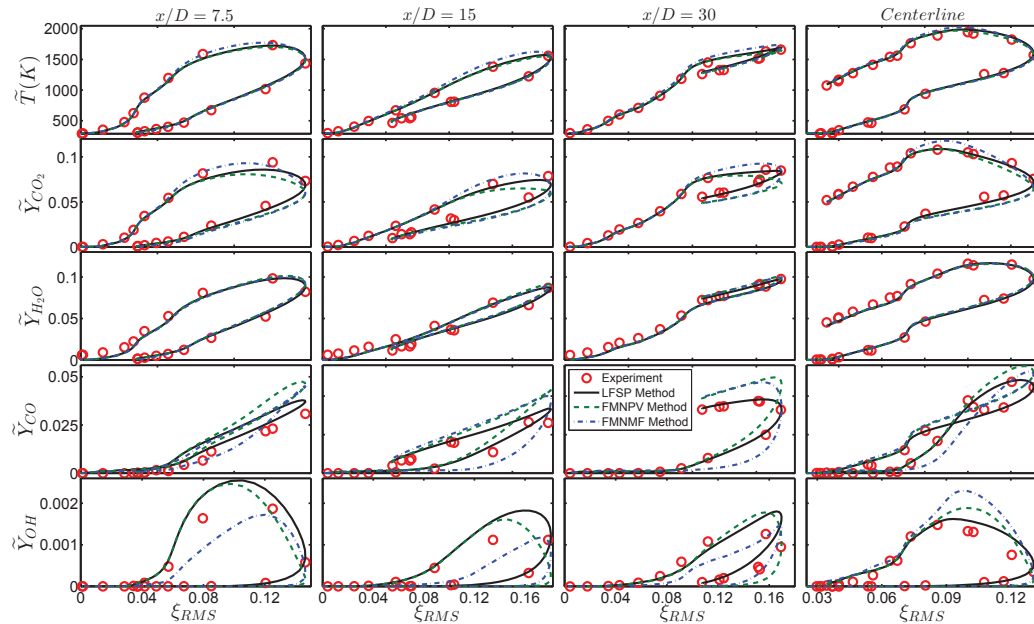


Figure 5.7.: The profiles of dependent variables mean temperature \tilde{T} , mean mass fractions of species CO_2 , H_2O , CO , and OH against the RMS mixture fraction ξ_{RMS} at the axial locations $x/D = 7.5, 15, \text{ and } 30$ along with the centerline in Sandia flame D. The values of $(\tilde{\xi}, \xi_{RMS}, \tilde{C})$ used for looking up the table are taken directly from the experiment [7].

approaches. From the figure we can see that there is an excellent overall agreement between the predictions and experiment, and very little difference in the predictions of \tilde{T} , \tilde{Y}_{CO_2} and \tilde{Y}_{H_2O} (maximum relative error about 5%, 7%, and 3%, respectively in comparison to experiment near the peak locations) by using the different flamelet tables. For the mean mass fraction of CO , the LFSP method yields the best agreement with experiment with a relative error of around 16%, 15%, 2% and 1% when compared with the experiment near the peak locations at $x/D = 7.5, 15, 30$ and centerline respectively, while with the FMNPV method and the FMNMF method, the maximum relative error can reach up to 38% at the peak locations. Some evident difference in the predictions of the mean mass fraction of OH is also seen with the different table integration approaches, with the maximum relative error up to 27%, 30% and 44%

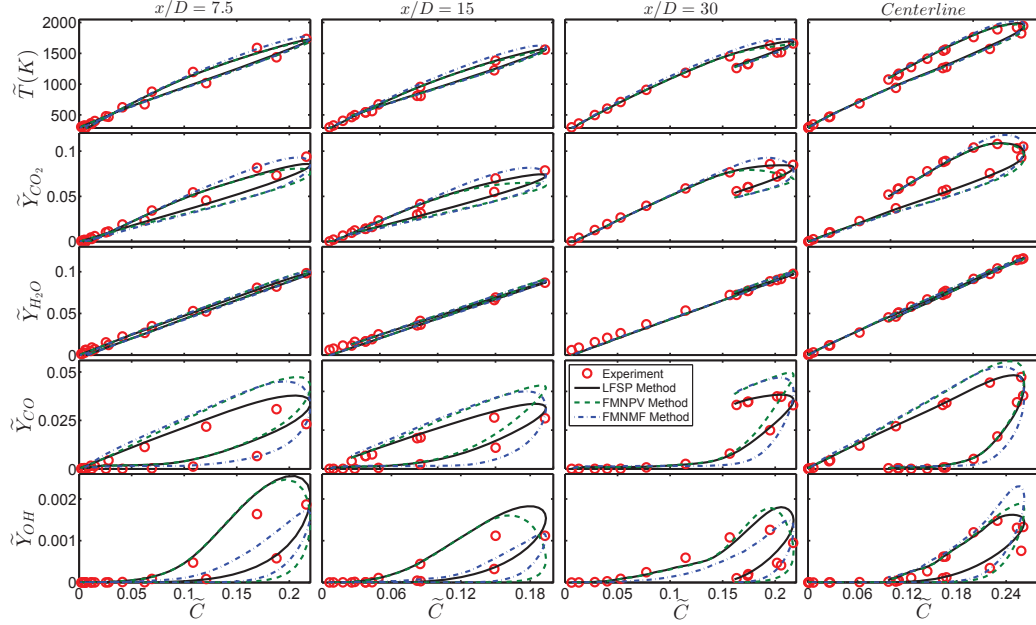


Figure 5.8.: The profiles of dependent variables mean temperature \tilde{T} , mean mass fractions of species CO_2 , H_2O , CO , and OH against the mean progress variable \tilde{C} at the axial locations $x/D = 7.5$, 15 , and 30 along with the centerline in Sandia flame D. The values of $(\tilde{\xi}, \xi_{RMS}, \tilde{C})$ used for looking up the table are taken directly from the experiment [7].

near the peak locations for the LFSP, FMNPV, FMNMF methods respectively, when compared with experiment.

Figures 5.6-5.8 continue the *a priori* testing by further examining the thermochemical scalars in the flamelet independent variable space $(\tilde{\xi}, \xi_{RMS}, \tilde{C})$. In this way, the error involved in the table part of flamelet implementation is effectively isolated from many other errors involved in flamelet modeling. Meanwhile, we are also able to use the experimental data of Sandia flame D to directly quantify the errors involved in the flamelet tables. Figure 5.6 shows the profiles of mean temperature \tilde{T} , mean mass fractions of species CO_2 , H_2O , CO , and OH against the mean mixture fraction $\tilde{\xi}$ at the axial locations $x/D = 7.5$, 15 , and 30 along with the centerline. The results show a remarkable agreement between the LFSP table results and the experimental

data for most quantities including CO. The FMNPV and FMNMF results also have reasonable agreement with the experimental data but the discrepancy is also evident for CO and OH. Figure 5.7 shows the profiles of \tilde{T} , mean mass fractions of CO₂, H₂O, CO, and OH against ξ_{RMS} at the axial locations $x/D = 7.5, 15,$ and 30 along with the centerline. A good agreement between the LFSP table results and the experimental data is observed. FMNPV and FMNMF yields results in a good agreement with the experimental data for \tilde{T} and major species. For CO and OH, the results show some evident deviation from the experimental data. Figure 5.8 shows the same set of quantities as in Figure 5.7 against \tilde{C} and similar observations can be made. These comparisons provide an effective approach to study the isolated flamelet table errors. The experimental data strongly support the superiority of the LFSP method over the FMNPV and FMNMF methods as the table integration approach.

A priori testing of the flamelet table accuracy is conducted in this section to isolate the flamelet table error from other errors. The difference in the numerical results observed in this section is purely due to the different table integration approaches and we can see the difference evidently for some quantities such as the intermediate and minor species. The performance difference of the different table integration approaches is also informed by the experimental data of Sandia flame D. In the following Section 5.1.7, *a posteriori* testing is conducted to compare the performance of the different table integration approaches in actual simulations of Sandia flame D.

5.1.7 *A Posteriori* Testing of Flamelet Table Accuracy

In this section, we analyze the predictions of the actual dependent variables in Sandia flame D from the simulations with $(\tilde{\xi}, \xi_{RMS}, \tilde{C})$ computed from the simulations. Figure 5.9 shows the predictions of the mean temperature \tilde{T} and mean species mass fractions of CO₂, H₂O, CO, and OH. Due to the prediction error in $(\tilde{\xi}, \xi_{RMS}, \tilde{C})$ shown in Figure 5.4, the agreement between the predictions and experiment in Figure 5.9 is worse than that observed in the *a priori* testing in Figure 5.5. At all the radial

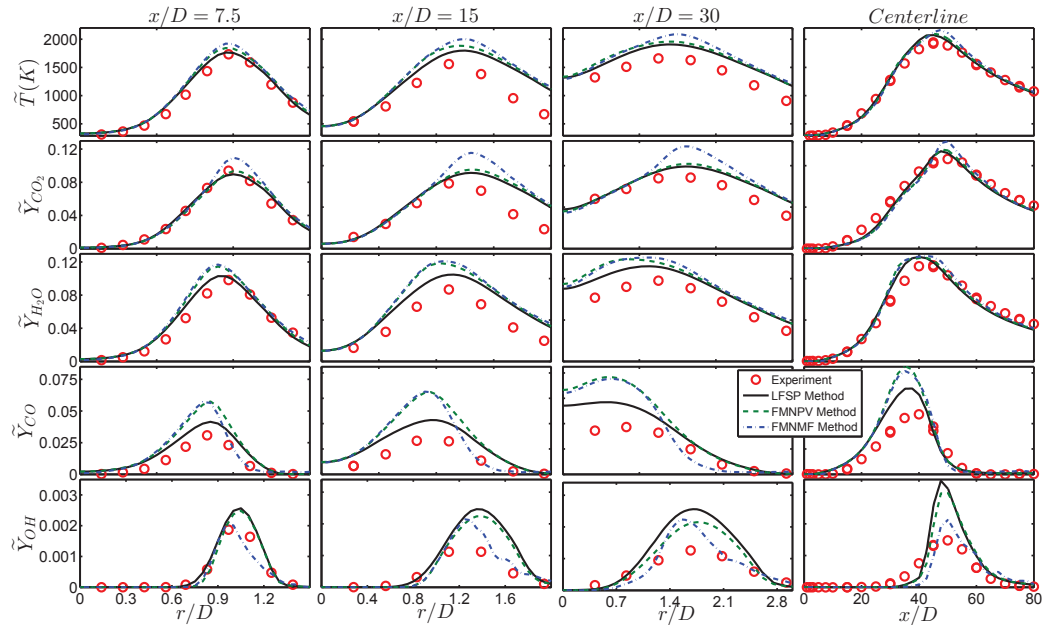


Figure 5.9.: Radial profiles of the mean temperature \tilde{T} , mean mass fraction of species CO_2 , H_2O , CO , and OH at the axial locations $x/D = 7.5$, 15 , and 30 along with the centerline profiles. The model results are obtained using the FPV model with the three different table integration approaches.

locations it can be seen that the peak mean temperature \tilde{T} predicted by the FMNMF method is higher than that predicted by the other two methods with a maximum relative error of 30% relative to the experiment near the peak locations, in contrast with 13% and 17% for the LFSP method and the FMNPV method, respectively. For the species CO_2 , the maximum relative error near the peak location for the LFSP method and the FMNPV method with respect to the experimental data is 13% and 16% respectively, while for the FMNMF method it is 32%. The H_2O mean mass fraction prediction from the LFSP method is closest to the experiment [7] with the maximum relative error 17% as opposed to 26% for the FMNPV method and 28% for the FMNMF method. The difference among the different table integration approaches is also evident in the predictions of CO with the LFSP method showing better agreement with experiment (maximum relative error near peak location 32%)

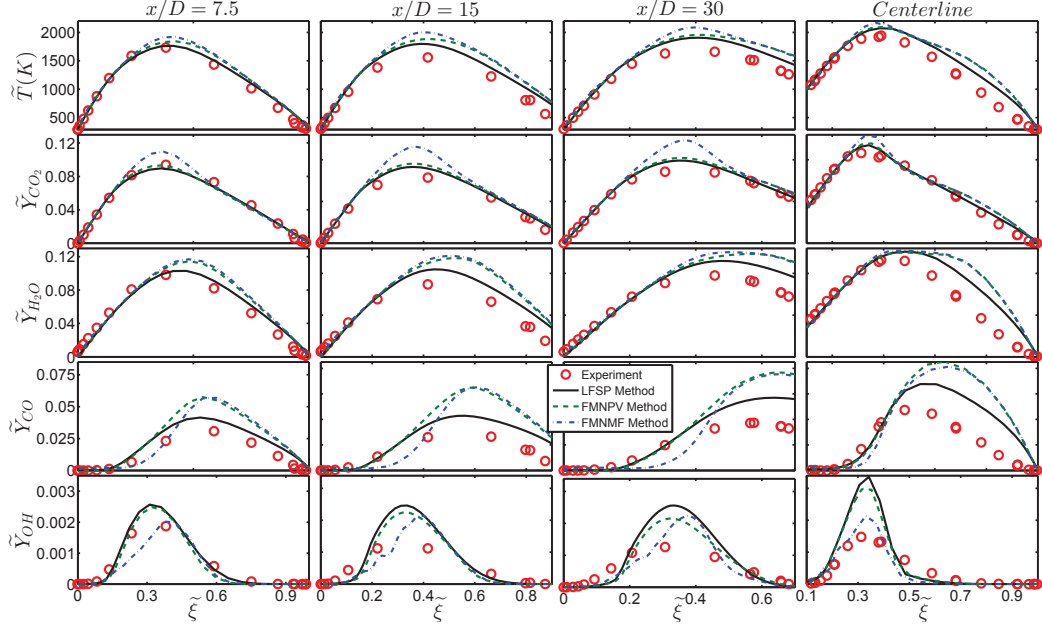


Figure 5.10.: The profiles of the mean temperature \tilde{T} , mean mass fractions of species CO_2 , H_2O , CO , and OH against the mean mixture fraction $\tilde{\xi}$ at the axial locations $x/D = 7.5$, 15 , and 30 along with the centerline in Sandia flame D. The model results are obtained using the FPV model with the three different table integration approaches.

than the FMNPV method (maximum relative error near peak location 52%) and the FMNMF method (maximum relative error near peak location 51%).

The performance difference of the table integration approaches in the *a priori* testing in Figure 5.5 and *a posteriori* testing in Figure 5.9 is mainly caused by the prediction errors of the flamelet independent variables $(\tilde{\xi}, \xi_{RMS}, \tilde{C})$. This is quite useful for narrowing down the source of errors of the flamelet model so that further targeted model enhancement can be done. To investigate the individual source of errors caused by each flamelet independent variable, we further compare the thermochemical scalars in the flamelet independent space in Figures 5.10-5.12. Figure 5.10 shows the profiles of the actual predictions of the mean temperature \tilde{T} , mean mass fractions of species CO_2 , H_2O , CO , and OH against the mean mixture fraction $\tilde{\xi}$ at

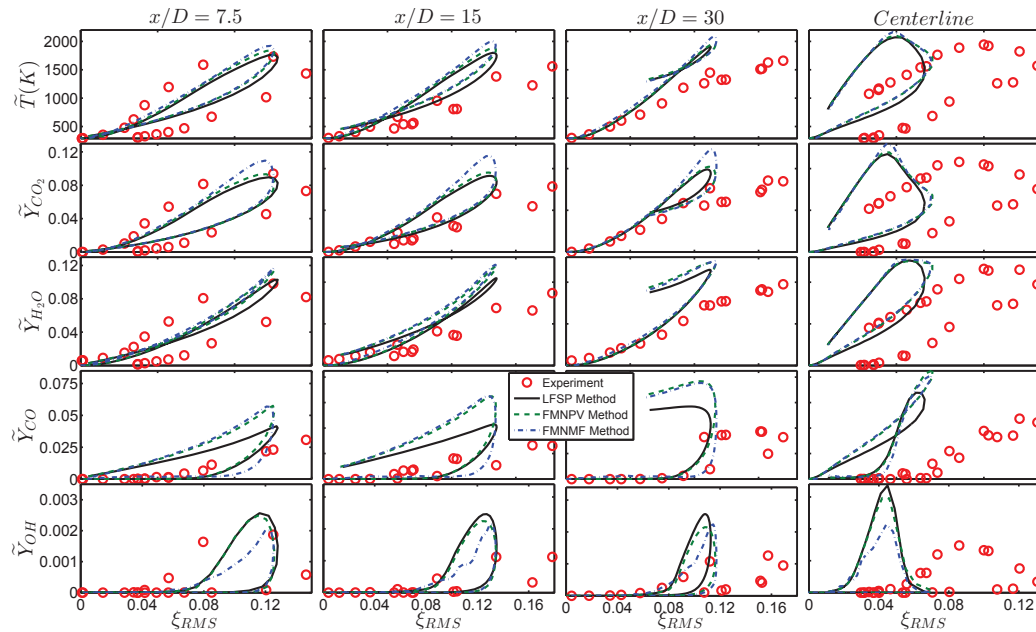


Figure 5.11.: The profiles of the mean temperature \tilde{T} , mean mass fractions of species CO_2 , H_2O , CO , and OH against the mixture fraction RMS ξ_{RMS} at the axial locations $x/D = 7.5$, 15 , and 30 along with the centerline in Sandia flame D. The model results are obtained using the FPV model with the three different table integration approaches.

the axial locations $x/D = 7.5$, 15 , and 30 along with the centerline. It is noticed that the dependence of the model results on $\tilde{\xi}$ in this figure is quite different from that in Figure 5.6 although the same table is used for each table integration approach. This difference is caused by the difference of (ξ_{RMS}, \tilde{C}) at each location used together with $\tilde{\xi}$ for the flamelet table lookup. Thus the results in Figure 5.10 contain the flamelet table errors as well as the prediction errors of (ξ_{RMS}, \tilde{C}) . Figures 5.11 and 5.12 show the same set of quantities against ξ_{RMS} and \tilde{C} , respectively. Comparing the results in Figures 5.10-5.12, we can see that the biggest discrepancy between the model results and experimental data appears to be in Figure 5.11 due to the predictions of ξ_{RMS} . This is consistent with Figure 5.4 where the predictions of ξ_{RMS} show the least agreement with the experimental data among the three flamelet

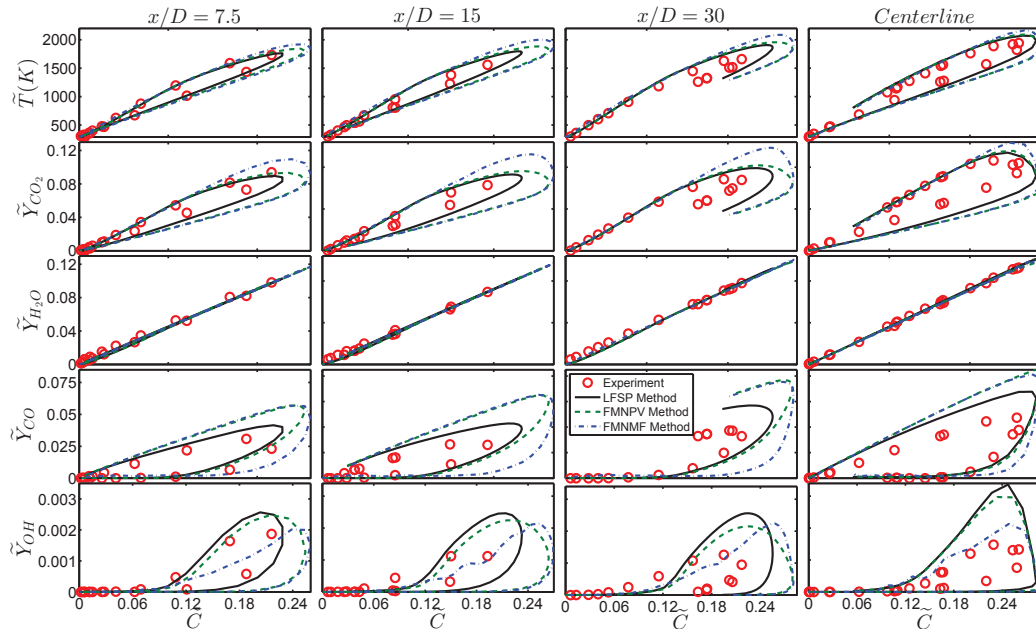


Figure 5.12.: The profiles of the mean temperature \tilde{T} , mean mass fractions of species CO_2 , H_2O , CO , and OH against the mean progress variable \tilde{C} at the axial locations $x/D = 7.5$, 15, and 30 along with the centerline in Sandia flame D. The model results are obtained using the FPV model with the three different table integration approaches.

independent variables. The model predictions of ξ_{RMS} has been a topic in many existing studies (e.g., [138–141]). It is expected that a more accurate prediction of ξ_{RMS} can improve the model agreement with the experimental data in Figures 5.9–5.12. Such an improvement is not the subject of this study.

5.2 Self-Excited Resonance Model Rocket Combustor

A more challenging model rocket combustor is also employed in this study to further examine the effect flamelet table integration on the simulation results of a practically relevant combustion problem. The rocket problem is highly unstable with significant variation of pressure in the combustor. It provides a challenging test case to examine the effect of table integration as well as the FPV model performance in

problems with highly transient hydrodynamics and combustion dynamics. There are not comprehensive experimental data from the combustor, so the discussion is kept as brief as possible.

In the following Section 5.2.1, we first examine the flamelet tables generated under the rocket combustor condition by using the different table integration approaches in Section 4.3.1. In Section 5.2.2, we compare the pressure signal and the power spectral density (PSD) of the signal predicted by using the three flamelet table integration approaches with the experiment [76]. Finally, in Section 5.2.3, we briefly compare the predictions of time-averaged statistics.

5.2.1 Examination of Integrated Flamelet Tables

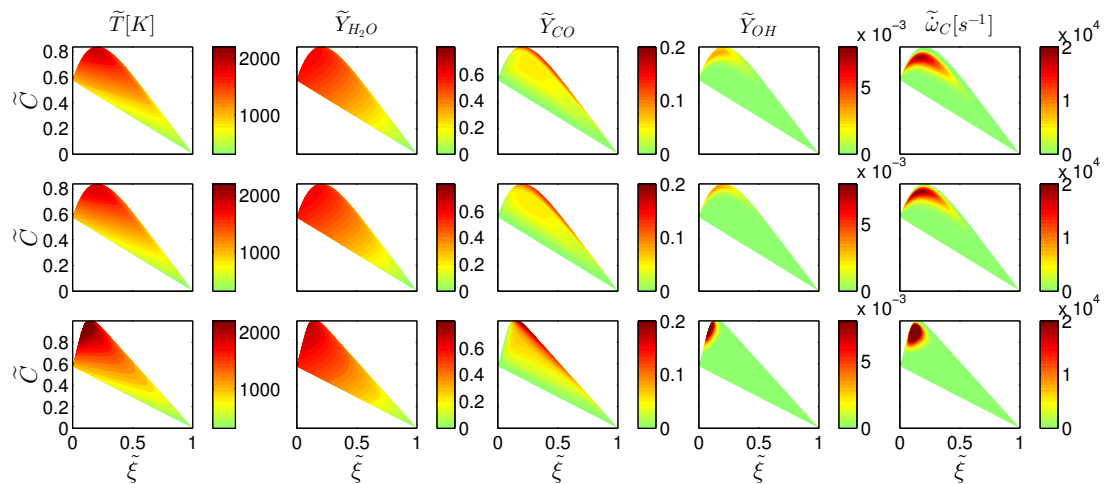


Figure 5.13.: Contour plots of the mean temperature \tilde{T} , the mean mass fractions of species H₂O, CO, and OH, and the mean reaction rate $\tilde{\omega}_C$ for the progress variable C , in the mean mixture fractions $\tilde{\xi}$ and mean progress variable space \tilde{C} are shown from the integrated flamelet tables for the LFSP method (the first row), the FMNPV method (the second row) and the FMNMF method (the third row) in the model rocket combustor. The normalized variance of the mixture fraction is fixed at $\xi_v = \tilde{\xi}''^2 / (\tilde{\xi}(1 - \tilde{\xi})) = 0.1$ and the pressure is at 15 atm.

Figure 5.13 compares the flamelet tables generated by using the three different table integration approaches for the self-excited rocket combustor test case. Similar to Sandia flame D in Section 5.1.3, a two dimensional slice is taken for the normalized variance value of $\xi_v = \widetilde{\xi''^2}/(\widetilde{\xi}(1-\widetilde{\xi})) = 0.1$ and pressure at 15 atm so that the contour plots of the dependent variables can be generated in the mean mixture fraction $\widetilde{\xi}$ and mean progress variable \widetilde{C} space. The dependent variables shown in the figure are mean temperature \widetilde{T} , mean mass fractions of species H_2O , CO , and OH , and the mean reaction rate for \widetilde{C} , $\widetilde{\omega}_C$. We can clearly see the difference among the different tables although they are generated from the same set of laminar flamelet solutions. In the following section, we examine the effect of the different flamelet tables on the actual predictions of the combustor.

5.2.2 Predictions of Pressure Fluctuation and Power Spectral Density (PSD)

Table 5.1.: Comparison of the time-averaged pressure $\langle P_c \rangle$ in the combustor, the level of combustion instability ($\langle P_{pp} \rangle / \langle P_c \rangle$), the frequency (f_1) and the amplitude (A_1) of the first mode from the experiment [76] with simulations using the different table integration approaches.

	Experiment	LFSP	FMNPV	FMNMF
$\langle P_c \rangle$ (MPa)	1.43	1.44	1.44	1.43
$\langle P_{pp} \rangle / \langle P_c \rangle$	45%	36%	34%	34%
f_1 (Hz)	1360	1535	1543	1508
A_1 (kPa ² /Hz)	646.3	206.2	133.6	100.8

The time-averaged pressure $\langle P_c \rangle$ in the combustor at $x/D_{ox} = 18$ near the wall is about 1.43 MPa in the experiment [76] while the predictions of $\langle P_c \rangle$ by the three

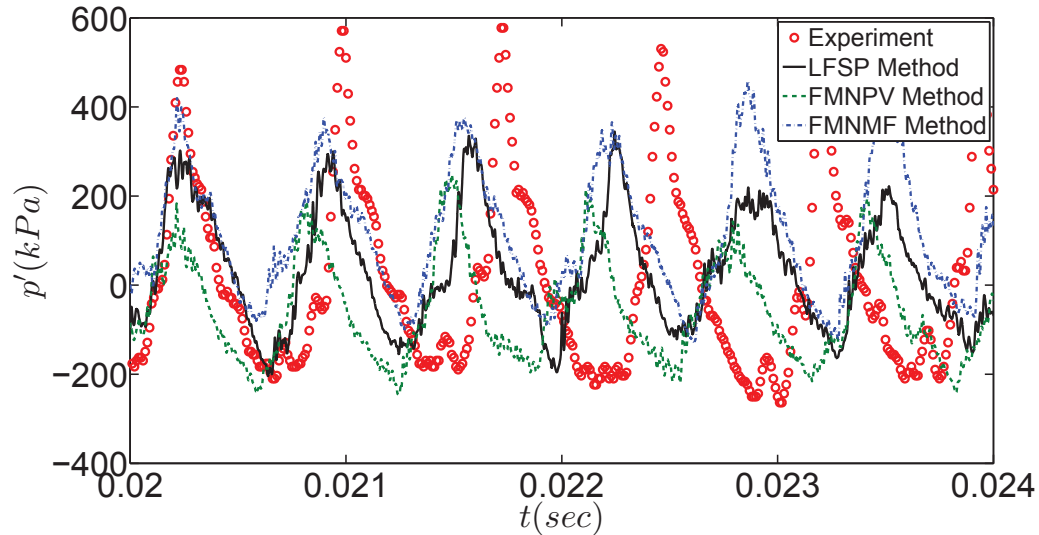


Figure 5.14.: Fluctuating pressure signal p' at $x/D_{ox} = 18$ in the model rocket combustor. The model results are obtained by using the FPV model with the three different table integration approaches.

table integration approaches are shown in Table 5.1 and are in a close agreement with the experiment [76]. Figure 5.14 compares the instantaneous pressure fluctuation p' predicted by the three table integration approaches at $x/D_{ox} = 18$ with the experiment [76]. The pressure fluctuation p' is obtained by passing the instantaneous, raw pressure data through a high-pass filter with a cut-off frequency of 1 Hz to filter out the low-frequency pressure waves corresponding to the time-averaged pressure. The peak-to-peak amplitude of the pressure fluctuation p' predicted by the LFSP method is slightly greater than the other two methods. The ratio $\langle P_{pp} \rangle / \langle P_c \rangle$ for the LFSP method is closer to the experiment as shown in Table 5.1. The power spectral density (PSD) analysis of the pressure signal [65, 142] is shown in Figure 5.15 to identify the dominant instability modes. The amplitude A_1 and frequency f_1 of the first mode for the three table integration approaches are compared in Table 5.1. It can be seen that the frequency of the first dominant mode is very close to each other for all the three approaches and higher than that in the experiment [76] (by about 10%). The

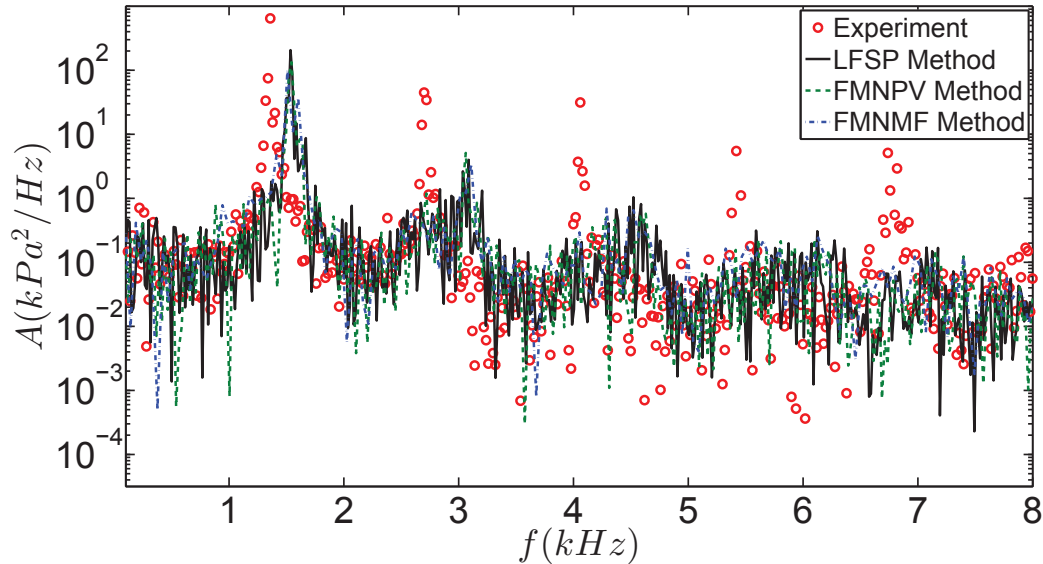


Figure 5.15.: PSD of raw pressure data at $x/D_{ox} = 18$ in the model rocket combustor. The model results are obtained by using the FPV model with the three different table integration approaches.

PSD amplitude of the first mode A_1 is highest from the LFSP method and is closest to the experiment [76] although it is only about one-third of the measurement. The difference is expected to be mainly because of the model error involved in using the FPV model to predict the physics. The maximum relative difference among the different table integration approaches in terms of the prediction of the PSD amplitudes is up to 100%, indicating the significance of choosing the more accurate flamelet table integration approach.

In summary, from the analysis of pressure fluctuation in the rocket combustor, we observed evident difference among the different table integration approaches, *e.g.*, the maximum relative difference for the dominant mode PSD amplitude can reach 100% among the different table integration approaches. In the following sections, we continue to make quantitative comparisons of the effect of the different table integration approaches on the predictions of time-averaged thermo-chemical fields.

5.2.3 Predictions of Time-Averaged Fields

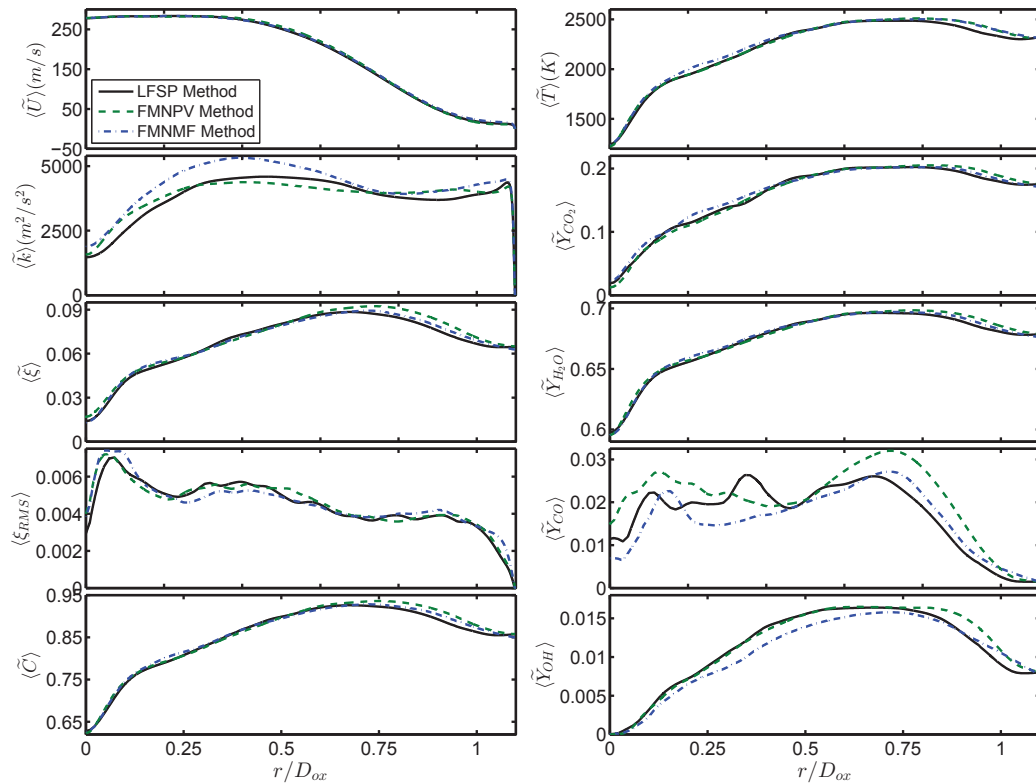


Figure 5.16.: Radial profiles of the time-averaged axial velocity $\langle \tilde{U} \rangle$, time-averaged turbulent kinetic energy $\langle \tilde{k} \rangle$, time-averaged mixture fraction $\langle \tilde{\xi} \rangle$, RMS mixture fraction $\langle \xi_{RMS} \rangle$, time-averaged progress variable $\langle \tilde{C} \rangle$, time-averaged temperature $\langle \tilde{T} \rangle$ and mass fractions of species CO_2 , H_2O , CO , and OH at the axial location $x/D_{ox} = 10$ in the model rocket combustor. The model results are obtained using the FPV model with the three different table integration approaches.

Figure 5.16 compares the radial profiles of time-averaged axial velocity $\langle \tilde{U} \rangle$, turbulent kinetic energy $\langle \tilde{k} \rangle$, mixture fraction $\langle \tilde{\xi} \rangle$, RMS of mixture fraction $\langle \xi_{RMS} \rangle$, progress variable $\langle \tilde{C} \rangle$, temperature $\langle \tilde{T} \rangle$ and mass fraction of species CO_2 , H_2O , CO , and OH predicted by using the three table integration approaches at the axial locations $x/D_{ox} = 10$ in the rocket combustor. The time-averaging is done over 12 flow-through times based on the mean inlet velocity of the fuel and oxidizer stream.

An overall observation we can make from the figure is that there is no substantial difference among the different table integration approaches for the predictions of the time-averaged statistics. This observation is true for other axial locations in the model rocket combustor as well and hence the predictions at these locations are not shown here. Without comprehensive experimental data for flow and turbulence fields, and thermo-chemical scalars, we cannot appraise the different table integration approaches even if they yield slightly different results, *e.g.*, the predictions of \tilde{k} , CO, and OH. Thus we will not discuss the results in further detail. One useful observation is that it appears that the effect of different table integration approaches is different for different quantities. For the rocket case, the effect is more prevailing for the temporal pressure fluctuations and PSD than the time-averaged statistics of the thermochemical properties.

To summarize, we first inspected the flamelet tables generated by integrating the same laminar flamelet solutions with the three table integration approaches discussed in Section 4.3.1 for the rocket combustor test case. It is observed that there is a significant difference in the integrated flamelet tables. To evaluate the effect of the different table integration approaches, we compared the pressure fluctuation signal predicted by the three table integration approaches with the experimental results. The level of combustion instability, quantified by $\langle P_{pp} \rangle / \langle P_c \rangle$, is noticeably affected by the different table integration approaches. The difference is also observed in the PSD amplitude of the dominant first mode by using the different table integration approaches with the LFSP method showing the closest agreement with the experiment. The effect of the table integration approaches is then compared for the predictions of the time-averaged statistics. Overall, time averaging eliminates some of the difference among the different table integration approaches observed in the PSD data, and no substantial difference is observed in most of the time-averaged results. It also indicates that the different table integration approaches have a different impact on different statistics.

In the following chapter, using LFSP method for the flamelet table integration, we study the interaction between chemical kinetics, transient flame dynamics like flame extinction and reignition, turbulence chemical kinetics and acoustics using the SFL model, FPV model, and the two variants of the FPV model.

6. EFFECT OF COMBUSTION DYNAMICS, TURBULENCE AND CHEMICAL KINETICS, AND THEIR INTERACTIONS ON THERMO-ACOUSTIC INSTABILITY MODELING

In this chapter we investigate the complicated interactions between transient flame dynamics like extinction, reignition, detailed chemical kinetics, turbulence and combustion instabilities in the model rocket combustor using the flamelet modeling approach. Primarily, two flamelet models are considered, the steady flamelet (SFL) model and the flamelet progress/variable (FPV) model. The performance of these two models in predicting the pressure oscillations in the rocket combustor for a stable and unstable operating condition is examined first. To investigate the coupling between transient flame dynamics and combustion instability, a variant of the FPV model, we call the FPVB model is used. The transient flame dynamics are investigated on a global scale for the entire combustor and also on a local level by dividing the combustor into sections called bins and analyzing each bin separately. Lastly, the effect of neglecting turbulence-chemistry interaction is studied by a direct comparison between the FPV model and a modified FPV model with zero mixture fraction variance (FPV-ZV).

6.1 Experimental Validation

We first validate our numerical simulations with the experimental data for the model rocket combustor [76] operated under both the stable operating condition and the unstable operating condition shown in Table 5.1.

6.1.1 Simulation Setup

To reduce the computational cost of this study, we employ an assumption of 2D axisymmetric flow for the model rocket combustor following the previous practice for the same combustor [65, 79, 82]. This employed 2D assumption imposes some limitations to the study. The importance of the study is that through the 2D results we discovered a plausible mechanism of the self-excited and sustained thermo-acoustic instability in the model rocket combustor caused by the two-way coupling between local flame dynamics and thermo-acoustic interactions. This two-way coupling has rarely been studied in the past and hence there is an important value of the current study with 2D simulations although the identified mechanism needs to be confirmed in full 3D simulations. The mesh used for carrying out the simulations has around 110000 cells following Sardeshmukh et al. [65]. In the mesh, the cells are mainly concentrated in the shear mixing layer of the fuel stream and the oxidizer stream (see Figure 2.1) and in the heat release region near the dump plane at $x/D_{ox} = 0$.

Table 6.1.: Experimental inlet conditions for the fuel stream and oxidizer stream for the numerical simulations of the model rocket combustor.

	Fuel	Oxidizer
\dot{m} (kg/s)	0.024	0.323
\tilde{T} (K)	294	1030
\bar{p} (MPa)	1.38	1.38
\tilde{Y}_{CH_4}	1.0	0.0
\tilde{Y}_{O_2}	0.0	0.4235
\tilde{Y}_{H_2O}	0.0	0.5765
$\tilde{\xi}$	1.0	0.0
$\widetilde{\xi''^2}$	0.0	0.0
\tilde{C}	0.0	0.5765

The laminar flamelet table for the SLF model and the FPV model is generated using the FlameMaster code [89] with the GRI 1.2 mechanism [81]. The boundary conditions used for generating the laminar flamelet table specified according to the experimental conditions in Table 7.5. The background pressure p used to generate the flamelet table is varied from 0.1 MPa - 2.5 MPa since the raw pressure data in the experiment [76] for the unstable operating condition lies within this range. The total number of flamelets used in the laminar flamelet table is 558, including 93 different scalar dissipation rates and 6 pressure values. The resolution of the integrated flamelet table has 100 points in the mean mixture fraction $\tilde{\xi}$, 20 points in the mixture fraction variance $\tilde{\xi}''^2$, 100 points in the mean progress variable \tilde{C} (or in the scalar dissipation rate), and 6 points in the mean pressure.

In the flow simulations, for the inlet boundary condition of the fuel stream and the oxidizer stream, the mass flow rate \dot{m} , mean temperature \tilde{T} , mean pressure \bar{p} , mean mixture fraction $\tilde{\xi}$, mixture fraction variance $\tilde{\xi}''^2$ and mean progress variable \tilde{C} is specified. The values of these variables for the fuel stream and oxidizer stream are given in Table 7.5, following the experimental conditions. The walls of the combustor are assumed to be adiabatic and the no-slip boundary condition is applied. At the nozzle outlet, the mean back pressure \bar{p}_b is specified to be equal to the atmospheric pressure (1 atm). The physical time step size Δt is 10^{-7} s for all the simulations so that the CFL number is close to 1. The pseudo time step size $\Delta \tau$ is calculated by specifying the pseudo CFL number which is set to 200 in the current simulations. The maximum number of pseudo inner iterations is fixed to be 8. The total computational cost for each simulation is around 80 hours on 320 processor cores (25600 cpu-hours in total per simulation).

6.1.2 Predictions of Pressure Signals

The time-averaged pressure $\langle P_c \rangle$ near the combustor wall measured at $x/D_{ox} = 18$ in the experiment is 1.44 MPa and 1.43 MPa for the stable and unstable operating

Table 6.2.: Comparison of the time-averaged pressure $\langle P_c \rangle$ at $x/D_{ox} = 18$ near the combustor wall, level of thermo-acoustic instability $\langle P_{pp} \rangle / \langle P_c \rangle$, frequency f_1 and amplitude A_1 of the first mode from the experiment [76] with the simulations using the SLF model and FPV model for the stable operating condition and the unstable operating condition in the model rocket combustor [76].

	Stable Operating Condition			Unstable Operating Condition				
	Experiment	SLF	FPV	Experiment	SLF	FPV	FPV-B	FPV-ZV
$\langle P_c \rangle$ (MPa)	1.44	1.34	1.41	1.43	1.36	1.44	1.35	1.45
$\langle P_{pp} \rangle / \langle P_c \rangle$	13%	8%	15%	45%	13%	36%	11%	35%
f_1 (Hz)	1440	-	1732	1360	1475	1512	1493	1570
A_1 (kPa ² /Hz)	2.7	-	20.5	646.3	1.9	247.4	1.6	138.5

condition respectively and that predicted by the SLF model and the FPV model for the two operating conditions is shown in Table 6.2. The predictions of the FPV-B model and the FPV-ZV model are also shown in Table 6.2. The results for these two models which will be discussed in the following Section 6.2. For the stable operating condition, both the SLF model (7%) and the FPV model (2%) under predict $\langle P_c \rangle$, whereas for the unstable operating condition, the SLF model under predicts $\langle P_c \rangle$ by around 5% but the FPV model is able to accurately predict within 1% error. The ratio $\langle P_{pp} \rangle / \langle P_c \rangle$ used to quantify the level of thermo-acoustic instability can be seen in Table 6.2 for the SLF model and the FPV model. Compared to the stable operating condition, for the unstable operating condition the prediction of $\langle P_{pp} \rangle / \langle P_c \rangle$ for the two models are widely different. For the unstable operating condition, the SLF model significantly under predicts $((45-13)/45 \times 100 \approx 70\%)$ the value of $\langle P_{pp} \rangle / \langle P_c \rangle$ in comparison to the experiment indicating that for the unstable operating condition, the SLF model predicts a stable condition. The FPV model shows good agreement with the experiment for the unstable operating condition and the error in the prediction is around 20% $((45-36)/45 \times 100 = 20\%)$. In order to identify the different modes in the raw pressure data, a power spectral density (PSD) analysis is carried out. The

amplitude of the first mode A_1 and the frequency f_1 for the experiment and the model predictions is tabulated in Table 6.2. For the stable operating condition, the SLF model does not show distinct modes and the FPV model over predicts f_1 by about 20% in comparison to the experiment. Similar observation is made in previous modeling studies [64,65,79] of the model rocket combustor. The PSD amplitude A_1 is also over predicted by the FPV model by almost 700%. For the unstable operating condition, the SLF model and the FPV model over predict the frequency of the first mode f_1 by around 9% and 11% respectively. The PSD amplitude A_1 is under predicted by both the models (SLF model: 99%, FPV model: 60%).

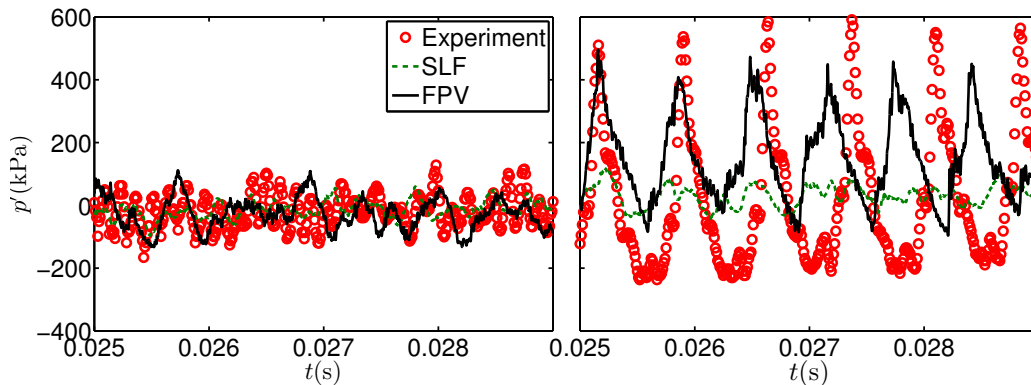


Figure 6.1.: Fluctuating pressure signal p' at $x/D_{ox} = 18$ near the combustor wall for stable operating condition (left) and unstable operating condition (right). The model results are obtained by using the SLF model and the FPV model.

Figure 6.1 compares the instantaneous pressure fluctuation inside the model rocket combustor measured at the axial location $x/D_{ox} = 18$ with the experiment data [76] for both the operating conditions. To obtain pressure fluctuation p' from the raw pressure data, a high-pass filter with a cut-off frequency of 1 Hz is used to filter out the low-frequency pressure waves. For the stable operating condition, it can be seen that the amplitude of the peak-to-peak oscillation for the SLF model is relatively lower in comparison to the FPV model and the FPV model prediction is in better agreement with the experiment. For the unstable operating condition, the peak-to-

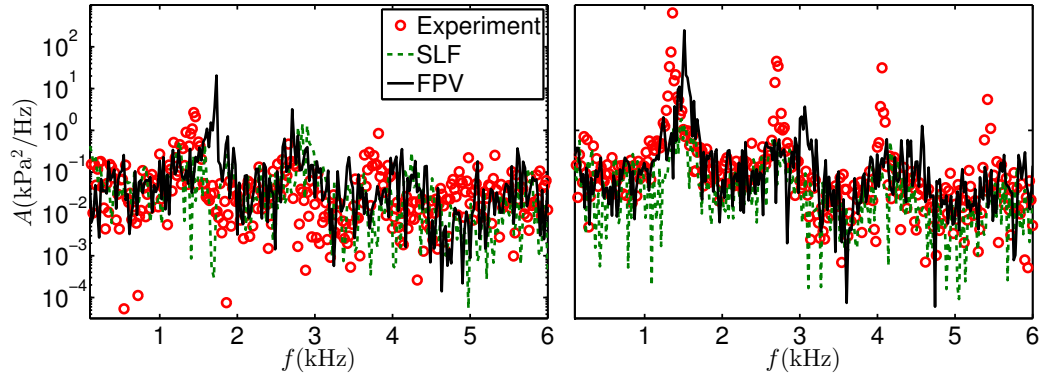


Figure 6.2.: PSD of raw pressure data at $x/D_{ox} = 18$ near the combustor wall for stable operating condition (left) and unstable operating condition (right). The model results are obtained by using the SLF model and the FPV model.

peak amplitude of the pressure oscillation for the FPV model is substantially higher than the SLF model and is in good agreement with the experiment. Figure 6.2 shows the PSD analysis for the predictions of the pressure by both the models for the two operating conditions. For the SLF model, the peaks are not distinct and it is difficult to identify the various modes specifically for the stable condition. The FPV model shows sharp distinct peaks for the first two modes.

In summary, for the stable operating condition, the predictions of the pressure fluctuation using the SLF model and FPV model is quite similar. For the unstable operating condition, the performance of the two models is significantly different. The SLF model significantly under predicts the peak-to-peak amplitude of the pressure fluctuation for the unstable operating condition and it predicts a stable condition. The FPV model is able to capture the amplitude of the peak-to-peak oscillations and the frequency and amplitude of the first mode quite accurately for the both operating conditions.

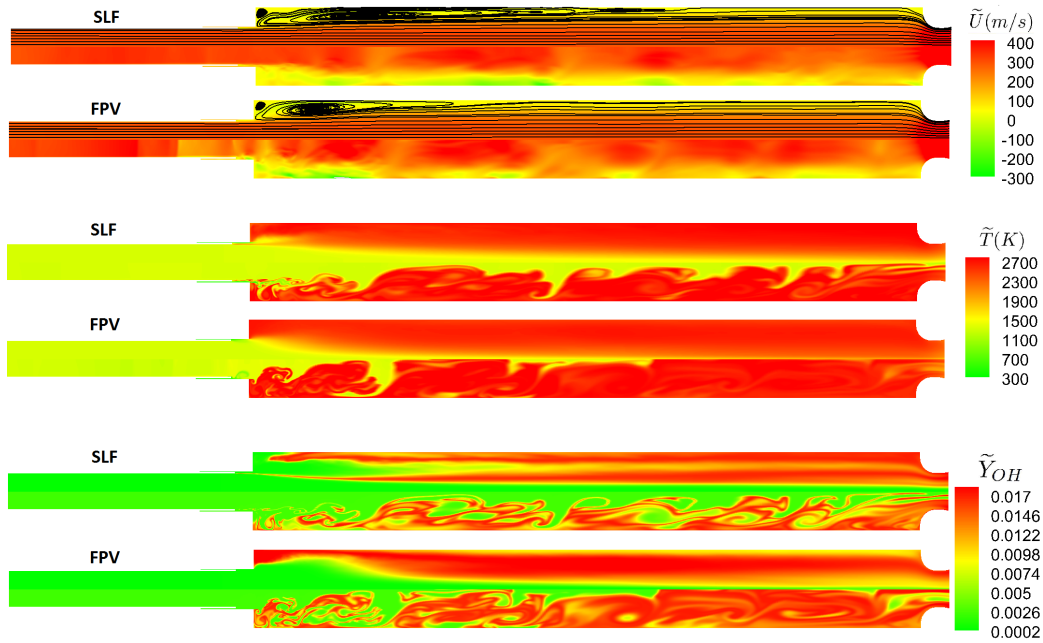


Figure 6.3.: Contour plots of the axial velocity \tilde{U} (with streamlines) (top), temperature \tilde{T} (middle) and the mass fraction of OH species (bottom) for the SLF model (top contour plot for each variable) and the FPV model (bottom contour plot for each variable) for the unstable operating condition. The upper half of each contour plot is the time-averaged result and the lower half is the instantaneous result.

6.1.3 Prediction of Flow Field and Scalars

To provide a better overview of the simulation results, here we briefly show the predictions of the flow field and thermo-chemical scalars. Figure 6.3 shows the contours of the time-averaged and instantaneous predictions of the axial velocity \tilde{U} , temperature \tilde{T} and the mass fraction of OH species for the SLF model and the FPV model for the unstable operating conditions. In the two contour plots for each variable, the first contour plot is the prediction of the SLF model and the second is the FPV model prediction. In each contour plot, the upper half represents the time-averaged result and the lower half represents the instantaneous prediction. The streamlines in the axial velocity contour plot help to identify the recirculation zone downstream of the

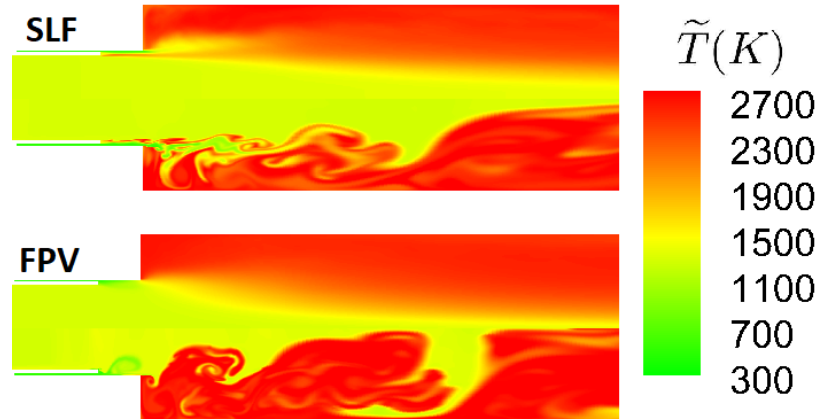


Figure 6.4.: Contour plot of temperature \tilde{T} near the dump plane for the SLF model (top contour plot) and the FPV model (bottom contour plot) for the unstable operating condition. The upper half of the contour plot is the time-averaged result and the lower half is the instantaneous result.

dump plane located at $x/D_{ox} = 0$. This recirculation zone stabilizes the flame in the combustor. It can be observed that the length of the recirculation zone for the SLF model is larger relative to the FPV model. This difference is caused by the substantial difference in the predicted flow and turbulence fields by using the two different models. In the simulation results for both the SLF and FPV models using the DES turbulence model, it is observed that the RANS model is used only in regions near the combustor wall while the LES model which resolves a part of the turbulence is used in critical regions of the combustor like the region just upstream of the dump plane where the fuel and oxidizer mix and downstream of the dump plane where the flame is anchored and there is a strong interaction between transient flame dynamics and thermo-acoustic instability.

For a better discussion of the results, the contour plot of temperature \tilde{T} in Figure 6.3 zoomed into the region near the dump plane and is shown in Figure 6.4. For the SLF model predictions, a high-temperature region is visible between the injector tip and dump plane which cannot be seen in the predictions of the FPV model. This

indicates the ignition of a mixture of fuel and oxidizer. In the SLF model, the flame is assumed to be always burning and there is no time delay between mixing of the fuel and the oxidizer, and ignition. In the model rocket combustor, the fuel and the oxidizer mix in the region between the injector tip and the dump plane. As a result, the SLF model predicts ignition in this region and it appears that the flame is stabilized at the injector tip. The FPV model is able to take into account the ignition delay and predicts ignition of the mixture of the fuel and oxidizer downstream of the dump plane. In this work, we use ignition delay to loosely describe the slow chemistry due to the finite rate effect.

For the SLF model, in the contour plot for the OH species, OH can be seen upstream of the dump plane as well where the fuel and oxidizer ignite and the flame is attached to the injector tip. The FPV model predicts the significantly higher concentration of OH just downstream of the dump plane in comparison to the SLF model.

To summarize, in Section 6.1 we compared the prediction of the SLF model and the FPV model with the experiment for a stable operating condition and an unstable operating condition of the model rocket combustor. For the stable operating condition, the peak-to-peak amplitude of the pressure fluctuation for both the models shows good agreement with the experiment. In the case of the unstable operating condition, the predictions of the two models are significantly different. Based on the level of thermo-acoustic instability $\langle P_{pp} \rangle / \langle P_c \rangle$, it is observed that the SLF model predicts stable operating condition for the unstable operating condition. The FPV model shows good agreement with the experiment for $\langle P_{pp} \rangle / \langle P_c \rangle$ (20% error) and frequency of the first mode f_1 (11% error). An intriguing question that arises from the results in this section is, what causes the dramatic difference in the performance of the SLF model and the FPV model under the different rocket operating conditions. This question will be answered in the following Section 6.2.

6.2 Parametric Studies of Modeling of Thermo-Acoustic instability

In Section 6.2.1, we aim to pinpoint the main reason for the drastic difference between the SLF model and the FPV model for the predictions of the unstable rocket operating condition, by introducing the FPV-B model which serves as an intermediate model between the SLF model and the FPV model. Then in Section 6.2.2, we study the effect of artificially amplifying the global Damkholer number (Da) on thermo-acoustic instability. Lastly in Section 6.2.3, we study the effect of neglecting turbulence-chemistry interactions on the thermo-acoustic instability in the model rocket combustor.

6.2.1 Effect of Transient Flame Dynamics

The difference in the predictions of the unstable operation condition by the SLF model and the FPV model in Section 6.1 is attributed to the difference of the models. Two major differences between the SLF model and the FPV model are: (A) the SLF model uses the scalar dissipation rate to parameterize the flamelet while the FPV model uses the progress variable; (B) the SLF model contains steady flamelet solutions along the stable burning branch of the S-curve while the FPV model includes flamelet solutions along the entire S-curve. Here we try to identify which modeling aspect difference is causing the dramatic difference in the performance of the two models for the unstable operating condition. To do that, we use the FPV-B model discussed in Section 3.2.3 as an intermediate model between the SLF model and the FPV model such that there is only one difference between the FPV model and the FPV-B model and between the SLF model and the FPV-B model. The only difference between the FPV model and the FPV-B model is the aforementioned difference (B), and the only difference between the SLF model and the FPV-B model is the above difference (A). Figure 6.5 (top row) shows the comparison of the predictions of instantaneous pressure fluctuations by the SLF, FPV and FPV-B models, measured at the axial location $x/D_{ox} = 18$ near the combustor wall for the unstable operating

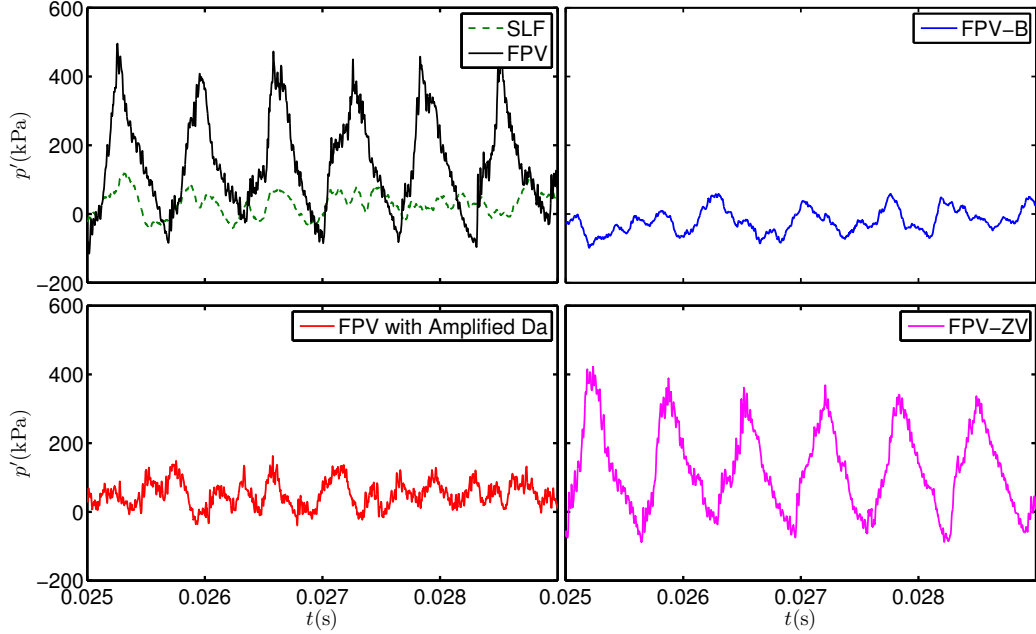


Figure 6.5.: Fluctuating pressure signal p' at $x/D_{ox} = 18$ near the combustor wall for unstable operating condition. The model results are obtained by using the SLF model and FPV model (top left), FPV-B model (top right), FPV model with amplified Damkohler number Da (bottom left) and FPV-ZV model (bottom right).

condition. The SLF and FPV models results are repeated from Figure 6.1 for easy comparison. It can be seen that the amplitude of the pressure oscillation predicted by the FPV-B model is similar to the SLF model. The level of thermo-acoustic instability $\langle P_{pp} \rangle / \langle P_c \rangle$ for the FPV-B model is given in Table 6.2 and it is close to the prediction of the SLF model. The frequency f_1 and amplitude A_1 of the first dominant mode for the FPV-B model is also very similar to the SLF model with a relative difference of around 1% and 15% in the prediction of f_1 and A_1 respectively. This comparison clearly indicates that the dramatic difference between the SLF model and the FPV model for the predictions of the unstable operating condition is mainly caused by the aforementioned difference (B). Arguably, by including flamelets along the entire S-curve, the FPV model is capable of capturing highly transient flame dynamics such as ignition delay, partially burning flame, flame extinction, and flame re-ignition. In

contrast, the SLF model always yields instantaneous burning following mixing and a well-burning flame throughout the combustor. The fact that the FPV model reproduces correctly the unstable operating condition while the SLF model cannot imply that the severe pressure fluctuations under the unstable operating condition in the model rocket combustor is closely related to the occurrence of highly transient flame dynamics in the combustor. This is an important finding to correlate thermo-acoustic instability to complicated transient flame dynamics. A thorough understanding of the effect of transient flame dynamics is expected to be critically important to the understanding of the fundamental mechanism of thermo-acoustic instability in practical gas turbine and rocket combustors. Fundamentally, transient flame dynamics such as ignition delay and local extinction is arguably caused by the strong coupling between turbulence and chemical kinetics, *i.e.*, there is no clear separation of turbulence time scale and chemical time scale and the Damkohler number (Da) is close to unity. To confirm this, in the following Section 6.2.2, we artificially amplify the Da number in the rocket combustion simulations and examine its effect on the thermo-acoustic instability predictions.

6.2.2 Effect of Artificial Amplification of Global Damkohler Number

The Da number is the ratio of the flow time scale to the chemical time scale. Artificially amplifying the Da number separates the turbulent flow from chemical kinetics and the flame becomes more mixing controlled. This means that there is a lower probability of observing transient flame dynamics and the flame has a higher probability of being close to the steady burning branch on the S-curve. In other words, by artificially amplifying the Da number for the entire combustor we largely reduce the possibility of transient flame dynamics such as ignition delay and local extinction. As a result, we can examine the role of these flame dynamics in producing the thermo-acoustic instability in the rocket combustor.

To determine a global Da number, we need to define a flow time scale and chemical time scale. For the flow time scale τ_f , we use the mean inlet velocity for the fuel and oxidizer streams and the entire length of the combustor when the oxidizer post length is $L_{ox} = 13.97$ cm corresponding to the unstable operating condition. Based on this, the flow time scale is $\tau_f \approx 0.004$ s. The chemical time scale τ_c is determined as the inverse of the extinction scalar dissipation rate χ_q (point B in Figure 3.1). For the model rocket combustor $\chi_q = 2668.18 \text{ s}^{-1}$ so that $\tau_c = 1/2668.18 \approx 0.0004$ s. The global Da number is then $Da = \tau_f/\tau_c \approx 10$. We now amplify Da by scaling up the reaction source term $\tilde{\omega}_c$ in Equation (4.10) by a large factor say 10^5 . Scaling the reaction source term is equivalent to decreasing the chemical time scale which increases the Da number.

The bottom left plot of Figure 6.5 shows the predicted pressure fluctuation signal by the FPV model with the amplified global Da number for the unstable operating condition. It can be observed that pressure oscillations are significantly damped when the global Da number is scaled by a factor of 10^5 in comparison to the FPV model without tuning in the top left plot of Figure 6.5. By amplifying artificially the Da number, we can largely reduce the occurrence of highly transient flame dynamics such as ignition delay and local extinction. This causes the stabilization of the thermo-acoustic instability in the rocket combustor. This study provides further support to the important role of transient flame dynamics in the generation of the thermo-acoustic instability.

6.2.3 Effect of Neglecting Mixture Fraction Fluctuations

The transient flame dynamics discussed in Section 6.2.2 is the result of strong turbulence-chemistry interactions. In this section, we continue to examine the effect of turbulence-chemistry interactions on thermo-acoustic instability predictions from a slightly different angle point of view. We neglect the mixture fraction fluctuations ($\widetilde{\xi''^2} = 0$) in the FPV model (FPV-ZV model in Section 3.2.4), *i.e.*, a presumed δ -

PDF is used for mixture fraction. This means the mean (or filtered) reaction rate of the progress variable is the reaction rate evaluated at the mean (or filtered) mixture fraction $\tilde{\xi}$ and progress variable \tilde{C} . This is equivalent to a laminar chemistry model that is widely used for the rocket thermo-acoustic instability study [65, 79, 85], in which case the complicated turbulence-chemistry interactions is modeled through the interaction between the mean (or filtered) turbulence fields and chemical kinetics.

The predictions of the pressure fluctuation inside the combustor with the FPV-ZV model are shown in the bottom plot of Figure 6.5. The level of thermo-acoustic instability $\langle P_{pp} \rangle / \langle P_c \rangle$ with the FPV-ZV model is given in Table 6.2 and it can be seen that there is not a significant difference in comparison to the value of $\langle P_{pp} \rangle / \langle P_c \rangle$ for the FPV model. The frequency f_1 for the FPV-ZV model is slightly higher (relative difference 4%) in comparison to the FPV model and the amplitude A_1 for the FPV-ZV model is lower compared to the FPV model by around 44%. This indicates that the thermo-acoustic instability is hardly affected by the fluctuating part contributing to the mean (or filtered) chemical reaction rate in the rocket combustor simulations.

To sum up, in Section 6.2, we conduct parametric studies to identify the exact source of difference that caused the dramatic different performance of the SLF model and the FPV model for the unstable rocket operation condition. It is found that the occurrence of highly transient flame dynamics and its inclusion in the modeling can make a dramatic difference in the modeling results. This indicates the importance of accurate modeling of turbulence-chemistry interactions in the modeling of turbulent combustion in rocket combustor since highly transient flame dynamics is the result of turbulence-chemistry interactions. Other aspects of turbulence-chemistry interactions are also investigated such as the effect of Da number and neglecting scalar fluctuations in the evaluation of mean (or filtered) chemical reaction rate. These findings are important to understanding the overall combustion dynamics and its global coupling with thermo-acoustic instability in the rocket combustor. In the following Section 6.3, we delve into a more detailed level analysis of the effect of transient flame dynamics and its interactions with the thermo-acoustic instability by using the FPV model.

6.3 Examination of Transient Flame Dynamics

From Section 6.2, we have demonstrated the global effect of transient flame dynamics on the predictions of thermo-acoustic instability. In the following Section 6.3.1, we attempt to localize this effect by examining local flame dynamic events on the overall instability, in order to gain deeper insights into the effect of flame dynamics. Meanwhile, it is noted that the thermo-acoustic instability in the rocket combustor under unstable operating condition is self-excited and sustainable [76]. It is hypothetically possible that the produced thermo-acoustic instability can impact the flame dynamics which in turn can fuel the instability development. This hypothesis will be examined in Section 6.3.2.

6.3.1 Effect of Local Dynamic Flame Events on Thermo-Acoustic Instability

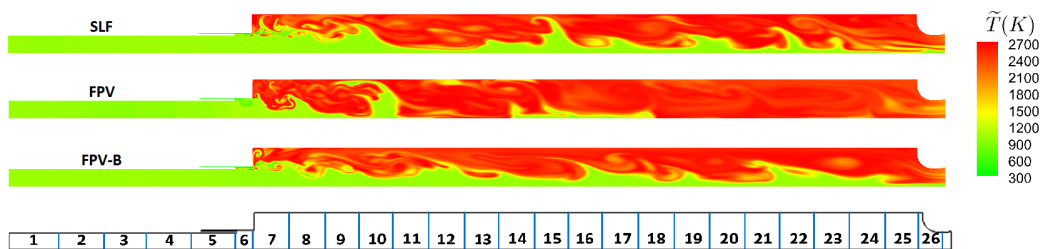


Figure 6.6.: Contour plots of the instantaneous temperature \tilde{T} for the SLF model, FPV model and FPV-B model. The bottom plot shows the 26 computational bins into which the combustor computational domain is divided.

To identify the local flame dynamics in the rocket combustor, we divide the computational domain of the combustor into 26 bins as shown in the bottom plot in Figure 6.6 where the contour plots are shown for the instantaneous temperature \tilde{T} with the SLF model, FPV model, and FPV-B model. Overall, the results for all the three models are qualitatively close to each other, with the difference mainly evident in the region near the dump plane. Figure 6.7 further shows the temperature contour

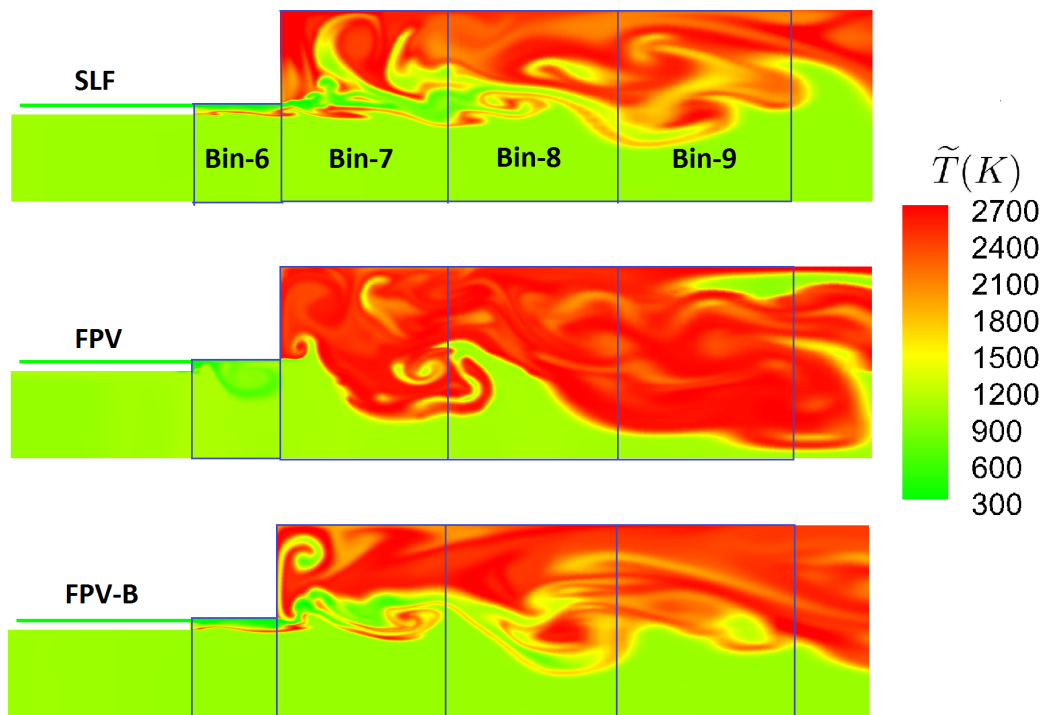


Figure 6.7.: Zoomed-in view of contour plots of the instantaneous temperature \tilde{T} for Bin-6, Bin-7, Bin-8 and Bin-9 for the SLF model, FPV model and FPV-B model.

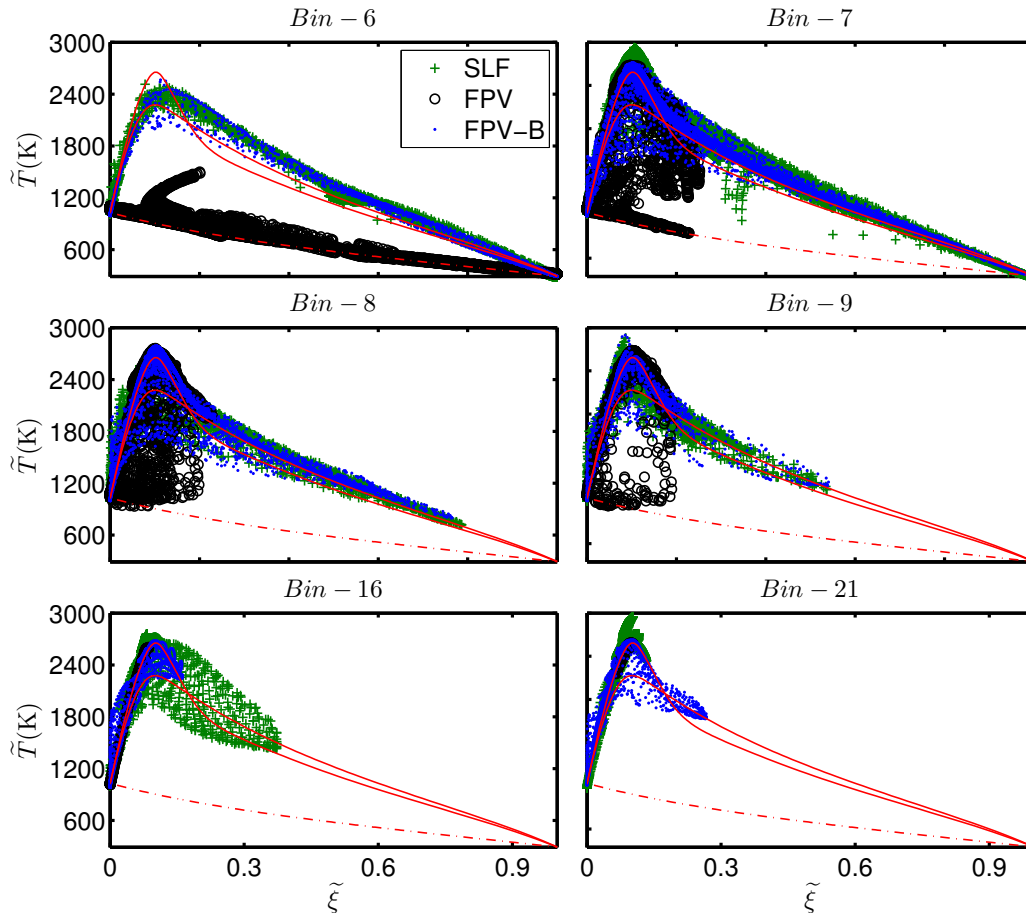


Figure 6.8.: Scatter plot of the instantaneous temperature \tilde{T} against mixture fraction $\tilde{\xi}$ for Bin-6, Bin-7, Bin-8, Bin-9, Bin-16 and Bin-21 for unstable operating condition. The model results are obtained using the SLF model, FPV model and FPV-B model. The red solid lines indicate the burning flamelet solutions for a near-equilibrium condition $\tilde{\xi}''^2 = 0$, $\chi_{st} = 0.1 \text{ s}^{-1}$, $\bar{p} = 1.5 \text{ MPa}$ and close to extinction limit condition $\tilde{\xi}''^2 = 0$, $\chi_{st} = 2668.18 \text{ s}^{-1}$, $\bar{p} = 1.5 \text{ MPa}$. The red dash-dotted lines indicate pure mixing between fuel and oxidizer for the condition $\tilde{\xi}''^2 = 0$, $\chi_{st} = 2668.18 \text{ s}^{-1}$, $\bar{p} = 1.5 \text{ MPa}$.

plots zoomed into the region near the dump plane where Bin-6 to Bin-9 are located, and the biggest difference between the FPV, SLF and FPV-B models is observed in Bin-6 where the temperature predicted by the FPV model is significantly lower in

comparison to the SLF and FPV-B models. This difference is due to the fact that the FPV model takes into account ignition delay whereas the SLF model and the FPV-B model assume instantaneous burning as soon as the fuel and oxidizer mix.

In order to identify the transient local dynamic flame events in a single bin, we examine the scatter plot for temperature \tilde{T} against mixture fraction $\tilde{\xi}$ for the different bins. Figure 6.8 compares the scatter plot for the three models in each bin from Bin-6 to Bin-9, and Bin-16 and Bin-21. Two flamelet solutions along the steady burning branch of the S-curve corresponding to near-equilibrium limit $\chi_{st} = 0.1 \text{ s}^{-1}$ (close to point A on the S-curve) and extinction limit $\chi_{st} = 2668.18 \text{ s}^{-1}$ (point B on the S-curve) for $\tilde{\xi}^{n^2} = 0$ and $\bar{p} = 1.5 \text{ MPa}$ are shown as solid lines in the each scatter plot as references. The pure mixing line which indicates mixing between the fuel and oxidizer without reaction can also be seen in the figure as dash-dotted lines. We can see that from Bin-6 to Bin-9, the predictions of the SLF model and the FPV-B model are quite similar and are significantly different from the predictions of the FPV model. In Bin-6, for the FPV model, it can be seen that the majority of the points lie close to the pure mixing line and this is because the FPV model takes into account ignition delay. Since the SLF model and the FPV-B model neglect ignition delay, most of the data points for these two models lie away from the mixing line and near the two reference flamelet solutions. In Bin-7, Bin-8, and Bin-9 which are just downstream of the dump plane, for the FPV model, the number of points that lie around the pure mixing line decreases successively indicating that more amount of unburned mixture of fuel and oxidizer gets ignited as we move downstream of the dump plane. The transient flame dynamics involving ignition delay become less significant as we move downstream and for Bin-16 and Bin-21, the FPV model predictions are qualitatively close to the SLF model and FPV-B model, although some subtle difference exists. Given the fact that the main difference between results of the FPV model and the SLF model (and FPV-B model) is the predictions of the ignition delay, it becomes evident that the ignition delay, which appears as a local dynamic flame event, is mainly responsible for the cause of the strong thermo-acoustic instability in the unstable operating condition

of the model rocket combustor. With this local flame event eliminated, the thermo-acoustic instability is significantly reduced. This conclusion is potentially useful for developing new control approaches for mitigating thermo-acoustic instability.

6.3.2 Effect of Thermo-Acoustic Instability on Transient Flame Dynamics

In Section 6.3.1, we have found that the occurrence of transient flame dynamics can affect thermo-acoustic instability by interrogating the results with different models. An interesting question arises which is, whether the thermo-acoustic instability can reversely affect the transient flame dynamics. To answer this question, we examine the temporal evolution of local dynamic flame events in different bins when the pressure wave passes through these bins. Here we analyze the effect of thermo-acoustic instability on the flame dynamics by looking at the temperature scatter plot in the different bins for different instances of time.

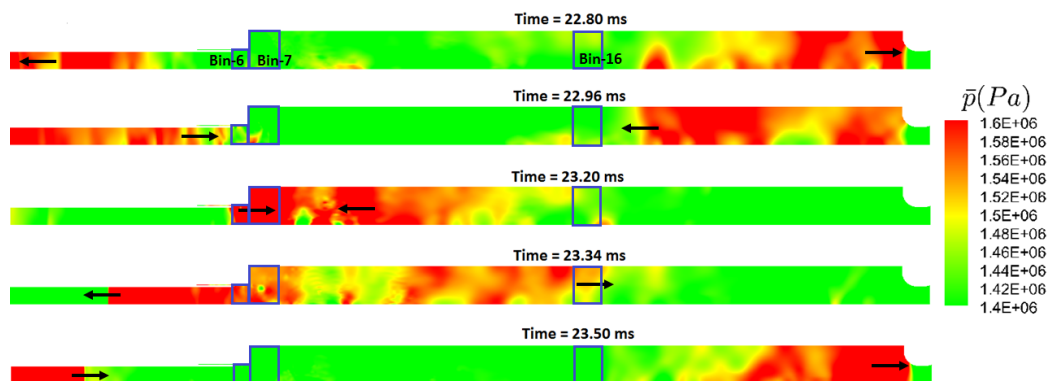


Figure 6.9.: Contour plots of instantaneous pressure \bar{p} at different times for the unstable operating condition. The model results are obtained by using the FPV model.

Figure 6.9 shows the contours of the instantaneous pressure \bar{p} inside the model rocket combustor at different instances of time for the unstable operating condition obtained by using the FPV model. The thermo-acoustic instability in the rocket combustor gives rise to two pressure waves, one wave propagates inside the main

combustion chamber and the other wave propagates inside the oxidizer post. At Time = 22.80 ms, the pressure wave in the combustion chamber is propagating towards the right and the pressure wave in the oxidizer post is propagating towards the left. These two waves reflect from the choked nozzle and the choked oxidizer inlet respectively and meet just downstream of the dump plane at Time = 23.20 ms. After this, the two pressure waves again propagate through the combustion chamber and the oxidizer post as can be seen in the last two plots of Figure 6.9 and this process cycles over and over again.

We next look at the effect of the propagating pressure waves on the instantaneous temperature \tilde{T} for an individual bin. Figure 6.10 shows the scatter plot of \tilde{T}

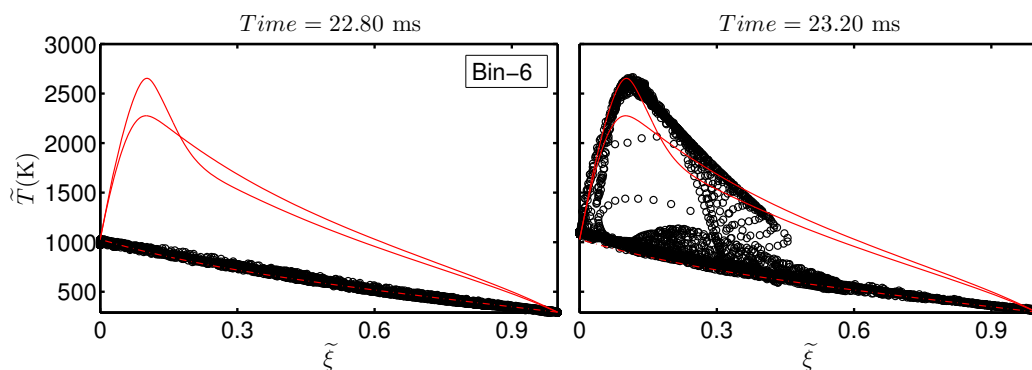


Figure 6.10.: Scatter plot of the instantaneous temperature \tilde{T} against mixture fraction $\tilde{\xi}$ in Bin-6 when pressure wave inside the combustion chamber is far away from the bin (left) and when it passes through the bin (right). The red solid lines indicate the burning flamelet solutions for a near-equilibrium condition $\tilde{\xi}''^2 = 0$, $\chi_{st} = 0.1 \text{ s}^{-1}$, $\bar{p} = 1.5 \text{ MPa}$ and close to extinction limit condition $\tilde{\xi}''^2 = 0$, $\chi_{st} = 2668.18 \text{ s}^{-1}$, $\bar{p} = 1.5 \text{ MPa}$. The red dash-dotted lines indicate pure mixing between fuel and oxidizer for the condition $\tilde{\xi}''^2 = 0$, $\chi_{st} = 2668.18 \text{ s}^{-1}$, $\bar{p} = 1.5 \text{ MPa}$. The model results are obtained using the FPV model for the unstable operating condition.

against $\tilde{\xi}$ in Bin-6 at Time = 22.80 ms and Time = 23.20 ms. At Time = 22.80 ms, the two pressure waves in the combustor are far away from Bin-6 and all the points lie close to mixing line indicating that the mixture of fuel and oxidizer is

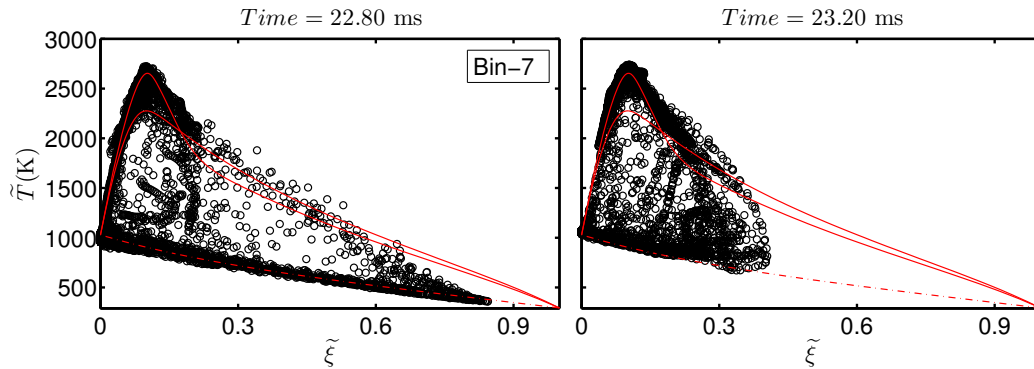


Figure 6.11.: Scatter plot of the instantaneous temperature \tilde{T} against mixture fraction $\tilde{\xi}$ in Bin-7 when pressure wave inside the combustion chamber is far away from the bin (left) and when it passes through the bin (right). The red solid lines indicate the burning flamelet solutions for a near-equilibrium condition $\tilde{\xi}''^2 = 0$, $\chi_{st} = 0.1 \text{ s}^{-1}$, $\bar{p} = 1.5 \text{ MPa}$ and close to extinction limit condition $\tilde{\xi}''^2 = 0$, $\chi_{st} = 2668.18 \text{ s}^{-1}$, $\bar{p} = 1.5 \text{ MPa}$. The red dash-dotted lines indicate pure mixing between fuel and oxidizer for the condition $\tilde{\xi}''^2 = 0$, $\chi_{st} = 2668.18 \text{ s}^{-1}$, $\bar{p} = 1.5 \text{ MPa}$. The model results are obtained using the FPV model for the unstable operating condition.

unburned. At Time = 23.20 ms, the pressure waves reach Bin-6 and burning events are observed. It appears that the passing pressure wave tends to promote ignition because of the reduced ignition delay due to the increased residence time caused by the pressure wave. Similar observation is made for Bin-7 in Figure 6.11 which shows the temperature scatter plot for Bin-7 for the two instances of time. At Time = 22.80 ms, when the two pressure waves in the combustor are away from Bin-7, the data points in the scatter plot lie within a range of the mixture fraction $0 < \tilde{\xi} < 0.8$ and the mixture seems to be ignited. When the pressure waves pass through the bin at Time = 23.20 ms, the range of $\tilde{\xi}$ is significantly reduced to $0 < \tilde{\xi} < 0.4$. The reduction in the range of the mixture fraction indicates that the fuel is being consumed due to reduction in ignition delay which is promoted by the presence of the pressure wave. Further downstream in Bin-16, where the transient flame dynamics are not present, the presence of the passing pressure wave does not have a significant

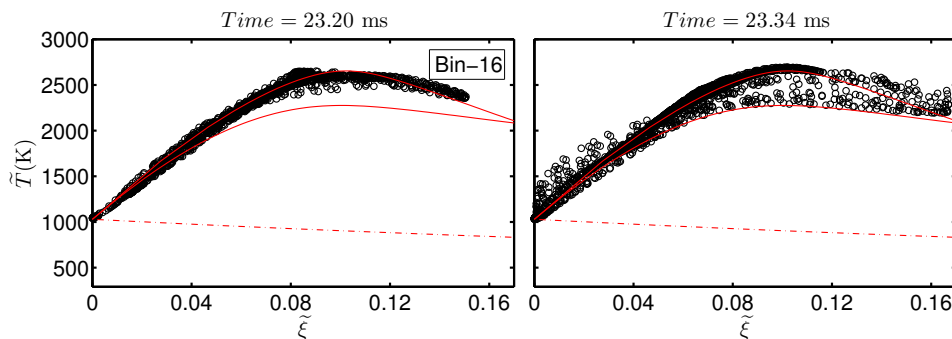


Figure 6.12.: Scatter plot of the instantaneous temperature \tilde{T} against mixture fraction $\tilde{\xi}$ in Bin-16 when pressure wave inside the combustion chamber is far away from the bin (left) and when it passes through the bin (right). The red solid lines indicate the burning flamelet solutions for a near-equilibrium condition $\tilde{\xi}''^2 = 0$, $\chi_{st} = 0.1$ s⁻¹, $\bar{p} = 1.5$ MPa and close to extinction limit condition $\tilde{\xi}''^2 = 0$, $\chi_{st} = 2668.18$ s⁻¹, $\bar{p} = 1.5$ MPa. The red dash-dotted lines indicate pure mixing between fuel and oxidizer for the condition $\tilde{\xi}''^2 = 0$, $\chi_{st} = 2668.18$ s⁻¹, $\bar{p} = 1.5$ MPa. The model results are obtained using the FPV model for the unstable operating condition.

impact on temperature versus mixture fraction scatter plot as can be seen in Figure 6.12. For both the time instances, the scatter plot is quite similar in terms of range of $\tilde{\xi}$ and the distribution of the data points of the scatter plot. The results suggest that the thermo-acoustic instability (in terms of the propagating pressure wave) affect the transient flame dynamics. In particular, the ignition delay time is reduced when the pressure wave passes through to increase the residence time of the fuel/oxidizer mixture so that they have more time to burn before moving downstream.

The two-way coupling between the transient flame dynamics and the thermo-acoustic instability observed above provides a plausible mechanism of the self-excited and sustained thermo-acoustic instability in the combustor. The occurrence of ignition delay due to the strong interactions between turbulent mixing and finite-rate chemical kinetics can cause thermo-acoustic instability as evidenced in Section 6.1. The produced instability is observed to alter the fluid flow in terms of the residence

time which consequently reduces the ignition delay time so that the mixed fuel and oxidizer burn more rapidly. The rapid burn produces more heat release which plausibly, in turn, fuels the thermo-acoustic instability to sustain in the combustor. The identification of this two-way coupling provides an unprecedented new understanding of thermo-acoustic instability observed in rocket combustors.

In the next chapter, we look at predictions of the EMCF method on a wide variety of test-cases including thermo-acoustic instability modeling of the model rocket combustor.

7. TRANSPORTED PDF MODELING OF COMPRESSIBLE TURBULENT REACTIVE FLOWS BY USING THE EULERIAN MONTE CARLO FIELDS METHOD

In the framework of the PDF-EMCF method, in Chapter 3 and Chapter 4 we discussed different physical models and numerical implementation schemes which can be summarized as:

1. Mixing models: IEM and IPEM mixing models
2. EMCF consistency methods: EMCF-O, EMCF-M and EMCF-C2 methods
3. Density formulations: Density 1 and Density 2
4. Implementation of mixing models: Analytical and Euler implementations
5. Gradient limiters for Wiener term

It is possible to have different combinations of the models and implementations when using the EMCF method. In this chapter we demonstrate the effect of using a few of the combinations which we believe have significant impact on the predictions. We consider a wide variety of flows ranging from a one-dimensional turbulent mixing layer problem, to subsonic and supersonic canonical jet flows and flames and lastly a laboratory-scale model rocket combustor.

7.1 One-Dimensional Turbulent Mixing Layer

For the first test case, we consider a single-scalar, constant density turbulent mixing layer in forced homogenous isotropic turbulence. We conduct RANS simulations

of the mixing layer by modeling the mixing layer as a statistically one-dimensional and transient. The parameters used to specify the mixing-layer are shown in Table 7.1. The initial condition of the filtered of the scalar $\tilde{\phi}$ is,

Table 7.1.: Parameters for one-dimensional turbulent mixing layer.

Parameter	Value
Density $\bar{\rho}$	1.0 kg/m ³
Kinematic Viscosity ν	1.65×10^{-5} m ² /s
Turbulent Kinetic Energy k	5×10^{-4} m ² /s ²
Reynolds Number Re	20
Turbulent kinetic energy dissipation rate $\epsilon = 2k^2/(3\nu Re)$	5.0505×10^{-4} m ² /s ³
Turbulent eddy viscosity $\nu_t = 0.09k^2/\epsilon$	4.455×10^{-5} m ² /s
Molecular Schmidt number Sc	0.7
Turbulent Schmidt Number Sc_t	0.9
Molecular Diffusivity $\Gamma = \nu/Sc$	2.3571×10^{-5} m ² /s
Turbulent Diffusivity $\Gamma_t = \nu_t/Sc_t$	4.95×10^{-5} m ² /s
Mixing constant C_ϕ	2.0
Scalar mixing frequency $\omega = C_\phi\epsilon/(2k)$	1.0101 s ⁻¹
Simulation end time t_e	9×10^{-3} s

$$\tilde{\phi} = \frac{\tilde{\phi}_R - \tilde{\phi}_L}{2} \left[1 + \operatorname{erf} \left(\frac{x}{2\sqrt{(\Gamma + \Gamma_t)t_0}} \right) \right], \quad (7.1)$$

where the $\tilde{\phi}_R$ and $\tilde{\phi}_L$ denote values of the scalar ϕ at the right and left boundaries respectively, $\operatorname{erf}(\cdot)$ is the error function and $t_0 = 0.01$ s is a reference time. The initial variance for the scalar $\tilde{\phi}^2$ is zero. The simulation is run from $t = 0$ to $t = t_e$. A uniform grid with 400 grid cells is used. Figure 7.1 compares the predictions of the scalar mean $\langle \phi \rangle$, scalar root mean square (RMS) ϕ_{RMS} , scalar skewness ϕ_γ

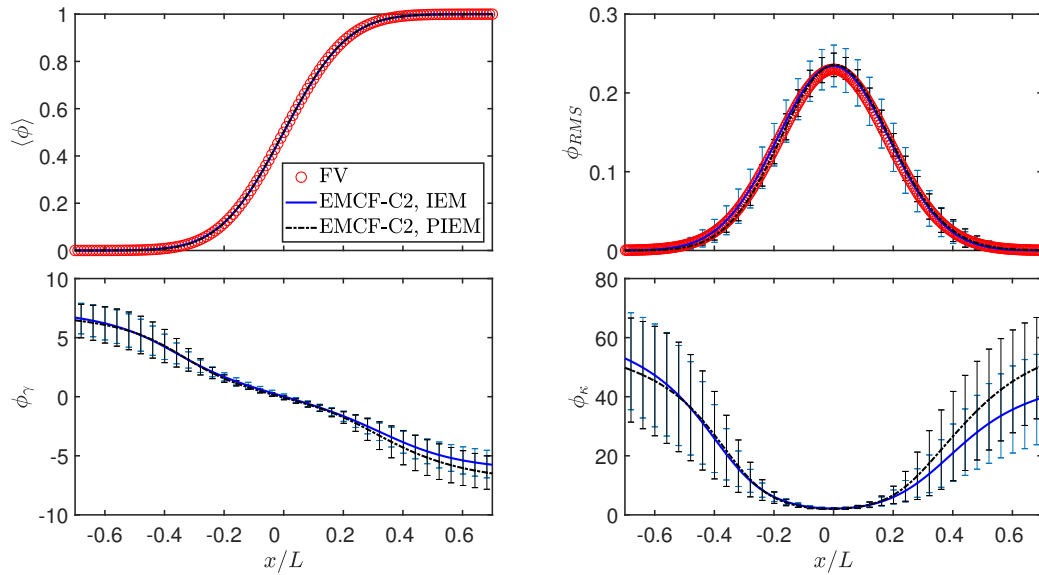


Figure 7.1.: The predicted profiles of the scalar mean $\langle \phi \rangle$, scalar RMS ϕ_{RMS} , scalar skewness ϕ_γ and scalar kurtosis ϕ_κ for the single-scalar turbulent mixing layer by using the FV approach and IEM and IPEM mixing models.

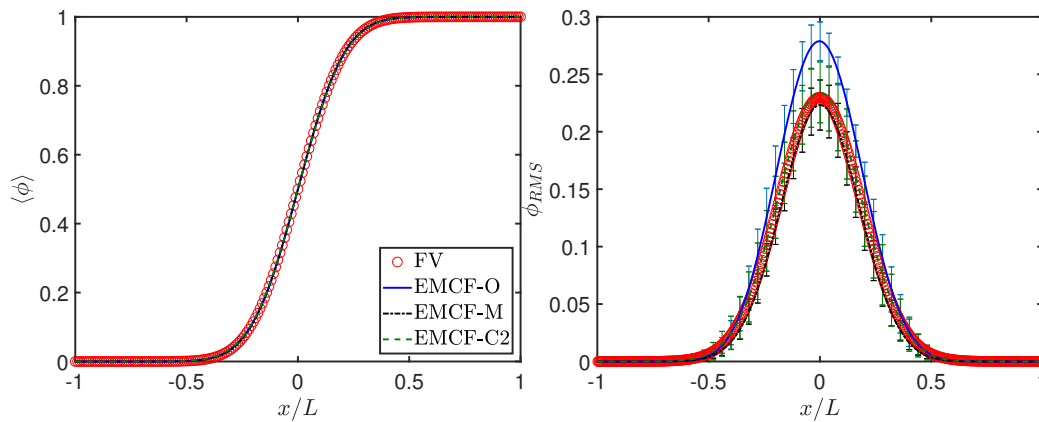


Figure 7.2.: The predicted profiles of the scalar mean $\langle \phi \rangle$ and scalar RMS ϕ_{RMS} for the single-scalar turbulent mixing layer by using the FV approach and EMCF-O, EMCF-M and EMCF-C2 methods.

and scalar kurtosis ϕ_κ for the IEM and IPEM mixing models with a reference finite-volume (FV) approach solution. The simulation results with the EMCF method are

obtained using Density 2 formulation with analytical implementation of the mixing models and without considering the effect of the gradient limiters for the Wiener term for stagnation enthalpy and species by setting them to 1. For each of the mixing model, we conducted the numerical simulations with number of fields $N_{sf} = 64$ and 10 simulation trials. The error bars indicate 95% confidence interval based on the simulation trials. From the figure we can see that the predictions of $\langle\phi\rangle$ and ϕ_{RMS} are very similar for both the mixing models and compare well with the FV solution. The maximum relative difference between the predicted value of ϕ_{RMS} for the FV solution and both the mixing models is around 2%. The scalar skewness ϕ_γ and scalar kurtosis ϕ_κ are the third and fourth moments of ϕ respectively, and are defined as $\phi_\gamma = 1/N_f \sum_{n=1}^{N_f} [(\phi^n - \langle\phi\rangle)/\phi_{RMS}]^3$ and $\phi_\kappa = 1/N_f \sum_{n=1}^{N_f} [(\phi^n - \langle\phi\rangle)/\phi_{RMS}]^4$. For the predictions of ϕ_γ and ϕ_κ using the two different mixing models, we do observe slight difference and the maximum relative difference in the predicted ϕ_κ is about 25%.

In Figure 7.2 we observe the predicted profiles of $\langle\phi\rangle$ and ϕ_{RMS} for EMCF-O, EMCF-F and EMCF-C2 methods with analytical implementation of the IEM model using Density 2 formulation and without the gradient limiters. For $\langle\phi\rangle$, predictions for all the three methods overlap. The EMCF-O method over predicts the peak value of ϕ_{RMS} by more than 20% in comparison to the FV solution while the EMCF-M method slightly under predicts by 3%. The EMCF-C2 method shows the best agreement with the FV solution in terms of the peak value (relative error 1.5%) and the profile of ϕ_{RMS} . These observations are consistent with those made by Wang et al. [114].

For this test case, we did not observe significant difference in the predictions for the two different density formulations, implementations of the mixing models and the effect of using gradient limiters.

7.2 Subsonic Non-Reactive Propane Round Jet

The turbulent mixing layer discussed in Section 7.1 is a highly simplified academic test case with many assumptions such as homogeneous turbulence and constant density. In this section we consider a more realistic test case, a laboratory scale variable density non-reactive round jet. Scalar measurements for the jet were carried out by Schefer et al. [143] and the flow field was measured by Schefer et al. [144]. The experiment consists of round jet of propane and coflow of air. The Reynolds number for the propane jet is $Re = 68,000$ based on a bulk velocity \tilde{U}_b of 53 m/s jet diameter $D = 5.26\text{mm}$. The velocity of the coflow air is 9.2 m/s. We conduct 2D axisymmetric simulations of the round jet. The computational grid has around 10,000 and is finalized based on grid convergence studies. For the EMCF method, we select $N_{sf} = 8$ and a value of $C_\phi = 3.0$.

Table 7.2.: Inlet conditions for the numerical simulations of the subsonic turbulent round jet based on experiment [143].

Parameter	Fuel Jet	Coflow
$\tilde{U}_b(\text{m/s})$	53	9.2
$\tilde{T}(\text{K})$	294	294
$\tilde{Y}_{C_3H_8}$	1.0	0.0
\tilde{Y}_{O_2}	0.0	0.233
\tilde{Y}_{N_2}	0.0	0.767

We first analyze the effect of using different mixing models and the EMCF consistency methods on the predictions of the mean axial velocity \tilde{U} , mean mixture fraction $\tilde{\xi}$ and mixture fraction RMS ξ_{RMS} . Figure 7.3 shows the predictions of these quantities at three different axial locations $x/D = 15, 30$ and 50 along with the centerline profile for the EMCF-O method and the EMCF-C2 method with analytical

IEM model, EMCF-O method with analytical IPEM model and EMCF-O method with Euler IEM model. Density 2 formulation and gradient limiters are used for all the predictions. The predictions of the EMCF-M method with both the mixing models is quite similar to the EMCF-O and EMCF-C2 methods and hence the EMCF-M method results are not included in Figure 7.3. We can observe that there is not significant difference in the predictions of \tilde{U} and $\tilde{\xi}$ for the four different simulations and all the simulations show good agreement with the experiment. For ξ_{RMS} , we do see some difference between the four simulations and the maximum relative difference among the four simulations is close to 8%. The mixture fraction skewness ξ_γ and mixture fraction kurtosis ξ_κ predictions shown in Figure 7.4 also show difference among the four simulations. However we do not observe a particular simulation showing the best agreement with the experiments at all the locations.

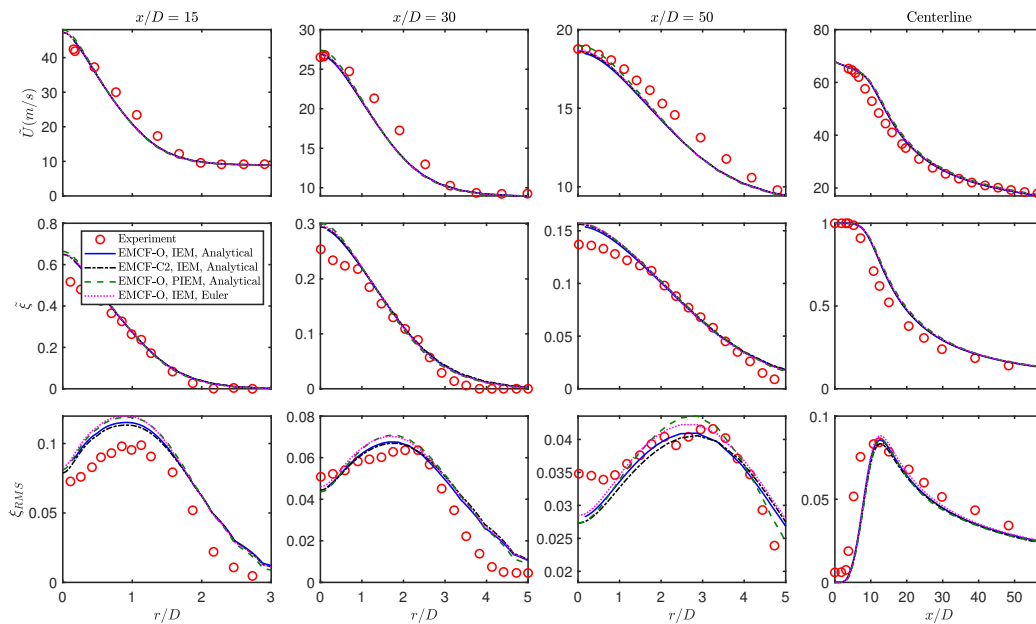


Figure 7.3.: Radial profile of mean velocity \tilde{U} , mean mixture fraction $\tilde{\xi}$ and mixture fraction RMS ξ_{RMS} at the axial locations $x/D = 15, 30$ and 50 along with the centerline profile for the propane round jet test case for the EMCF-O method and EMCF-C2 method with analytical IEM model, EMCF-O method with analytical IPEM model and EMCF-O method with Euler IEM model.

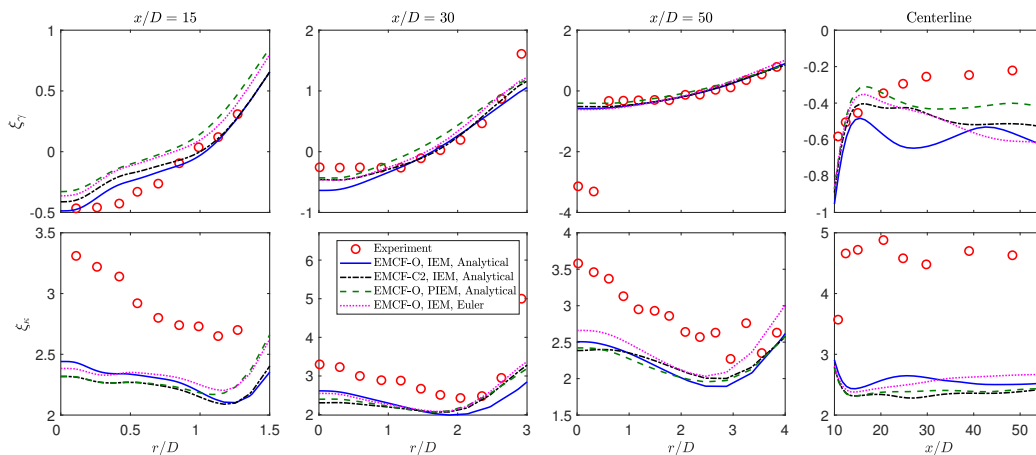


Figure 7.4.: Radial profile of mixture fraction skewness ξ_γ and mixture fraction kurtosis ξ_κ at the axial locations $x/D = 15, 30$ and 50 along with the centerline profile for the propane round jet test case for the EMCF-O method and EMCF-C2 with analytical IEM model, EMCF-O method with analytical IPEM model and EMCF-O method with Euler IEM model.

To examine the effect of the density formulation and gradient limiter, we now select the EMCF-O method with the analytical IEM mixing model and conduct three simulations, the first simulation with Density 1 formulation and with the gradient limiters, second simulation with Density 2 formulation and with gradient limiters and the last simulation with Density 2 and without gradient limiters. Figure 7.5 compares the predicted profiles of \tilde{U} , $\tilde{\xi}$ and ξ_{RMS} for the three simulations. In general we can observe that although we do not observe any evident difference between the predicted profiles of \tilde{U} and ξ_{RMS} for the three simulations, while for ξ_{RMS} Density 2 shows slightly better agreement with the experiment in terms of the radial profile. In summary, in this section we examined the effect of the different mixing models and their implementation, EMCF-C2 method, and the two different density formulations coupled with gradient limiter for a round propane jet case. We observed that the IEM and IPEM mixing models and their implementation along with the EMCF-C2 method does not have significant impact on the predictions. The effect of density formulation is slightly more pronounced with Density 2 formulation being more accurate than

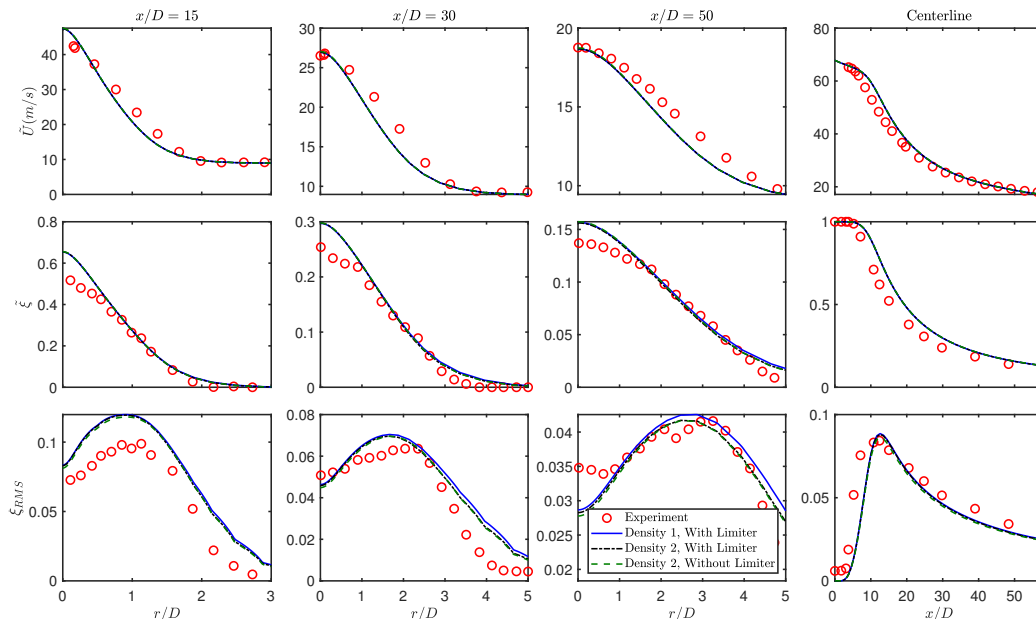


Figure 7.5.: Radial profile of mean velocity \tilde{U} , mean mixture fraction $\tilde{\xi}$ and mixture fraction RMS ξ_{RMS} at the axial locations $x/D = 15, 30$ and 50 along with the centerline profile for the propane round jet test case for the Density 1 with gradient limiter, Density 2 with gradient limiter and Density 2 without gradient limiter.

Density 1. In the following section we continue examining the effect of the different physical models and numerical implementations by considering a more challenging test case, a turbulent jet flame.

7.3 Subsonic Turbulent Jet Flame

In this section we increase the complexity of the test cases by considering a subsonic, incompressible lifted turbulent jet flame with the fuel jet issuing into a coflow of hot products of lean combustion. The burner was developed by Cabra et al. [145] to study complicated lifted flames which may be autoigniting. In this study we consider the experiment with H_2/N_2 as the fuel. The jet diameter is $D = 4.57$ mm and the Reynolds number is $Re = 23,600$. Additional details of the experiment can be found in Cabra et al. [145].

We assume axisymmetry for the numerical simulations of the jet flame to reduce the computational cost and conduct RANS simulations. The total number of cells in the computational domain is close to 12,000. The inflow conditions for the fuel jet and the coflow based on the experiment [145] are given in Table 7.3. The Li detailed mechanism [146] with 10 species and 21 reactions is used. For all the simulations we specify the number of stochastic fields $N_{sf} = 8$ and the mixing constant $C_\phi = 2.0$. We first look at the predictions of the EMCF-O, EMCF-M and EMCF-C2

Table 7.3.: Inlet conditions for the numerical simulations of the subsonic turbulent jet flame based on experiment [145].

Parameter	Fuel Jet	Coflow
$\tilde{U}_b(\text{m/s})$	107	3.5
$\tilde{T}(\text{K})$	305	1033
\tilde{Y}_{H_2}	0.0233	0.0
\tilde{Y}_{O_2}	0.0	0.17
\tilde{Y}_{H_2O}	0.07	0.0
\tilde{Y}_{N_2}	0.9767	0.76

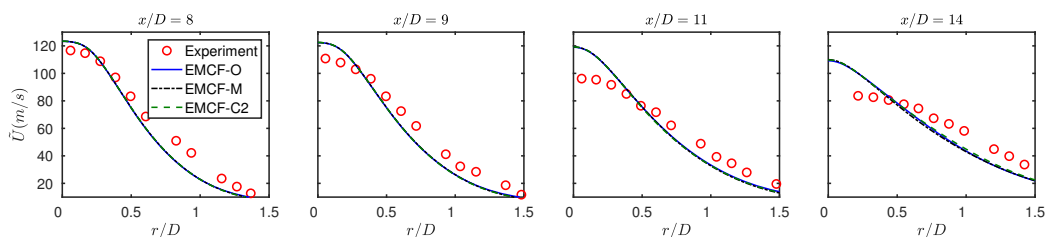


Figure 7.6.: Radial profile of mean axial velocity \tilde{U} at the axial locations $x/D = 8, 9, 11$ and 14 for Cabra flame for the EMCF-O, EMCF-M and EMCF-C2 methods.

methods using the analytical IEM mixing model with Density 2 formulation and the gradient limiters. Figure 7.6 compares the predictions of the mean axial velocity \tilde{U}

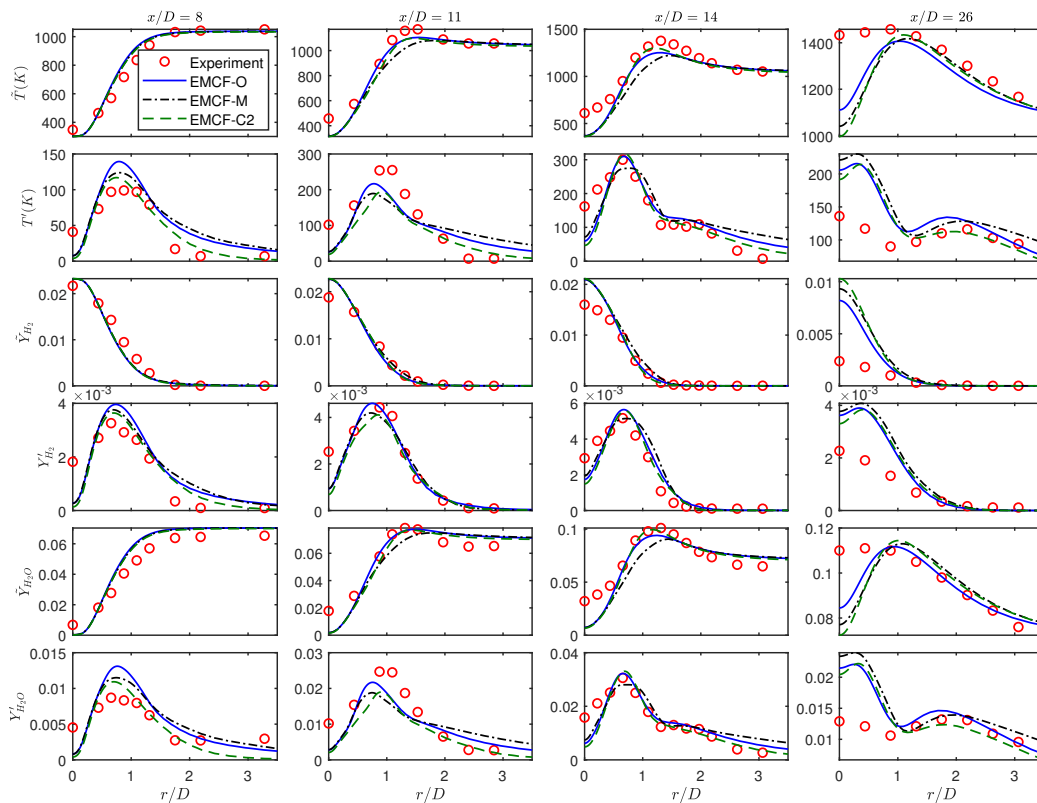


Figure 7.7.: Radial profile of mean temperature \tilde{T} , temperature RMS T' , mean mass fraction of H_2 species \tilde{Y}_{H_2} , RMS mass fraction of H_2 species Y'_{H_2} , mean mass fraction of H_2O species and RMS mass fraction of H_2O species Y'_{H_2O} at the axial locations $x/D = 8, 9, 11$ and 14 for Cabra flame for EMCF-O, EMCF-M and EMCF-C2 methods.

and Figure 7.7 compares the predicted profiles of thermo-chemical scalars such as the mean temperature \tilde{T} , temperature RMS T' , mean H_2 mass fraction \tilde{Y}_{H_2} , RMS H_2 mass fraction Y'_{H_2} , mean H_2O mass fraction \tilde{Y}_{H_2O} and RMS H_2O mass fraction for the three methods at different axial locations. We can see that the radial profiles of \tilde{U} for all the three methods almost overlap and show reasonably good agreement with the experiments. For the thermo-chemical scalars we do observe difference in the predictions of the three methods. In general, the EMCF-C2 method shows the best agreement for all the scalars at the different axial locations. The maximum relative difference between the peak values of \tilde{T} and T' among all the axial locations is close

to 10% and 20% respectively. For the mean mass fraction of H_2 the maximum relative difference in the peak value is around 30% while for H_2O species it is slightly greater than 10%.

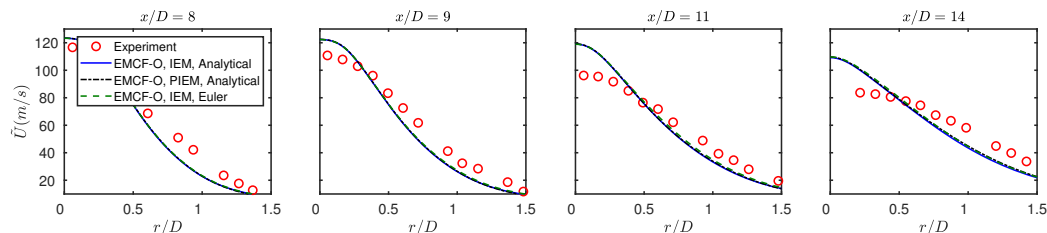


Figure 7.8.: Radial profile of mean axial velocity \tilde{U} at the axial locations $x/D = 8, 9, 11$ and 14 for Cabra flame for EMCF-O method with the analytical IEM mixing model, analytical IPEM mixing model and Euler IEM mixing model.

To study the effect of the mixing model and its implementation, we select the EMCF-O method with Density 2 formulation with the gradient limiter and then use the IEM and IPEM mixing models with the two different formulations. Figure 7.8 shows the radial profiles of the mean axial velocity \tilde{U} for the three different cases and the maximum relative difference between the cases is less than 1%. The thermochemical scalar predictions for the three cases can be seen in Figure 7.9. For the mean temperature and mean species mass fraction we do not observe significant effect of the mixing models or the implementation. But for the RMS values of the scalars, the Euler IEM tends to over predict in comparison to the analytical implementation of the IEM and IPEM mixing models especially at the upstream axial locations $x/D = 8$ and 11 .

Up to this point for all the cases considered for the Cabra flame we have used Density 2 formulation with the gradient limiter. In the last set of simulations we investigate two effects, firstly the consequence of using Density 1 instead of Density 2 and secondly the effect of not using the gradient limiters by setting them to 1. Figure 7.10 and Figure 7.11 show the predictions of the mean axial velocity \tilde{U} and thermo-chemical scalars respectively for three cases, using Density 1 with the gradient

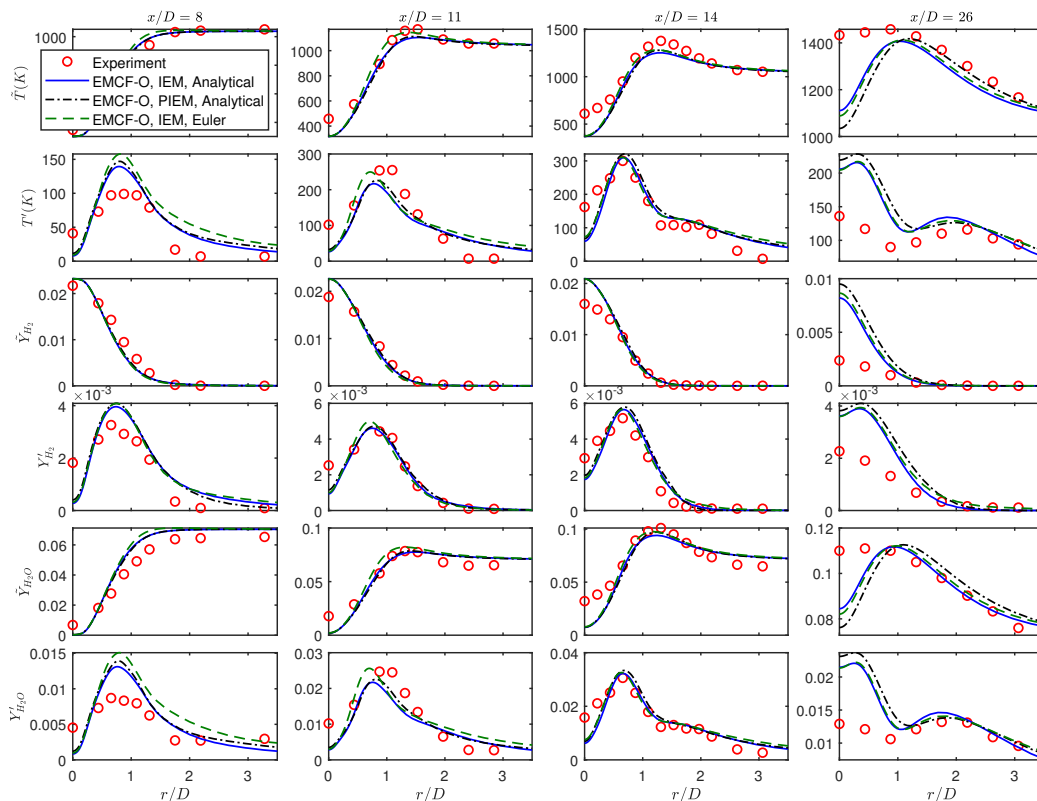


Figure 7.9.: Radial profile of mean temperature \tilde{T} , temperature RMS T' , mean mass fraction of H_2 species \tilde{Y}_{H_2} , RMS mass fraction of H_2 species Y'_{H_2} , mean mass fraction of H_2O species and RMS mass fraction of H_2O species Y'_{H_2O} at the axial locations $x/D = 8, 11, 14$ and 26 for Cabra flame for EMCF-O method with the analytical IEM mixing model, analytical IPEM mixing model and Euler IEM mixing model.

limiters, Density 2 with the gradient limiters and Density 2 without the gradient limiters. For all the three cases we select the EMCF-O method with the analytical IEM model. For \tilde{U} we see negligible difference in the predictions for the three cases at all the axial locations. For the thermo-chemical scalars in Figure 7.11 we observe evident difference in the predicted radial profiles especially for the RMS quantities. Firstly we can see that the Density 2 formulation shows marginally better agreement with the experiment in comparison to Density 1. Secondly we can see that the Density 2 formulation with the gradient limiters significantly improves the predicted profiles

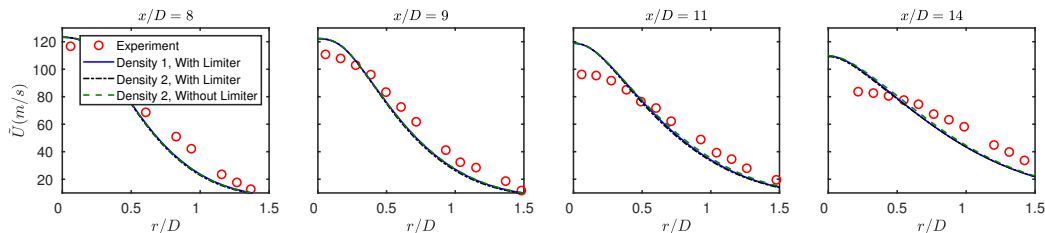


Figure 7.10.: Radial profile of mean axial velocity \tilde{U} at the axial locations $x/D = 8, 9, 11$ and 14 for Cabra flame for Density 1 with gradient limiter, Density 2 with gradient limiter and Density 2 without gradient limiter.

in comparison to the case for Density 2 without the gradient limiters. For these two cases, the maximum relative difference in the peak value is close to 20%, 10% and 25% for T' , Y'_{H_2} and Y'_{H_2O} respectively. To further add to the discussion of the importance of using the gradient limiters, we also conducted numerical simulations for Sandia Flame D [7] which is a piloted methane/air diffusion flame using the EMCF-O method with analytical IEM model and Density 2 formulation. For Flame D we observed that the EMCF-method solver diverges when the gradient limiters are not used. Since we did not obtain final results for Flame D, we do not show the results here. However, this test case also highlights the importance of using the gradient limiters for the Wiener term.

To sum up, in this section for the Cabra flame, similar to the propane round jet in Section 7.2, we inspected the effect of selecting different physical models and numerical implementations in the framework of the EMCF method. The EMCF-C2 method in general improves the predicted profiles of the thermo-chemical scalars in comparison to the EMCF-O method and EMCF-M method. For the mixing models, it is seen that the analytical implementation of the mixing models shows slight improvement in the prediction of RMS of scalars. The gradient limiters for the Wiener term are fundamentally important in predicting the correct RMS profiles for the scalars. In the following Section 7.4, we extend the study by considering a supersonic turbulent jet flame.

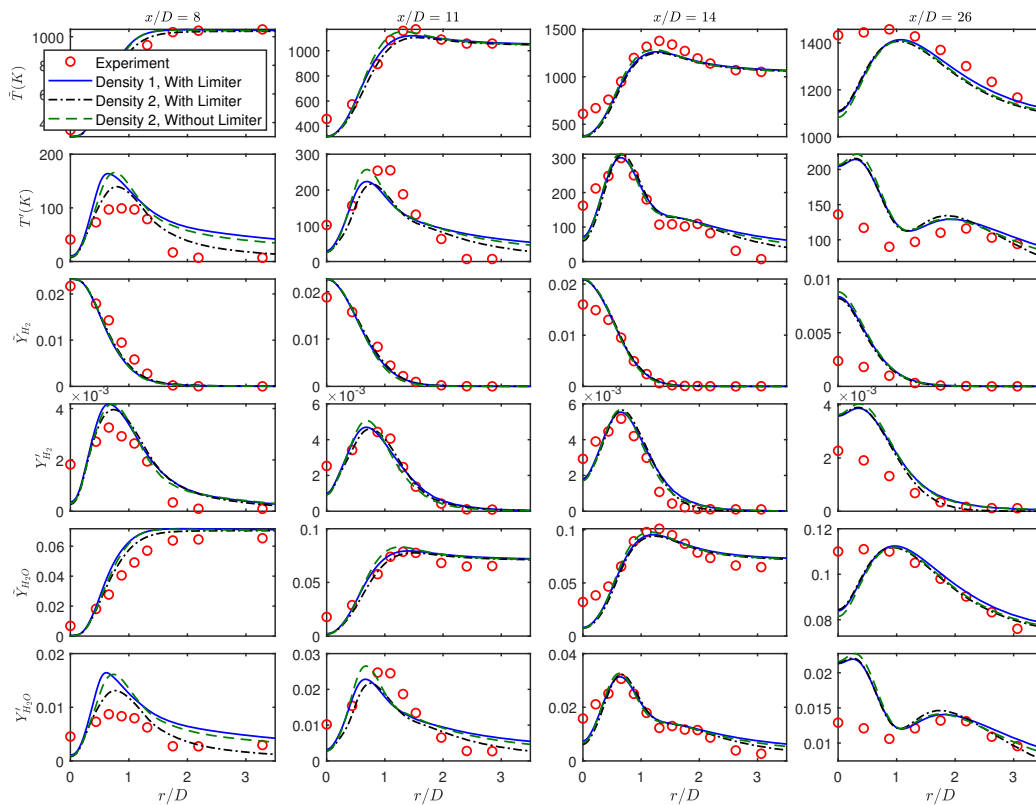


Figure 7.11.: Radial profile of mean temperature \tilde{T} , RMS temperature T' , mean mass fraction of H_2 species \tilde{Y}_{H_2} , RMS mass fraction of H_2 species Y'_{H_2} , mean mass fraction of H_2O species and RMS mass fraction of H_2O species Y'_{H_2O} at the axial locations $x/D = 8, 11, 14$ and 26 for Cabra flame for Density 1 with gradient limiter, Density 2 with gradient limiter and Density 2 without gradient limiter.

7.4 Supersonic Hydrogen Jet Flame

The last canonical test case is a supersonic hydrogen jet flame based on the experiment by Evans et al. [147]. In the experiment, hydrogen is the fuel and is injected through a central jet flame into a vitiated coflow of air. The Mach number Ma for the fuel is 2.0 and for the air is 1.9. We again conduct 2D RANS axisymmetric simulations of the flame like the previous test cases and the grid has around 12,000 cells. Table 7.4 summarizes the inflow boundary conditions for the simulation. The

Li mechanism [146] used in Cabra flame in Section 7.3 is used here as well. For the EMCF method, we use $N_{sf} = 8$ and $C_\phi = 2.0$.

Table 7.4.: Inlet conditions for the numerical simulations of the supersonic turbulent jet flame based on experiment [147].

Parameter	Fuel Jet	Coflow
\bar{p} (MPa)	0.1	0.1
\tilde{U}_b (m/s)	2432	1510
\tilde{T} (K)	251	1495
\tilde{Y}_{H_2}	1.0	0.0
\tilde{Y}_{O_2}	0.0	0.278
\tilde{Y}_{H_2O}	0.0	0.475
\tilde{Y}_{N_2}	0.0	0.247

For the supersonic jet flame we start by looking at the effect of the EMCF-O, EMCF-M and EMCF-C2 methods with the analytical IEM mixing model with Density 2 formulation and with the gradient limiters. Figure 7.12 compares the predicted radial profiles of the normalized pitot pressure P_{pit}/P_{ref} at four different axial locations. P_{pit} is defined as $P_{pit} = \bar{p} + \bar{\rho} (\tilde{U}^2 + \tilde{V}^2)$ using the mean axial velocity \tilde{U} and mean radial velocity \tilde{V} . P_{ref} is a reference pressure at each axial location and it is defined in Evans et al. [147]. We can see that all the three methods show reasonably good agreement with the experiment with the EMCF-O method predictions relatively better than the other two methods. The predictions of the mean mass fraction of H₂O, H₂, O₂ and N₂ species is shown in Figure 7.13. For all the species at all the axial locations, we can see that the predictions of the EMCF-O method and EMCF-M method are only marginally different from each other while the EMCF-C2 method predictions are distinctively different for H₂O, H₂ and N₂. The EMCF-C2 method is able to capture the peak values of H₂O at the axial locations $x/D = 8.26$ and 15.5

and the radial profiles of H_2 and N_2 at all the axial locations more accurately than the other two methods. A comparison of the radial profiles of the RMS of temperature and species mass fraction of H_2O , H_2 , O_2 and N_2 can be observed in Figure 7.14. For the RMS quantities the experimental data is not available. The difference in the predictions for all the three methods is evident and the maximum relative difference between the three methods for T' , Y'_{H_2O} , Y'_{H_2} , Y'_{O_2} and Y'_{N_2} is around 10%, 25%, 24%, 24% and 18% respectively.

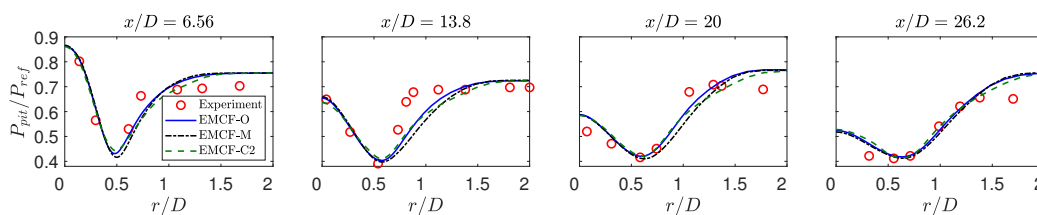


Figure 7.12.: Radial profile of the normalized pitot pressure P_{pit}/P_{ref} at the axial locations $x/D = 6.56, 13.8, 20$ and 26.2 for the supersonic turbulent jet test case for the EMCF-O, EMCF-M and EMCF-C2 methods.

We now look at the effect of the analytical and Euler implementation of the IEM mixing model using the EMCF-O method with Density 2 and including the gradient limiters in the simulations. The predictions of the normalized pitot pressure, mean mass fraction and RMS mass fraction of the species is shown in Figures 7.15, 7.16 and 7.17 respectively. The predictions for the IPEM mixing model with either of the analytical and Euler implementations were almost identical to the IEM mixing model predictions and hence in this set of cases we do not show results for the PEIM mixing model. From all the three figures we can see that the two cases show distinctively different predictions of all the quantities. The analytical IEM mixing model is able to capture the profiles of the normalized pitot pressure and the mean mass fraction of the species significantly more accurately than the Euler IEM mixing model. It seems that the Euler implementation of the IEM mixing model leads to over-prediction of the mixing for the supersonic turbulent jet case.

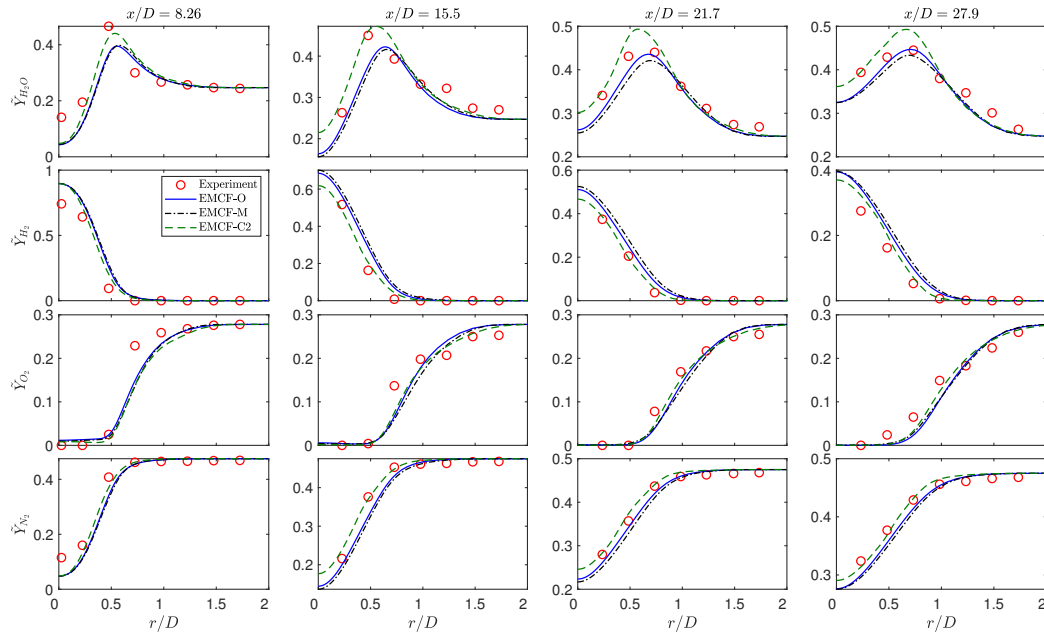


Figure 7.13.: Radial profile of mean mass fraction of H_2O species $\tilde{Y}_{\text{H}_2\text{O}}$, H_2 species \tilde{Y}_{H_2} , O_2 species \tilde{Y}_{O_2} and N_2 species \tilde{Y}_{N_2} at the axial locations $x/D = 8.26, 15.5, 21.7$ and 27.9 for the supersonic turbulent jet test case for the EMCF-O, EMCF-M and EMCF-C2 methods.

In the last set of simulations of the supersonic jet flame, we investigate the effect of the different density formulations and the gradient limiters. To study these effects we select the EMCF-O method with the analytical IEM mixing model and then chose either of the two different density formulations with and without the gradient limiters. From the radial profiles of P_{pit}/P_{ref} in Figure 7.18 we do observe a difference when the two different density formulations are used with Density 2 showing the best agreement with the experiment. The effect of the gradient limiters is not that significant and the maximum relative difference between the Density 2 with gradient limiters and without gradient limiters results is less than 5%. For the mean mass fraction of the species, the effect of the density formulation and gradient limiters is not very significant as can be seen in Figure 7.19. Figure 7.20 compares the prediction of T' , $Y'_{\text{H}_2\text{O}}$, Y'_{H_2} , Y'_{O_2} and Y'_{N_2} . It can be observed that for the RMS of the scalars, the results for the

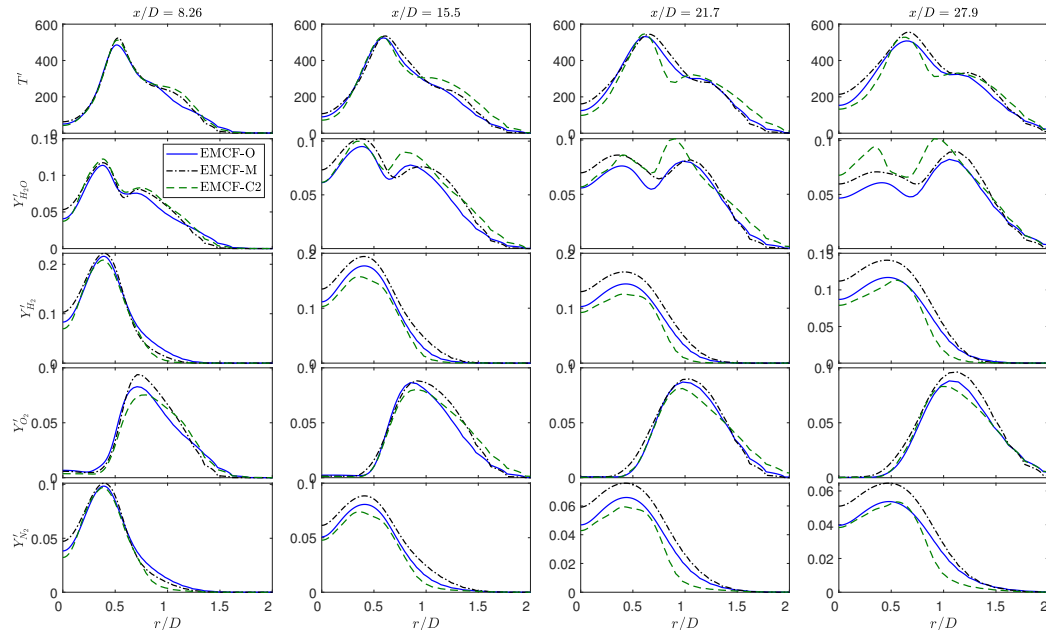


Figure 7.14.: Radial profile of the RMS temperature T' , RMS mass fraction of H_2O species Y'_{H_2O} , H_2 species Y'_{H_2} , O_2 species Y'_{O_2} and N_2 species Y'_{N_2} at the axial locations $x/D = 8.26, 15.5, 21.7$ and 27.9 for the supersonic turbulent jet test case for the EMCF-O, EMCF-M and EMCF-C2 methods.

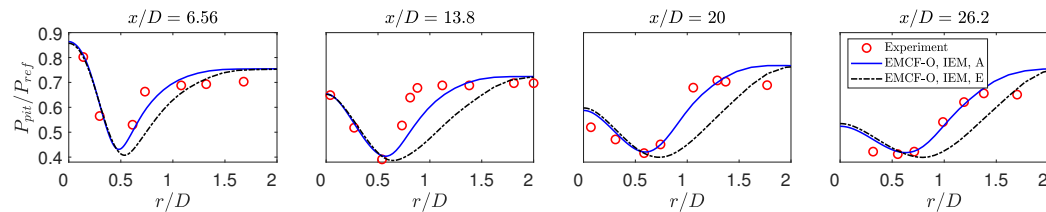


Figure 7.15.: Radial profile of the normalized pitot pressure P_{pit}/P_{ref} at the axial locations $x/D = 6.56, 13.8, 20$ and 26.2 for the supersonic turbulent jet test case for EMCF-O method with the analytical IEM mixing model and the Euler IEM mixing model.

different density formulations do not vary much. Without the gradient limiters for the Density 2 formulation, the peak value of the RMS decreases for all the scalars at all the locations.

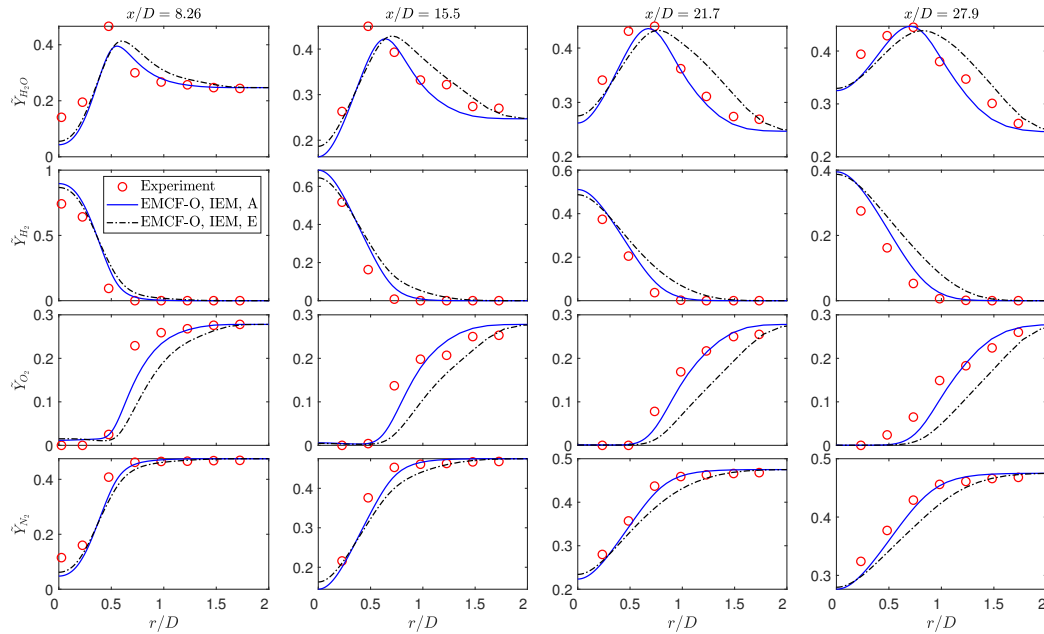


Figure 7.16.: Radial profile of mean mass fraction of H_2O species \tilde{Y}_{H_2O} , H_2 species \tilde{Y}_{H_2} , O_2 species \tilde{Y}_{O_2} and N_2 species \tilde{Y}_{N_2} at the axial locations $x/D = 8.26, 15.5, 21.7$ and 27.9 for the supersonic turbulent jet test case for EMCF-O method with the analytical IEM mixing model and the Euler IEM mixing model.

To summarize, for the the supersonic turbulent jet flame we identified that the numerical implementation of mixing model has significant impact on the numerical accuracy of the predictions and the analytical implementation of the mixing model should be the preferred option. The effect of the gradient limiters for the Weiner term is not quite as significant for the supersonic jet flame in comparison to the subsonic Cabra flame in Section 7.3.

7.5 Self-Excited Resonance Model Rocket Combustor

The final test case is the self-excited resonance model rocket combustor [75, 76] discussed in Chapter 2.

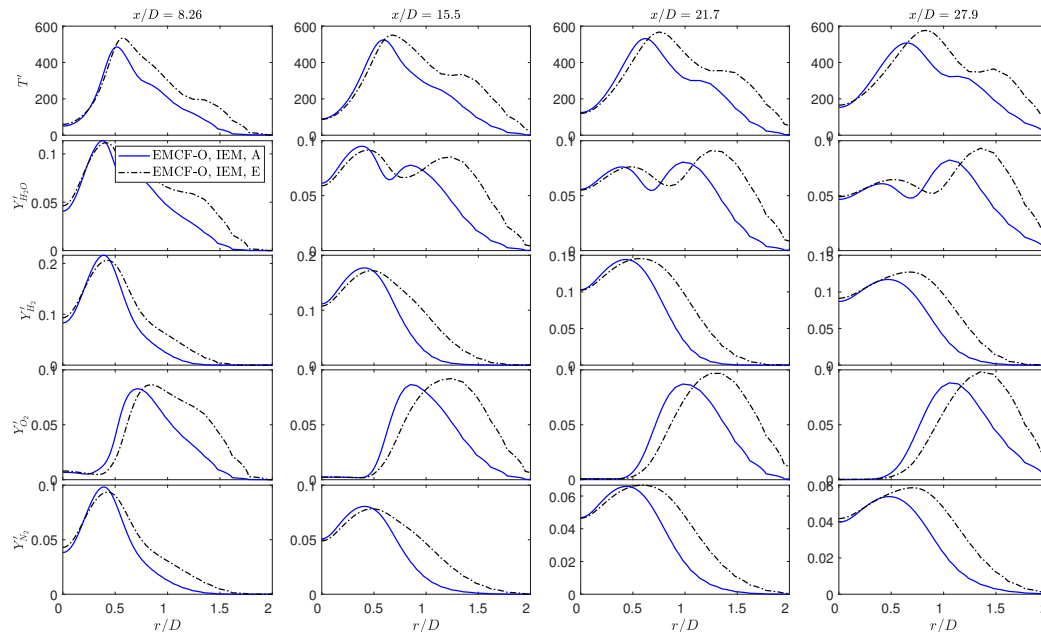


Figure 7.17.: Radial profile of the RMS temperature T' , RMS mass fraction of H_2O species Y'_{H_2O} , H_2 species Y'_{H_2} , O_2 species Y'_{O_2} and N_2 species Y'_{N_2} at the axial locations $x/D = 8.26, 15.5, 21.7$ and 27.9 for the supersonic turbulent jet test case for for EMCF-O method with the analytical IEM mixing model and the Euler IEM mixing model.

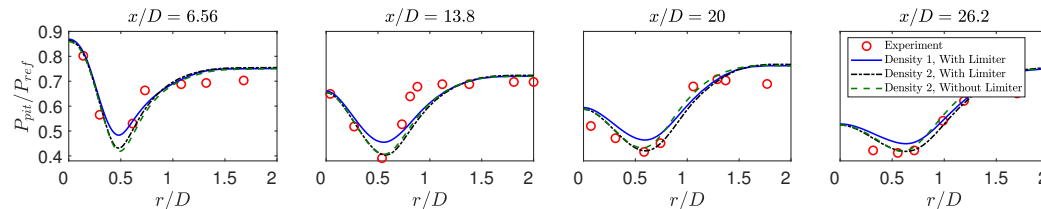


Figure 7.18.: Radial profile of the normalized pitot pressure P_{pit}/P_{ref} at the axial locations $x/D = 6.56, 13.8, 20$ and 26.2 for the supersonic turbulent jet test case for Density 1 with gradient limiters, Density 2 with gradient limiters and Density 2 without gradient limiters.

We conduct 2D axisymmetric simulations of the model rocket combustor for both the stable and unstable operating conditions. Previous numerical studies [65, 79, 82,

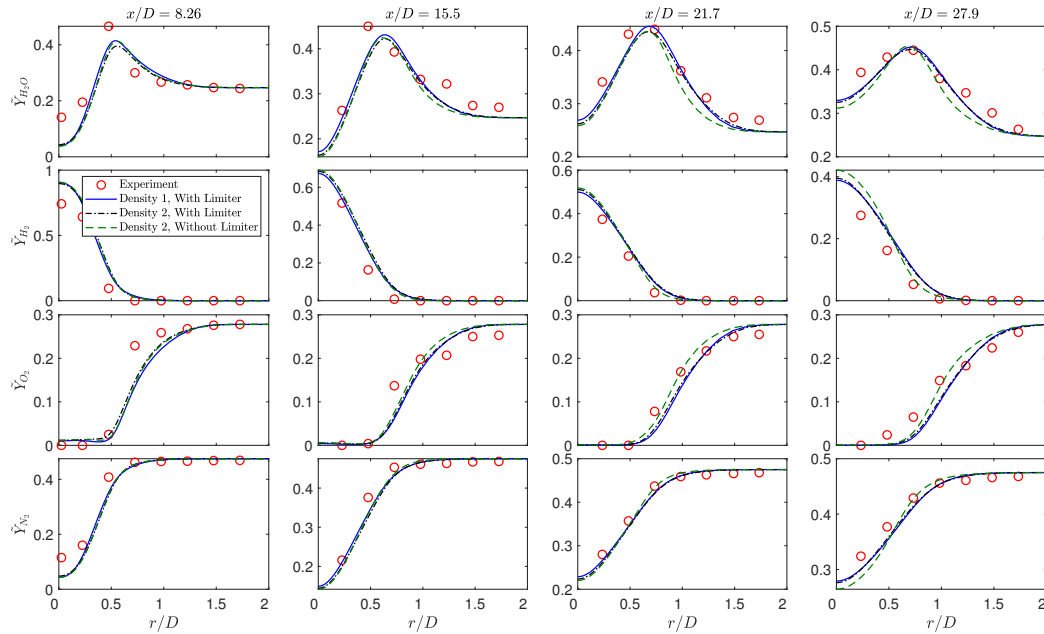


Figure 7.19.: Radial profile of mean mass fraction of H_2O species \tilde{Y}_{H_2O} , H_2 species \tilde{Y}_{H_2} , O_2 species \tilde{Y}_{O_2} and N_2 species \tilde{Y}_{N_2} at the axial locations $x/D = 8.26, 15.5, 21.7$ and 27.9 for the supersonic turbulent jet test case for Density 1 with gradient limiters, Density 2 with gradient limiters and Density 2 without gradient limiters.

117, 118, 148] of the model rocket combustor using the axisymmetry assumption have shown good agreement with the experiment. The mesh used has around 110000 cells based on previous work by Sardeshmukh et al. [65]. In the simulations, for the inlet boundary condition of the fuel stream and the oxidizer stream, the mass flow rate \dot{m} , mean pressure \bar{p} , temperature of the n^{th} stochastic field T^n and mass fraction of the i^{th} species for the n^{th} stochastic field Y_i^n is specified. We assume zero scalar variance at the inlets so that $T^n = \tilde{T}$ and $Y_i^n = \tilde{Y}_i$. The mean values of the inlet boundary condition variables for the fuel stream and oxidizer stream are given in Table 7.5, following the experimental conditions. The walls of the combustor are assumed to be adiabatic and the no-slip boundary condition is applied. At the nozzle outlet, the

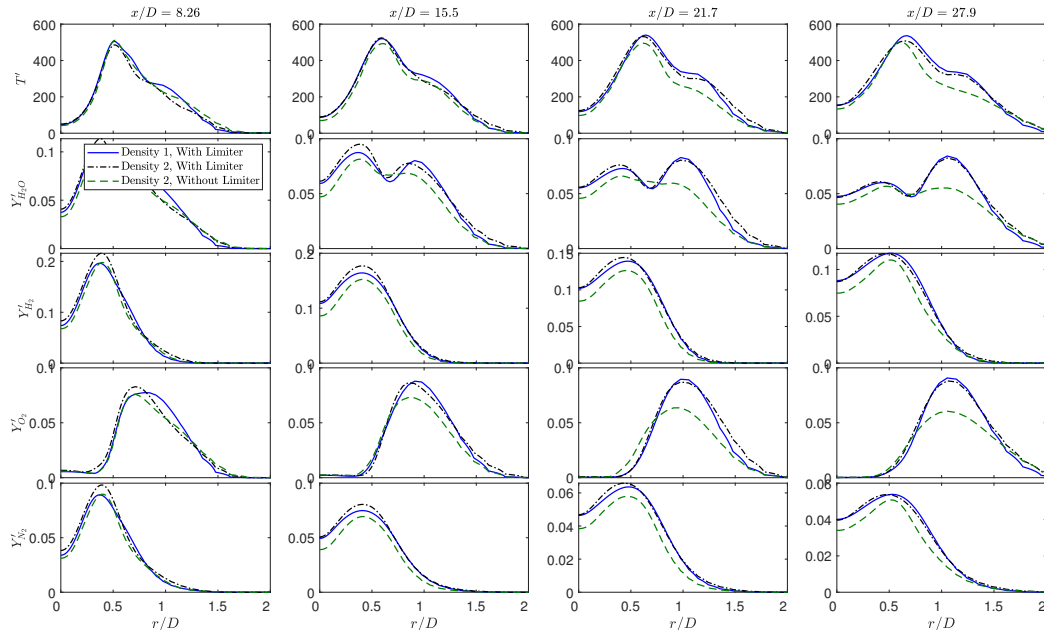
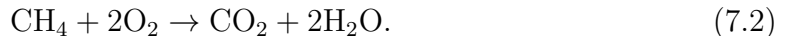


Figure 7.20.: Radial profile of the RMS temperature T' , RMS mass fraction of H_2O species Y'_{H_2O} , H_2 species Y'_{H_2} , O_2 species Y'_{O_2} and N_2 species Y'_{N_2} at the axial locations $x/D = 8.26, 15.5, 21.7$ and 27.9 for the supersonic turbulent jet test case for Density 1 with gradient limiters, Density 2 with gradient limiters and Density 2 without gradient limiters.

mean back pressure \bar{p}_b specify the mixing constant value $C_\phi = 2.0$. The reaction mechanism is a single step global reaction mechanism [80],



The importance of using detailed chemical kinetics has been highlighted by Sardeshmukh et al. [65]. However in the EMCF method, the computational cost of using a detailed chemical mechanism like GRI 1.2 mechanism [81] is significantly higher in comparison to other combustion models like the flamelet model, CMC model, DTF model, LEM model and the laminar chemistry model. Hence to reduce the computational cost, we use the single-step reaction mechanism in Equation (7.2) which has been previously used by Harvazinski et al. [64]. For the current simulations of the model rocket combustor with the EMCF method we specify $N_{sf} = 8$ and $C_\phi = 2.0$.

Table 7.5.: Inlet conditions for the fuel stream and oxidizer stream for the numerical simulations of the model rocket combustor based on experiment [76].

	Fuel	Oxidizer
\dot{m} (kg/s)	0.024	0.323
\bar{p} (MPa)	1.38	1.38
\tilde{T} (K)	294	1030
\tilde{Y}_{CH_4}	1.0	0.0
\tilde{Y}_{O_2}	0.0	0.4235
\tilde{Y}_{H_2O}	0.0	0.5765

The simulations are conducted with the EMCF-O method, with analytical implementation of the IEM mixing and model and Density 2 formulation with gradient limiters [149].

7.5.1 Prediction of Fluctuating Pressure Signal

Figure 7.21 compares the instantaneous pressure fluctuations and the power spectral density (PSD) analysis of the raw pressure data measured inside the model rocket combustor at $x/D_{ox} = 18$ for both the operating conditions. The pressure fluctuation p' is obtained from the raw pressure data by using a high-pass filter with a cut-off frequency of around 1Hz which eliminates the low frequency pressure waves. For both the operating conditions, we can see that the peak-to-peak amplitude of the pressure fluctuations predicted by the PDF model shows good agreement with the experiment. The level of thermo-acoustic instability $\langle P_{pp} \rangle / \langle P_c \rangle$ for both the operating conditions is compared with the experiment in Table 7.7. The relative error in the prediction of $\langle P_{pp} \rangle / \langle P_c \rangle$ in comparison to the experiment for the stable operating condition is around 12% and for the unstable operating condition is less than 3%. A PSD analy-

Table 7.6.: Comparison of the level of thermo-acoustic instability ($\langle P_{pp} \rangle / \langle P_c \rangle$) and the frequencies (f_1, f_2) and the amplitudes (A_1, A_2) of the first two modes from the experiment [76] with the simulations for $L_{ox} = 13.97\text{cm}$. The pressure data is measured at measured at $x/D_{ox} = 18$ near the combustor wall. The model results are obtained for the EMCF-O method with analytical implementation of the IEM mixing model and Density 2 formulation with gradient limiters.

	Experiment	EMCF Method
$\langle P_{pp} \rangle / \langle P_c \rangle$	45%	43.7%
f_1 (Hz)	1360	1553
f_2 (Hz)	2659	3076
A_1 (kPa ² /Hz)	646.3	221.1
A_2 (kPa ² /Hz)	44.8	27.26

sis of the raw pressure data helps to identify the different acoustic modes which are indicated by distinct peaks in the PSD plot. For the stable operating condition we can see that in the experiment around three distinct peaks can be identified. For the prediction of the stable operating condition we can observe a distinct peak corresponding to the first mode but the other two peaks are smeared to some degree. In case of the unstable operating condition, the numerical simulation predicts three distinct peaks. Table 7.7 compares the frequencies f_1, f_2 and amplitudes A_1, A_2 of the first two modes for the experiment and the PDF model predictions. The frequency f_2 and amplitude A_2 for the second mode of the stable operating condition using the PDF model is not reported since a distinct second peak cannot be observed. For both the frequency f_1 and amplitude A_1 of the first mode of the stable operating condition, the PDF model over predicts in comparison to the experiment by around 12% and 500 % respectively. For the unstable operating condition, the frequencies f_1 (14%) and f_2 (15%) are over-predicted for both the modes by the PDF model. Similar trend

of over-prediction of the frequency of the modes for the unstable operating condition has been observed for all the previous numerical studies [?, 58, 64, 65, 82] of the model rocket combustor. The amplitudes A_1 and A_2 are under-predicted by around 65% and 39% respectively for the unstable operating condition.

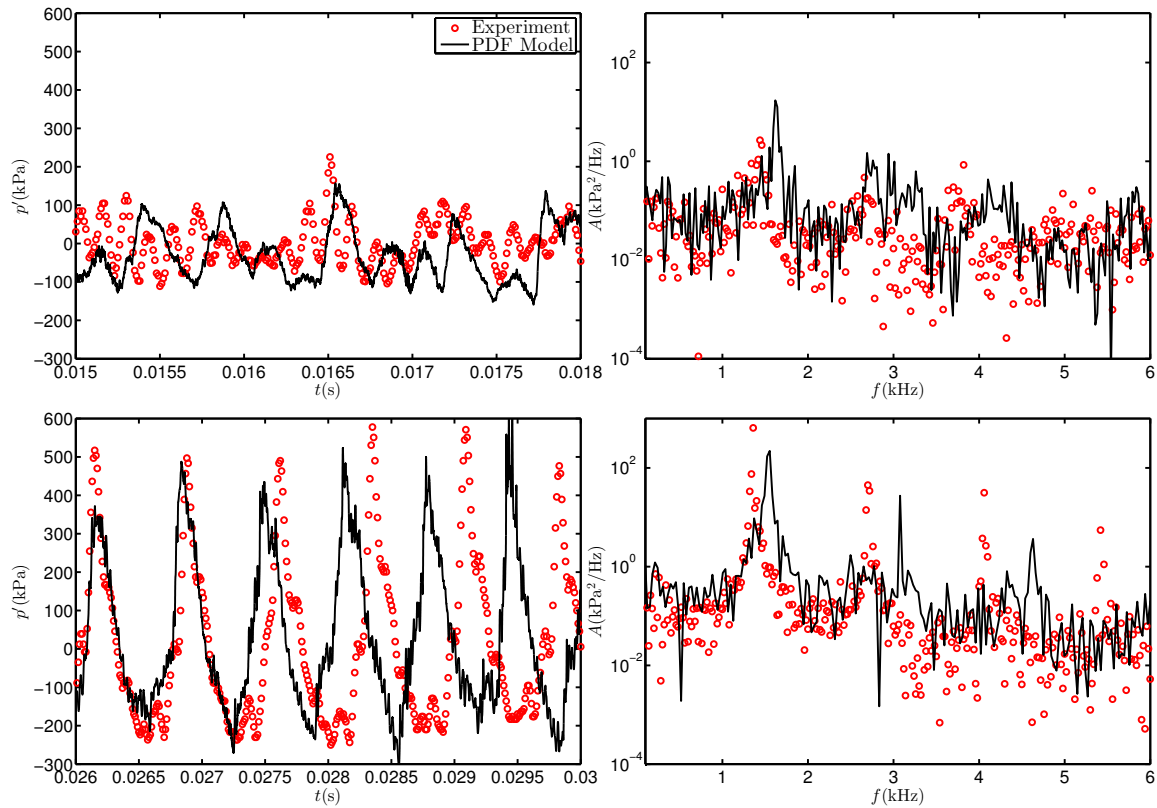


Figure 7.21.: Fluctuating pressure signal p' (left) and PSD of raw pressure data (right) measured at $x/D_{ox} = 18$ near the combustor wall in the model rocket combustor for the stable operating condition (top row) and unstable operating condition (bottom row). The model results are obtained for the EMCF method parameters $N_{sf} = 8$ and $C_\phi = 2.0$.

Table 7.7.: Comparison of the level of thermo-acoustic instability ($\langle P_{pp} \rangle / \langle P_c \rangle$) and the frequencies (f_1, f_2) and the amplitudes (A_1, A_2) of the first two modes from the experiment [76] with the simulations using the PDF model for the stable operating condition and the unstable operating condition. The pressure data is measured at measured at $x/D_{ox} = 18$ near the combustor wall. The model results are obtained for the EMCF method parameters $N_{sf} = 8$ and $C_\phi = 2.0$.

	Stable Operating Condition		Unstable Operating Condition	
	Experiment	PDF	Experiment	PDF
$\langle P_{pp} \rangle / \langle P_c \rangle$	13%	14.6%	45%	43.7%
f_1 (Hz)	1440	1619	1360	1553
f_2 (Hz)	2659	-	2659	3076
A_1 (kPa ² /Hz)	2.668	17.12	646.3	221.1
A_2 (kPa ² /Hz)	0.4696	-	44.8	27.26

7.5.2 Prediction of Flow Field and Scalars

A better overview of the numerical simulations can be obtained by looking at the contour plots of the flow field and thermo-chemical scalars. One reason which makes the PDF method an attractive turbulent combustion model is the fact that any m^{th} moment of a thermo-chemical scalar can be easily obtained from the stochastic fields as discussed in Section 3.4. The left column of contour plots in Figure 7.22 shows the contours of the time-averaged and instantaneous predictions of the axial velocity \tilde{U} , temperature \tilde{T} , mass fraction of CO₂ species \tilde{Y}_{CO_2} and heat release rate \tilde{Q} . The right column of plots shows the time-averaged and instantaneous root mean square (RMS) values of sub-grid scale mass fraction of CH₄ species Y'_{CH_4} , temperature T' , sub-grid scale mass fraction of Y'_{CO_2} and heat release rate \dot{Q}' . In the contour plot for each variable, the upper half is the time-averaged result and the lower half is the instantaneous result. The flame is stabilized at the at the dump plane located at $x/D_{ox} = 0$ by the recirculation zone downstream of the dump plane. The mean heat release \tilde{Q} is concentrated mainly in the region just downstream of the dump plane.

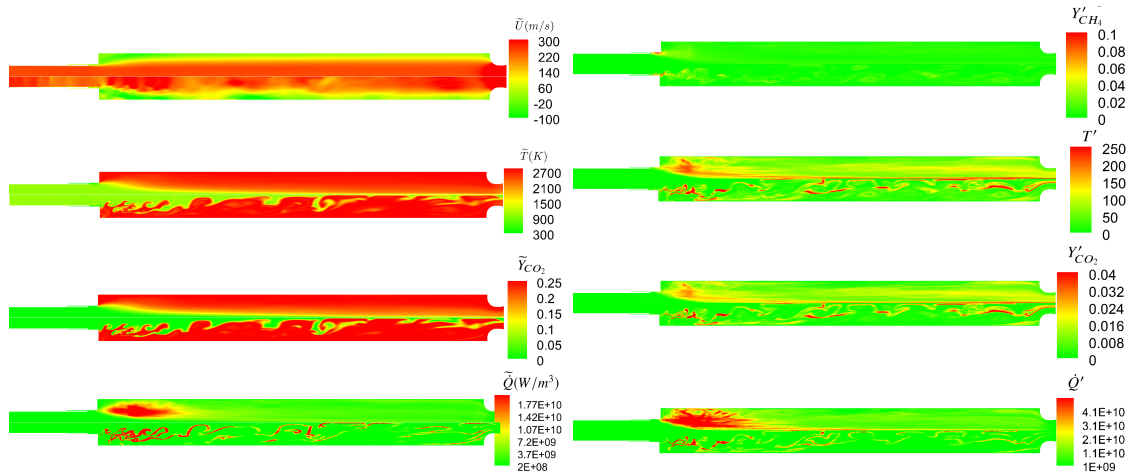


Figure 7.22.: Contour plots of the mean axial velocity \tilde{U} , temperature \tilde{T} , mass fraction of CO_2 species and heat release rate \tilde{Q} (left column) and sub-grid RMS of mass fraction of CH_4 species, temperature T' , CO_2 species and heat release rate \dot{Q}' (right column) for the stable operating condition. The upper half of each contour plot is the time-averaged result and the lower half is the instantaneous results. The model results are obtained for the EMCF method parameters $N_{sf} = 8$ and $C_\phi = 2.0$.

The RMS values of the sub-grid scale CH_4 mass fraction, Y'_{CH_4} are significantly higher just upstream of the dump plane where the fuel and oxidizer mix. For T' , Y'_{CO_2} and \dot{Q}' the values much larger in the flame stabilization region just downstream of the dump plane and the values go on decreasing as we move further downstream. In general, for the two operating conditions, there is not a significant difference in the RMS values of the thermo-chemical throughout the combustor. There is some difference in the RMS values for the two operating condition just downstream of the dump plane where for the unstable operating condition, the magnitude of fluctuation in the scalars seems to significantly higher in the corner formed by the dump plane and the main combustion chamber wall as compared to the stable operating condition.

To summarize, in this section, we compared the predictions for the EMCF method with the experiment for the stable operating condition and unstable operating con-

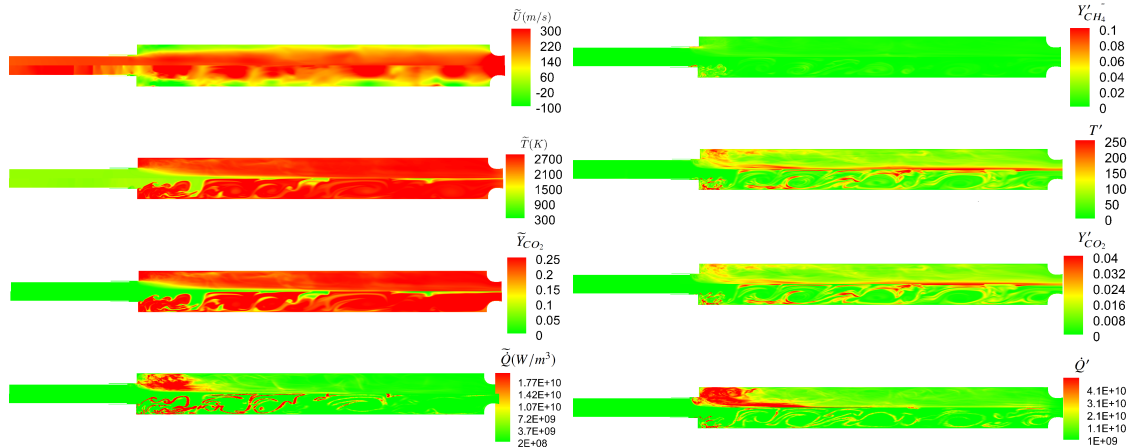


Figure 7.23.: Contour plots of the mean axial velocity \tilde{U} , temperature \tilde{T} , mass fraction of CO_2 species and heat release rate \tilde{Q} (left column) and sub-grid RMS of mass fraction of CH_4 species, temperature T' , CO_2 species and heat release rate \dot{Q}' (right column) for the unstable operating condition. The upper half of each contour plot is the time-averaged result and the lower half is the instantaneous results. The model results are obtained for the EMCF method parameters $N_{sf} = 8$ and $C_\phi = 2.0$.

dition. For both the operating conditions, the numerical simulation is able to predict the level of pressure fluctuation in terms of the peak-to-peak amplitude accurately in comparison to the experiment. The frequencies of the different modes is slightly over-predicted by the numerical simulation. One possible reason for this is that the single step global reaction predicts slightly higher peak temperature inside the combustor. The RMS values of sub-grid thermo-chemical scalars for both the operating conditions are quite similar. For the numerical simulations in this section using the EMCF method, we specified $N_{sf} = 8$ and $C_\phi = 2.0$. In the following section we study the sensitivity of the level of pressure fluctuations in the model rocket combustor to these two parameters.

7.5.3 Parametric Studies of the EMCF Method

In the EMCF method discussed in Section 3.4, there are primarily two hyper-parameters, the number of stochastic fields N_{sf} for each composition PDF scalar and the mixing constant C_ϕ . The use of a finite number of stochastic fields adds a numerical bias error in the EMCF method predictions and this error scales as N_{sf}^{-1} [150–152]. The mixing constant C_ϕ controls the mixing time scale of the scalars, larger the value of C_ϕ , higher is the rate of mixing. A number of studies have been done in the past to study the effect of these two parameters in the EMCF method [106, 108, 110, 153–155]. However no work has been done to study the effect of these two parameters in the context of modeling of thermo-acoustic instability. In Section 7.5.3, we first study the effect of changing the number of stochastic fields N_{sf} for C_ϕ value of 2.0 and then in Section 7.5.3 we set $N_{sf} = 8$ and vary C_ϕ . The grid that is used for conducting parametric studies in this section is a relatively coarse grid in comparison to the grid used in Section 7.5.1 with around 15000 cells. The relative difference in the prediction of the peak-to-peak amplitude of the pressure fluctuations for both of these grids is less than 5% for the unstable operating condition for $N_{sf} = 8$ and $C_\phi = 2.0$ and hence this grid is considered adequate for conducting parametric studies.

Effect of Number of Stochastic Fields

In this section we consider three different values of the number of stochastic fields $N_{sf} = 4, 8$ and 16. The value of the mixing constant is fixed to $C_\phi = 2.0$. Figure 7.24 compares the pressure fluctuation predictions and PSD of pressure data inside the model rocket combustor for $N_{sf} = 4, 8$ and 16 with the experiment. The level of thermo-acoustic instability $\langle P_{pp} \rangle / \langle P_c \rangle$ and the frequencies f_1, f_2 and PSD amplitudes A_1, A_2 of the first two modes are tabulated in Table 7.8. We can see that changing the number of stochastic fields does not have a significant impact on the frequencies f_1 and f_2 with a maximum relative difference of less than 1% for the three values of

N_{sf} for both the frequencies. There is some difference in the amplitudes A_1 and A_2 with $N_{sf} = 4$ case showing the best agreement (Relative error: $A_1 = 30\%$, $A_2 = 68\%$) with experiment. The difference between the simulations with different values of N_{sf} is evident when we look at the initial growth of thermo-acoustic instability inside the combustor. Figure 7.25 shows the raw pressure data inside the combustor measured at $x/D_{ox} = 18$ from the start of the simulation for the three different values. We can see that for $N_{sf} = 4$, the transition from the initial state to the limit-cycle is much faster as compared to $N_{sf} = 8$ and $N_{sf} = 16$. One plausible reason for the rapid growth of instability for $N_{sf} = 4$ can be the higher numerical bias error in the pressure predictions introduced due to lower number stochastic fields.

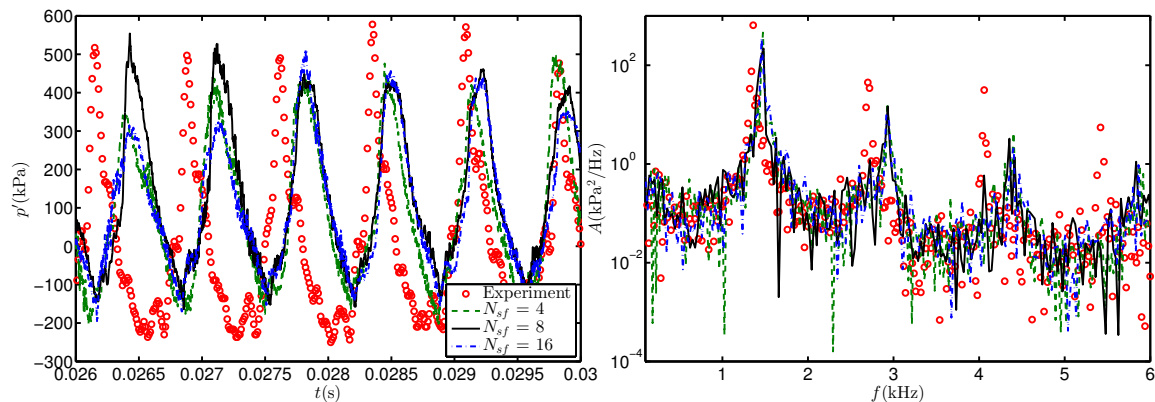


Figure 7.24.: Fluctuating pressure signal p' (left) and PSD of raw pressure data (right) measured at $x/D_{ox} = 18$ near the combustor wall in the model rocket combustor for the unstable operating condition. The model results are obtained for $N_{sf} = 4, 8$ and 16 for $C_\phi = 2.0$.

Effect of Mixing Constant

To study the effect of C_ϕ , we carry out numerical simulations for $C_\phi = 2.0, 4.0$ and 8.0 for $N_{sf} = 8$. A comparison of the fluctuating pressure signal and the PSD for the three different values of C_ϕ can be found in Figure 7.26. From Table 7.9 we

Table 7.8.: Comparison of the level of thermo-acoustic instability ($\langle P_{pp} \rangle / \langle P_c \rangle$) and the frequencies (f_1, f_2) and amplitudes (A_1, A_2) of the first two modes from the experiment [76] with simulations using the PDF model for the unstable operating condition. The pressure data is measured at measured at $x/D_{ox} = 18$ near the combustor wall. The model results are obtained for $N_{sf} = 4, 8$ and 16 and $C_\phi = 2.0$.

	Experiment	$N_{sf} = 4$	$N_{sf} = 8$	$N_{sf} = 16$
$\langle P_{pp} \rangle / \langle P_c \rangle$	45%	42.8%	43.1%	43.6%
f_1 (Hz)	1360	1474	1470	1458
f_2 (Hz)	2659	2928	2932	2916
A_1 (kPa ² /Hz)	646.3	458.7	218.6	357.3
A_2 (kPa ² /Hz)	44.8	17.36	14.53	10.56

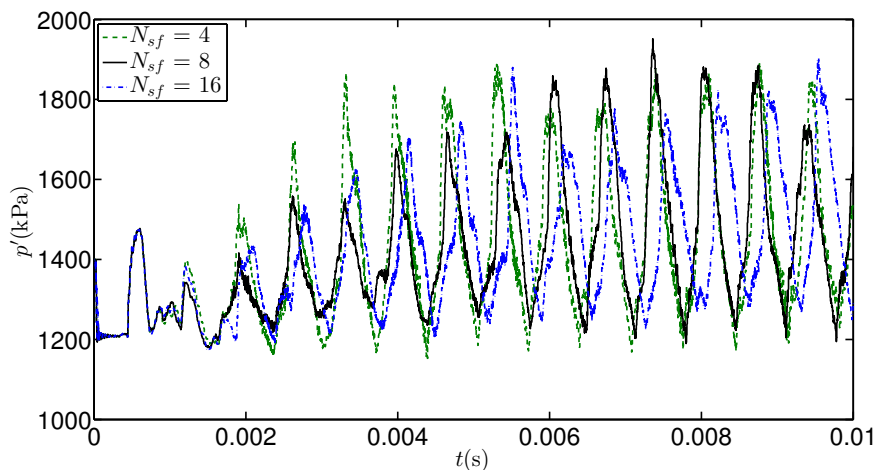


Figure 7.25.: Initial raw pressure signal measured at $x/D_{ox} = 18$ in the model rocket combustor. The model results are obtained for $N_{sf} = 4, 8$ and 16 for $C_\phi = 2.0$.

can see that C_ϕ does not have a significant impact on the level of pressure fluctuation $\langle P_{pp} \rangle / \langle P_c \rangle$ and the frequencies of the first two modes f_1 and f_2 . However, the PSD amplitudes for the first two modes seem to be significantly affected by the value of

C_ϕ . For A_1 , $C_\phi = 4.0$ shows the best agreement with the experiment with a relative error of less than 1% while the relative error for $C_\phi = 2.0$ and $C_\phi = 8.0$ is 66% and 35% respectively. The PSD amplitude A_2 is under-predicted for all the three values of C_ϕ with $C_\phi = 8.0$ showing the best agreement (51% relative error) with experiment. In Figure 7.27 we make a quantitative comparison of the effect of

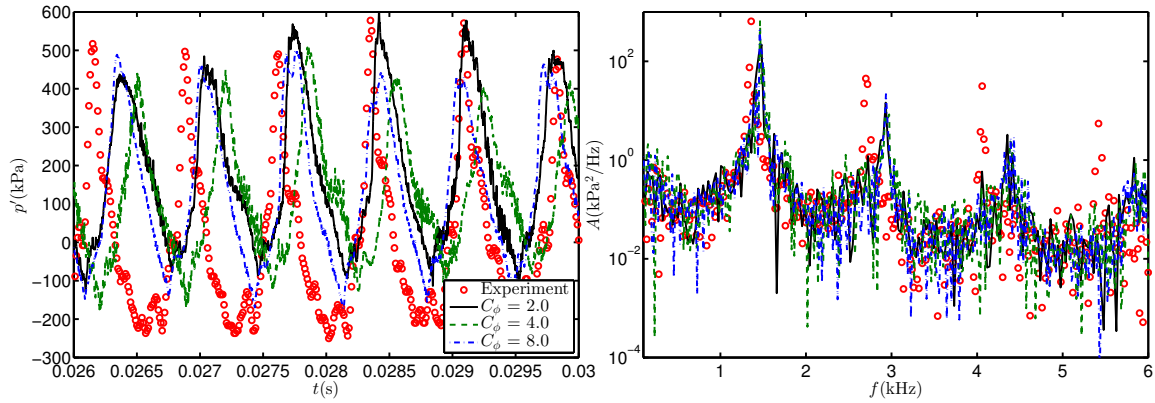


Figure 7.26.: Fluctuating pressure signal p' (left) and PSD of raw pressure data (right) measured at $x/D_{ox} = 18$ near the combustor wall in the model rocket combustor for the unstable operating condition. The model results are obtained for $N_{sf} = 8$ and for $C_\phi = 2.0, 4.0$ and 8.0 .

the value of C_ϕ on the time-averaged filtered axial velocity $\langle \tilde{U} \rangle$, turbulent kinetic energy $\langle \tilde{k} \rangle$, temperature $\langle \tilde{T} \rangle$ and mass fraction of CO_2 species and time-averaged RMS of sub-grid temperature $\langle T' \rangle$ and CO_2 mass fraction $\langle Y'_{CO_2} \rangle$. The figure shows the radial profiles of these quantities at three locations $x/D_{ox} = 2, 8$ and 18 which are downstream of the dump plane ($x/D_{ox} = 0$). For the filtered quantities, $\langle \tilde{U} \rangle$, $\langle \tilde{k} \rangle$, $\langle \tilde{T} \rangle$ and $\langle \tilde{Y}_{CO_2} \rangle$ we do not see a significant effect of varying the value of C_ϕ . The effect of different values of C_ϕ is evident in the RMS of sub-grid quantities namely $\langle T' \rangle$, $\langle Y'_{CO_2} \rangle$. We can see that as the value of C_ϕ increases the time-averaged RMS value goes on decreasing. This is because increasing the value of C_ϕ reduces the mixing time scale for the scalars leading to rapid mixing of the scalars and hence decrease in the RMS value.

Table 7.9.: Comparison of the level of thermo-acoustic instability ($\langle P_{pp} \rangle / \langle P_c \rangle$) and the frequencies (f_1, f_2) and amplitudes (A_1, A_2) of the first two modes from the experiment [76] with simulations using the PDF model for the unstable operating condition. The pressure data is measured at measured at $x/D_{ox} = 18$ near the combustor wall. The model results are obtained for the EMCF method parameters $N_{sf} = 8$ and $C_\phi = 2.0, 4.0$ and 8.0 .

	Experiment	$C_\phi = 2.0$	$C_\phi = 4.0$	$C_\phi = 8.0$
$\langle P_{pp} \rangle / \langle P_c \rangle$	45%	45.2%	44.2%	44.1%
f_1 (Hz)	1360	1481	1463	1458
f_2 (Hz)	2659	2932	2926	2935
A_1 (kPa ² /Hz)	646.3	218.6	650.2	419.5
A_2 (kPa ² /Hz)	44.8	14.53	10.69	21.68

To sum up, in Section 7.5.3 we conducted parametric studies of the EMCF method to study the sensitivity of the thermo-acoustic instability inside the combustor to two parameters, the number of stochastic fields and the value of the mixing constant. It is found that the level of pressure fluctuation inside the combustor is not very sensitive to the number of stochastic fields during the limit-cycle. During the transition period from the initial state to the limit-cycle, the effect of the number of stochastic fields is evident with the simulation with four stochastic fields showing the quickest transition to the limit-cycle from the initial state. The value of the mixing constant also does significantly not affect the peak-to-peak amplitude of the pressure fluctuation and the frequencies of the different acoustic modes. However, the PSD amplitude shows strong correlation with the mixing constant value.

In summary, in this chapter we validated the EMCF method framework using a series of test-cases ranging from pure mixing to a supersonic turbulent jet flame with increasing level complexity using different combinations of the physical models and

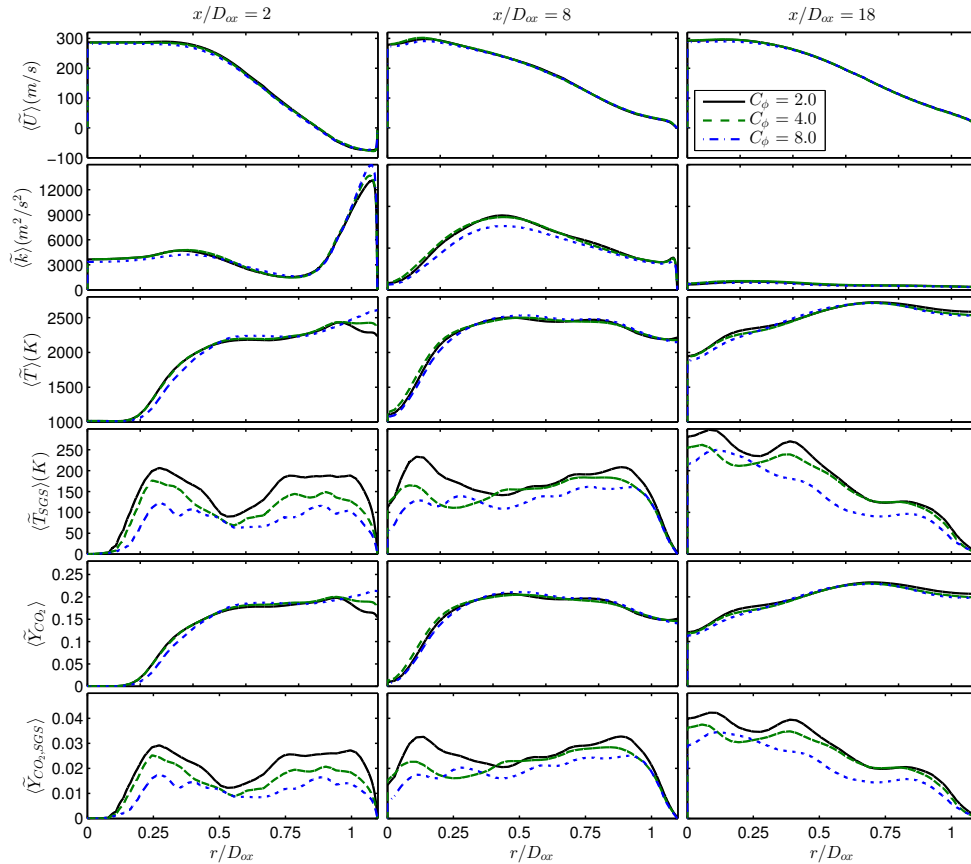


Figure 7.27.: Radial profiles of the time-averaged axial velocity $\langle \tilde{U} \rangle$, time-averaged turbulent kinetic energy $\langle \tilde{k} \rangle$, time-averaged temperature $\langle \tilde{T} \rangle$, time-averaged SGS temperature $\langle \tilde{T}_{SGS} \rangle$, time-averaged CO₂ mass fraction and time-averaged SGS CO₂ mass fraction $\langle \tilde{Y}_{CO_2,SGS} \rangle$ at the axial locations $x/D_{ox} = 2, 8$ and 18 in the model rocket combustor. The model results are obtained for $C_\phi = 2.0, 4.0$ and 8.0 .

their numerical implementations. In general the predictions show good agreement with the experiment for all test-cases for the EMCF-O method with analytical implementation of the IEM mixing model and using Density 2 formulation with gradient limiters. The EMCF method is then used to predict thermo-acoustic instability in the model rocket combustor for the stable and unstable operating conditions. The amplitude and frequency of the pressure fluctuations show very good agreement with the experiment. A parametric study is conducted in the end for the model rocket

combustor to investigate the effect of mixing time scale and number of stochastic fields.

8. CONCLUSIONS

In this study we conduct advance numerical modeling studies of thermo-acoustic instability in self-excited resonance combustor using two popular turbulent combustion models, the flamelet model and the transported PDF method.

For the flamelet model, we first examine the effect of different presumed PDF table integration approaches on flamelet model predictions. The FPV model is chosen as a representative flamelet model, and three different presumed PDF table integration approaches are compared to examine the effect of table integration on flamelet model predictions of two real flames, a laboratory size turbulent free jet flame, Sandia flame D, and a self-excited resonance model rocket combustor. Two different classes of table integration approaches are considered, one preserving laminar flamelet structure during integration and the other not. Three different table integration approaches (LFSP method, FMNPV method, FMNMF method) are employed, among which, the LFSP method preserves the laminar flamelet structures during the integration while the FMNPV method and the FMNMF method do not. The simulation results from the three different table integration approaches have been compared with the available experimental data. In Sandia flame D, the different flamelet table integration approaches have a non-negligible effect except on the velocity fields and mixture fraction. For the progress variable, the LFSP method yields the best agreement with the experiment and the maximum relative error in comparison with the experiment for the three methods is 26% (LFSP method), 29% (FMNPV method), and 30% (FMNMF method). Similar observations are made in the *a priori* and the *a posteriori* testing, with the LFSP method performing relatively better than the other two methods in predicting the mean temperature (LFSP method relative error 22% with experiment) and mass fractions of species CO₂ (relative error 28%), H₂O (relative error 20%) and CO (relative error 32%). The effect of different sources of errors in the

flamelet model is also investigated. In the self-excited rocket combustor, the pressure fluctuation signal from the experiment and its power spectral density is used to validate the numerical simulations using the three flamelet table integration approaches. The level of combustion instability determined from the pressure fluctuation is noticeably affected by the different table integration approaches. The predictions of the frequency and PSD amplitude of the first dominant mode with the LFSP is relatively in better agreement with experiment and the maximum relative difference among the three approaches is close to 100% for the PSD amplitude. The effect of the different table integration approaches on the time-averaged results is found to be relatively small.

Following the study of the effect of the different table integration approaches in the flamelet modeling framework, we conduct simulation studies to examine the physical coupling between transient flame dynamics and thermo-acoustic instability in a self-excited resonance combustor with the LFSP method for presumed-PDF integration. The study is valuable for a thorough understanding of thermo-acoustic instability caused by thermo-acoustic interactions in combustors of high-speed propulsion devices like gas turbines and rockets. Two types of flamelet models are employed for the simulations, the SLF model and the FPV model (and its two variants, FPV-B and FPV-ZV). It is observed that the SLF model correctly predicts the stable operation condition of the combustor but fails to reproduce the unstable condition, while the FPV model correctly captures both the stable and unstable operating conditions. The dramatic difference in the predictions of the SLF model and FPV model of the combustor under unstable operation condition strongly suggests that highly transient flame dynamics, which are missing in the SLF model, have a significant impact on the onset of thermo-acoustic instability. We conduct parametric studies to provide further support to this observation, by examining the effect of eliminating transient flame dynamics in the FPV model, the effect of increasing Da number, and the effect of neglecting mixture fraction fluctuations. A particular local dynamic event, ignition delay, is identified as the major source of the effect of transient flame dynamics on thermo-acoustic instability, by examining local flame behavior in different regions

of the combustor. The reverse effect of thermo-acoustic instability on the transient flame dynamics is also investigated and such an effect is supported by examining the temporal evolution of local flame behavior in conjunction with the pressure wave propagation. The observed two-way coupling between the transient flame dynamics and the thermo-acoustic instability provides a plausible mechanism of the self-excited and sustained thermo-acoustic instability in the combustor. The reported mechanism of thermo-acoustic instability above is identified from the 2D simulations. Such a mechanism will need to be further confirmed in full 3D simulations in future studies.

In the second part of this study, we conduct numerical studies using the transported PDF method. The EMCF method is used to solve the transport equation of the PDF of the thermo-chemical scalars. The EMCF method is extended to account for the compressibility and viscous dissipation effects. In the context of the EMCF method, new physical models and different numerical implementations of the models are discussed. A new mixing model, IPEM model, is introduced to improve the prediction of the evolution of the PDF in comparison to the IEM model which is typically used in the EMCF method. The mathematical consistency of the EMCF method in low Re number flows is discussed. Two different models for density are developed. The primary difference between the two density models is that the one model calculates the molecular weight of the species mixture for each of the stochastic fields individually whereas the second model assumes equal molecular weight of the mixture for each stochastic field and calculates it based on the mean species mass fraction. For the numerical implementation of the mixing models, two approaches are considered. The first approach is an analytical implementation which does not put restrictions on the time step size and the second implementation is the Euler implementation which tends to be numerically unstable if the time step size is too large. For the stochastic term in the SPDE of the thermo-chemical scalars, it is necessary to limit its magnitude in regions of high local gradients to make the numerical discretization scheme robust.

In order to test the different combinations of the above discussed models and their implementations a series of test-cases are considered. The different test cases include, a single-scalar, constant density turbulent mixing in forced homogeneous isotropic turbulence, a subsonic round-jet, a subsonic turbulent jet flame and a supersonic turbulent jet flame. Based on the predictions of these test cases, the best possible combination physical models and their numerical implementations is identified and this combination is used to conduct numerical studies of the model rocket combustor for the stable and unstable operating condition. For both the operating conditions, the EMCF method shows very good agreement with the experiments. Further, parametric studies are conducted to study the effect of mixing time scale and number of stochastic fields on the pressure fluctuation predictions. It is observed that the initial growth of thermo-acoustic instability is affected by changing the number of stochastic fields.

To summarize, the major contributions of this work are:

1. A framework to model thermo-acoustic instability in a self-excited model resonance combustor using detailed chemical kinetics with the flamelet modeling approach to account for turbulence-chemistry interaction has been developed and validated extensively
2. A two-way coupling between transient flame dynamics and thermo-acoustic instability is observed in the combustor which provides a plausible mechanism for the self-excited and self-sustained nature of instability in the combustor
3. To further advance the capability of the transported PDF method using the EMCF method to model compressible turbulent reactive flows, new physical models and their numerical implementation is discussed and validated using a series of test-cases ranging from pure mixing to supersonic turbulent reactive jet

4. The EMCF method is implemented in GEMS, an in-house compressible flow solver, and modeling studies of thermo-acoustic instability are conducted using the transported PDF method for the first time

8.1 Scope for Future Work

Future numerical studies of thermo-acoustic instability in the model rocket combustor using the EMCF method would include a more detailed analysis of the different physics inside the combustor, especially the transient flame dynamics since the transported PDF method has shown the capability to capture these effects in previous studies. It is necessary to incorporate a more detailed reaction mechanism for conducting these studies to capture the correct ignition-delay, extinction and reignition events. 3D numerical studies of the model rocket combustor would help further support the existence of the observed two-way coupling between transient flame dynamics and thermo-acoustic instability.

REFERENCES

- [1] D Santavicca and T Lieuwen. Combustion dynamics in multi-nozzle combustors operating on high-hydrogen fuels. Technical report, Pennsylvania State University, University Park, PA (United States), 2013.
- [2] FEC Culick and V Yang. Overview of combustion instabilities in liquid-propellant rocket engines. *Liquid Rocket Engine Combustion Instability*, 169:3–37, 1995.
- [3] M Fleifil, AM Annaswamy, ZA Ghoneim, and AF Ghoniem. Response of a laminar premixed flame to flow oscillations: A kinematic model and thermoacoustic instability results. *Combustion and Flame*, 106(4):487–510, 1996.
- [4] JWS Rayleigh. The explanation of certain acoustical phenomena. *Nature*, 18(455):319–321, 1878.
- [5] BT Zinn and TC Lieuwen. Combustion instabilities: Basic concepts. *Combustion Instabilities in Gas Turbine Engines: Operational Experience, Fundamental Mechanisms, and Modeling*, 210:3–26, 2005.
- [6] V Sankaran, M Harvazinski, W Anderson, and D Talley. Progress and challenges in liquid rocket combustion stability modeling. Technical report, Air Force Research Lab Edwards AFB, CA, 2012.
- [7] RS Barlow and JH Frank. Effects of turbulence on species mass fractions in methane/air jet flames. *Proceedings of Combustion Institute*, 27(1):1087–1095, 1998.
- [8] CH Schneider, A Dreizler, J Janicka, and EP Hassel. Flow field measurements of stable and locally extinguishing hydrocarbon-fuelled jet flames. *Combustion and Flame*, 135(1):185–190, 2003.
- [9] MS Sweeney, S Hochgreb, MJ Dunn, and RS Barlow. The structure of turbulent stratified and premixed methane/air flames i: Non-swirling flows. *Combustion and Flame*, 159(9):2896–2911, 2012.
- [10] MS Sweeney, S Hochgreb, MJ Dunn, and RS Barlow. The structure of turbulent stratified and premixed methane/air flames ii: Swirling flows. *Combustion and Flame*, 159(9):2912–2929, 2012.
- [11] AR Masri, RW Bilger, and RW Dibble. The local structure of turbulent non-premixed flames near extinction. *Combustion and Flame*, 81(3-4):260–276, 1990.
- [12] AR Masri, RW Dibble, and RS Barlow. The structure of turbulent nonpremixed flames revealed by Raman-Rayleigh-LIF measurements. *Progress in Energy and Combustion Science*, 22(4):307–362, 1996.

- [13] H Wang, M Juddoo, SH Starner, AR Masri, and SB Pope. A novel transient turbulent jet flame for studying turbulent combustion. *Proceedings of the Combustion Institute*, 34(1):1251–1259, 2013.
- [14] S Candel. Combustion dynamics and control: Progress and challenges. *Proceedings of the Combustion Institute*, 29(1):1–28, 2002.
- [15] N Noiray, D Durox, T Schuller, and S Candel. A unified framework for nonlinear combustion instability analysis based on the flame describing function. *Journal of Fluid Mechanics*, 615:139–167, 2008.
- [16] AP Dowling and R Stow. Acoustic analysis of gas turbine combustors. *Journal of Propulsion and Power*, 19(5):751–764, 2003.
- [17] CF Silva, F Nicoud, T Schuller, D Durox, and S Candel. Combining a Helmholtz solver with the flame describing function to assess combustion instability in a premixed swirled combustor. *Combustion and Flame*, 160(9):1743–1754, 2013.
- [18] SB Pope. *Turbulent flows*, 2001.
- [19] L Crocco. Aspects of combustion stability in liquid propellant rocket motors part i: fundamentals. low frequency instability with monopropellants. *Journal of the American Rocket Society*, 21(6):163–178, 1951.
- [20] AP Dowling and S Hubbard. Instability in lean premixed combustors. *Proceedings of the Institution of Mechanical Engineers, Part A: Journal of Power and Energy*, 214(4):317–332, 2000.
- [21] AP Dowling. Modeling and control of combustion oscillations. In *Proceedings of the ASME Turbo Expo*, 2005.
- [22] J Eckstein and T Sattelmayer. Low-order modeling of low-frequency combustion instabilities in aeroengines. *Journal of Propulsion and Power*, 22(2):425–432, 2006.
- [23] M Summerfield. A theory of unstable combustion in liquid propellant rocket systems. *Journal of the American Rocket Society*, 21(5):108–114, 1951.
- [24] FE Marble and DW Cox. Servo-stabilization of low-frequency oscillations in a liquid bipropellant rocket motor. *ARS Journal*, 23:63–74, 1953.
- [25] L Crocco and S Cheng. Theory of combustion instability in liquid propellant rocket motors. Technical report, Princeton University, NJ, 1956.
- [26] BT Zinn and ME Lores. Application of the galerkin method in the solution of non-linear axial combustion instability problems in liquid rockets. *Combustion Science and Technology*, 4(1):269–278, 1971.
- [27] T Poinsot and SM Candel. A nonlinear model for ducted flame combustion instabilities. *Combustion Science and Technology*, 61(4-6):121–153, 1988.
- [28] FE Marble and SM Candel. An analytical study of the non-steady behavior of large combustors. In *Symposium (International) on Combustion*, volume 17, pages 761–769. Elsevier, 1979.

- [29] AP Dowling. Nonlinear self-excited oscillations of a ducted flame. *Journal of Fluid Mechanics*, 346:271–290, 1997.
- [30] AP Dowling. A kinematic model of a ducted flame. *Journal of Fluid Mechanics*, 394:51–72, 1999.
- [31] SR Stow and AP Dowling. Low-order modelling of thermoacoustic limit cycles. *ASME Paper No. GT2004-54245*, 2004.
- [32] T Lieuwen. Modeling premixed combustion-acoustic wave interactions: A review. *Journal of Propulsion and Power*, 19(5):765–781, 2003.
- [33] BE Launder and DB Spalding. The numerical computation of turbulent flows. *Computer Methods in Applied Mechanics and Engineering*, 3(2):269–289, 1974.
- [34] T Shih, WW Liou, A Shabbir, Z Yang, and J Zhu. A new k- eddy viscosity model for high reynolds number turbulent flows. *Computers & Fluids*, 24(3):227–238, 1995.
- [35] V Yakhot, SA Orszag, S Thangam, TB Gatski, and CG Speziale. Development of turbulence models for shear flows by a double expansion technique. *Physics of Fluids A: Fluid Dynamics*, 4(7):1510–1520, 1992.
- [36] DC Wilcox. Turbulence modeling for CFD. *La Canada, California: DCW Industries*, 5354:124–128, 1998.
- [37] DC Wilcox. Formulation of the $k-\omega$ turbulence model revisited. *AIAA Journal*, 46(11):2823–2838, 2008.
- [38] BE Launder, G Reece, and W Rodi. Progress in the development of a reynolds-stress turbulence closure. *Journal of Fluid Mechanics*, 68(3):537–566, 1975.
- [39] J Smagorinsky. General circulation experiments with the primitive equations: I. the basic experiment. *Monthly Weather Review*, 91(3):99–164, 1963.
- [40] M Germano, U Piomelli, P Moin, and WH Cabot. A dynamic subgrid-scale eddy viscosity model. *Physics of Fluids A: Fluid Dynamics*, 3(7):1760–1765, 1991.
- [41] DK Lilly. A proposed modification of the Germano subgrid-scale closure method. *Physics of Fluids A: Fluid Dynamics*, 4(3):633–635, 1992.
- [42] M Strelets. Detached eddy simulation of massively separated flows. In *39th Aerospace sciences meeting and exhibit*, page 879, 2001.
- [43] D Veynante and T Poinso. Large eddy simulation of combustion instabilities in turbulent premixed burners. *Annual Research Briefs*, pages 253–274, 1997.
- [44] O Colin, F Ducros, D Veynante, and T Poinso. A thickened flame model for large eddy simulations of turbulent premixed combustion. *Physics of Fluids*, 12(7):1843–1863, 2000.
- [45] S Menon, PA McMurtry, and AR Kerstein. A linear eddy mixing model for large eddy simulation of turbulent combustion, 1993.

- [46] CE Smith and AD Leonard. CFD modeling of combustion instability in pre-mixed axisymmetric combustors. *ASME paper*, (97-GT):305, 1997.
- [47] GA Richards and MC Janus. Characterization of oscillations during premix gas turbine combustion. In *ASME 1997 International Gas Turbine and Aeroengine Congress and Exhibition*, pages V002T06A033–V002T06A033. American Society of Mechanical Engineers, 1997.
- [48] SJ Brookes, RS Cant, IDJ Dupere, and AP Dowling. Computational modelling of self-excited combustion instabilities. In *ASME Turbo Expo 2000: Power for Land, Sea, and Air*, pages V002T02A024–V002T02A024. American Society of Mechanical Engineers, 2000.
- [49] PJ Langhorne. Reheat buzz: an acoustically coupled combustion instability. part 1. experiment. *Journal of Fluid Mechanics*, 193:417–443, 1988.
- [50] S Menon and WH Jou. Large-eddy simulations of combustion instability in an axisymmetric ramjet combustor. *Combustion Science and Technology*, 75(1-3):53–72, 1991.
- [51] UG Hegde, D Reuter, and BT Zinn. Fluid mechanically coupled combustion-instabilities in ramjet combustors. 1987.
- [52] C Angelberger, D Veynante, and F Egolfopoulos. LES of chemical and acoustic forcing of a premixed dump combustor. *Flow, Turbulence and Combustion*, 65(2):205–222, 2000.
- [53] CE Martin, L Benoit, Y Sommerer, F Nicoud, and T Poinso. Large-eddy simulation and acoustic analysis of a swirled staged turbulent combustor. *AIAA Journal*, 44(4):741–750, 2006.
- [54] B Franzelli, E Riber, LYM Gicquel, and T Poinso. Large eddy simulation of combustion instabilities in a lean partially premixed swirled flame. *Combustion and Flame*, 159(2):621–637, 2012.
- [55] P Schmitt, T Poinso, B Schuermans, and KP Geigle. Large-eddy simulation and experimental study of heat transfer, nitric oxide emissions and combustion instability in a swirled turbulent high-pressure burner. *Journal of Fluid Mechanics*, 570:17–46, 2007.
- [56] K Doebbeling, A Eroglu, F Joos, and J Hellat. Novel technologies for natural gas combustion in turbine systems. *Eurogas*, 99:25–27, 1999.
- [57] P Wolf, R Balakrishnan, G Staffelbach, LYM Gicquel, and T Poinso. Using LES to study reacting flows and instabilities in annular combustion chambers. *Flow, Turbulence and Combustion*, 88(1):191–206, 2012.
- [58] S Srinivasan, R Ranjan, and S Menon. Flame dynamics during combustion instability in a high-pressure, shear-coaxial injector combustor. *Flow, Turbulence and Combustion*, 94(1):237–262, 2015.
- [59] YC Yu, JC Sisco, S Rosen, A Madhav, and WE Anderson. Spontaneous longitudinal combustion instability in a continuously variable resonance combustor. *Journal of Propulsion and Power*, 28(5):876–887, 2012.

- [60] P Tudisco, R Ranjan, S Menon, S Jaensch, and W Polifke. Application of the time-domain impedance boundary condition to large-eddy simulation of combustion instability in a shear-coaxial high pressure combustor. *Flow, Turbulence and Combustion*, 99(1):185–207, 2017.
- [61] Y Huang, HG Sung, SY Hsieh, and V Yang. Large-eddy simulation of combustion dynamics of lean-premixed swirl-stabilized combustor. *Journal of Propulsion and Power*, 19(5):782–794, 2003.
- [62] N Peters. *Turbulent combustion*. Cambridge university press, 2000.
- [63] JC Broda, S Seo, RJ Santoro, G Shirhattikar, and V Yang. An experimental study of combustion dynamics of a premixed swirl injector. In *Symposium (International) on Combustion*, volume 27, pages 1849–1856. Elsevier, 1998.
- [64] ME Harvazinski, C Huang, V Sankaran, TW Feldman, WE Anderson, CL Merkle, and DG Talley. Coupling between hydrodynamics, acoustics, and heat release in a self-excited unstable combustor. *Physics of Fluids*, 27(4):045102, 2015.
- [65] SV Sardeshmukh, SD Heister, and WE Anderson. Prediction of combustion instability with detailed chemical kinetics. In *53rd AIAA Aerospace Sciences Meeting*, page 1826, 2015.
- [66] S Matsuyama, D Hori, T Shimizu, S Tachibana, S Yoshida, and Y Mizobuchi. Large-eddy simulation of high-frequency combustion instability in a single-element atmospheric combustor. *Journal of Propulsion and Power*, 2016.
- [67] T Shimizu, S Tachibana, S Yoshida, D Hori, S Matsuyama, and Y Mizobuchi. Intense tangential pressure oscillations inside a cylindrical chamber. *AIAA Journal*, 49(10):2272–2281, 2011.
- [68] Y Huang and V Yang. Dynamics and stability of lean-premixed swirl-stabilized combustion. *Progress in Energy and Combustion Science*, 35(4):293–364, 2009.
- [69] J O’Connor, V Acharya, and T Lieuwen. Transverse combustion instabilities: Acoustic, fluid mechanic, and flame processes. *Progress in Energy and Combustion Science*, 49:1–39, 2015.
- [70] T Poinsot. Prediction and control of combustion instabilities in real engines. *Proceedings of the Combustion Institute*, 36(1):1–28, 2017.
- [71] SB Pope. PDF methods for turbulent reactive flows. *Progress in Energy and Combustion Science*, 11(2):119–192, 1985.
- [72] N Peters. Laminar diffusion flamelet models in non-premixed turbulent combustion. *Progress in Energy and Combustion Science*, 10(3):319–339, 1984.
- [73] CD Pierce and P Moin. Progress-variable approach for large-eddy simulation of non-premixed turbulent combustion. *Journal of Fluid Mechanics*, 504:73–97, 2004.
- [74] L Valiño. A field monte carlo formulation for calculating the probability density function of a single scalar in a turbulent flow. *Flow, Turbulence and Combustion*, 60(2):157–172, 1998.

- [75] YC Yu. *Experimental and analytical investigations of longitudinal combustion instability in a continuously variable resonance combustor (CVRC)*. PhD thesis, Purdue University, 2009.
- [76] JS Hardi, WZ Hallum, C Huang, and WE Anderson. Approaches for comparing numerical simulation of combustion instability and flame imaging. *Journal of Propulsion and Power*, 32(2):279–294, 2016.
- [77] KJ Miller. Experimental study of longitudinal instabilities in a single element rocket combustor. Master’s thesis, 2005.
- [78] JC Sisco. *Measurement and analysis of an unstable model rocket combustor*. PhD thesis, Purdue University, 2007.
- [79] ME Harvazinski. *Modeling self-excited combustion instabilities using a combination of two-and three-dimensional simulations*. PhD thesis, Purdue University, 2012.
- [80] CK Westbrook and FL Dryer. Simplified reaction mechanisms for the oxidation of hydrocarbon fuels in flames. *Combustion Science and Technology*, 27(1-2):31–43, 1981.
- [81] M Frenklach, H Wang, C Yu, M Goldenberg, C Bowman, R Hanson, D Davidson, E Chang, G Smith, D Golden, et al. Gri-mech-1.2, an optimized detailed chemical reaction mechanism for methane combustion. *Gas Research Institute*, 1995.
- [82] R Garby, L Selle, and T Poinso. Large-eddy simulation of combustion instabilities in a variable-length combustor. *Comptes Rendus Mécanique*, 341(1-2):220–229, 2013.
- [83] B Franzelli, E Riber, M Sanjosé, and Thierry Poinso. A two-step chemical scheme for kerosene–air premixed flames. *Combustion and Flame*, 157(7):1364–1373, 2010.
- [84] WP Jones and RP Lindstedt. Global reaction schemes for hydrocarbon combustion. *Combustion and Flame*, 73(3):233–249, 1988.
- [85] ME Harvazinski, DG Talley, and V Sankaran. Comparison of laminar and linear eddy model closures for combustion instability simulations. *AIAA*, 3842:2015, 2015.
- [86] D Li, G Xia, V Sankaran, and CL Merkle. Computational framework for complex fluid physics applications. In *Computational Fluid Dynamics 2004*, pages 619–624. Springer, 2006.
- [87] C Lian, G Xia, and CL Merkle. Solution-limited time stepping to enhance reliability in CFD applications. *Journal of Computational Physics*, 228(13):4836–4857, 2009.
- [88] C Lian, G Xia, and CL Merkle. Impact of source terms on reliability of CFD algorithms. *Computers & Fluids*, 39(10):1909–1922, 2010.
- [89] H Pitsch. Flamemaster: A C++ computer program for 0D combustion and 1D laminar flame calculations. <http://web.stanford.edu/group/pitsch/FlameMaster.htm>, 1998.

- [90] C Han and H Wang. A comparison of different approaches to integrate flamelet tables with presumed-shape PDF in flamelet models for turbulent flames. *Combustion Theory and Modelling*, 21(4):603–629, 2017.
- [91] M Ihme, CM Cha, and H Pitsch. Prediction of local extinction and re-ignition effects in non-premixed turbulent combustion using a flamelet/progress variable approach. *Proceedings of the Combustion Institute*, 30(1):793–800, 2005.
- [92] M Ihme and H Pitsch. Prediction of extinction and reignition in nonpremixed turbulent flames using a flamelet/progress variable model: 1. A priori study and presumed PDF closure. *Combustion and Flame*, 155(1):70–89, 2008.
- [93] M Ihme and H Pitsch. Prediction of extinction and reignition in nonpremixed turbulent flames using a flamelet/progress variable model: 2. Application in LES of Sandia Flames D and E. *Combustion and Flame*, 155(1):90–107, 2008.
- [94] Amirreza Saghafian, Lee Shunn, David A Philips, and Frank Ham. Large Eddy Simulations of the hifire scramjet using a compressible flamelet/progress variable approach. *Proceedings of the Combustion Institute*, 35(2):2163–2172, 2015.
- [95] César Dopazo and Edward E O’Brien. An approach to the autoignition of a turbulent mixture. *Acta Astronautica*, 1(9-10):1239–1266, 1974.
- [96] J Janicka, W Kolbe, and W Kollmann. Closure of the transport equation for the probability density function of turbulent scalar fields. *Journal of Non-Equilibrium Thermodynamics*, 4(1):47–66, 1979.
- [97] PA Nooren, HA Wouters, TWJ Peeters, DJEM Roekaerts, U Maas, and D Schmidt. Monte carlo pdf modelling of a turbulent natural-gas diffusion flame. 1997.
- [98] S Subramaniam and SB Pope. A mixing model for turbulent reactive flows based on euclidean minimum spanning trees. *Combustion and Flame*, 115(4):487–514, 1998.
- [99] BJ Delarue and SB Pope. Application of PDF methods to compressible turbulent flows. *Physics of Fluids*, 9(9):2704–2715, 1997.
- [100] BJ Delarue and SB Pope. Calculations of subsonic and supersonic turbulent reacting mixing layers using probability density function methods. *Physics of Fluids*, 10(2):487–498, 1998.
- [101] Heeseok Koo, Pratik Donde, and Venkat Raman. A quadrature-based les/transported probability density function approach for modeling supersonic combustion. *Proceedings of the Combustion Institute*, 33(2):2203–2210, 2011.
- [102] A Banaeizadeh, Z Li, and FA Jaber. Compressible scalar filtered mass density function model for high-speed turbulent flows. *AIAA Journal*, 49(10):2130–2143, 2011.
- [103] L Valiño, R Mustata, and KB Letaief. Consistent behavior of eulerian monte carlo fields at low reynolds numbers. *Flow, Turbulence and Combustion*, 96(2):503–512, 2016.

- [104] Vladimir Sabelnikov and Olivier Soulard. Rapidly decorrelating velocity-field model as a tool for solving one-point fokker-planck equations for probability density functions of turbulent reactive scalars. *Physical Review E*, 72(1):016301, 2005.
- [105] J Villiermaux and JC Devillon. Représentation de la coalescence et de la redispersion des domaines de ségrégation dans un fluide par un modele dinteraction phénoménologique. In *Second International Symposium on Chemical Reaction Engineering*, Elsevier, New York, pages 1–13, 1972.
- [106] WP Jones and VN Prasad. Large eddy simulation of the Sandia Flame series (D–F) using the eulerian stochastic field method. *Combustion and Flame*, 157(9):1621–1636, 2010.
- [107] WP Jones, AJ Marquis, and VN Prasad. Les of a turbulent premixed swirl burner using the eulerian stochastic field method. *Combustion and Flame*, 159(10):3079–3095, 2012.
- [108] Amer Avdić, Guido Kuenne, Francesca di Mare, and Johannes Janicka. Les combustion modeling using the eulerian stochastic field method coupled with tabulated chemistry. *Combustion and Flame*, 175:201–219, 2017.
- [109] Werner JA Dahm, Kenneth B Southerland, and Kenneth A Buch. Direct, high resolution, four-dimensional measurements of the fine scale structure of sc 1 molecular mixing in turbulent flows. *Physics of Fluids A: Fluid Dynamics*, 3(5):1115–1127, 1991.
- [110] IA Dodoulas and S Navarro-Martinez. Large eddy simulation of premixed turbulent flames using the probability density function approach. *Flow, turbulence and combustion*, 90(3):645–678, 2013.
- [111] WP Jones, AJ Marquis, and F Wang. Large eddy simulation of a premixed propane turbulent bluff body flame using the eulerian stochastic field method. *Fuel*, 140:514–525, 2015.
- [112] Cheng Gong, Mehdi Jangi, Xue-Song Bai, Jian-Han Liang, and Ming-Bo Sun. Large eddy simulation of hydrogen combustion in supersonic flows using an eulerian stochastic fields method. *International Journal of Hydrogen Energy*, 42(2):1264–1275, 2017.
- [113] T Poinso and D Veynante. *Theoretical and numerical combustion*. RT Edwards, Inc., 2005.
- [114] Haifeng Wang, Pei Zhang, and Tejas Pant. Consistency and convergence of eulerian monte carlo field method for solving transported probability density function equation in turbulence modeling. *Physics of Fluids*, 30(11):115106, 2018.
- [115] Haifeng Wang, Tejas Pant, and Pei Zhang. Les/pdf modeling of turbulent premixed flames with locally enhanced mixing by reaction. *Flow, Turbulence and Combustion*, 100(1):147–175, 2018.
- [116] S Venkateswaran and CL Merkle. Alaa 95-007% dual time stepping and preconditioning for unsteady computations. 1995.

- [117] Tejas Pant, Chao Han, and Haifeng Wang. Examination of errors of table integration in flamelet/progress variable modeling of a turbulent non-premixed jet flame. *Applied Mathematical Modelling*, 72:369–384, 2019.
- [118] Tejas Pant, Chao Han, and Haifeng Wang. Computational investigations of the coupling between transient flame dynamics and thermo-acoustic instability in a self-excited resonance combustor. *Combustion Theory and Modelling*, pages 1–31, 2019.
- [119] C Olbricht, F Hahn, A Ketelheun, and J Janicka. Strategies for presumed PDF modeling for LES with premixed flamelet-generated manifolds. *Journal of Turbulence*, 11(38):1–18, 2010.
- [120] PAM Kalt, YM Al-Abdell, AR Masri, and RS Barlow. Swirling turbulent non-premixed flames of methane: flow field and compositional structure. *Proceedings of the Combustion Institute*, 29(2):1913–1919, 2002.
- [121] YM Al-Abdell and AR Masri. Stability characteristics and flowfields of turbulent non-premixed swirling flames. *Combustion Theory and Modelling*, 7(4):731–766, 2003.
- [122] H Pitsch and H Steiner. Large eddy simulation of a turbulent piloted methane/air diffusion flame (Sandia Flame D). *Physics of Fluids*, 12(10):2541–2554, 2000.
- [123] MRH Sheikhi, TG Drozda, P Givi, FA Jaber, and SB Pope. Large eddy simulation of a turbulent nonpremixed piloted methane jet flame (Sandia Flame D). *Proceedings of the Combustion Institute*, 30(1):549–556, 2005.
- [124] AW Vreman, BA Albrecht, JA Van Oijen, LPH De Goey, and RJM Bastiaans. Premixed and nonpremixed generated manifolds in large-eddy simulation of Sandia Flame D and F. *Combustion and Flame*, 153(3):394–416, 2008.
- [125] MB Nik, SL Yilmaz, P Givi, MR H. Sheikhi, and SB Pope. Simulation of Sandia Flame D using velocity-scalar filtered density function. *AIAA Journal*, 48(7):1513–1522, 2010.
- [126] Y Ge, MJ Cleary, and AY Klimenko. A comparative study of Sandia Flame series (D–F) using sparse-lagrangian MMC modelling. *Proceedings of the Combustion Institute*, 34(1):1325–1332, 2013.
- [127] E Süli and DF Mayers. *An introduction to numerical analysis*. Cambridge University Press, 2003.
- [128] FS Lien, H Liu, E Chui, and CJ McCartney. Development of an analytical β -function pdf integration algorithm for simulation of non-premixed turbulent combustion. *Flow, turbulence and combustion*, 83(2):205–226, 2009.
- [129] Timothy Barth and Dennis Jespersen. The design and application of upwind schemes on unstructured meshes. In *27th Aerospace sciences meeting*, page 366, 1989.
- [130] Richard H Pletcher, John C Tannehill, and Dale Anderson. *Computational fluid mechanics and heat transfer*. CRC Press, 2012.

- [131] PL Roe. Approximate riemann solvers, parameter vectors, and difference schemes. *Journal of Computational Physics*, 43(2):357–372, 1981.
- [132] CR Mitchell. Improved reconstruction schemes for the navier-stokes equations on unstructured meshes. *AIAA paper*, 642:1994, 1994.
- [133] DSK Kapilavai. *Unsteady computational analysis of shrouded plug nozzle flows and reacting impinging jets*. PhD thesis, Purdue University, 2011.
- [134] X Zeng. *Convergence and Robustness Issues in Computational Fluids*. PhD thesis, University of Tennessee, 2004.
- [135] W J S Ramaekers, J A van Oijen, and L P H De Goey. A priori testing of flamelet generated manifolds for turbulent partially premixed methane/air flames. *Flow, Turbulence and Combustion*, 84:439–458, 2010.
- [136] Yuntao Chen and Matthias Ihme. Large-eddy simulation of a piloted premixed jet burner. *Combustion and Flame*, 160:2896–2910, 2013.
- [137] Yee Chee See and Matthias Ihme. Large eddy simulation of a partially-premixed gas turbine model combustor. *Proceedings of the Combustion Institute*, 35:1225–1234, 2015.
- [138] Konstantin A Kemenov, Haifeng Wang, and Stephen B Pope. Modelling effects of subgrid-scale mixture fraction variance in LES of a piloted diffusion flame. *Combustion Theory and Modelling*, 16(4):611–638, 2012.
- [139] Guillaume Balarac, Heinz Pitsch, and Venkat Raman. Development of a dynamic model for the subfilter scalar variance using the concept of optimal estimators. *Physics of fluids*, 20(3):035114, 2008.
- [140] Charles D Pierce and Parviz Moin. A dynamic model for subgrid-scale variance and dissipation rate of a conserved scalar. *Physics of Fluids*, 10(12):3041–3044, 1998.
- [141] C Jiménez, F Ducros, Benedicte Cuenot, and Benoit Bédard. Subgrid scale variance and dissipation of a scalar field in large eddy simulations. *Physics of Fluids*, 13(6):1748–1754, 2001.
- [142] Tejas Pant, Cheng Huang, Chao Han, Swanand V Sardeshmukh, William E Anderson, and Haifeng Wang. Flamelet modeling studies of a continuously variable resonance combustor. In *54th AIAA Aerospace Sciences Meeting*, page 1941, 2016.
- [143] R Schefer and R Dibble. Rayleigh scattering measurements of mixture fraction in a turbulent nonreacting propane jet. In *24th Aerospace Sciences Meeting*, page 278, 1986.
- [144] RW Schefer, V Hartmann, and RW Dibble. Conditional sampling of velocity in a turbulent nonpremixed propane jet. *AIAA journal*, 25(10):1318–1330, 1987.
- [145] R Cabra, J-Y Chen, RW Dibble, AN Karpetsis, and RS Barlow. Lifted methane–air jet flames in a vitiated coflow. *Combustion and Flame*, 143(4):491–506, 2005.

- [146] Juan Li, Zhenwei Zhao, Andrei Kazakov, and Frederick L Dryer. An updated comprehensive kinetic model of hydrogen combustion. *International journal of chemical kinetics*, 36(10):566–575, 2004.
- [147] John S Evans and Charles J Schexnayder. Influence of chemical kinetics and unmixedness on burning in supersonic hydrogen flames. *AIAA journal*, 18(2):188–193, 1980.
- [148] Tejas Pant and Haifeng Wang. Flamelet modeling of transverse thermo-acoustic instability in a multi-element combustor. In *57th AIAA Aerospace Sciences Meeting*, 2019.
- [149] Tejas Pant and Haifeng Wang. Transported pdf modeling of thermo-acoustic instability in a self-excited model rocket combustor using eulerian monte carlo fields method. In *AIAA Scitech 2019 Forum*, page 1496, 2019.
- [150] J Xu and SB Pope. Assessment of numerical accuracy of pdf/monte carlo methods for turbulent reacting flows. *Journal of Computational Physics*, 152(1):192–230, 1999.
- [151] Haifeng Wang and Stephen B Pope. Time-averaging strategies in the finite-volume/particle hybrid algorithm for the joint pdf equation of turbulent reactive flows. *Combustion Theory and Modelling*, 12(3):529–544, 2008.
- [152] Haifeng Wang, Pei Zhang, and Tejas Pant. Consistency and convergence of eulerian monte carlo field method for solving transported probability density function equation in turbulence modeling. *Physics of Fluids*, 30(11):115106, 2018.
- [153] Radu Mustata, Luis Valiño, Carmen Jiménez, WP Jones, and S Bondi. A probability density function eulerian monte carlo field method for large eddy simulations: application to a turbulent piloted methane/air diffusion flame (sandia d). *Combustion and Flame*, 145(1-2):88–104, 2006.
- [154] WP Jones and S Navarro-Martinez. Large eddy simulation of autoignition with a subgrid probability density function method. *Combustion and Flame*, 150(3):170–187, 2007.
- [155] J Jaishree and DC Haworth. Comparisons of lagrangian and eulerian pdf methods in simulations of non-premixed turbulent jet flames with moderate-to-strong turbulence-chemistry interactions. *Combustion Theory and Modelling*, 16(3):435–463, 2012.

A. Derivation and Analysis of Piece-Wise Semi-Analytical (PWSA) Integration Scheme

To integrate equation (4.16) numerically, we assume a piece-wise linear function of $\phi(\xi)$ (flamelet solutions) between the known values of $\phi(\xi_i)$ at the grid points ξ_i in the mixture fraction space,

$$\phi_i(\xi) \approx c_i \xi + d_i, \quad (\xi_i \leq \xi \leq \xi_{i+1}), \quad (\text{A.1})$$

where $c_i = (\phi_{i+1} - \phi_i)/(\xi_{i+1} - \xi_i)$ and $d_i = (\phi_i \xi_{i+1} - \phi_{i+1} \xi_i)/(\xi_{i+1} - \xi_i)$. Substituting Equation (A.1) into Equation (4.16), we obtain

$$\widetilde{\phi}^n(\widetilde{\xi}, \widetilde{\xi}^{n^2}) \approx \sum_{i=1}^{n_\xi-1} \mathbb{I}_i^n, \quad (\text{A.2})$$

in which

$$\begin{aligned} \mathbb{I}_i^n &= \int_{\xi_i}^{\xi_{i+1}} \phi_i^n(\eta) \widetilde{f}_\xi(\eta; a, b) d\eta = \int_{\xi_i}^{\xi_{i+1}} (c_i \eta + d_i)^n \widetilde{f}_\xi(\eta; a, b) d\eta \\ &= \sum_{k=0}^n \frac{n!}{k!(n-k)!} c_i^k d_i^{(n-k)} \int_{\xi_i}^{\xi_{i+1}} \eta^k \widetilde{f}_\xi(\eta; a, b) d\eta. \end{aligned} \quad (\text{A.3})$$

The last integration term in Equation (A.3) can be evaluated analytically by using the β -PDF in Equation (4.17),

$$\begin{aligned} \int_{\xi_i}^{\xi_{i+1}} \eta^k \widetilde{f}_\xi(\eta; a, b) d\eta &= \int_{\xi_i}^{\xi_{i+1}} \eta^k \frac{\eta^{a-1} (1-\eta)^{b-1}}{B(a, b)} d\eta \\ &= \frac{B(a+k, b)}{B(a, b)} \int_{\xi_i}^{\xi_{i+1}} \widetilde{f}_\xi(\eta; a+k, b) d\eta \\ &= \frac{B(\xi_{i+1}; a+k, b) - B(\xi_i; a+k, b)}{B(a, b)}, \end{aligned} \quad (\text{A.4})$$

where $B(\xi_i; a+k, b)$ is the incomplete β function. Substituting equations (A.3) and (A.4) into (A.2), we obtain the final integration scheme,

$$\widetilde{\phi}^n(\widetilde{\xi}, \widetilde{\xi}^{n^2}) \approx \sum_{i=1}^{n_\xi-1} \sum_{k=0}^n \frac{n!}{k!(n-k)!} c_i^k d_i^{(n-k)} \cdot \frac{B(\xi_{i+1}; a+k, b) - B(\xi_i; a+k, b)}{B(a, b)}. \quad (\text{A.5})$$

The advantage of the above integration scheme is that it can be done analytically (assuming that the β functions can be obtained analytically) for any order of moment and it does not generate singularities at conditions where $\tilde{f}_\xi(\eta; a, b) \rightarrow \infty$. We call this β -PDF integration scheme a piece-wise semi-analytical (PWSA) integration scheme.

The formal second-order accuracy of the PWSA scheme can be readily obtained by performing a leading order analysis with Taylor series expansion. The error arises from the linear approximation in Equation (A.1). An approximation for $\phi_i(\xi)$ carrying the leading order error based on Taylor series expansion is

$$\phi_i(\xi) \approx c_i(\xi - \xi_i) + (d_i + c_i\xi_i) + \frac{1}{2}\phi_i''(\xi_i) \cdot (\xi - \xi_i)^2 + \dots, \quad (\xi_i \leq \xi \leq \xi_{i+1}), \quad (\text{A.6})$$

where $\phi_i''(\xi_i) = \partial^2\phi_i/\partial\xi^2|_{\xi=\xi_i}$ and $\Delta\xi = \xi_{i+1} - \xi_i$ (uniform grid spacing is assumed in the error analysis). Substituting equation (A.6) into (4.16) and retaining leading-order error terms, we can obtain the leading-order error involved in the PWSA scheme as

$$\begin{aligned} \epsilon &\approx \sum_{i=1}^{n_\xi-1} \frac{1}{2}\phi_i''(\xi_i) \cdot \int_{\xi_i}^{\xi_{i+1}} n(c_i\eta + d_i)^{n-1}(\eta - \xi_i)^2 \tilde{f}_\xi(\eta; a, b) d\eta \quad (\text{A.7}) \\ &\approx \frac{1}{6} \sum_{i=1}^{n_\xi-1} \phi_i''(\xi_i) \cdot n(c_i\xi_{i,m} + d_i)^{n-1} \tilde{f}_\xi(\xi_{i,m}; a, b) \Delta\xi \cdot \Delta\xi^2 \\ &= \frac{1}{6} C_I \cdot \Delta\xi^2, \end{aligned}$$

where $\xi_{i,m}$ is some number between $[\xi_i, \xi_{i+1}]$ and C_I is an approximation to the integral $\int_0^1 n\phi''\phi^{n-1}\tilde{f}_\xi d\eta$ that is independent of $\Delta\xi$. Thus, the formal second-order accuracy $O(\Delta\xi^2)$ is established for the PWSA scheme.

B. Formulation of Jacobians $\bar{\Gamma}_p$ and ${}^{-1}_p$

In terms of Q_p , the pseudo derivative can be written as $\partial Q/\partial\tau = (\partial Q/\partial Q_p)(\partial Q_p/\partial\tau) = \Gamma_p(\partial Q_p/\partial\tau)$ where the jacobian $\Gamma_p = \partial Q/\partial Q_p$ [79] is given by,

The terms in $\bar{\Gamma}_p$ are,

$$\begin{aligned}\rho_{\bar{p}} &= \frac{\partial \bar{\rho}}{\partial \bar{p}}, \\ \rho_{T^n} &= \frac{\partial \bar{\rho}}{\partial T^n}, \\ \rho_{Y_i^n} &= \frac{\partial \bar{\rho}}{\partial Y_i^n}, \\ H_{\bar{p}}^n &= \rho_{\bar{p}} h^{0n} + \bar{\rho} h_{\bar{p}}^{0n} - 1, \\ H_{T^m}^n &= \rho_{T^m} h^{0n} + \bar{\rho} h_{T^m}^{0n}, \\ H_{Y_i^m}^n &= \rho_{Y_i^m} h^{0n} + \bar{\rho} h_{Y_i^m}^{0n}, \\ \gamma_{i,\bar{p}}^n &= \rho_{\bar{p}} Y_i^n + \bar{\rho} Y_{i,\bar{p}}^n, \\ \gamma_{i,T^m}^n &= \rho_{T^m} Y_i^n + \bar{\rho} Y_{i,T^m}^n, \\ \gamma_{i,Y_j^m}^n &= \rho_{Y_j^m} Y_i^n + \bar{\rho} Y_{i,Y_j^m}^n,\end{aligned}$$

where,

$$\begin{aligned}h_{\bar{p}}^{0n} &= \frac{\partial h^{0n}}{\partial \bar{p}} = 0, \\ h_{T^m}^{0n} &= \frac{\partial h^{0n}}{\partial T^m} = \frac{\partial h^n}{\partial T^m} = \begin{cases} \sum_{i=1}^{N_s} h_{i,T^m}^n Y_i^n, & \text{if } n = m \\ 0, & \text{if } n \neq m \end{cases} \\ h_{Y_i^m}^{0n} &= \frac{\partial h^{0n}}{\partial Y_i^m} = \frac{\partial h^n}{\partial Y_i^m} = \begin{cases} (h_i^n - h_{N_s}^n), & \text{if } n = m \\ 0, & \text{if } n \neq m \end{cases} \\ Y_{i,\bar{p}}^n &= \frac{\partial Y_i^n}{\partial \bar{p}} = 0, \\ Y_{i,T^m}^n &= \frac{\partial Y_i^n}{\partial T^m} = 0, \\ Y_{i,Y_j^m}^n &= \frac{\partial Y_i^n}{\partial Y_j^m} = \begin{cases} \delta_{ij}. & \text{if } n = m \\ 0. & \text{if } n \neq m \end{cases}\end{aligned}$$

The formulations for the partial derivatives $\partial \bar{\rho} / \partial \bar{p}$, $\partial \bar{\rho} / \partial T^n$ and $\partial \bar{\rho} / \partial Y_i^n$ for Method 1 and Method 2 of calculation of the filtered density $\bar{\rho}$ have been discussed in Section 3.8.1 and Section 3.8.2.

The expression for jacobian $\bar{\Gamma}_p^{-1}$ is,

where,

$$\begin{aligned}
\Pi_i^{h^0} &= \prod_{i=1}^{N_f} h_{T^i}^{0^i}, \\
\Pi_{i,j}^{h^0} &= \prod_{i=1, i \neq j}^{N_f} h_{T^i}^{0^i}, \\
\Pi_{i,j,k}^{h^0} &= \prod_{i=1, i \neq j, i \neq k}^{N_f} h_{T^i}^{0^i}, \\
|\vec{U}|^2 &= \tilde{u}^2 + \tilde{v}^2 + \tilde{w}^2, \\
d' &= \sum_{m=1}^{N_f} \Pi_{r,m}^{h^0} \rho_{T^m} + \Pi_m^{h^0} \bar{\rho} \rho'_p, \\
\bar{\Gamma}_{\bar{p}_{1,1}}^{-1} &= \frac{1}{d'} \left[\Pi_m^{h^0} \bar{\rho} + \sum_{m=1}^{N_f} \Pi_{r,m}^{h^0} \left(h^{0^m} - |\vec{U}|^2 \right) \rho_{T^m} + \sum_{i=1}^{N_s-1} \sum_{n=1}^{N_f} Y_i^n \left(\Pi_m^{h^0} \rho_{Y_i^n} - \Pi_{m,n}^{h^0} h_{Y_i^n}^{0^n} \rho_{T^n} \right) \right], \\
\bar{\Gamma}_{\bar{p}_{1,2}}^{-1} &= \frac{\tilde{u}}{d'} \sum_{m=1}^{N_f} \Pi_{r,m}^{h^0} \rho_{T^m}, \\
\bar{\Gamma}_{\bar{p}_{1,3}}^{-1} &= \frac{\tilde{v}}{d'} \sum_{m=1}^{N_f} \Pi_{r,m}^{h^0} \rho_{T^m}, \\
\bar{\Gamma}_{\bar{p}_{1,4}}^{-1} &= \frac{\tilde{w}}{d'} \sum_{m=1}^{N_f} \Pi_{r,m}^{h^0} \rho_{T^m}, \\
\bar{\Gamma}_{\bar{p}_{1,T^n}}^{-1} &= -\frac{\rho_{T^n}}{d'} \Pi_{m,n}^{h^0}, \\
\bar{\Gamma}_{\bar{p}_{1,Y_i^n}}^{-1} &= \frac{1}{d'} \left[\Pi_{r,n}^{h^0} \left(h_{Y_i^n}^{0^n} \rho_{T^n} - h_{T^n}^{0^n} \rho_{Y_i^n} \right) \right], \\
\bar{\Gamma}_{\bar{p}_{T^n,1}}^{-1} &= \frac{1}{\bar{\rho} d'} \left[\Pi_{m,n}^{h^0} \left(\bar{\rho} \rho_{\bar{p}} |\vec{U}|^2 + \bar{\rho} \right) - h^{0^n} \left(\sum_{r=1, r \neq n}^{N_f} \Pi_{m,r,n}^{h^0} \rho_{T^r} + \rho_{\bar{p}} \bar{\rho} \Pi_{r,n}^{h^0} \right) \right. \\
&\quad + \sum_{m=1, m \neq n}^{N_f} \rho_{T^m} h^{0^m} \Pi_{r,m,n}^{h^0} + \sum_{i=1}^{N_s-1} \left[\left(\Pi_{r,n}^{h^0} \rho_{Y_i^n} + \Pi_{r,n}^{h^0} h_{Y_i^n}^{0^n} \bar{\rho} \rho_{\bar{p}} \right. \right. \\
&\quad \left. \left. + \sum_{r=1, r \neq n}^{N_f} \Pi_{m,r,n}^{h^0} h_{Y_i^n}^{0^n} \rho_{T^r} Y_i^n + \sum_{m=1, m \neq n}^{N_f} \left(\Pi_{r,n}^{h^0} \rho_{Y_i^m} - \Pi_{r,m,n}^{h^0} h_{Y_i^m}^{0^m} \rho_{T^m} \right) Y_i^m \right] \right], \\
\bar{\Gamma}_{\bar{p}_{T^n,2}}^{-1} &= -\tilde{u} \frac{\rho_{\bar{p}}}{d'} \Pi_{m,n}^{h^0},
\end{aligned}$$

$$\begin{aligned}
\bar{\Gamma}_{\bar{\rho}_{T^n,3}}^{-1} &= -\tilde{v} \frac{\rho_{\bar{p}}}{d'} \Pi_{m,n}^{h^0}, \\
\bar{\Gamma}_{\bar{\rho}_{T^n,4}}^{-1} &= -\tilde{w} \frac{\rho_{\bar{p}}}{d'} \Pi_{m,n}^{h^0}, \\
\bar{\Gamma}_{\bar{\rho}_{T^n, T^m}}^{-1} &= \begin{cases} -\frac{1}{\bar{\rho} d'} \Pi_{r,n,m}^{h^0} \rho_{T^m}, & \text{if } n \neq m \\ \frac{1}{\bar{\rho} d'} \left[\sum_{r=1, r \neq n}^{N_f} \Pi_{q,n,r}^{h^0} \rho_{T^r} + \bar{\rho} \rho_{\bar{p}} \Pi_{r,n}^{h^0} \right], & \text{if } n = m \end{cases} \\
\bar{\Gamma}_{\bar{\rho}_{T^n, Y_i^m}}^{-1} &= \begin{cases} -\frac{1}{\bar{\rho} d'} \left[\Pi_{r,n}^{h^0} \rho_{Y_i^m} - \Pi_{r,n,m}^{h^0} \rho_{T^m} h_{Y_i^m}^{0m} \right], & \text{if } n \neq m \\ -\frac{1}{\bar{\rho} d'} \left[\sum_{r=1, r \neq n}^{N_f} \Pi_{q,r,n}^{h^0} \rho_{T^r} h_{Y_i^n}^{0n} + \Pi_{r,n}^{h^0} \left(\rho_{Y_i^n} + \rho \rho_p h_{Y_i^n}^{0n} \right) \right]. & \text{if } n = m \end{cases}
\end{aligned}$$

C. Formulation of Inviscid Jacobian $\bar{\Gamma}_f$, Viscous Jacobian $\bar{\Gamma}_g$, and Source Term Jacobian $\bar{\Gamma}_h$

C.1 Formulation of Jacobians $\bar{\Gamma}_f$, $\bar{\Gamma}_g$, $\bar{\Gamma}_h$ and $\bar{\Gamma}_p^{-1}$

C.1.1 Inviscid Flux Jacobian

$$\bar{\Gamma}_f = \begin{bmatrix} \rho_{\bar{p}}\hat{U} & \bar{\rho}n_x & \bar{\rho}n_y & \bar{\rho}n_z & \rho_{T^1}\hat{U} & \dots & \rho_{T^{N_f}}\hat{U} & 0 & 0 & \rho_{Y_1^1}\hat{U} & \dots & \rho_{Y_{N_s}^{N_f}}\hat{U} \\ \bar{\Gamma}_{f_{2,1}} & \bar{\Gamma}_{f_{2,2}} & \bar{\rho}\hat{u}n_y & \bar{\rho}\hat{u}n_z & \rho_{T^1}\hat{U}\hat{u} & \dots & \rho_{T^{N_f}}\hat{U}\hat{u} & 0 & 0 & \rho_{Y_1^1}\hat{U}\hat{u} & \dots & \rho_{Y_{N_s}^{N_f}}\hat{U}\hat{u} \\ \bar{\Gamma}_{f_{3,1}} & \bar{\rho}\hat{u}n_x & \bar{\Gamma}_{f_{3,3}} & \bar{\rho}\hat{v}n_z & \rho_{T^1}\hat{U}\hat{v} & \dots & \rho_{T^{N_f}}\hat{U}\hat{v} & 0 & 0 & \rho_{Y_1^1}\hat{U}\hat{v} & \dots & \rho_{Y_{N_s}^{N_f}}\hat{U}\hat{v} \\ \bar{\Gamma}_{f_{4,1}} & \bar{\rho}\hat{w}n_x & \bar{\rho}\hat{w}n_y & \bar{\Gamma}_{f_{4,4}} & \rho_{T^1}\hat{U}\hat{w} & \dots & \rho_{T^{N_f}}\hat{U}\hat{w} & 0 & 0 & \rho_{Y_1^1}\hat{U}\hat{w} & \dots & \rho_{Y_{N_s}^{N_f}}\hat{U}\hat{w} \\ (H_{\bar{p}}^1 + 1)\hat{U} & \bar{\Gamma}_{f_{h^{0^1,2}}} & \bar{\Gamma}_{f_{h^{0^1,3}}} & \bar{\Gamma}_{f_{h^{0^1,4}}} & H_{T^1}^1\hat{U} & \dots & H_{T^{N_f}}^1\hat{U} & 0 & 0 & H_{Y_1^1}^1\hat{U} & \dots & H_{Y_{N_s}^{N_f}}^1\hat{U} \\ \dots & 0 & 0 & \dots & \dots & \dots \\ (H_{\bar{p}}^{N_f} + 1)\hat{U} & \bar{\Gamma}_{f_{h^{0^{N_f,2}}}} & \bar{\Gamma}_{f_{h^{0^{N_f,3}}}} & \bar{\Gamma}_{f_{h^{0^{N_f,4}}}} & H_{T^1}^{N_f}\hat{U} & \dots & H_{T^{N_f}}^{N_f}\hat{U} & 0 & 0 & H_{Y_1^1}^{N_f}\hat{U} & \dots & H_{Y_{N_s}^{N_f}}^{N_f}\hat{U} \\ \rho_{\bar{p}}\hat{U}k & \bar{\rho}kn_x & \bar{\rho}kn_y & \bar{\rho}kn_z & \rho_{T^1}\hat{U}k & \dots & \rho_{T^{N_f}}\hat{U}k & \rho\hat{U} & 0 & \rho_{Y_1^1}\hat{U}k & \dots & \rho_{Y_{N_s}^{N_f}}\hat{U}k \\ \rho_{\bar{p}}\hat{U}\omega & \bar{\rho}\omega n_x & \bar{\rho}\omega n_y & \bar{\rho}\omega n_z & \rho_{T^1}\hat{U}\omega & \dots & \rho_{T^{N_f}}\hat{U}\omega & 0 & \rho\hat{U} & \rho_{Y_1^1}\hat{U}\omega & \dots & \rho_{Y_{N_s}^{N_f}}\hat{U}\omega \\ \rho_{\bar{p}}\hat{U}Y_1^1 & \bar{\rho}Y_1^1 n_x & \bar{\rho}Y_1^1 n_y & \bar{\rho}Y_1^1 n_z & \rho_{T^1}Y_1^1\hat{U} & \dots & \rho_{T^{N_f}}Y_1^1\hat{U} & 0 & 0 & \gamma_{1,Y_1^1}^1\hat{U} & \dots & \gamma_{1,Y_{N_s}^{N_f}}^1\hat{U} \\ \dots & 0 & 0 & \dots & \dots & \dots \\ \rho_{\bar{p}}\hat{U}Y_{N_s}^{N_f} & \bar{\rho}Y_{N_s}^{N_f} n_x & \bar{\rho}Y_{N_s}^{N_f} n_y & \bar{\rho}Y_{N_s}^{N_f} n_z & \rho_{T^1}Y_{N_s}^{N_f}\hat{U} & \dots & \rho_{T^{N_f}}Y_{N_s}^{N_f}\hat{U} & 0 & 0 & \gamma_{N_s,Y_1^1}^{N_f}\hat{U} & \dots & \gamma_{N_s,Y_{N_s}^{N_f}}^{N_f}\hat{U} \end{bmatrix} \quad (\text{C.1})$$

$$\begin{aligned}
\bar{\Gamma}_{f_{2,1}} &= \rho_{\bar{p}} \hat{U} \tilde{u} + n_x, \\
\bar{\Gamma}_{f_{3,1}} &= \rho_{\bar{p}} \hat{U} \tilde{v} + n_y, \\
\bar{\Gamma}_{f_{4,1}} &= \rho_{\bar{p}} \hat{U} \tilde{w} + n_z, \\
\bar{\Gamma}_{f_{2,2}} &= \bar{\rho} \left(\tilde{u} n_x + \hat{U} \right), \\
\bar{\Gamma}_{f_{3,3}} &= \bar{\rho} \left(\tilde{v} n_y + \hat{U} \right), \\
\bar{\Gamma}_{f_{4,4}} &= \bar{\rho} \left(\tilde{w} n_z + \hat{U} \right), \\
\bar{\Gamma}_{f_{h^{0n},2}} &= \bar{\rho} \left(\hat{U} \tilde{u} + n_x h^{0n} \right), \\
\bar{\Gamma}_{f_{h^{0n},3}} &= \bar{\rho} \left(\hat{U} \tilde{v} + n_y h^{0n} \right), \\
\bar{\Gamma}_{f_{h^{0n},4}} &= \bar{\rho} \left(\hat{U} \tilde{w} + n_z h^{0n} \right).
\end{aligned}$$

C.1.2 Viscous Flux Jacobian

Let \vec{n} is normal vector of a cell face as mentioned before and \vec{m} is the vector in the direction of the gradient $\nabla\phi$ of a scalar ϕ .

$$\vec{n} \cdot \vec{m} = n_x m_x + n_y m_y + n_z m_z \quad (\text{C.2})$$

The different terms in the jacobian are,

$$\begin{aligned}
\bar{\Gamma}_{g_{2,2}} &= (\mu + \mu_t) \left(\frac{4}{3} m_x n_x + m_y n_y + m_z n_z \right), \\
\bar{\Gamma}_{g_{2,3}} &= (\mu + \mu_t) \left(-\frac{2}{3} m_y n_x + m_x n_y \right), \\
\bar{\Gamma}_{g_{2,4}} &= (\mu + \mu_t) \left(-\frac{2}{3} m_z n_x + m_x n_z \right), \\
\bar{\Gamma}_{g_{3,2}} &= (\mu + \mu_t) \left(-\frac{2}{3} m_x n_y + m_y n_x \right), \\
\bar{\Gamma}_{g_{3,3}} &= (\mu + \mu_t) \left(m_x n_x + \frac{4}{3} m_y n_y + m_z n_z \right), \\
\bar{\Gamma}_{g_{3,4}} &= (\mu + \mu_t) \left(-\frac{2}{3} m_z n_y + m_y n_z \right), \\
\bar{\Gamma}_{g_{4,2}} &= (\mu + \mu_t) \left(-\frac{2}{3} m_x n_z + m_z n_x \right), \\
\bar{\Gamma}_{g_{4,3}} &= (\mu + \mu_t) \left(-\frac{2}{3} m_y n_z + m_z n_y \right), \\
\bar{\Gamma}_{g_{4,4}} &= (\mu + \mu_t) \left(m_x n_x + m_y n_y + \frac{4}{3} m_z n_z \right), \\
\bar{\Gamma}_{g_{T^n, T^m}} &= \begin{cases} 0, & \text{if } n \neq m \\ \left(\rho D + \frac{\mu_t}{Pr_t} \right) \frac{\partial h^n}{\partial T^n} (\vec{n} \cdot \vec{m}), & \text{if } n = m \end{cases} \\
\bar{\Gamma}_{g_{T^n, Y_i^m}} &= \begin{cases} 0, & \text{if } n \neq m \\ \left(\rho D + \frac{\mu_t}{Pr_t} \right) h_i^n (\vec{n} \cdot \vec{m}), & \text{if } n = m \end{cases} \\
\bar{\Gamma}_{g_{k,k}} &= \left(\mu + \sigma_k \frac{\bar{\rho} k}{\omega} \right) (\vec{n} \cdot \vec{m}), \\
\bar{\Gamma}_{g_{\omega, \omega}} &= \left(\mu + \sigma_\omega \frac{\bar{\rho} k}{\omega} \right) (\vec{n} \cdot \vec{m}), \\
\bar{\Gamma}_{g_{Y_i^n, Y_j^m}} &= \begin{cases} 0, & \text{if } n \neq m \\ \delta_{ij} \left(\rho D + \frac{\mu_t}{Pr_t} \right) (\vec{n} \cdot \vec{m}), & \text{if } n = m \end{cases}
\end{aligned}$$

C.1.3 Source Term Jacobian

$$\begin{aligned}
\bar{\Gamma}_{h_{T^n},1} &= \rho_{\bar{p}} \left(\frac{M_{h^n}}{\bar{\rho}} + \frac{1}{2} \sqrt{2 \frac{(\Gamma_{ch} + \Gamma_t)}{\bar{\rho}}} \phi_{h^n} \frac{\partial h^n}{\partial x_k} \frac{\eta_k}{\sqrt{dt}} \right), \\
\bar{\Gamma}_{h_{T^n},T^m} &= \rho_{T^m} \frac{M_{h^n}}{\bar{\rho}} - \bar{\rho} C_{\phi} \Omega \left(\frac{\partial h^n}{\partial T^m} - \frac{1}{N_f} \frac{\partial h^m}{\partial T^m} \right) \\
&+ \sqrt{2 \frac{(\Gamma_{ch} + \Gamma_t)}{\bar{\rho}}} \phi_{h^n} \frac{\eta_k}{\sqrt{dt}} \left(\frac{\rho_{T^m}}{2} \frac{\partial h^n}{\partial x_k} + \bar{\rho} \frac{\partial}{\partial x_k} \left(\frac{\partial h^n}{\partial T^m} \right) \right), \\
\bar{\Gamma}_{h_{T^n},\omega} &= \frac{M_{h^n}}{\Omega} \frac{\partial \Omega}{\partial \omega}, \\
\bar{\Gamma}_{h_{T^n},Y_i^m} &= \rho_{Y_i^m} \frac{M_{h^n}}{\bar{\rho}} - \bar{\rho} C_{\phi} \Omega \left(\frac{\partial h^n}{\partial Y_i^m} - \frac{1}{N_f} \frac{\partial h^m}{\partial Y_i^m} \right) \\
&+ \sqrt{2 \frac{(\Gamma_{ch} + \Gamma_t)}{\bar{\rho}}} \phi_{h^n} \frac{\eta_k}{\sqrt{dt}} \left(\frac{\rho_{Y_i^m}}{2} \frac{\partial h^n}{\partial x_k} + \bar{\rho} \frac{\partial}{\partial x_k} \left(\frac{\partial h^n}{\partial Y_i^m} \right) \right), \\
\dot{\omega}_k &= \tilde{\tau}_{t,jk} \frac{\partial \tilde{u}_j}{\partial x_k} - \beta^* \bar{\rho} k \omega, \\
\dot{\omega}_\omega &= \frac{\gamma \omega}{k} \tilde{\tau}_{t,jk} \frac{\partial \tilde{u}_j}{\partial x_k} - \beta \bar{\rho} \omega^2 + \bar{\rho} \frac{\sigma_d}{\omega} \frac{\partial k}{\partial x_j} \frac{\partial \omega}{\partial x_j}, \\
\bar{\Gamma}_{h_{k,k}} &= \dot{\omega}_k / k, \\
\bar{\Gamma}_{h_{k,\omega}} &= -\frac{\tilde{\tau}_{t,jk}}{\omega} \frac{\partial \tilde{u}_j}{\partial x_k} - \beta^* \bar{\rho} k, \\
\bar{\Gamma}_{h_{\omega,k}} &= 0, \\
\bar{\Gamma}_{h_{\omega,\omega}} &= -2\beta \bar{\rho} \omega - \frac{\partial \beta}{\partial \omega} \bar{\rho} \omega^2 - \bar{\rho} \frac{\sigma_d}{\omega^2} \frac{\partial k}{\partial x_j} \frac{\partial \omega}{\partial x_j}, \\
\bar{\Gamma}_{h_{Y_i^n},1} &= \rho_{\bar{p}} \dot{\omega}_i^n + \bar{\rho} \frac{\partial \dot{\omega}_i^n}{\partial \bar{p}} + \rho_{\bar{p}} \left(\frac{M_{Y_i^n}}{\bar{\rho}} + \frac{1}{2} \sqrt{2 \frac{(\Gamma_{cY_i} + \Gamma_t)}{\bar{\rho}}} \phi_{Y_i^n} \frac{\partial Y_i^n}{\partial x_k} \frac{\eta_k}{\sqrt{dt}} \right), \\
\bar{\Gamma}_{h_{Y_i^n},T^m} &= \frac{\partial \dot{\omega}_i^n}{\partial T^m} \delta_{nm} + \rho_{T^m} \frac{M_{Y_i^n}}{\bar{\rho}} - \bar{\rho} C_{\phi} \Omega \left(\frac{\partial Y_i^n}{\partial T^m} - \frac{1}{N_f} \frac{\partial Y_i^n}{\partial T^m} \right) \\
&+ \sqrt{2 \frac{(\Gamma_{cY_i} + \Gamma_t)}{\bar{\rho}}} \phi_{Y_i^n} \frac{\eta_k}{\sqrt{dt}} \left(\frac{\rho_{T^m}}{2} \frac{\partial Y_i^n}{\partial x_k} + \bar{\rho} \frac{\partial}{\partial x_k} \left(\frac{\partial Y_i^n}{\partial T^m} \right) \right), \\
\bar{\Gamma}_{h_{Y_i^n},\omega} &= \frac{M_{Y_i^n}}{\Omega} \frac{\partial \Omega}{\partial \omega}, \\
\bar{\Gamma}_{h_{Y_i^n},Y_j^m} &= \frac{\partial \dot{\omega}_i^n}{\partial Y_j^m} \delta_{nm} + \rho_{Y_j^m} \frac{M_{Y_i^n}}{\bar{\rho}} - \bar{\rho} C_{\phi} \Omega \left(\frac{\partial Y_i^n}{\partial Y_j^m} - \frac{1}{N_f} \frac{\partial Y_i^n}{\partial Y_j^m} \right) \\
&+ \sqrt{2 \frac{(\Gamma_{cY_i} + \Gamma_t)}{\bar{\rho}}} \phi_{Y_i^n} \frac{\eta_k}{\sqrt{dt}} \left(\frac{\rho_{Y_j^m}}{2} \frac{\partial Y_i^n}{\partial x_k} + \bar{\rho} \frac{\partial}{\partial x_k} \left(\frac{\partial Y_i^n}{\partial Y_j^m} \right) \right),
\end{aligned}$$

The terms, $\frac{\partial \dot{\omega}_i^n}{\partial p}$, $\frac{\partial \dot{\omega}_i^n}{\partial T^n}$ and $\frac{\partial \dot{\omega}_i^n}{\partial Y_j^n}$ are obtained from the current implementation in GEMS.

VITA

Tejas Pant was born on May 25, 1989 in Nanded, India. He completed his undergraduate studies at Visvesvaraya National Institute of Technology, Nagpur majoring in Mechanical Engineering. During his undergraduate studies he was selected for the summer fellowship program at the Indian Institute of Technology Madras, Chennai. He also completed a six month internship during his Masters study at BMW AG, Munich, Germany during the summer and fall of 2013. Tejas received a Master of Science degree in Mechanical Engineering from Purdue University, West Lafayette in summer 2014. Later that summer, he moved to the School of Aeronautics and Astronautics Engineering to start his PhD study. During his PhD study he was worked on a wide variety of turbulent combustion modeling problems. After completing his PhD study he plans to join the industry.